



AFRL-RY-HS-TR-2011-0001 Volume II

**PROCEEDINGS OF THE 2010 ANTENNA APPLICATIONS SYMPOSIUM
Volume II of II**

Daniel Schaubert et al.

**University of Massachusetts at Amherst
Electrical and Computer Engineering
100 Natural Resources Road
Amherst MA 01003**

Final Report

December 2010

APPROVED FOR PUBLIC RELEASE; DISTRIBUTION UNLIMITED

**AIR FORCE RESEARCH LABORATORY
Sensors Directorate
Electromagnetics Technology Division
80 Scott Drive
Hanscom AFB MA 01731-2909**

NOTICE AND SIGNATURE PAGE

Using Government drawings, specifications, or other data included in this document for any purpose other than Government procurement does not in any way obligate the U.S. Government. The fact that the Government formulated or supplied the drawings, specifications, or other data does not license the holder or any other person or corporation; or convey any rights or permission to manufacture, use, or sell any patented invention that may relate to them.

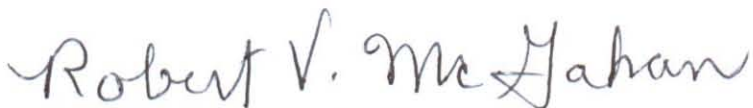
This report was cleared for public release by the Electronic Systems Center Public Affairs Office for the Air Force Research Laboratory Electromagnetic Technology Division and is available to the general public, including foreign nationals. Copies may be obtained from the Defense Technical Information Center (DTIC) (<http://www.dtic.mil>).

AFRL-RY-HS-TR-2011-0001 HAS BEEN REVIEWED AND IS APPROVED FOR PUBLICATION IN ACCORDANCE WITH ASSIGNED DISTRIBUTION STATEMENT.



DAVID D. CURTIS

Chief, Antenna Technology Branch



ROBERT V. McGAHAN

Technical Communications Advisor
Electromagnetic Technology Division

This report is published in the interest of scientific and technical information exchange, and its publication does not constitute the Government's approval or disapproval of its ideas or findings.

REPORT DOCUMENTATION PAGE

*Form Approved
OMB No. 0704-0188*

Public reporting burden for this collection of information is estimated to average 1 hour per response, including the time for reviewing instructions, searching existing data sources, gathering and maintaining the data needed, and completing and reviewing this collection of information. Send comments regarding this burden estimate or any other aspect of this collection of information, including suggestions for reducing this burden to Department of Defense, Washington Headquarters Services, Directorate for Information Operations and Reports (0704-0188), 1215 Jefferson Davis Highway, Suite 1204, Arlington, VA 22202-4302. Respondents should be aware that notwithstanding any other provision of law, no person shall be subject to any penalty for failing to comply with a collection of information if it does not display a currently valid OMB control number. **PLEASE DO NOT RETURN YOUR FORM TO THE ABOVE ADDRESS.**

1. REPORT DATE (DD-MM-YYYY) December 2010	2. REPORT TYPE FINAL REPORT	3. DATES COVERED (From - To) 21 Sep 2010 – 23 Sep 2010		
4. TITLE AND SUBTITLE Proceedings of the 2010 Antenna Applications Symposium, Volume II			5a. CONTRACT NUMBER 5b. GRANT NUMBER 5c. PROGRAM ELEMENT NUMBER	
6. AUTHOR(S) Daniel Schaubert, et al.			5d. PROJECT NUMBER 4916 5e. TASK NUMBER HA 5f. WORK UNIT NUMBER 01	
7. PERFORMING ORGANIZATION NAME(S) AND ADDRESS(ES) University of Massachusetts Amherst Electrical and Computer Engineering 100 Natural Resources Road Amherst, MA 01003			8. PERFORMING ORGANIZATION REPORT	
9. SPONSORING / MONITORING AGENCY NAME(S) AND ADDRESS(ES) Electromagnetics Technology Division Sensors Directorate Air Force Research Laboratory 80 Scott Drive Hanscom AFB MA 01731-2909			10. SPONSOR/MONITOR'S ACRONYM(S) AFRL-RY-HS 11. SPONSOR/MONITOR'S REPORT NUMBER(S) AFRL-RY-HS-TR-2011-0001	
12. DISTRIBUTION / AVAILABILITY STATEMENT APPROVED FOR PUBLIC RELEASE; DISTRIBUTION UNLIMITED				
13. SUPPLEMENTARY NOTES Volume I contains pages 1- 255 Public Affairs release Number 66 ABW-2011-0024 Volume II contains pages 256-513				
14. ABSTRACT The Proceedings of the 2010 Antenna Applications Symposium is a collection of state-of-the art papers relating to antenna arrays and elements, millimeter wave antennas, simulation and measurement of antennas, integrated antennas, and antenna bandwidth and radiation improvements.				
15. SUBJECT TERMS Antennas, phased arrays, digital beam forming, millimeter waves, metamaterials, antenna measurements, airborne antenna applications, Vivaldi antennas, waveguide antenna arrays, broadband arrays, electrically small antennas				
16. SECURITY CLASSIFICATION OF:		17. LIMITATION OF ABSTRACT UU	18. NUMBER OF PAGES 269	19a. NAME OF RESPONSIBLE PERSON David D. Curtis 19b. TELEPHONE NUMBER (include area code) N/A
a. REPORT Unclassified	b. ABSTRACT Unclassified	c. THIS PAGE Unclassified		

2010 ANTENNA APPLICATIONS SYMPOSIUM

21 - 23 September 2010
Monticello, Illinois

The Long Road to Affordable Phased Arrays L. Coryell, R. Hoffman, R. Lau and J. Shields	1
A Ku-band Parasitic Array for Data Link Systems J.P. Doane and L.M. Paulsen	17
Evolution of a Commercial Phased Array J.M. Carey	31
A 8X8 Wideband Ribcage-Dipole Array for Directed Power Applications and Its Characteristics D.D. Harty, B. Janice, S.N. Makarov and F. Scire Scappuzzo	46
Polyomino Subarrays for Time-Delay Insertion: Recent Results R.J. Mailloux, S.G. Santarelli and T.M. Roberts	64
A Compact Stackable Antenna for Multiband Systems J.P. Doane and R.J. Legge	79
Self-Supporting Coaxial Antenna with an Integrated Balun and a Linear Array Thereof V. Iyer, A. Cavanaugh, S.N. Makarov, R.J. Duckworth and D. Cyganski	91
Fabrication and Performance of Broadband, Waveguide-to-Stripline Transition for Phased Arrays M.J. Buckley, W. Elsallal, B.J. Herting, J. Mather, J. Wolf and J. West	109
Wide Band and Wide Scan Metamaterial Loaded Radiating Elements M.J. Buckley, J. Wolf, B.J. Herting, S. Patten, J. Mather, D. Manson and J.B. West	124

Antenna Design Using a Metamaterial Ground Plane	139
H.L. Southall, T.H. O'Donnell, J.S. Derov and J.W. Allen	
Variable UHF-Band Artificial Magnetic Conductors	150
D.J. Gregoire, C.R. White, J.S. Colburn, and G.P. Johnson	
Resonant Antennas Based on Coupled Transmission-Line Metamaterials	166
C. Merola and D-H. Kwon	
Time Domain Characterization of Equiangular and Archimedean Spiral Antennas	185
M.A. Elmansouri and D.S. Filipovic	
Asymmetrical Low Frequency Conformal Antennas for Small Unmanned Aerial Vehicles: Dipole and Monopole Tradeoffs	197
B.T. Strojny and R.G. Rojas	
Impact of Varactor Placement on Radiation Efficiency of Electrically Small Frequency Reconfigurable Antennas	209
S. Yong and J. Bernhard	
A Fully Planar Ultrawideband Array	221
S.S. Holland and M.N. Vouvakis	
A Phase-Reconfigurable Reflectarray Element Using Fluidic Networks	233
S.A. Long and G.H. Huff	
Miniaturized Patch Antennas with Multiple Bands of Operation for Microwave Breast Imaging	245
M. Al-Joumayly, S. Aguilar, N. Behdad and S.C. Hagness	
Tuning Small Monopole Antennas: Modes, Stubs and Q	256
J.J. Adams and J.T. Bernhard	
Backscatter of Small Resonant Plates with Linear Slots Revisited	270
C. Van Niekerk and J.T. Bernhard	
Carter Dipoles and Resonant Dipoles	282
R.C. Hansen	

Artificial Impedance Surface Antenna Design and Simulation	288
D.J. Gregoire and J.S. Colburn	
uCAST - A New Generation UTD Code for Radiation Pattern Predictions of Antennas on Aircraft Models	304
Ç. Tokgöz and C. J. Reddy	
Electrically Small Antenna Design for Low Frequency Systems	315
E.A. Richards, H.G. Schantz, J.A. Unden, K.A. von Laven, D. Compston and C. Weil	
Super-Resolving Biomimetic Electrically Small Antennas and Their Applications	340
N. Behdad and M.A. Al-Joumayly	
Compact Multiband Planar Mobile Antenna Operating Over LTE, GSM, WLAN and WiMAX Bands	352
M.R. Khan, M. Morsy, D.W. Addison and F.J. Harackiewicz	
Efficiency Improvements of a Directly-Driven Antenna-Based AM Transmitter over the AM Frequency Band	372
O.O. Olaode, W.T. Joines and W.D. Palmer	
Development of Conformal Space Suit Antennas for Enhanced EVA Communications and Wearable Computer Applications	389
T.G. Campbell, C.W. Hearn, C. J. Reddy, R.C. Boyd, T. Yang, W.A. Davis, A. Persans and S. Scarborough	
A Low-Profile Antenna Design Approach for Conformal Space Suit and Other Wearable Applications	418
T. Yang, W.A. Davis, T.G. Campbell and C.J. Reddy	
Investigation of Miniaturized and Dual-Band Slot Antennas for RFID Systems	441
J.E. Ruyle and J.T. Bernhard	
Wideband Horizontally Polarized Omni-Directional Antenna	455
R. Pickles	

Investigation into a Frequency Reconfigurable MIMO Dielectric Resonator Antenna	467
J-B.Yan and J.T Bernhard	
Millimeter-Wave Dielectric Loss Characterization with One-Dimensional Grating	486
V.I. Litvinov, V.A. Manasson, M. Felman and L.S. Sadovnik	
A Low-Cost, Multi-Channel, S-Band Transmit/Receive Module for Phased Array Communication Systems	494
S.S. Bharj, B. Tomasic, J. Turtle, R. Turner, G. Scalzi and S. Liu	

Identifiers for Proceedings of Symposia
The USAF Antenna Research and Development Program

Year	Symp. No.	Identifier
1951	First	
1952	Second	ADB870006
1953	Third	ADB283180
1954	Fourth	AD63139
1955	Fifth	AD90397
1956	Sixth	AD114702
1957	Seventh	AD138500
1958	Eighth	AD301151
1959	Ninth	AD314721
1960	Tenth	AD244388 (Vol. 1) AD319613 (Vol. 2)
1961	Eleventh	AD669109 (Vol. 1) AD326549 (Vol. 2)
1962	Twelfth	AD287185 (Vol. 1) AD334484 (Vol. 2)
1963	Thirteenth	AD421483
1964	Fourteenth	AD609104
1965	Fifteenth	AD474238L
1966	Sixteenth	AD800524L
1967	Seventeenth	AD822894L
1968	Eighteenth	AD846427L
1969	Nineteenth	AD860812L
1970	Twentieth	AD875973L
1971	Twenty-First	AD888641L
1972	Twenty-Second	AD904360L
1973	Twenty-Third	AD914238L

Antenna Applications Symposium

Year	Symposium	Technical Report #	Identifier
1977	First	None	ADA 955413
1978	Second	None	ADA 955416
1979	Third	_____	ADA 077167
1980	Fourth	_____	ADA 205907
1981	Fifth	_____	ADA 205816
1982	Sixth	_____	ADA 129356
1983	Seventh	_____	ADA 142003; 142754
1984	Eighth	85-14	ADA 153257; 153258
1985	Ninth	85-242	ADA 166754; 165535
1986	Tenth	87-10	ADA 181537; 181536
1987	Eleventh	88-160	ADA 206705; 206704
1988	Twelfth	89-121	ADA 213815; 211396
1989	Thirteenth	90-42	ADA 26022; 226021
1990	Fourteenth	91-156	ADA 37056; 237057
1991	Fifteenth	92-42	ADA 253681; 253682
1992	Sixteenth	93-119	ADA 268167; 266916
1993	Seventeenth	94-20	ADA 277202; 277203
1994	Eighteenth	95-47	ADA 293258; 293259
1995	Nineteenth	96-100	ADA 309715; 309723
1996	Twentieth	97-189	ADA 341737
1997	Twenty First	1998-143	ADA 355120
1998	Twenty Second	1999-86	ADA 364798
1999	Twenty Third	2000-008 (I) (II)	ADA 386476; 386477
2000	Twenty Fourth	2002-001 Vol I & II	ADA 405537; 405538
2001	Twenty Fifth	2002-002 Vol I & II	ADA 405328; 405327
2002	Twenty Sixth	2005-001 Vol I & II	ADA 427799; 427800
2003	Twenty Seventh	2005-005 Vol I & II	ADA 429122
2004	Twenty Eighth	2005-016 Vol I & II	ADA431338; 431339
2005	Twenty Ninth	2005-039 Vol I & II	ADM001873
2006	Thirtieth	2006-0047 Vol I & II	ADA464059
2007	Thirty First	2007-0037 Vol I & II	ADA475327, 475333
2008	Thirty Second	2008-0026 Vol I & II	ADA494632, 494633
2009	Thirty Third	2010-0001 Vol I & II	ADA520099, 520100

2010 Author Index

Adams, J.J.	256	Makarov, S.N.	46, 91
Addison, D.W.	352	Manasson, V.A.	486
Aguilar, S.	245	Manson, D.	124
Al-Joumayly, M.	245, 340	Mather, J.	109, 124
Allen, J.W.	139	Merola, C.	166
Behdad, N.	245, 340	Morsy, M.	352
Bernhard, J.	209, 256, 270, 441, 467	O'Donnell, T.H.	139
Bharj, S.S.	494	Olaode, O.O.	372
Boyd, R.C.	389	Palmer, W.D.	372
Buckley, M.J.	109, 124	Patten, S.	124
Campbell, T.G.	389, 418	Paulsen, L.M.	17
Carey, J.M.	31	Persans, A.	389
Cavanaugh, A.	91	Pickles, R	455
Colburn, J.S.	150, 288	Reddy, C.J.	304, 389, 418
Compston, D.	315	Richards, E.A.	315
Coryell, L.	1	Roberts, T.M.	64
Cyganski, D.	91	Rojas, R.G.	197
Davis, W.A.	389, 418	Ruelle, J.E.	441
Derov, J.S.	139	Sadovnik, L.S.	486
Doane, J.P.	17, 79	Santarelli, S.G.	64
Duckworth, R.J.	91	Scalzi, G.	494
Elmansouri, M.A.	185	Scarborough, S.	389
Elsallal, W.	109	Schantz, H.G.	315
Felman, M.	486	Scire Scappuzzo, F.	46
Filipovic, D.S.	186	Shields, J.	1
Gregoire, D.J.	150, 288	Southall, H.L.	139
Hagness, S.C.	245	Strojny, B.T.	197
Hansen, R.C.	282	Tokgoz, C.	304
Harackiewicz, F.J.	352	Tomasic, B.	494
Harty, D.D.	46	Turner, R.	494
Hearn, C.W.	389	Turtle, J.	494
Herting, B.J.	109, 124	Unden, J.A.	315
Hoffman, R.	1	Van Niekerk, C.	270
Holland, S.S.	221	von Laven, K.A.	315
Huff, G.H.	233	Vouvakis, M.N.	221
Iyer, V.	91	Weil, C.	315
Janice, B.	46		
Johnson, G.P.	150		
Joines, W.T.	372		
Khan, M.R.	352		
Kwon, D-H.	166		
Lau, R.	1		
Legge, R.J.	79		
Litvinov, V.I.	486		
Liu, S.	494		
Long, S.A.	233		
Mailloux, R.J.	64		

TUNING SMALL MONPOLE ANTENNAS: MODES, STUBS, AND Q

Jacob J. Adams and Jennifer T. Bernhard

Electromagnetics Laboratory

University of Illinois at Urbana-Champaign, Urbana, IL 61801

<http://antennas.ece.illinois.edu>; E-mail: jbernhar@illinois.edu, jjadams@illinois.edu

Abstract: Electrically small monopole antennas can often be impedance matched using shorted stubs. This technique has some advantages over other matching techniques in that it is compact and easily realized and integrated. A characteristic mode analysis of the stub matching geometry leads to a new conception of the technique, and reveals that some earlier discussions about the matching mechanism were incomplete. It becomes readily apparent that this method is only guaranteed to work for certain classes of antennas, and we describe the conditions under which it can be applied. The stub geometry affects each mode differently and independently, but the modal interactions govern the total response. Calculating the characteristic modes of the structure, we develop a physics-based circuit model for the modal impedance and examine the Q-preserving behavior of the stub match. The characteristic mode analysis reveals that almost any space-filling structure supports a low Q mode, and leads us to a new design paradigm for small antennas.

1. Introduction

Electrically small antennas have well-known limitations in terms of their gain and quality factor (Q) [1]. In terms of their practical use, they must be impedance matched to a particular system impedance. When the antennas are electrically small, they often have very large reactances that must be matched out in addition to very small resistances that must be transformed. Matching networks typically consist of lumped or transmission line components external to the antenna. However, these components add additional size to the antenna structure. Instead, stubs of wire shorted to ground have occasionally been used to match the antenna, reducing the space required. These are often referred to as stub matched, shunt-excited, or gamma match antennas.

We previously developed a singly-resonant electrically small antenna that could be matched to a variety of system impedances by using a higher-order mode as a tuning circuit [2]. We then created a multi-resonant antenna by adjusting the higher-order mode so that it also had good radiating characteristics [3]. However, by using the tuning mode from [2] as an additional radiating mode in [3], the design lost a degree of freedom that allows selection of the impedance. In order to match the multi-resonant antenna without an external network, another mode is required. Some recent work suggests that small antennas can be matched with a shorted stub [4], [5]. Altschuler qualitatively describes

the effect as the addition of a parallel inductance, but this interpretation is not entirely satisfying, especially when compared to the Smith charts provided [4]. In order to use this technique for the matching of a multimode antenna, we need to understand the matching mechanism in more detail.

First, we review the history of the stub matching approach, and the foundations of characteristic mode theory. Characteristic mode theory suggests a circuit model for the antenna, which we then analyze to determine possible constraints of the stub match. We then examine the physical behavior of the antenna modes and relate them to the circuit model and matching procedure. Finally, we discuss antenna Q, its fundamental nature and the implications for small antenna design.

2. Background

Decades ago, antenna engineers realized that they could excite monopole antennas by shorting the base and feeding a shunt stub without significantly affecting the radiation pattern of the antenna [6], [7]. While this was originally done to reduce construction costs, Baudoux [7] did note that the input resistance of the antenna differed substantially from a standard monopole. Around the same time, folded dipoles became a significant research topic [8] for their impedance transformation properties. Related to both of these designs is the stub match or gamma match, which consists of a shorted wire parallel to the main antenna wire, but not necessarily shorted to the top of the antenna as in a folded dipole. Analysis of these antennas typically uses transmission line theory, calculating differential and common mode impedances to find the total impedance. The transmission line approach applies to simple geometries like straight, parallel wires, but would fail to explain the behavior of complex geometries like the genetic antenna of [4]. A comprehensive review of the transmission line approach to these types of antennas can be found in [9]. This paper does not seek to replace the existing theories, but instead demonstrates an alternate approach to the problem using modes and lumped circuits. The result is new physical insight into small antenna behavior that cannot be gained from the transmission line approach.

To understand the matching technique at a fundamental level, we apply characteristic mode theory (CMT) [10-12] to the structure. CMT is a method for numerically calculating a set of solutions to Maxwell's equations that form an orthogonal basis for the current on a metal structure. Thus, the total current on the structure can be expressed as a sum of the characteristic modes. This enables us to examine the behavior of each mode individually, rather than studying a summation of several modes.

At the core of CMT is the solution of a generalized eigenvalue problem, resulting in a set of eigenvalues (λ_n) and eigenvectors (J_n) such that

$$[\mathbf{X}]J_n = \lambda_n [\mathbf{R}]J_n \quad (1)$$

where [R] and [X] are the real and imaginary parts of the Moment Method impedance matrix, respectively. Using the procedure discussed in [3], this eigenvalue problem is solved at every frequency of interest, yielding a set of eigenmodes at each frequency.

The total current on the antenna is a weighted sum of the eigencurrents, thus the input admittance can be expressed as a summation of the admittances of each mode. For a gap voltage source at position \bar{r}_{feed} on a wire, the input admittance can be calculated as [13]

$$Y_{in}(\bar{r}_{feed}) = \sum_n \frac{J_n(\bar{r}_{feed})^2}{1 + \lambda_n^2} (1 - j\lambda_n). \quad (2)$$

Two types of characteristic modes are typically observed in small antennas: resonant and non-resonant modes. Resonant modes are capacitive at low frequencies, resonate, and become inductive beyond their resonance. Non-resonant modes (inductive modes) begin as inductive modes and never resonate, only ever contributing inductive susceptance to the antenna [14]. As we will see, both of these types of modes combine in the stub matched structure to transform the impedance to the desired value.

The impedance of a resonant mode can often be modeled by a series RLC circuit. Consider the admittance of such a circuit, expressed as

$$Y = \frac{1}{R(1 + Q^2\Omega^2)} (1 - jQ\Omega) \quad (3)$$

where $\Omega(f) \equiv \left(\frac{f}{f_r} - \frac{f_r}{f} \right)$ and f_r is the resonant frequency of the circuit.

Comparing the series RLC admittance in (3) to the expression for a single mode admittance from (2), we find some interesting equivalences: $R = \frac{1}{J(\bar{r}_{feed})^2}$ and $Q\Omega = \lambda$.

For most small antennas, λ has the same frequency variation as Ω , so the model of a series RLC circuit applies.

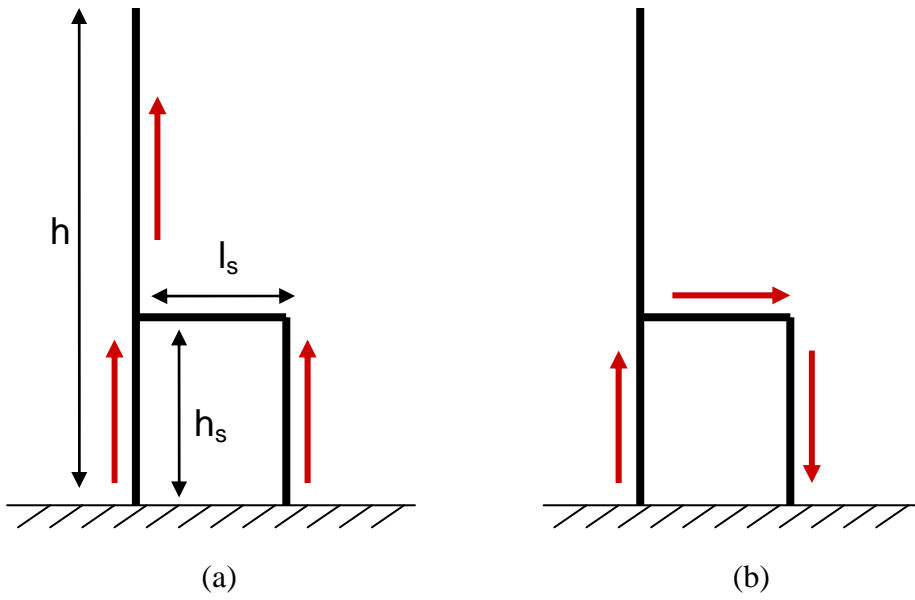


Figure 1: a) Mode 1 (common) and b) Mode 0 (differential) currents of a straight monopole with a single stub.

3. Simple Circuit Model for the Stub Matched Geometry

Consider the basic stub-matched straight monopole shown in Figure 1. Solving for the characteristic modes reveals that there are indeed two modes excited by the feed point, as envisioned by the transmission line model. Characteristic mode theory gives us a natural way of modeling the impedance of these two modes. In the case of the small monopole antenna, the circuit model is quite simple, and mirrors the one suggested by Altshuler [4]. The simple model consists of a radiating mode (series RLC resonator) in parallel with an inductor as shown in Figure 2a. However, we will see shortly that the shunt stub's effect encompasses much more than just adjusting the shunt inductance.

Let us consider the limitations of the matching technique that are implied by this simple circuit model. First, we note that the shunt inductor in parallel acts as an impedance transformer from the natural resonant resistance (R_1) to a higher resistance. For example, the conductance of a series RLC circuit, representing the radiating mode, is shown in Figure 2b. The radiating mode's self-resonance occurs at the peak, where the input resistance is R_1 (5Ω in this example). Below the resonant frequency, the modal admittance is capacitive and can be resonated with the shunt inductor. The resonant resistance is then the inverse of the admittance at that frequency. Because the conductance peak occurs at the modal self-resonant frequency, it is apparent that the resistance can only be transformed to a higher value. When the antenna is electrically small, the modal resistance tends to be small as well, so this should not present a problem. However, we observe that the modal conductance falls very quickly away from the self-resonant frequency. This suggests that the mode must be self-resonant just above

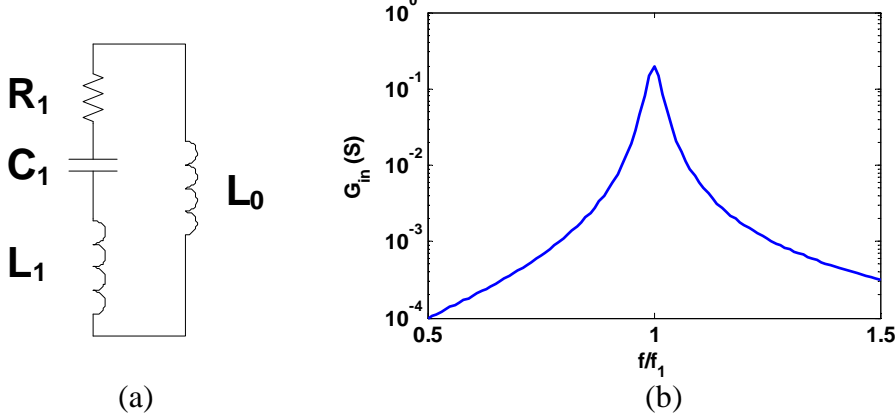


Figure 2: a) Circuit model of the stub-matched electrically small antenna and b) example conductance variation of Mode 1 ($R_1 = 5 \Omega$).

the desired match frequency, or the modal conductance will be very small, resulting in an input resistance orders of magnitude above most standard system impedances.

Second, we observe that the impedance of the series RLC in Figure 2a is given as

$$Z_1 = R_1(1 + jQ_1\Omega_1(f)) \quad (4)$$

where $\Omega_1(f) = \left(\frac{f}{f_1} - \frac{f_1}{f} \right)$. Applying the definition of Q from [15], we find

$$Q(f) = \begin{cases} Q_1 \frac{f}{f_1} & f > f_1 \\ Q_1 \frac{f_1}{f} & f < f_1 \end{cases}. \quad (5)$$

As we move away from the self-resonance of the mode, the apparent Q of the mode becomes larger. For example, if we try to match a straight monopole (self-resonant at $\lambda/4$) at a height of $\lambda/20$, the Q at that size will be a factor of 5 larger than the Q at resonance.

Considering these two problems, we should expect this matching technique to be most useful when the desired match frequency is near the self-resonant frequency of the radiating mode. For an electrically small straight monopole, this is not the case and the stub matching technique is not well-suited for the task. Self-resonance can be induced at a lower frequency using a variety of techniques to increase the mode's inductance or capacitance [16]. For instance, Altshuler's antenna was self-resonant before matching due to randomly oriented wires chosen based on a genetic algorithm [4]. However, because the simpler geometry allows some analytical calculations, we will briefly examine the impedances of the straight monopole. We then will investigate a helical monopole to force the radiating mode to be self-resonant in the electrically small region.

h_s (cm)	Predicted L_0 (nH)	Simulated L_0 (nH)	R_1 (Ω)	Q_1
--	--	--	7.5	67.4
1.0	10	12	21.0	67.2
2.5	23	26	24.2	66.5
5.0	45	48	25.1	63.6
10.0	89	88	32.3	44.0

Table 1: Circuit parameters at 300 MHz (see Fig. 2a) for straight monopole with $h = 10$ cm, wire radius = 1 mm, $l_s = 1$ cm.

l_s (cm)	Predicted L_0 (nH)	Simulated L_0 (nH)	R_1 (Ω)	Q_1
--	--	--	7.5	67.4
2	17	18	16.4	67.2
4	29	31	12.6	67.2
10	65	64	9.4	66.8
20	124	106	7.3	68.6

Table 2: Circuit parameters at 300 MHz (see Fig. 2a) for straight monopole with $h = 10$ cm, wire radius = 1 mm, $h_s = 1$ cm.

4. Stub Matched Straight Monopole

Although we have predicted that the stub matching technique will not work well for the small, straight monopole, it is instructive to study this simple structure initially. Consider a stub-matched straight monopole with dimensions as given in Figure 1. As previously discussed, there are two modes excited when the stub is grounded, Mode 0 and Mode 1. The Mode 0 currents circulate from one grounded point to the other, making it a non-resonant mode that always has an inductive admittance. It is also a very poor radiator so its impedance can be approximated by a single inductor. The inductance of Mode 0 is well-approximated by the inductance of a rectangular loop over a ground plane [17]. Tables 1 and 2 show the Mode 0 inductance compared to theoretical values of the inductance as h_s and l_s are changed.

Since the inductance of Mode 0 is easily calculated, it appears that we could easily match the Mode 1 susceptance at the required frequency by changing h_s and l_s . However, from Tables 1 and 2, we also can see that Mode 1 is not independent of the stub parameters.

In fact, the Mode 1 resonant parameters are strongly linked to the stub geometry. For this electrically short antenna, the resonance is much higher in frequency than the operating band, so we will ignore it for now. Let us examine the other two parameters as we change the stub geometry as shown in Tables 1 and 2. The Mode 1 resistance varies significantly as the stub is changed and also differs greatly from the resistance of the monopole without stub (7.5Ω). However, Q_1 remains mostly constant and very close to

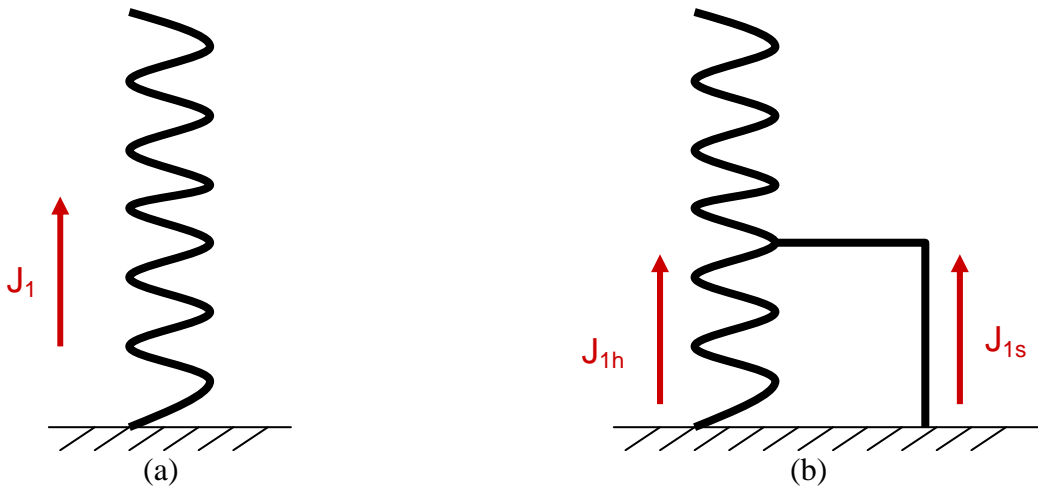


Figure 3: Schematics of the a) helical antenna currents and b) helix and stub currents.

the stub-less Q (67.4). Q_1 only begins to differ from this value when the stub approaches the same height as the monopole. In this case, the volume of radiating portion of the antenna is significantly increased. Q_1 seems to be fundamentally related to the size of the radiating structure.

5. Stub Matched Helical Monopole

As discussed in Section 3, this matching technique cannot produce a useful conductance for the short straight monopole. To apply the technique, the radiating mode must be resonant near the desired operating frequency. In order to force the resonance to occur in the electrically small region, we wind the wire into a narrow, electrically short helix as shown in Fig. 3. With a rectangular stub attached, this structure now fulfills the conditions discussed in Section 3.

Under this configuration, Mode 0 does not change except that its inductance is slightly increased because the helix now makes up one of the sides of the rectangle instead of a straight wire. L_0 can be approximately calculated the same way, with a small adjustment for the increased inductance.

Before the stub is added, the helical monopole has a $Q_1 = 38.1$, $R_1 = 7.7 \Omega$, and the resonant frequency is 300 MHz, as designed. Table 3 presents the circuit parameters of Mode 1 for a feed point at the base of the helix (1h subscripts) or at the base of the stub (1s subscripts). R_1 takes on a variety of values as the stub is modified, but is never less than the stub-less helical monopole. The resonant frequency also changes significantly. However, once again the modal Q does not change much despite the large geometric modification, so the stub tuning method preserves the Q of the original radiating mode. It is lower than the Q of the straight monopole of the same height, due to the larger volume of the helical coil. This is more evidence that the modal Q is fundamentally related to the size of the radiating portion of the antenna.

Even using the helix, it again seems difficult to match the antenna to a desired impedance since not only is L_0 related to the stub parameters, but so are R_1 and f_1 . It may be instructive to understand the dependence of R_1 and f_1 on the stub geometry. First, let us study the dependence of the resistance. Because the characteristic modes are normalized to radiate unit power, we found in Section 2 that $R_1 = \frac{1}{J_1(\bar{r}_{feed})^2}$. Therefore, studying the behavior of the modal current will lead to an understanding of the input impedance.

If a perturbation such as the stub is added but the radiating portion of the antenna is not changed significantly, we expect the total current required to radiate unit power should not change appreciably. Consider the schematic of the stub-less helical antenna in Fig. 3a. The entirety of the required current can only be drawn from the wire connected to the ground plane. In the example given, the Mode 1 current required for the stub-less antenna to radiate unit power is 361 mA. When the stub is added, approximately the same amount of current should be needed to radiate unit power. However, the current at the center feed point drops significantly to 50-200 mA. The remaining current comes from the shorted end of the stub. Unlike Mode 0, where one shorted end draws current from the ground plane and the other deposits an equal amount of current onto the ground plane, the Mode 1 currents are both drawn *from* the ground plane at the two shorted points. Thus, the sum of these currents ($J_{1h} + J_{1s}$) should be approximately equal to the total current for the stub-less helix (J_1). Comparing the last column of Table 3, the total current tends to be equal to or slightly less than the current of the stub-less monopole. For some perspective on how similar these total current values are, we observe that for the same geometric modifications, the Mode 0 current ranges from 4,000 to 77,000 mA. It is important to realize that this is not the current on the actual antenna, but the amount of current needed to radiate 1 W if Mode 0 could be excited by itself with no mismatch loss. If these values seem large, it is because Mode 0 is very poor radiator, and behaves primarily as an inductor.

The stub reduces the Mode 1 current at both feed points below the current of the single feed. Therefore, in this shorted helix configuration, the stub acts like a transformer for the Mode 1 resistance. The stub also adjusts the division of the Mode 1 current between the potential feed points, and the impedance transformation ratio is a function of the stub geometry and the choice of feed point. Let $J_{1h} = \alpha J_1$, then $J_{1s} \approx (1 - \alpha)J_1$. Because CMT does not require that we choose a feed point until we calculate the input impedance, there are two possible resistances that can be seen at the input: $R_{1h} = \frac{R_1}{\alpha^2}$ and

$$R_{1s} = \frac{R_1}{(1 - \alpha)^2} .$$

h_s (cm)	f_1 (MHz)	R_{lh} (Ω)	Q_{lh}	J_{lh} (mA)	R_{ls} (Ω)	Q_{ls}	J_{ls} (mA)	J_{lt} (mA)
--	300	7.7	38.1	361	--	--	--	361
0.5	305	64	38.0	125	19.2	38.1	228	354
1.0	314	130	38.1	88	14.9	38.2	259	346
2.0	338	197	36.5	71	14.0	37.4	267	338
4.0	409	193	34.0	72	14.0	36.4	268	340
8.0	458	84	39.0	109	15.7	34.7	252	361

Table 3: Circuit parameters at 300 MHz for helical monopole of height = 10 cm, helix pitch = 6.37 mm, helix radius = 5 mm, wire radius = 1 mm, l_s = 1 cm.

l_s (cm)	f_1 (MHz)	R_{lh} (Ω)	Q_{lh}	J_{lh} (mA)	R_{ls} (Ω)	Q_{ls}	J_{ls} (mA)	J_{lt} (mA)
--	300	7.7	38.1	361	--	--	--	361
-0.5	316	1362	37.3	27	9.8	38.1	319	346
1.0	314	130	38.1	88	14.9	38.2	259	346
2.0	312	58	38.3	131	21.3	38.3	217	348
4.0	310	29	38.6	186	36.5	38.3	166	352

Table 4: Circuit parameters at 300 MHz for helical monopole of height = 10 cm, helix pitch = 6.37 mm, helix radius = 5 mm, wire radius = 1 mm, l_s = 1 cm.

In a practical scenario, the stub is close to the helix ($l_s < h_s$), and the current path through the stub is less inductive than the bottom portion of the helix. Therefore, α is usually less than 0.5 (*i.e.*, most of the current flows through the stub) so that $R_{lh} > R_{ls} > R_l$. In many cases, only a small impedance step up is needed (from 7.7 Ω to 50 Ω in this case), and the stub feed point provides this small increase while the helix-center feed sees a very large and undesirable impedance.

Interestingly, in the case of equal current division ($\alpha = 0.5$), this analysis predicts a 4:1 impedance step up, just as with a folded dipole. Furthermore, it predicts a N²:1 step up in the case of N stubs that each draw equal current, the same as an N-element folded dipole.

Kraus notes that feeding a shunt tap increases the impedance of the electrically small helix to match to common transmission lines [18]. However, no design intuition is given. Calculating precise formulas for the current division coefficient α is beyond the scope of this work, but it is useful to develop some general intuition for how α changes so that this approach can be applied to a variety of complex antenna shapes in addition to the short helix. From Table 3, we see that changing the height of the stub has little effect on the splitting of the current, so the height may be neglected when approximating the current division. However, it is clear from Table 4 that the distance between the stub and the helix has a large influence on the way the current splits. As the stub is moved farther away from the helix, the percentage of current drawn through the stub decreases. In general, when the inductance of one path is increased, the current flowing on that path

decreases. For example, if the wire radius of the stub is decreased, more of the current flows through the helix. Alternatively, if the antenna is made electrically smaller (i.e. the helix pitch is decreased), less current will flow through the helix for the same h_s , l_s because the helix path is now even more inductive.

Under most configurations, feeding the stub is preferable to feeding the helix center for reasons in addition to the stub's lower resistance. Most of the Mode 1 current usually flows through the stub, so Mode 1 is well-excited by the stub feed. Because the Mode 0 current circulates without much radiation, Mode 0 is excited equally at either feed. It is better to excite the radiating mode strongly while weakly exciting the matching mode, or the total response may be very inductive, high Q, and inefficient.

If only R_1 and L_0 depended on the stub geometry, the antenna could be readily matched to the desired impedance by making the antenna resonant slightly above the desired frequency, and selecting R_1 and L_0 as necessary to resonate the antenna at the desired frequency and resistance. However, there is one additional complication: the Mode 1 resonant frequency also changes with modifications to the stub. The frequency, f_1 , is primarily affected by h_s . If the stub taps the helix very close to the bottom, f_1 is only slightly higher than the original frequency. As the stub moves towards the top, f_1 becomes close to the resonant frequency of a short, straight monopole. For this particular geometry, the new f_1 can be approximated by

$$f'_1 \approx \frac{f_1}{1 + \frac{h_s}{h}(s-1)} \quad (6)$$

where s is the shortening ratio of the helix (i.e., the helix height divided by a quarter wavelength at resonance). Now using the physical intuition of the geometry and modes, we can design a match for an antenna of any height or geometry.

6. Modal Q, Antenna Size, and Matching

As we saw in our analysis of the stub matching technique, the modal Q seems to be fundamentally determined by the size of the antenna and factors like the feed location and small geometric features are extraneous. For monopole-like electrically small antennas, the lowest order mode exists with a particular Q regardless of these factors. However, they do play a significant role in the antenna's behavior. The feed point will affect how the low order and higher order modes are excited. The boundary conditions set by certain geometric features (e.g., helices, meanderlines) will determine the resonant frequency of the low order mode and the modal excitations. Thus, these factors will control the total input impedance and total Q.

The constancy of the Q also extends to three dimensional antennas. As an example, several cylindrical antennas were simulated and the Q of their lowest order mode and total Q were calculated. Some representative examples of the simulated structures are

shown in Fig. 4 along with their Q values. First, we observe that the low order modal Q is remarkably consistent regardless of geometry or feed point. Furthermore, a Q of 126 corresponds to the expected Q for a cylindrical antenna with the stated geometric parameters and an absorption efficiency approximately 1/2, indicating they utilize the space effectively [19]. Secondly, we notice that the total Q ranges over several orders of magnitude and never approaches the low order modal Q. Higher order modes excited by the feed configurations contribute to the increased Q. Although the structures support an effective radiating mode, this fact is masked by the higher order modes that are excited. The characteristic mode approach allows us to observe the low order mode alone, unlike measurements or traditional numerical analysis where the existence of a low Q mode would be obfuscated.

Traditionally, engineers have expended great effort designing low Q structures. However, since a space-filling, low Q mode is excited by a structure as simple as a conductive cylinder shorted to ground, a paradigm shift is needed in small antenna design. Rather than struggling to design complex, low Q structures, the focus should be on coupling into modes that exist in basic structures and minimizing higher order modes. A reasonable approach is to first fill the given space as fully as possible which should excite a low Q mode in addition to several other modes. Next, the structure should be made resonant near the desired operating frequency by introducing boundary conditions to force the current to follow a longer electrical path (e.g., helical coils, meanderlines). Once this is done, a matching technique, perhaps as simple as the stub technique discussed here, can be applied to excite the low Q mode with a useful impedance.

7. Conclusions & Future Work

We have examined the long-used but little-studied stub matching technique for small antennas using characteristic mode theory. We found that it is most applicable when the antenna has a low resonant resistance and is resonant near the desired operating frequency. For this reason, we studied an electrically small helical monopole for most of this work. Characteristic mode theory suggests a natural circuit model for the antenna, consisting of a radiating mode (RLC circuit) in parallel with an inductor. The parallel inductance can be approximately calculated using simple formulas, but circuit parameters of the radiating mode also depend on the stub geometry. At first glance, linking the radiating mode circuit with the geometry seems difficult, but by applying some principles from CMT, we explain the behavior of resistance and frequency. Interestingly, most stub modifications do not change the Q. The quality factor of the lowest order mode seems to be fundamentally related to the size of the radiating structure, even for three dimensional antennas. This low order mode is almost always hidden by a variety of excited high order modes, but can be strongly excited, in theory. Therefore, we propose that more research should focus on coupling into the existing low Q modes of simple structures rather than designing a variety of new, complex structures to achieve low Q. In future work, we plan to demonstrate some examples of this approach for common shapes like spheres, cylinders, and planar structures. We also plan to use the stub

matching approach to impedance match the multimode antenna from [3] without an external matching network.

Acknowledgments

This work is supported under a National Science Foundation Graduate Research Fellowship.

References

- [1] L. J. Chu, "Physical limitations of omni-directional antennas," *J. Appl. Phys.*, vol. 19, no. 12, pp. 1163–1175, Dec. 1948.
- [2] J. J. Adams and J. T. Bernhard, "Tuning method for a new electrically small antenna with low Q," *IEEE Antennas Wireless Propagat. Lett.*, vol. 8, pp. 303-306, 2009.
- [3] J. J. Adams and J. T. Bernhard, "Bandwidth enhancement of a small antenna by modal superposition," in *Proc. 2009 Antenna Appl. Symp.*, pp. 1-15, Monticello, IL.
- [4] E. E. Altshuler, "A method for matching an antenna having a small radiation resistance to a 50-ohm coaxial line," *IEEE Trans. Antennas Propag.*, vol. 53, no. 9, pp. 3086-3089, Sept. 2005.
- [5] S. R. Best, "A discussion on the quality factor of impedance matched electrically small wire antennas," *IEEE Trans. Antennas Propag.*, vol. 53, no. 1, pp. 502-508, Jan. 2005.
- [6] J. F. Morrison and P. H. Smith, "The shunt-excited antenna," *Proc. IRE*, vol. 25, no. 9, pp. 673-696, June 1937.
- [7] P. Baudoux, "Current distribution and radiation properties of a shunt-excited antenna," *Proc. IRE*, vol. 28, no. 6, pp. 271-275, June 1940.
- [8] C. W. Harrison and R. W. P. King, "Folded dipoles and loops," *IRE Trans. Antennas Propag.*, vol. 9, no. 2, pp. 171-187, Mar. 1961.
- [9] J. K. Raines, *Folded Unipole Antennas: Theory and Applications*, New York, NY: McGraw-Hill Inc., 2007.
- [10] R. J. Garbacz and R. H. Turpin, "A generalized expansion for radiated and scattered fields," *IEEE Trans. Antennas Propagat.*, vol. 19, no. 3, pp. 348–358, May 1971.
- [11] R. F. Harrington and J. R. Mautz, "Theory of characteristic modes for conducting bodies," *IEEE Trans. Antennas Propagat.*, vol. 19, no. 5, pp. 622–628, September 1971.
- [12] ——, "Computation of characteristic modes for conducting bodies," *IEEE Trans. Antennas Propagat.*, vol. 19, no. 5, pp. 629–639, September 1971.
- [13] A. O. Yee and R. J. Garbacz, "Self- and mutual-admittances of wire antennas in terms of characteristic modes," *IEEE Trans. Antennas Propagat.*, vol. 21, no. 6, pp. 868-871, November 1973.
- [14] M. Cabedo-Fabres, E. Antonino-Daviu, A. Valero-Nogueira, and M. Ferrando Bataller, "The theory of characteristic modes revisited: a contribution to the design of antennas for modern applications," *IEEE Antenna Propag. Mag.*, vol. 49, no. 5, pp. 52-68, Oct. 2007.

- [15] A. D. Yaghjian and S. R. Best, "Impedance, bandwidth, and Q of antennas," *IEEE Trans. Antennas Propagat.*, vol. 53, no. 4, pp. 1298–1324, April 2005.
- [16] S. R. Best, "A discussion on the properties of electrically small self-resonant wire antennas," *IEEE Antenna Propag. Mag.*, vol. 46, no. 6, pp. 9-22, Dec. 2004.
- [17] C. R. Paul, *Inductance: Loop and Partial*, John Wiley and Sons, Inc., 2009.
- [18] J. D. Kraus, *Antennas*, 2nd ed. New York, NY: McGraw-Hill Inc., 1988.
- [19] M. Gustafsson, C. Sohl, G. Kristensson, "Illustrations of new physical bounds on linearly polarized antennas," *IEEE Trans. Antennas Propag.*, vol. 57, no. 5, pp. 1319-1327, May 2009.

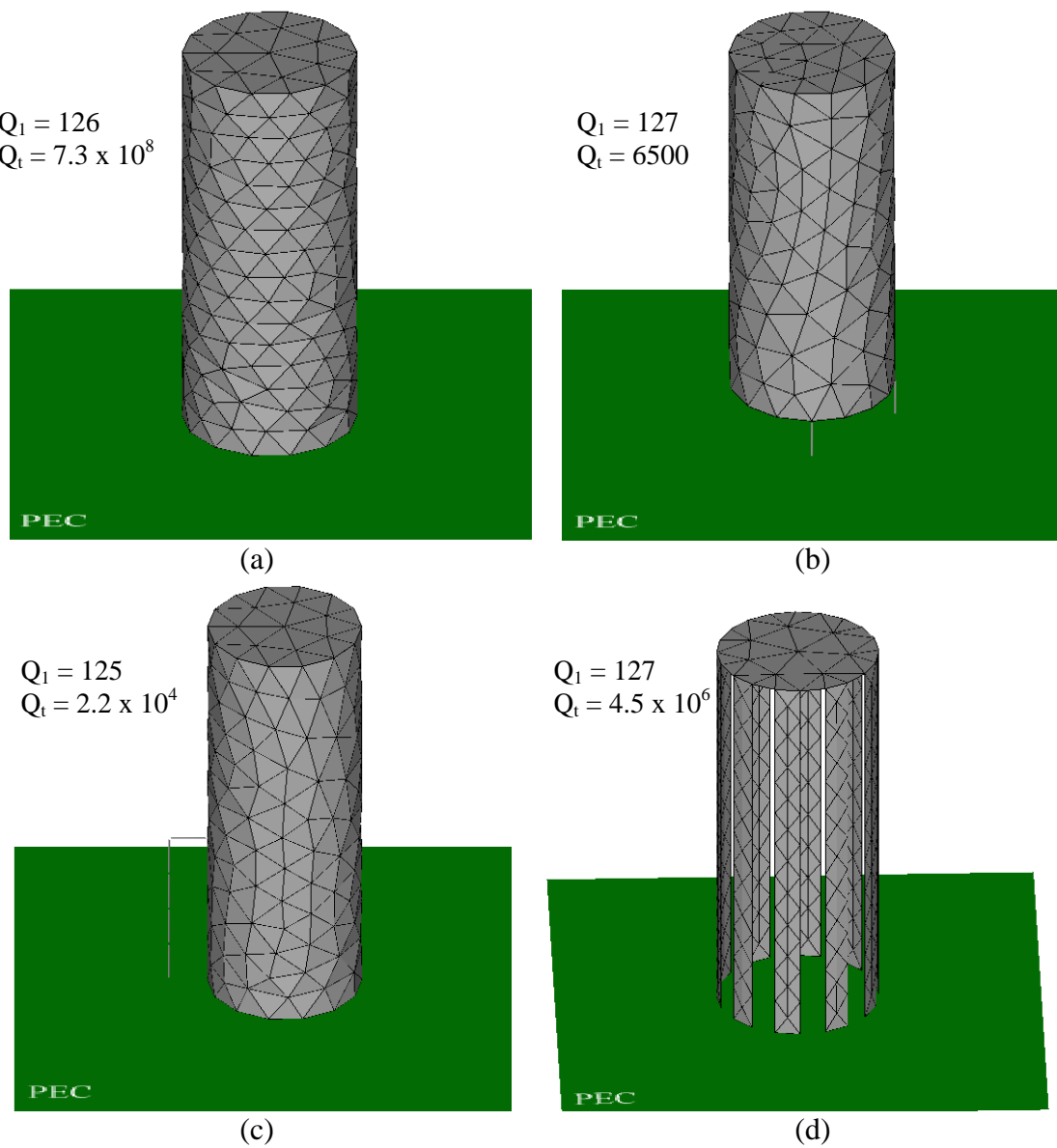


Figure 4: Several configurations of cylindrical antennas (height = 5 cm, radius = 1 cm) with their respective Q values at 300 MHz for the lowest order mode and the total Q at one of the feeds. (a) Shorted cylinder with feed wire along centerline. (b) Raised cylinder with three wires shorted to ground. (c) Shorted cylinder with feed wire along centerline and shorted stub. (d) Cylinder with several shorted arms and feed on centerline.

BACKSCATTER OF SMALL RESONANT PLATES WITH LINEAR SLOTS REVISITED

Carlo Van Niekerk* and Jennifer T. Bernhard
Electromagnetics Laboratory, Department of Electrical and Computer Engineering
University of Illinois at Urbana-Champaign, Urbana, IL 61801
cvannie2@illinois.edu;jbernhar@illinois.edu

A plate ($1/2 \lambda \times 1 \lambda$) with a center positioned linear slot ($1/10 \lambda \times 1 \lambda$) has been shown to have a reduced monostatic radar cross-section (RCS) compared to an identical solid plate by at least 8 dB. In Green's 1964 paper, he explains this phenomenon by treating the slotted plate as a receiving antenna and the realized drop in monostatic RCS resulting from the antenna impedance loading. In this paper we provide a careful study that helps to further illuminate the slotted plate's response by analyzing it in terms of destructive interference mechanisms between the plate and the slot. Both simulated and measured data are presented, as well as a discussion of future applications of this structure in granular materials sensing systems.

1. Introduction

The minimization of the scattering properties of antennas and other large structures has been of interest for many decades [1-6]. There has been extensive research in this area, especially in cylindrical or linear antennas. It is well known that the backscatter cross section of a half wavelength cylindrical antenna can be substantially reduced by introducing a reactive load impedance to the antenna terminals. Optimizing this effect is not completely understood however the works of Chen and others [3-6] have provided substantial clarity to the subject. It is noted in [6] that there are primarily three ways in which the addition of a central load can reduce the scattered field: 1) by reducing the magnitude of the induced current, 2) by reversing the phase of the induced current over a portion of the cylinder, and 3) by combining 1) and 2). Chen's methodology for analysis and optimization primarily involved the examination of the induced surface currents caused by plane wave illumination. Examination of the induced currents will prove important to the understanding of how the radar cross section of resonant plates is affected when linear slots are introduced.

The topic of antennas as scatterers is pertinent when antennas are operated in receiver mode [7-11]. A receiving antenna which is illuminated by an electromagnetic wave will scatter energy as a function of the load connected to its terminals. In [12] Collin models the complete system of free space, antenna and guide transmission line as a waveguide junction problem. The free space section is modeled by a waveguide with infinitely many spherical modes while the guided section is assumed to be a single propagating mode waveguide. Thus, the entire system is

analogous to a single-mode waveguide coupled through a junction to a multimode waveguide. This model allows for the derivation of useful expressions that relate the scattered field to the antenna impedance and load. Other models using mutual coupling theory have also been used effectively to derive expressions for antenna scattering based on loading [13-14].

In 1963 Robert Green published his PhD dissertation on the general theory of antenna scattering [15]. In it, he dedicates a chapter to scattering of a small rectangular plate with linear slot (a paper was published on this topic [16]). For the sake of brevity the small rectangular plate with linear slot will be called the “slotted plate”. Understanding the RCS reduction of the slotted plate compared to an ordinary plate is the focus of this paper. In Green’s paper he explains this drop off by the loading effect presented by the slot, since the slotted plate is acting as a receiving antenna. In this paper we offer a different thesis.

This paper starts with a review of the slot antenna geometry, properties and radiation characteristics. Next, the slotted plate is analyzed in terms of induced surface currents and scattered fields. Juxtaposing the characteristics of the slot antenna and the slotted plate provides insight into the cause of the reduced radar cross section for the slotted plate over the solid plate of identical size. Lastly, potential applications for the slotted plate are discussed and measured results are presented.

2. The Slot Antenna

A slot antenna is typically fed by coaxial cable where a voltage potential is applied across the slot between the inner and outer conductors of the coax. To illustrate the operation of the slot antenna it is useful to first analyze the slot wire model, depicted in Figure 1 [17]. The wire model is basically two quarter wavelength resonant stub sections connected in parallel, this topology forms an inefficient radiator. The long portions of each stub are closely spaced (since $w \ll \lambda$) and the current in each branch is in opposite directions and thus the resulting fields will cancel. The current in the end sections are in phase and thus the resulting fields from these sections are reinforced. These sections are too short to radiate efficiently and would require substantial currents in order to radiate noticeable amounts of power.

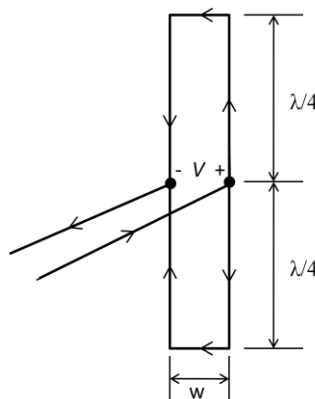


Figure 1: Wire Model for Slot Antenna

A more efficient topology (the slot antenna) is shown in Figure 2 where a slot is cut into a metal plate, now the currents are not confined to the slot edges but are distributed over the surface of the plate. The radiation from the slot antenna occurs equally on both sides of the plate. With the slot vertically aligned the radiated electric field will be horizontally polarized. Horizontal plate currents add up constructively while vertical currents generally cancel on either side of the slot.

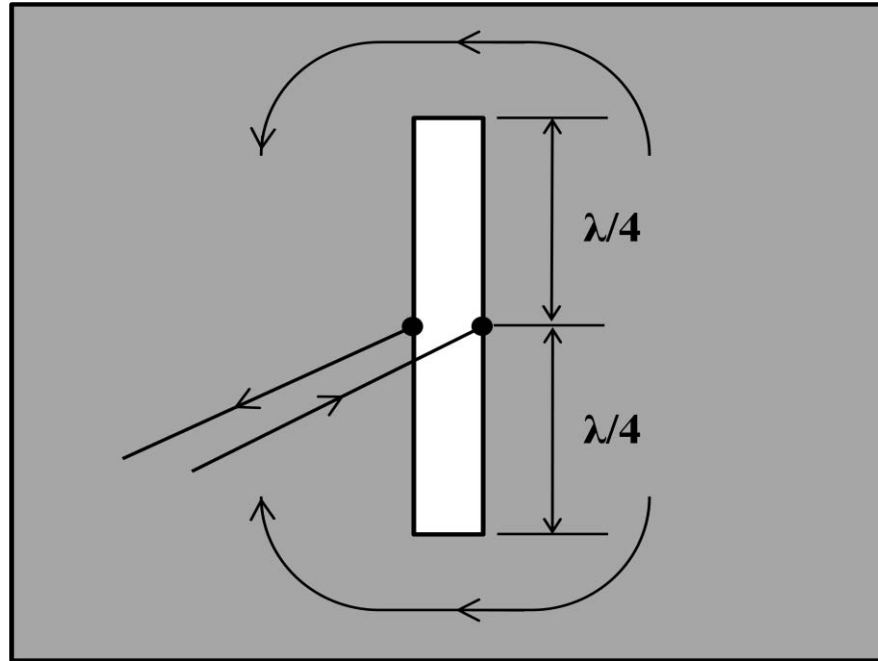


Figure 2: $\lambda/2$ Slot Antenna

The metal plate surrounding the slot is ideally infinitely large or practically many wavelengths in extent. The plate width is the most sensitive dimension and when the width is narrowed the radiated field pattern's main lobe is broadened and undulations in the pattern are reduced. Both E-plane and H-plane far field radiation pattern cut planes are shown in Figure 3. The actual slot antenna dimensions are the same as Figure 4. The field pattern is typical for single element, with a large single lobe at broadside for both cut planes. The E-plane and H-plane are correspondingly designated as the azimuthal and elevation planes. The azimuthal cut plane has a large null which corresponds to the position of the plate. The elevation plane is indented at the spatial position corresponding with the plate.

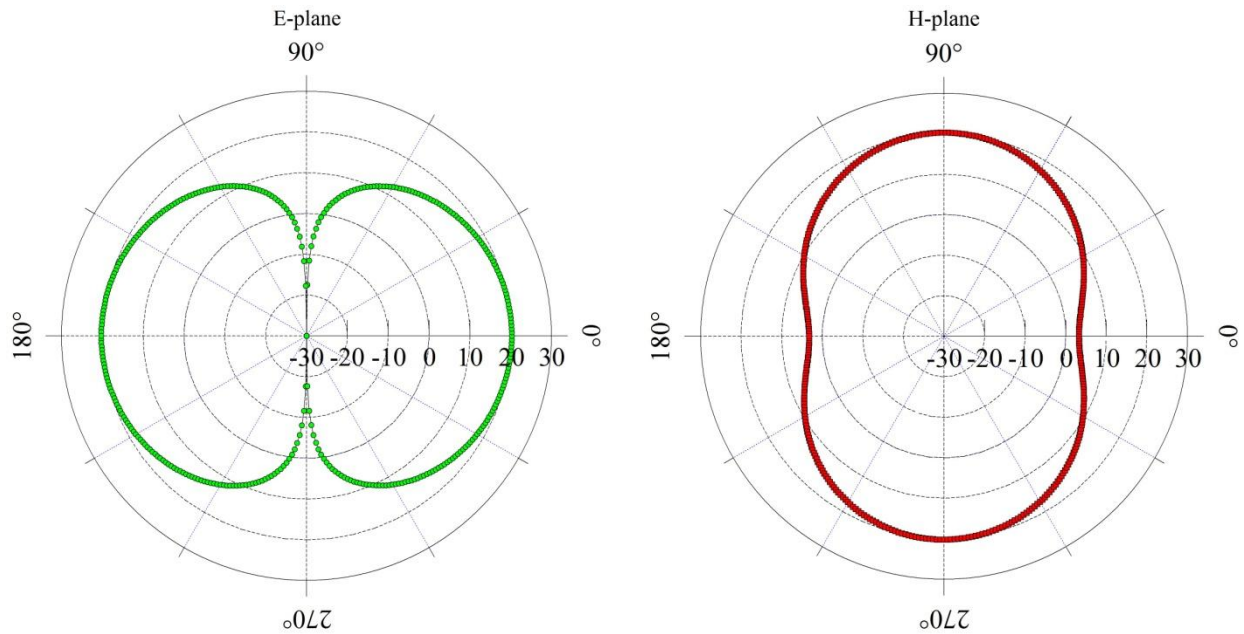


Figure 3: Simulated Electric Field for the actively-fed slot antenna for both E- and H-planes (HFSS)

3. The Slotted Plate

The slotted plate is shown in Figure 4. It is a small metalized plate with a rectangular slot cut out from its center. The plate width and slot length are of the same dimension, that being the resonant length of a half wavelength. The plate length is larger than its width to facilitate the placement of the vertically aligned slot.

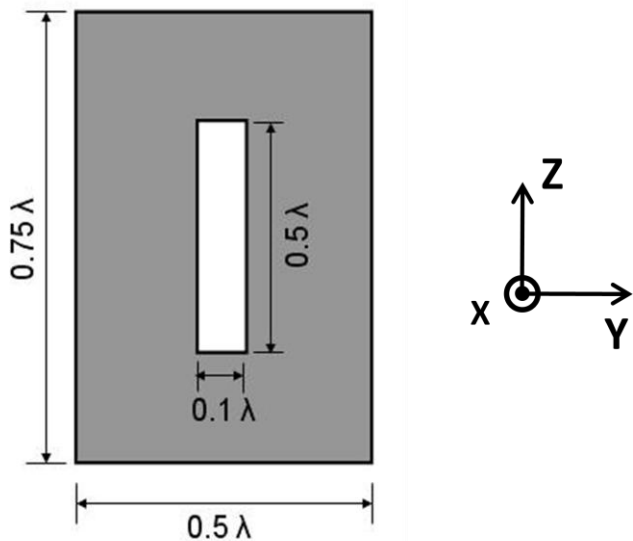


Figure 4: Slotted Plate

In order to evaluate the RCS of the slotted plate, it is illuminated by a plane wave. With the slotted plate in the YZ plane, the incident direction of the plane wave is $\phi = 0^\circ$ and $\theta = 90^\circ$. The polarization of the incoming field is strictly y-directed (or ϕ - polarized). The surface currents resulting from the incident wave are shown in Figure 5. Note the full wave solver HFSS was used to generate plots. The surface currents are concentrated in the horizontal regions above and below the slot, while currents in the area on either side of the slot are weak and therefore do not contribute significantly to radiation. The incident electric field is tangential to the plate and thus the scattered field should be exactly 180° out of phase with the incident field since the boundary condition of a zero tangential field at the plate surface must be satisfied. Thus the plate currents are oriented in the negative Y direction.

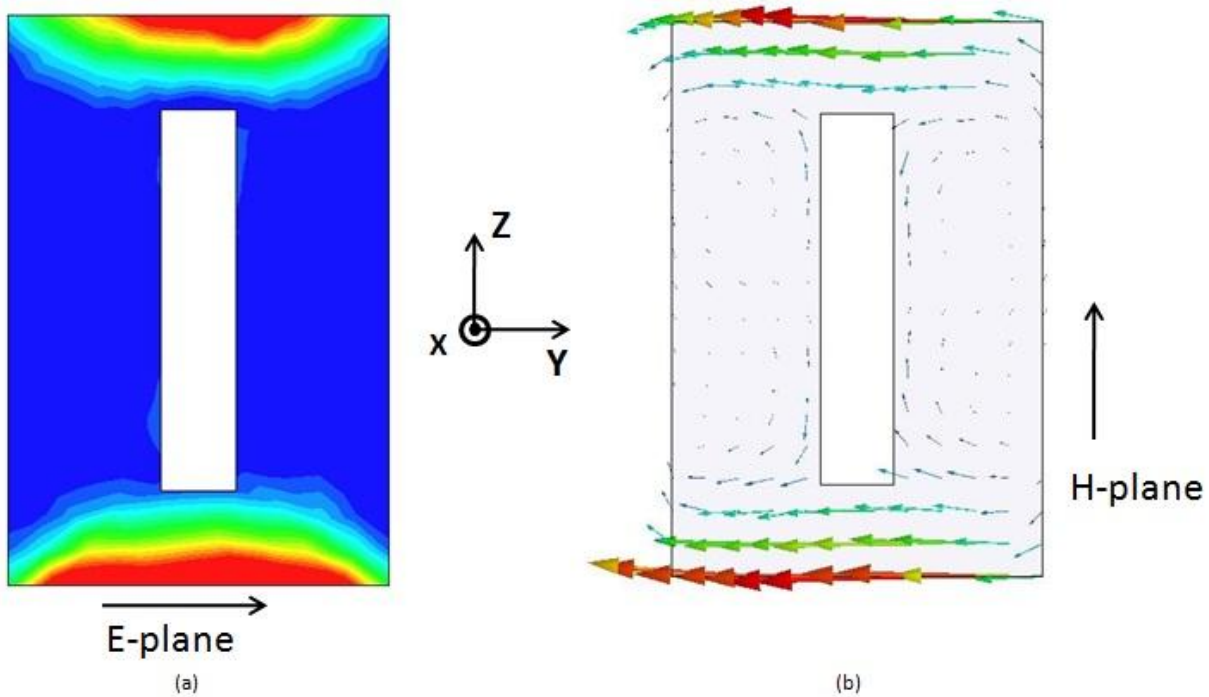


Figure 5: Current distributions on the slotted plate – Magnitude (a) and Vector representations (b) (HFSS)

The bistatic RCS pattern for primary cut planes are shown in Figure 6. The bistatic RCS response in the E-plane is similar to the response for an actively-fed slot antenna. The H-plane response is typical for a two element array fed in phase with spacing roughly $5/8 \lambda$.

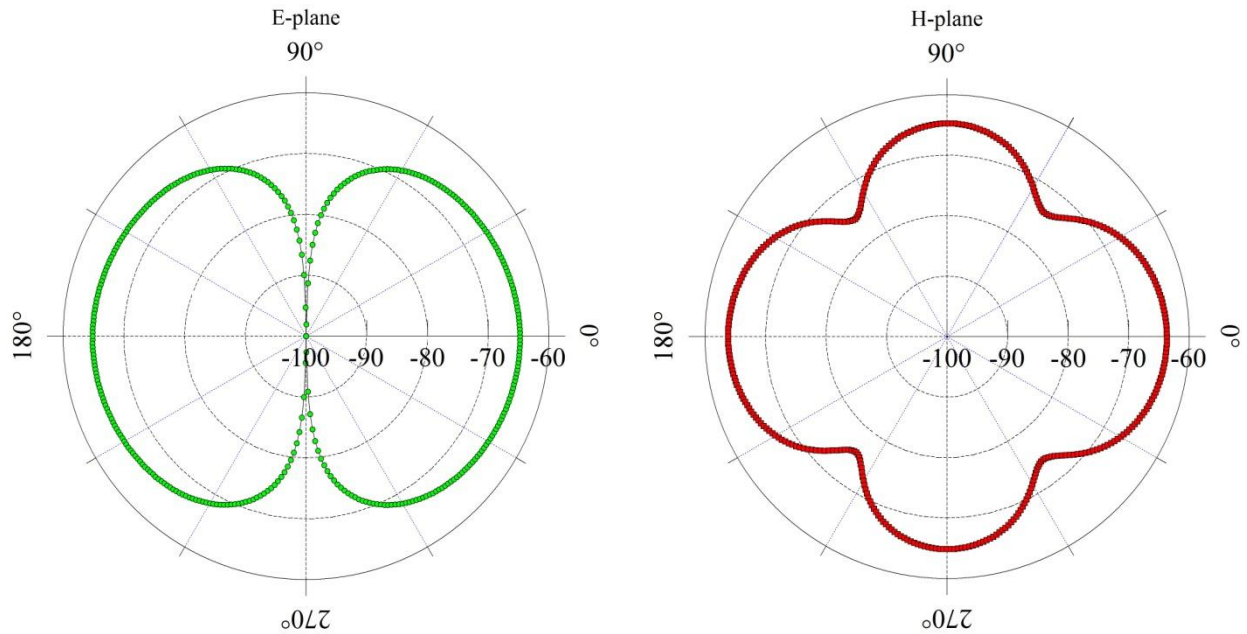


Figure 6: Simulated Bistatic Scattered Field Patterns of the Slotted Plate for the E- and H-planes

4. Reduction of RCS response

When comparing the case of a rectangular plate with and without the slot, there is a large drop in RCS when the slot is included. Figure 7 shows this phenomenon, where there is nearly a 20 dB difference between the solid plate and slotted plate RCS E-plane response.

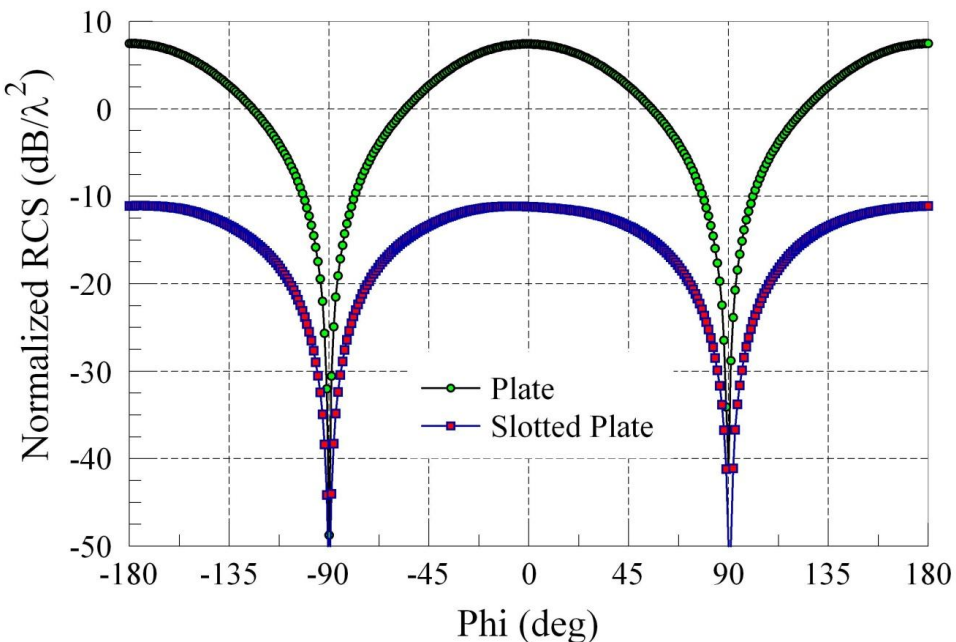


Figure 7: Normalized Bistatic RCS for regular plate and the slotted plate (simulated).

In Green's paper [16] he explains this drop off by the loading effect presented by the slot, since the slotted plate is acting as a receiving antenna. As a receiving antenna it presents a load to the incident wave which acts to absorb some of the incident energy, thereby accounting for the drop in backscatter energy. The argument for a dissipative load being the cause for the reduced scattered field would make more sense if this were a complex antenna with complicated feed network and connected to load at its terminals but this is merely a resonant plate with a slot. A large drop in RCS effectively means a loss in scattered energy, since RCS is a weighted ratio of scattered field to incident field. Reduction of RCS can be achieved if some of the incident energy is absorbed (usually by inclusion of a reactive load) and thereby effectively reducing the magnitude of the induced currents. The existence of a destructive mechanism whereby the induced currents phase is altered on some part of the structure relative to another can also explain the reduced RCS response. We contend that the cause for the RCS drop off is a destructive mechanism between the reflection from the plate and the re-radiation from the slot.

The surface currents on the plate are the superposed result of two distinct effects. The first effect is the surface current resulting from the incident field impinging on the PEC boundary. This surface current effect is the source for the plate reflected fields. The second effect is the current distributed over the plate due to the re-radiation by the slot. It is important to note that the plate reflection introduces a phase reversal. The currents on the plate due to the slot re-radiation has the same polarization and phase as the incident field (positive Y direction, see figure 8) but plate reflection currents are 180° out of phase relative to the incident field (i.e., negative Y direction). In fact, one can consider that the plate forms an array of planar dipoles with a larger aperture than the slot and thus it is the more dominant effect. Superposition of these two effects results in a reduced RCS response. Figure 8 shows this destructive interference mechanism in a simplified model.

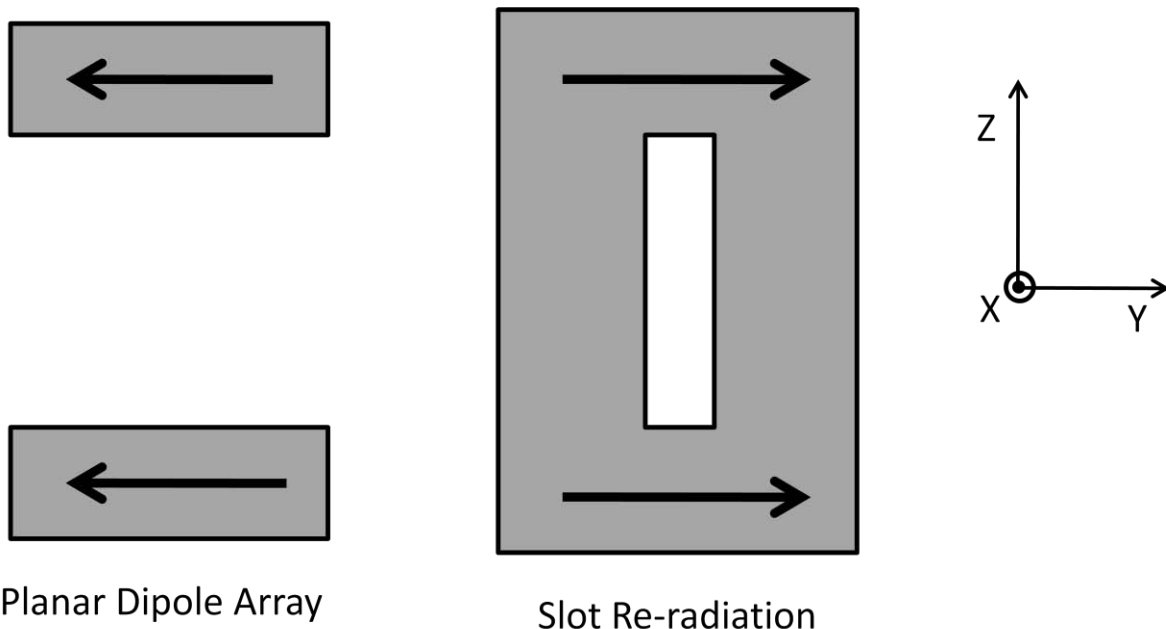


Figure 8: Simplified model highlighting the destructive interference mechanism

Antennas are generally regarded to have two modes of scattering, known as the structural and antenna modes [18]. The structural mode of scattering is due to the shape, size and material composition of the antenna. The antenna mode of the scattering occurs because the antenna is capable of both receiving and transmitting energy well. It is clear that the slot re-radiation effect is the antenna mode and the plate reflection is the structural mode scattering. For the slotted plate these modes are destructive.

The insertion of the slot into the plate disturbs the plate current distribution in such a way as to set up an effective planar dipole array in the horizontal orientation above and below the slot. The array factor for a two element array spaced by roughly $5/8 \lambda$ is very similar to the H-plane scattered field pattern for the slotted plate, as shown in figure 9. This is further validation that the plate scatter is the dominant radiation mechanism. Though not shown here, the phase of the H-plane scatter field and array factor compare very well.

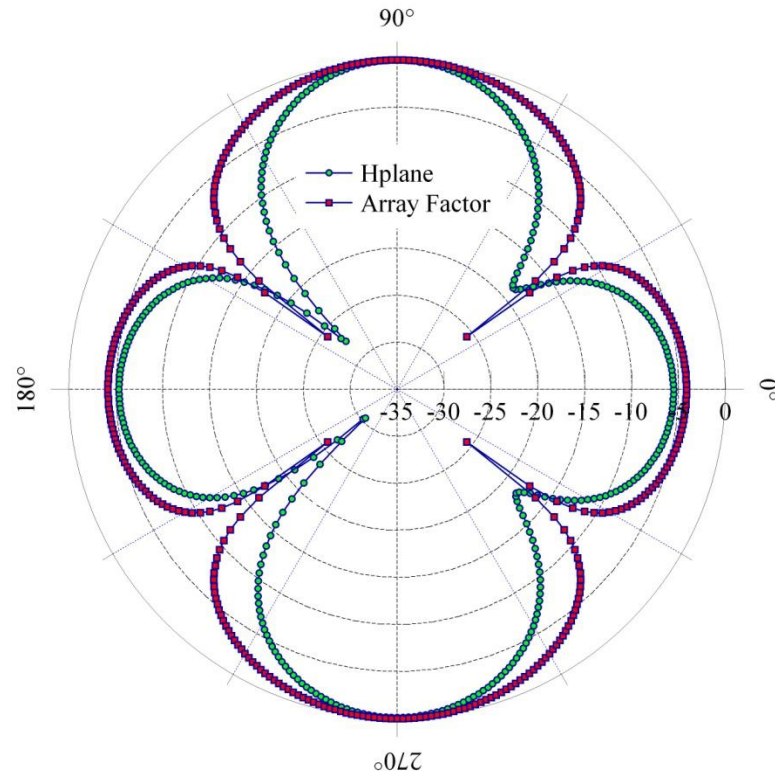


Figure 9: Comparison of H-plane scatter field for the slotted plate with a two element array factor (HFSS)

5. Applications for the slotted plate

Any application where it is desired to reduce the RCS of a planar metal object would suit the slotted plate because it provides significant RCS backscatter attenuation. Most large solid planar surfaces can be substituted for a tiled array configuration of slotted plates. Other potential applications are of the sensor-type, where the slotted plate can be used as a wireless passive

sensor [19]. One particular application in which we are interested is as a sensor for granular materials experiments. Granular materials research involves the study of movement and interaction of granularly shaped particles under vibrational excitation. Embedding a radar target in the experiment allows for minimally invasive measurements of particle localization and relative rotation during the life of the experiment. A good candidate for a radar target is a corner reflector since it provides a strong backscatter return. The incorporation of slots in the reflector plates (each individual plate in the corner reflector is now a slotted plate) makes the structure more frequency sensitive. Varying the slot dimensions slightly in adjacent plates allows for the determination of relative rotation of the target since the backscatter frequency response would change with target orientation relative to the source. Figure 10 shows an example of a slotted corner reflector (dihedral).

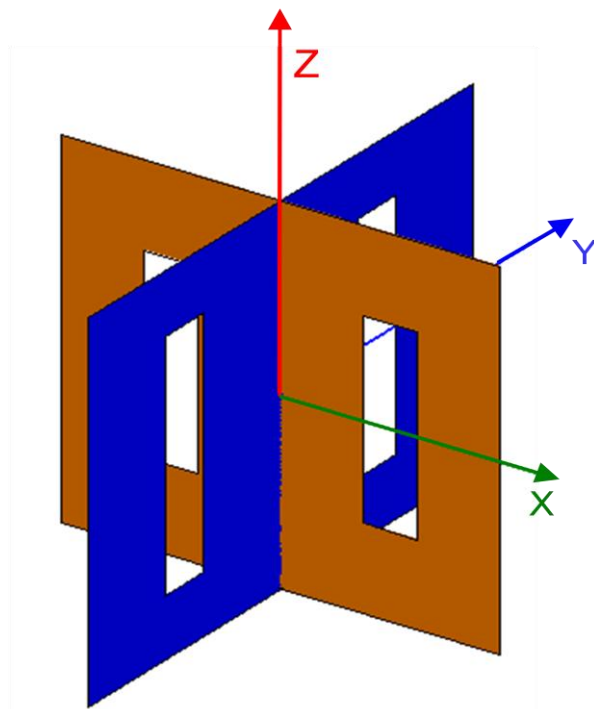


Figure 10: Slotted Dihedral Corner Reflector

Note that slotted plates in the XZ and YZ planes are different. Rotating the corner reflector azimuthally results in monostatic backscatter frequency response changes, providing a discernible signal to sense relative rotation. Because of symmetry, it is adequate to restrict evaluation to any one quadrant. Figure 11 shows a frequency shift in the reflector frequency response, which occurs when the reflector is rotated, a shift down indicates a clockwise azimuthal rotation and vice versa for a shift up.

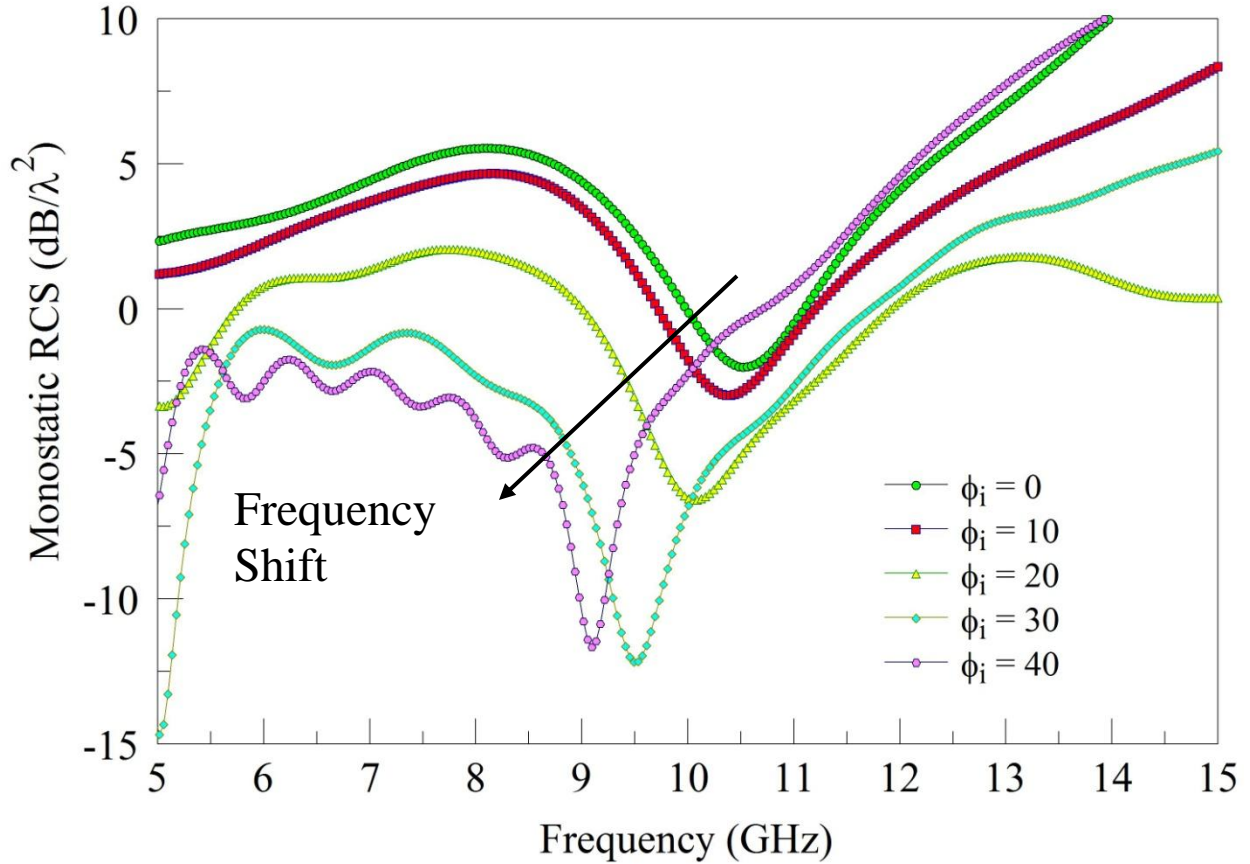


Figure 11: Monostatic RCS Frequency Response for the Slotted Dihedral Corner Reflector

6. Measurements

The slotted plate and ordinary plate were fabricated (using copper) to the physical dimensions where resonance would be around 10 GHz, thus the plate width and slot length were 15 mm. These targets were placed in the anechoic chamber and wideband S_{11} reflection measurements were taken using a UWB antenna and network analyzer. The radar equation was then used to calculate radar cross section given the measurement of reflected power [20]. The measured monostatic RCS frequency response for both the plate and slotted plate is shown in Figure 12. At 10 GHz, the slotted plate response has a trough while the ordinary plate response continues to increase monotonically. The difference of RCS backscatter for the two configurations at resonance is approximately $15 \text{ dB}/\lambda^2$. This data demonstrates the RCS backscatter attenuation effect of the slotted plate.

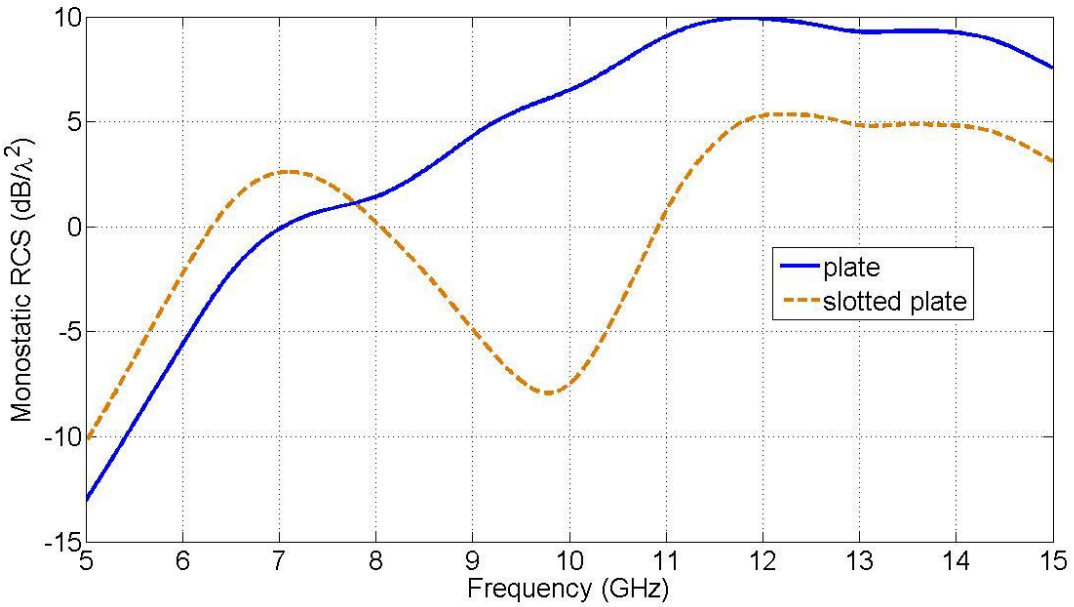


Figure 12: Measured monostatic RCS vs. Frequency for Slotted Plate and Ordinary Plate

7. Conclusions

The slotted plate has been evaluated to determine the reason for its weaker backscatter characteristics when compared with an equivalently sized solid plate. The reason for the reduced backscatter has been shown to be a destructive interaction between the antenna and structural scattering modes. These results were confirmed by examining the induced currents for the scattered field from the plate and the plate currents caused by re-radiation from the slot. It is observed that the structural mode is dominant for this uniquely sized plate because of the existence of a two element planar dipole array. Finally, the slotted plate has been shown to be well-suited to sensor type applications and can offer substantial benefits over traditional active sensors.

8. Acknowledgements

This work was done with the support of the NSF grant: CMMI 0625313.

9. References

- [1] J. K. Schindler and R. B. Mack, "The Control of Electromagnetic Scattering by Impedance Loading," *Proc. of the IEEE*, vol. 53, pp.993-1004, Aug 1965.
- [2] R. F. Harrington, "Theory of Loaded Scatterers," *Proc. IEE*, vol. 111, pp. 617-623, April 1964.

- [3] K. M. Chen, "Minimization of Backscattering of a Cylinder by Double Loading," *IEEE Trans. Antennas and Propagation*, vol. 13, no. 2, pp. 262-270, March 1965.
- [4] J. L. Lin and K. M. Chen, "Minimization of Backscattering of a Loop by Impedance Loading - Theory and Experiment," *IEEE Trans. Antennas and Propagation*, vol. 16, no. 3, pp. 299- 304, May 1968.
- [5] K. M. Chen, "Minimization of End-Fire Radar Echo of a Long Thin Body by Impedance Loading," *IEEE Trans. Antennas and Propagation*, vol. 14, no. 3, pp. 318- 323, May 1966.
- [6] K. M. Chen and V. Liepa, "Minimization of Backscattering of a Cylinder by Central Loading," *IEEE Trans. Antennas and Propagation*, vol. 12, no. 5, pp. 576-582, Sept 1964.
- [7] J. B. Andersen and R. G. Vaughan, "Transmitting, Receiving, and Scattering Properties of Antennas," *IEEE Antennas and Propagation Magazine*, vol. 45, no. 4, pp. 93-98, Aug 2003.
- [8] R. C. Hansen, "Relationships between Antennas as Scatterers and as Radiators," *Proc. of the IEEE*, vol. 77, no. 5, pp. 659-662, May 1989.
- [9] R. F. Harrington, "Electromagnetic Scattering by Antennas," *IEEE Trans. Antennas and Propagation*, vol. 11, no. 5, pp. 595-596, Sept 1963.
- [10] R. F. Harrington, "Small Resonant Scatterers and Their Use for Field Measurements," *IEEE Trans. on Microwave Theory and Techniques*, vol. 10, no. 3, pp. 165-174, May 1962.
- [11] R. B. Green, "Scattering of Conjugate-Matched Antennas," *IEEE Trans. Antennas and Propagation*, vol. 14, no. 1, pp. 17-21, Jan 1966.
- [12] R. E. Collin, "The Receiving Antenna," in *Antenna Theory*, Part I, New York: McGraw-Hill, 1969.
- [13] Y. Y. Hu, "Back-scattering Cross Section of a Center-Loaded Cylindrical Antenna," *IEEE Trans. Antennas and Propagation*, vol. 6, no. 1, pp. 140-148, Jan 1958.
- [14] C. A. Levis and C. T. Tai, "A Method of Analyzing Coupled Antennas of Unequal Sizes," *IEEE Trans. on Antennas and Propagation*, vol. 4, no. 2, pp. 128-132, April 1956.
- [15] R. B. Green, "The General Theory of Antenna Scattering," PhD Thesis, The Ohio State University, Columbus, OH, 1963.
- [16] R. B. Green, "The Echo Area of Small Rectangular Plates with Linear Slots," *IEEE Trans. Antennas and Propagation*, vol. 12, no. 1, pp. 101-104, Jan 1964.
- [17] J. D. Kraus, *Antennas*, 2nd ed. New York: McGraw-Hill, 1988.
- [18] B. Munk, *Finite Antenna Arrays and FSS*, New York: John Wiley & Sons, 2003.
- [19] L. Yang, S. S. Basat and M. M. Tentzeris, "Design and development of novel inductively coupled RFID antennas," *IEEE Antennas and Propagation Society International Symposium 2006*, pp. 1035-1038, 9-14 July 2006.
- [20] C. A. Balanis, *Antenna Theory: Analysis and Design*, 3rd ed. New York: John Wiley & Sons, 2005.

CARTER DIPOLES AND RESONANT DIPOLES

R. C. Hansen
R. C. Hansen, Inc.
P.O. Box 570215
Tarzana, CA 91357

Abstract: Carter dipole resistance is 73 ohms while measurements regularly show 85 ohms. Carter reactance is roughly 45 ohms, all for a half-wave dipole. This short paper explains the discrepancy in resistance, and why the half-wave dipole is not resonant.

1. Introduction

Carter (1932) derived dipole self and mutual impedance based on a sinusoidal current distribution. These results utilized Sine and Cosine Integrals. For half-wave dipoles the self-impedance is roughly $73 + j42$ ohms. Antenna simulation codes and measurements (King, 1956) give half-wave dipole self-impedance of roughly $85 + j45$ ohms. Antenna engineers should wonder why the 85 and not 73 ohms, and why the half-wave dipole is not resonant. This short paper explains both.

2. Calculations from Carter

The resistance and reactance of a half-wave dipole are (Jordan and Balmain, 1968):

$$R = 30 \operatorname{Cin}(2\pi) = 73.130 \text{ ohms} \quad (1)$$

$$X = 30 \operatorname{Si}(2\pi) = 42.545 \text{ ohms} \quad (2)$$

where dipole radius is small a , $k = 2\pi/\lambda$, and $\operatorname{Cin}(z) = \ln z + \gamma - \operatorname{Ci}(z)$. Euler's constant is $\gamma = .577216$,

Half-wave dipoles were modeled by a piecewise sinusoidal Moment Method code, on a 64-bit HP-UX workstation. Since library Si and Ci subroutines, such as the IBM Scientific Subroutine Library, Abramowitz and Stegen, and *Numerical Recipes*, give 32-bit results in spite of claims, a full 64-bit subroutine was written by using coefficients developed by Luke (1975). This subroutine required Chebyshev Polynomials; again 64-bit coefficients were calculated. To achieve stable result for

very small radii it is necessary that not only the Si Ci subroutines be full 64-bits, but all aspects of the Moment Method code, especially the equation solver, use the full 64-bits.

Half-wave dipole cases were run with radius $a = .001\lambda$ and $a = .000001\lambda$. Twenty PWS expansion functions were used, and 20 test functions; The Moment Method code written was thus Galerkin, which improves the accuracy. Calculations shown were for twenty segments over the dipole, but results were stable as long as the number of segments was more than fourteen.

Figure 1 shows the current distributions for the two half-wave dipoles. Even though the $a = .001$ dipole is fairly thin, Figure 1 shows that the dipole is slightly past resonance. Also the current, extrapolated to the dipole end, is not zero. The dipole end capacitance apparently augments the resonances, with the $85 + j45$ ohms results.

In contrast, the extremely thin dipole has its current maximum at the center and the current extrapolated to the dipole end is zero. The current distribution is closely sinusoidal. As a result the Moment Method impedance is $77 + j44$ ohms, approaching the Carter value of $73 + j42$ ohms! Thus the higher resistance is not an artifact of the numerical simulation technique, but is due to dipole end effects caused by a non-negligible dipole radius. The end capacitance also affects the phase slope. Figure 2 shows the phase along half of the dipole for the thin dipole and for the ultra-thin dipole. As the radius approaches zero, the phase approaches a constant, and appears to approach -30 deg. For these calculations the feed is simply a voltage source at the dipole center; the geometry does not appear to be a factor here. Thus as the radius of the dipole approaches zero, the resistance approaches 73 ohms.

3. Resonant Dipoles

Carter's formula for dipole reactance in terms of Cin and Si was recast using the more common Ci and Si functions by Schelkunoff (1943). This formula for reactance is:

$$X = 30 [2Si(2kh) + (2Si(2kh) - Si(4kh)) \cos 2kh - (\ln(h\lambda/a^2) - C - \ln 2\pi - Ci(4kh) + 2Ci(2kh)) \sin 2kh] \quad (3)$$

Using this formula resonant length was calculated and plotted for dipole radius from $.01\lambda$ to $10^{-7}\lambda$. Figure 3 shows that for very thin dipoles the resonant length is approaching $.49\lambda$. The half-wave dipole has the reactance of roughly 45 ohms because its electric stored energy is greater than its magnetic stored energy. Of course the converse is true for loop antennas. Shortening the dipole length allows the ratio of electric to magnetic stored energy to approach one, hence resonance.

4. Summary

For ultra-thin half-wave dipoles the current distribution is closely sinusoidal, and the phase is closely constant. Fatter dipoles have a higher radiation resistance. Shortening the dipole allows the stored energies to be equal and produces resonance. For the half-wave dipole the excess of electric stored energy results in a reactance of roughly 45 ohms.

5. References

5.1 Journal Articles and Conference papers

- [1] P. S. Carter, "Circuit Relations in Radiating Systems and Applications to Antenna Problems", Proc. IRE, vol. 20, pp. 1004-1041, June 1932

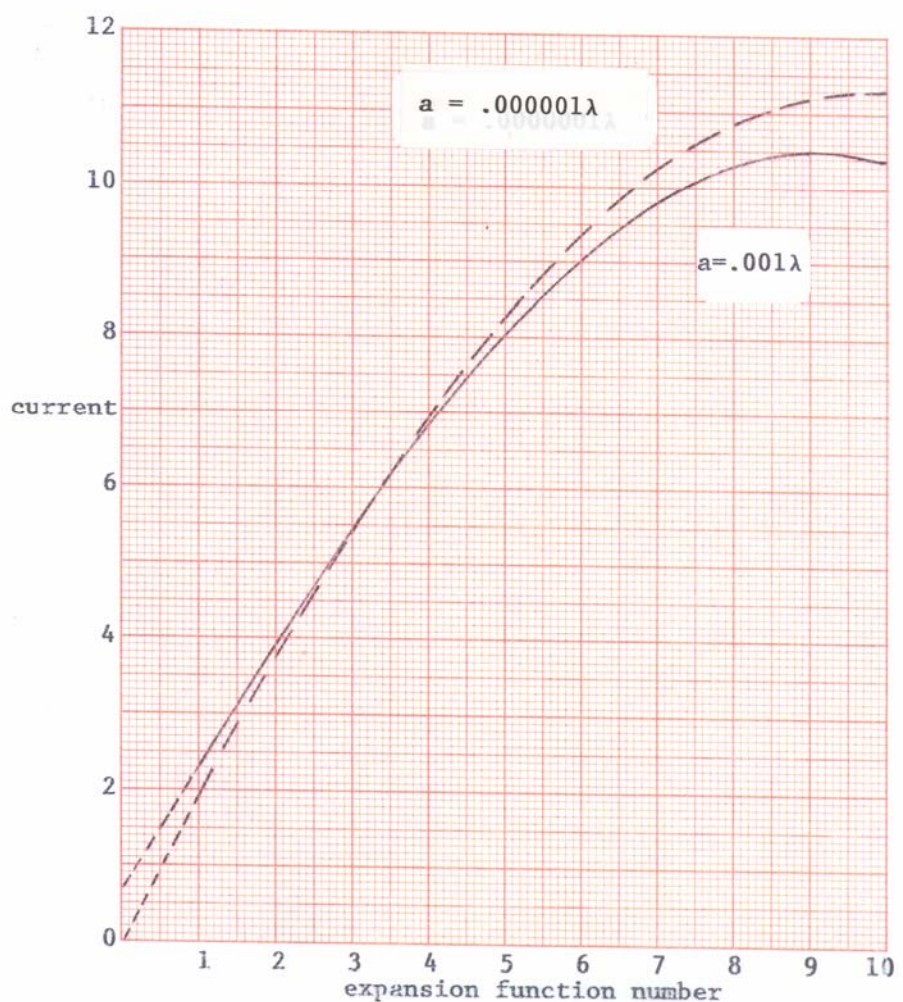
5.2 Book and Technical Reports

- [1] E. C. Jordan and K. G. Balmain, Electromagnetic Waves and Radiating Systems, second edition, section 14.04, Prentice-Hall, 1968

- [2] R. W. P. King, The Theory of Linear Antennas, Section II.37, Harvard University Press, 1956

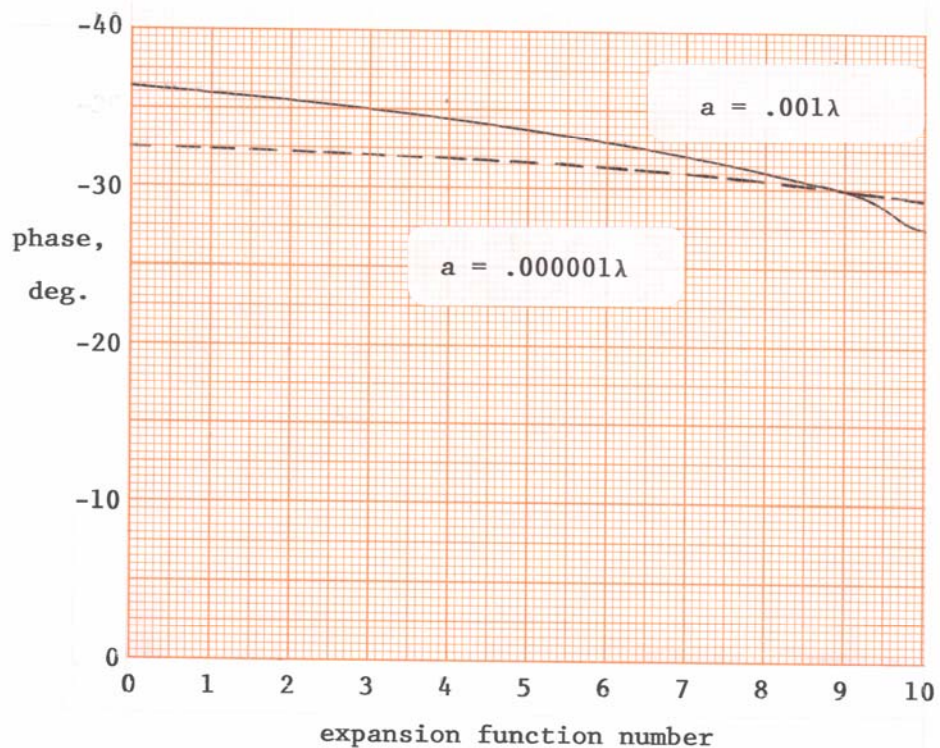
- [3] Y. L. Luke, Mathematical Functions and Their Approximations, Table 4.4, Academic Press, 1975

- [4] S. A. Schelkunoff, Electromagnetic Waves, p. 3
73, Van Nostrand Company, 1943



HALF-WAVE DIPOLE; $N = 20$

FIG. 1



HALF-WAVE DIPOLE; $N = 20$

Fig. 2

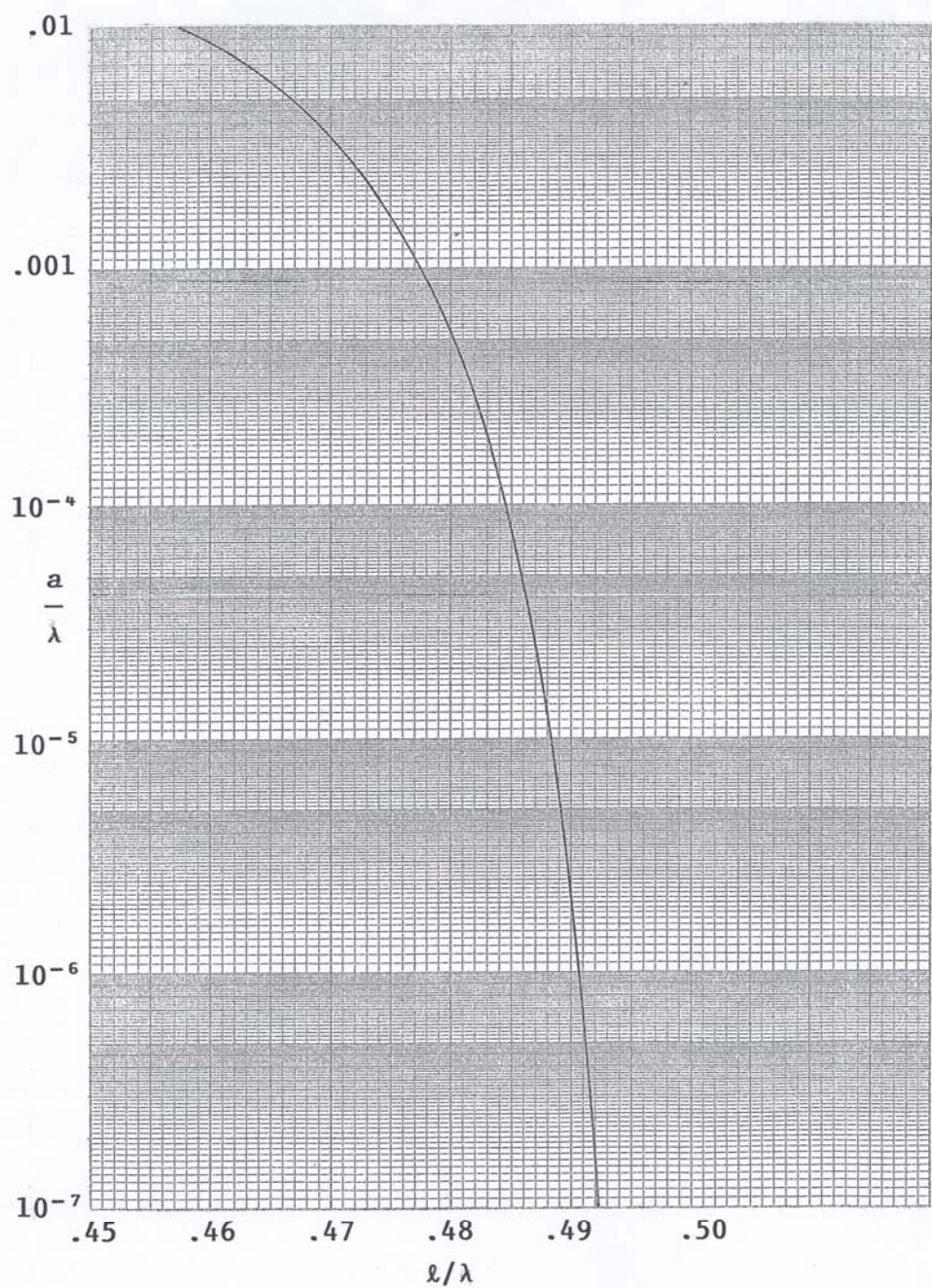


Fig. 3

Resonant Dipole Lengths

ARTIFICIAL IMPEDANCE SURFACE ANTENNA

DESIGN AND SIMULATION

D. J. Gregoire and J. S. Colburn
HRL Laboratories LLC
3011 Malibu Canyon Rd.
Malibu, CA 90265

Artificial impedance surface antennas (AISA) radiate by leaking surface waves from an artificial impedance surface (AIS) whose impedance is modulated to produce a preferred radiation pattern and polarization. In this paper, we present analysis, simulation and measurement techniques for AIS and AISA design. In previous work [1-4], AIS properties are modeled and designed using either full-wave electromagnetic simulation (e.g. HFSS), FDTD, or HRL's proprietary FastScat[®]. AISA radiation patterns simulated using FastScat typically require 72 hours of CPU time per frequency point. In this paper, we outline an approximate analytic method that computes the radiation pattern in less than a second on a laptop PC. We compare that method's results to FastScat models and laboratory measurements. We conclude with a discussion of the effects of AIS properties on AISA bandwidth and beam squint, the effects of non-sinusoidal AIS modulation profiles, and the effects of using transverse electric (TE) or transverse magnetic (TM) surface wave modes on AISA design.

1. Introduction

Artificial impedance surface antennas (AISA) are realized by launching a surface wave across an artificial impedance surface (AIS), whose impedance is spatially modulated across the AIS according a function that matches the phase fronts between the surface wave on the AIS and the desired far-field radiation pattern.

In this paper, we explore the parametric dependence of AIS design on AISA performance. We have developed a fast approximate technique for simulating AISA radiation patterns that enables examination of many configurations in a short time. We favorably compare this approximate method to measurements and to exact simulation methods requiring much more CPU time. We consider the limitations of AIS design on AISA bandwidth, beam squint, and radiation angle.

2. AISA Design Principles

In previous work [1-4], artificial impedance surface antennas (AISA) are formed from modulated artificial impedance surfaces (AIS). Patel[1] demonstrated a scalar AISA using a endfire-flare-fed one-dimensional, spatially-modulated AIS consisting of a linear array of metallic strips on a grounded dielectric. Sievenpiper[2], Colburn[3] and Fong[4] have demonstrated scalar and tensor AISAs on both flat and curved surfaces using waveguide- or dipole-fed, two-dimensional, spatially-modulated AIS consisting of a grounded dielectric topped with a grid of metallic patches.

The basic principle of AISA operation is to use the grid momentum of the modulated AIS to match the wave vectors of an excited surface-wave front to a desired plane wave. In the one-dimensional case, this can be expressed as

$$k_{sw} = k_o \sin \mathbf{q}_o - k_p \quad (1)$$

Where k_o is the radiation's free-space wavenumber at the design frequency, \mathbf{q}_o is the angle of the desired radiation with respect to the AIS normal, $k_p = 2\mathbf{p}/I_p$ is the AIS grid momentum where I_p is the AIS modulation period, and $k_{sw} = n_o k_o$ is the surface wave's wavenumber, where n_o is the surface wave's refractive index averaged over the AIS modulation. The AIS modulation wavenumber required to achieve the desired radiation is

$$k_p = \frac{2\mathbf{p}}{I_p} = k_o (n_o - \sin \mathbf{q}_o) \quad (2)$$

If we replace k_p by an integral multiple of it in Eqn. (1), then we can determine the radiation angles for higher-order radiation modes for any radiation wavenumber k .

$$\sin(\mathbf{q}_{(m-1)}) = n_o - m k_p / k, \quad m = 1, 2, 3, \dots \text{int}\left(\frac{k}{k_p}(n_0 + 1)\right) \quad (3)$$

where the main lobe angle is when $m=1$. Eqn.(3) can be used to quantify the AISA beam squint, i.e. how much \mathbf{q}_o increases with frequency. The beam squint is made worse by the frequency dependence of n_o . We will discuss this later in detail.

The AIS modulation for the one-dimensional AISA radiating at the angle \mathbf{q}_o and the wavenumber k_o can be expressed as periodic variation in the surface-wave propagation index. In the simplest case, we assume it is sinusoidal

$$n_{sw}(x) = n_o + dn \cos(k_p x) \quad (4)$$

where dn is the modulation amplitude, and k_p is described by Eqn. (2). Here, we have deviated from the AIS modulation convention assumed by our predecessors [1-4] who

have expressed it as variation in the surface reactance. Later in this paper, using index modulation leads to a more direct formulation of AISA radiation fields. It will be shown that the variation in AISA radiation patterns due to index or reactance modulation is small.

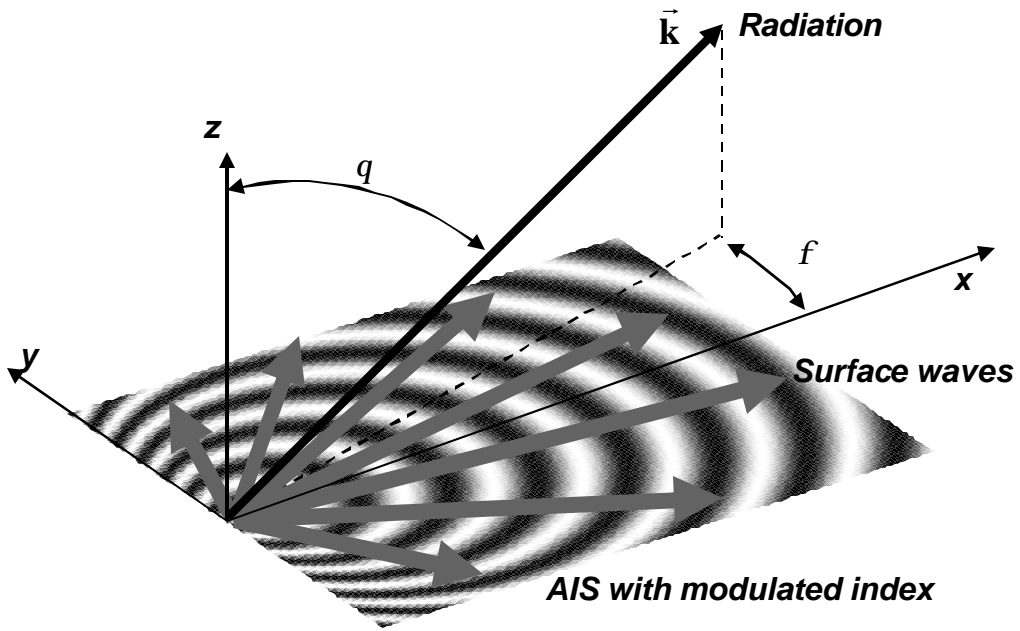
The AISA index modulation of Eqn. (4) can be generalized for an AISA of any shape as

$$n_{sw}(\vec{r}) = n_o + dn \cos(k_o n_o r - \vec{k}_o \cdot \vec{r}) \quad (5)$$

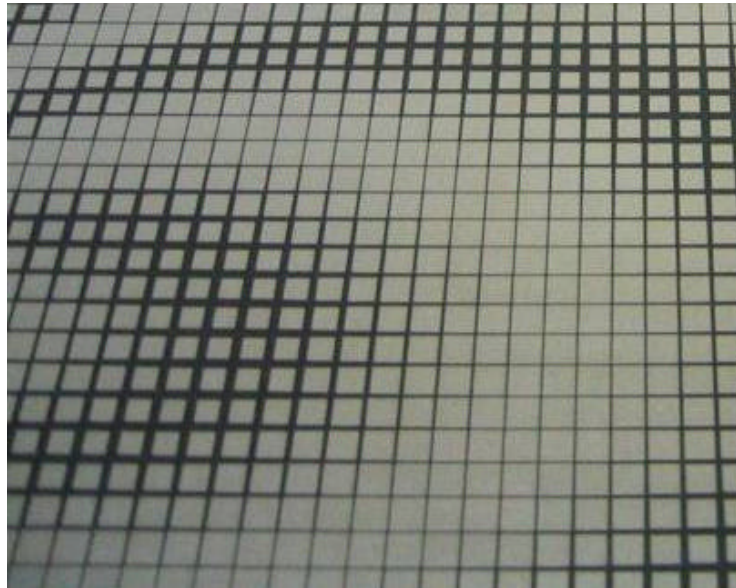
Where \vec{k}_o is the desired radiation wave vector, \vec{r} is the three-dimensional position vector of the AIS, and r is the distance along the AIS from the surface-wave source to \vec{r} along a geodesic on the AIS surface. This expression can be used to determine the index modulation for an AISA of any geometry, flat, cylindrical, spherical, or any arbitrary shape. In some cases, determining the value of r is geometrically complex. For a flat AISA, it is simply $r = \sqrt{x^2 + y^2}$. For a flat AISA designed to radiate at $\vec{k}_o = k_o (\sin q_o \hat{x} + \cos q_o \hat{z})$, with the surface wave source located at $x=y=0$, (See Figure 1) the modulation function is

$$n_{sw}(x, y) = n_o + dn \cos(k_o (n_o r - x \sin q_o)) \quad (6)$$

The \cos function in Eqns. (5) and (6) can be replaced with any periodic function and the AISA will still operate as designed, but the details of the side lobes, bandwidth and beam squint will be affected. We will illustrate this later in this paper.



a.)



b.)

Figure 1. a.) AIS Geometry showing surface waves, radiation and the associated geometries and angles used in the equations. b.) detailed photo of an AIS modulation showing how it is fabricated with square patches of various size.

3. AIS Antenna Fabrication

The AIS can be realized as a grid of metallic patches on a grounded dielectric that produces the desired index modulation (such as in Eqn. (6)) by varying the size of the patches according to a function that correlates the patch size to the surface wave index. Figure 1b shows a photo of square patches of various sizes on an AIS substrate. The correlation between index and patch size can be determined using simulations, calculation and/or measurement techniques. For example, Colburn [3] and Fong [4] use a combination of HFSS unit-cell eigenvalue simulations and near field measurements of test boards to determine their correlation function. Fast approximate methods presented by Simovskii [5] and Luukkonen [6] can also be used to calculate the correlation. However, empirical correction factors are often applied to these methods. In many regimes, these methods agree very well with HFSS eigenvalue simulations and near-field measurements. They break down when the patch size is large compared to the substrate thickness, or when the surface-wave phase shift per unit cell approaches 180° . Figure 2 plots the surface wave index as a function of the patch size and frequency for patches with a grid spacing of 2 mm on a substrate of 50-mil-thick Rogers 3010. The index function's strong dependence on frequency has a strong effect on the AISA's beam squint (as determined by Eqn. (3)) and bandwidth. Later in this paper, we will discuss how designing the AISA with a lower average index and lower modulation reduces these frequency effects.

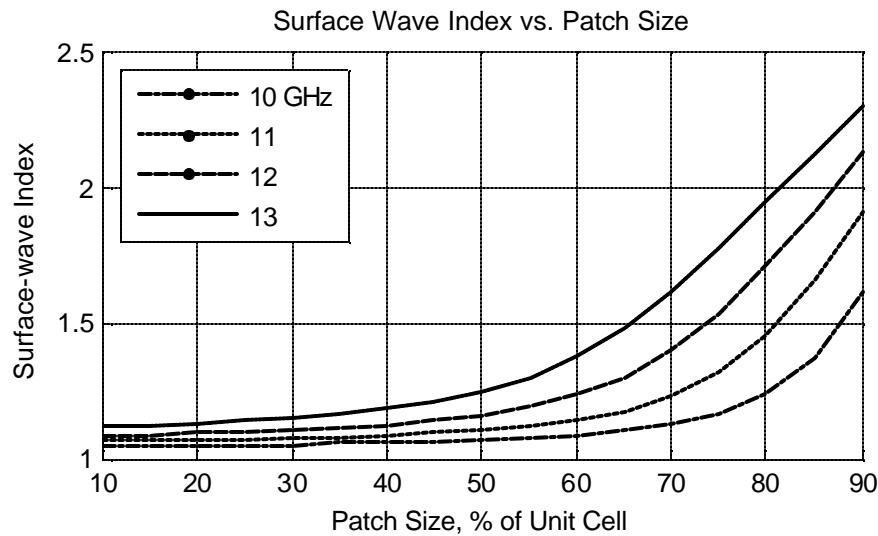


Figure 2 AIS Surface-wave Index vs. Patch Size. The surface-wave index for square patches spaced every 2 mm on a 0.050" thick Rogers 3010 substrate. The index is strongly dependent on frequency and this affects the bandwidth and beam squint of the AISA.

4. AISA Simulation

AISA radiation patterns can be simulated with full-wave electromagnetic modeling tools. For example, Sievenpiper [2], Colburn [3] and Fong [4] use FastScat® to simulate AISA radiation patterns. FastScat® is a full-wave, frequency-domain, method-of-moments EM modeling tool based on a high order, Nyström discretization [7,8]. In FastScat® simulations, the AIS is represented as an impedance boundary layer whose impedance varies according to the design's modulation function. A dipole or waveguide feed launches the surface wave across the AIS and the far-field radiation is calculated by the simulation. The simulation calculates the exact surface currents of the surface wave as it propagates across the AIS, and then computes the radiation field from the currents. The effects of radiation attenuation on the surface waves, and the effects of edges are included in the current and radiation calculations. A typical AISA simulation (e.g. a 10" by 16 " AISA radiating at 60° off normal at 12 GHz) using FastScat® requires approximately 72 hours CPU time per frequency point running on an SGI shared-memory, multi-processor cluster. At each frequency point, the impedance boundary model must also be recomputed to account for the frequency-dependence of the AIS patch size vs. impedance correlation function.

We have developed a fast approximate method of calculating AISA far-field patterns that takes less than 1.0 s CPU time on a Dell Latitude D630 laptop computer, and allows for rapid AISA parametric studies. The method assumes that the surface currents produced by the surface waves propagating across the AIS produce the radiation and that they can be accurately approximated as propagating along straight lines from the surface wave source. In this method, the radiation field is written exactly as the integral of the fields due to the surface wave currents [9] on the AIS, and is proportional to

$$\bar{\mathbf{E}}_{rad}(\bar{\mathbf{k}}) \sim \int_{AIS} \left[(\hat{\mathbf{k}} \times \vec{\mathbf{J}}_{sw}(\bar{\mathbf{r}})) \times \hat{\mathbf{k}} \right] e^{-i\bar{\mathbf{k}} \cdot \bar{\mathbf{r}}} d^2 r \quad (7)$$

where $\vec{\mathbf{J}}_{sw}$ is surface wave current, $\bar{\mathbf{r}}$ is the position on the AIS and $\bar{\mathbf{k}}$ is the radiation wavenumber, and. The surface wave current is expressed as

$$\vec{\mathbf{J}}_{sw}(\bar{\mathbf{r}}) = \vec{\mathbf{j}}_{sw}(\bar{\mathbf{r}}) e^{if_{sw}(\bar{\mathbf{r}})} e^{iwt} \quad (8)$$

where $\vec{\mathbf{j}}_{sw}(\bar{\mathbf{r}})$ represents the magnitude and polarization of the surface current at position $\bar{\mathbf{r}}$ on the AIS. The temporal variation expressed by e^{iwt} will be implicit in the following analysis. $f_{sw}(\bar{r})$ is the phase of the surface wave and it is expressed in terms of $n_{sw}(\bar{\mathbf{r}})$, the surface wave's propagation index, as

$$f_{sw}(\bar{\mathbf{r}}) = k \int_{L(\bar{\mathbf{r}})} n_{sw}(\bar{\mathbf{r}}') dl' \quad (9)$$

where $L(\vec{r})$ is the path of the surface from its source to the position \vec{r} , and $dl\hat{\mathbf{c}}$ is the increment along that path. (If n_{sw} is constant along the path, then $\mathbf{f}_{sw}(\vec{r}) = k n_{sw} \hat{\mathbf{r}}$.) We approximate this expression by choosing $L(\vec{r})$ to be a geodesic line from the surface wave source to \vec{r} . For flat AIS antennas, that geodesic is a straight line and the limits of the integral are from 0 to r . We ignore any deviation from a straight line caused by spatial variation of n_{sw} . As long as the index variations are gentle, the path can be accurately treated as a straight line. (In EM tools like FastScat \circledcirc , the meandering path is treated exactly.)

It is possible to use equations (7) through (9) to show that the integral of Eqn. (7) is maximized when a modulation function of the form of Eqn. (5) is used. This eliminates the ad-hoc phase matching arguments used in Section 2, but its presentation is beyond the scope of this paper.

For a flat AISA, applying Eqns. (8) and (9) into Eqn. (7) yields

$$\vec{\mathbf{E}}_{rad}(\vec{k}) \sim \int_{AIS} \left[(\hat{\mathbf{k}} \times \vec{\mathbf{j}}_{sw}(\vec{r})) \times \hat{\mathbf{k}} \right] e^{i[k \int_0^r n_{sw}(\vec{r}') dr' - \vec{k} \cdot \vec{r}]} d^2 r. \quad (10)$$

The field term $\left[(\hat{\mathbf{k}} \times \vec{\mathbf{j}}_{sw}(\vec{r})) \times \hat{\mathbf{k}} \right]$ is separated into a product of the surface current's magnitude, $j_{sw}(\vec{r})$, and the field's angular distribution, $\vec{\mathbf{P}} = \left[(\hat{\mathbf{k}} \times \hat{\mathbf{j}}_{sw}(\vec{r})) \times \hat{\mathbf{k}} \right]$. The distribution term depends on the polarization of the surface wave and whether it is transverse magnetic (TM) or transverse electric (TE). Using the approximation of straight-line propagation,

$$\hat{\mathbf{j}}_{sw}(\vec{r}) = \begin{cases} \hat{\mathbf{z}} \times \hat{\mathbf{r}}; & TM \\ \hat{\mathbf{r}} & TE \end{cases}, \quad (11)$$

where $\hat{\mathbf{z}}$ is normal to the AIS (See Figure 1a), and

$$\vec{\mathbf{P}} = \begin{cases} \cos(\mathbf{f} - \mathbf{f}_r) \cos(\mathbf{q}) \hat{\mathbf{q}} - \sin(\mathbf{f} - \mathbf{f}_r) \hat{\mathbf{f}}; & TM \\ -\cos(\mathbf{f} - \mathbf{f}_r) \hat{\mathbf{q}} - \sin(\mathbf{f} - \mathbf{f}_r) \cos(\mathbf{q}) \hat{\mathbf{f}}; & TE \end{cases} \quad (12)$$

where \mathbf{f} and \mathbf{q} denote the radiation's propagation direction, and \mathbf{f}_r is surface wave's propagation angle, $\cos(\mathbf{f}_r) = \hat{\mathbf{r}} \cdot \hat{\mathbf{x}}$.

The surface current magnitude, $j_{sw}(\vec{r})$, attenuates as the surface wave propagates away from the source due to 1) spreading of the wave across the antenna surface, and 2) to

power being radiated away. The first contribution is approximated by $j_{sw}(\vec{r}) \sim 1/r$. The second contribution is dependent on the details of the AIS's index modulation, and the calculation has not yet been attempted, but it can be approximated by an exponential attenuation whose factors are deduced empirically. Comparisons between measurements and these simulations show that the radiation attenuation has little impact on the important gross features of the radiation pattern. Codes such as FastScat[©] include the radiation attenuation explicitly.

We have implemented Eqn. (10) into Matlab[©] code to predict AIS antenna radiation patterns. The phase term of Eqn. (9) is calculated according to the geodesic method, and the surface current attenuation is approximated as described above. Figure 3 shows radiation patterns as calculated by our fast approximate method, and is compared to FastScat[©] calculations. The curves are normalized relative to their peak field intensity. The main lobe calculated by both methods agrees well to within a 1° shift. FastScat more accurately models the low-amplitude side-lobe radiation (e.g. at -20°). It also includes effects of direct radiation from the dipole feed that isn't coupled into the AIS.

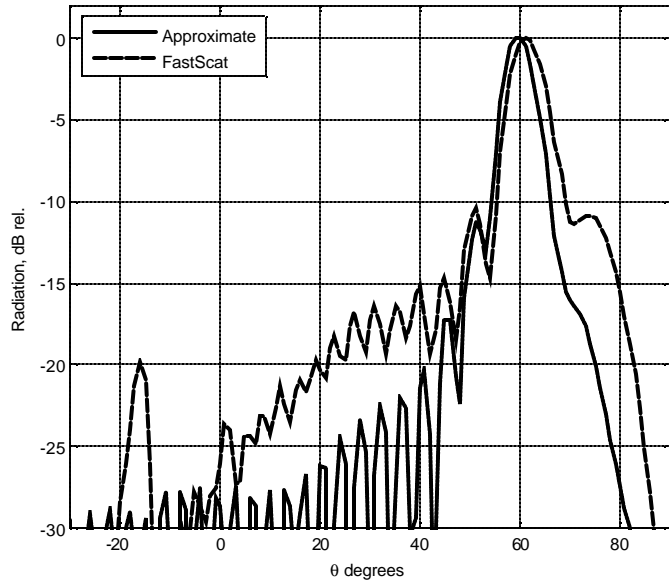


Figure 3 Comparison of the fast approximate method to FastScat

Fastscat more accurately models low-amplitude side-lobe radiation (e.g. at -20°). It also includes direct radiation from the dipole feed that isn't coupled into the AIS, e.g. the low-level radiation from 0° to 40° and the lobe at 75° .

Index vs. Reactance

In previous AISA work, the AIS modulation is treated as variation of the surface reactance, X_{sw} [1-4]. In our analysis, we use the index rather than the reactance because of the natural association of the surface wave phase to the index seen directly in Eqn. (9), and to its subsequent impact on simplifying the radiation calculations following from Eqns. (7) and (8). The surface wave index is related to the impedance by

$$n_{sw} = \sqrt{1 + X_{sw}^2}. \quad (13)$$

When $X_{sw} \gg 1$, the difference between using index and reactance is negligible.

The impact of simplifying the radiation formulation with the index instead of the reactance can be appreciated by considering a classic one-dimensional AIS antenna problem. The surface wave propagates along a path of a sinusoidal modulated reactance of the form

$$Z_{sw}(x) = jX \left[1 + M \cos(k_p x) \right] \quad (14)$$

Here, X is the average impedance, M is the fractional modulation factor and k_p is the modulation wavenumber. The result of applying Eqn. (14) to Eqns. (13) through (7) is

$$E_{rad} \sim \int_0^L e^{-i \left[\left\{ k \int_0^{x'} \sqrt{1+X^2(1+M \cos(k_p x''))^2} dx'' \right\} - k_x x' \right]} dx' \quad (15)$$

when the magnitude of the surface current $\vec{j}_{sw}(\vec{r})$ is magnitude is assumed constant.

Compare Eqn. (15) to the expression that results when the sinusoidal index modulation of Eqn. (4) is applied.

$$E_{rad} \sim \int_0^L e^{-i \left[(k n_o - k_x)x + \frac{dn}{k_p} \sin(k_p x) \right]} dx \quad (16)$$

The elimination of the integral in the exponential argument greatly simplifies calculation of the field integral; the case for the two-dimensional AISA applied to Eqn. (10) is analogous.

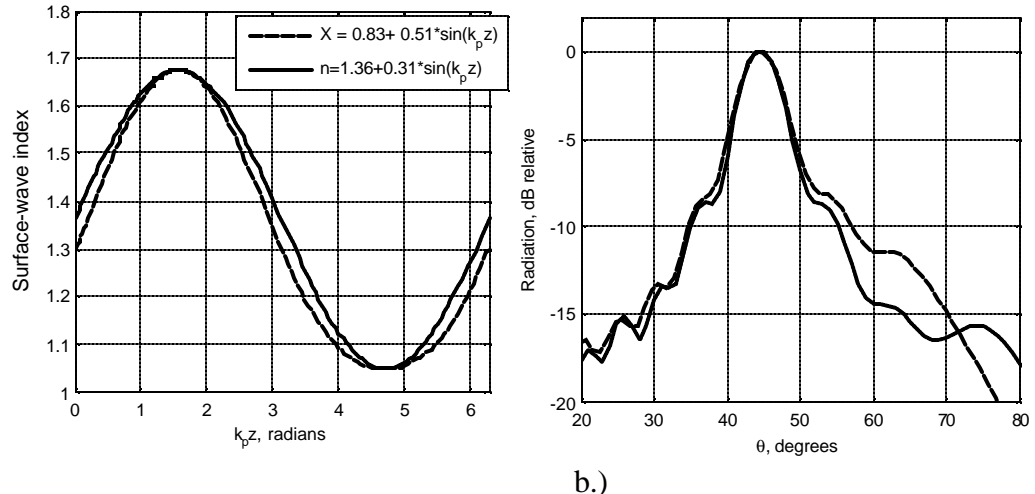


Figure 4 Comparison between sinusoidal index and sinusoidal impedance modulation. a.) The index and reactance modulation profiles. The reactance modulation varies slightly from the sinusoidal index modulation. b.) the radiation patterns (as calculated by FastScat) resulting from the index and reactance modulation show very little difference.

Figure 4a shows a comparison of how the index differs between a sinusoidal index modulation and an equivalent sinusoidal reactance modulation. In this example, the reactance modulation results in a slight broadening of the low-index region and a narrowing of the high-index region. Figure 4b compares simulations of the radiation patterns of two 45° , 10-GHz AISAs with the sinusoidal index or reactance modulation respectively. There is an increase in power radiated into angles greater than the main lobe, but very little difference in the rest of the pattern.

5. AISA bandwidth and frequency squint

The bandwidth of an AISA is limited by the beam squint of the radiation lobe with frequency. The peak radiation angle of an AISA antenna varies with frequency according to Eqn. (3) and the beam squint can be expressed as

$$\frac{d\mathbf{q}}{dk} = \frac{1}{\cos(\mathbf{q})} \left(\frac{dn_o}{dk} + \frac{k_p}{k^2} \right). \quad (17)$$

where the two contributions are due to 1) the AIS's index dispersion, $\frac{dn_o}{dk}$ and 2) the AIS modulation's Floquet term, $\frac{k_p}{k^2}$. The index dispersion is significant and can dominate the beam squint. It is determined by the AIS properties, and can be calculated by various analytic or simulation methods (See discussion preceding Figure 2). Figure 5 shows

measured and simulated beam squint for an AISA that radiates at 60° at 11.6 GHz . The peak intensity drops by 3 dB with a frequency shift of $\sim 100\text{ MHz}$. The beam squint at 11.6 GHz is $34^\circ/\text{GHz}$; the major contribution due to the index dispersion is $27^\circ/\text{GHz}$.

The beam squint can be reduced by designing the AIS modulation to minimize the index dispersion. If the index dispersion is eliminated, then the ultimate lower limit for the beam squint is the Floquet term which is $7.1^\circ/\text{GHz}$ in this example. [Note: if an AIS can be fabricated with negative dispersion such that $\frac{dn_o}{dk} = -\frac{k_p}{k^2}$, then there will be no beam squint at all.]

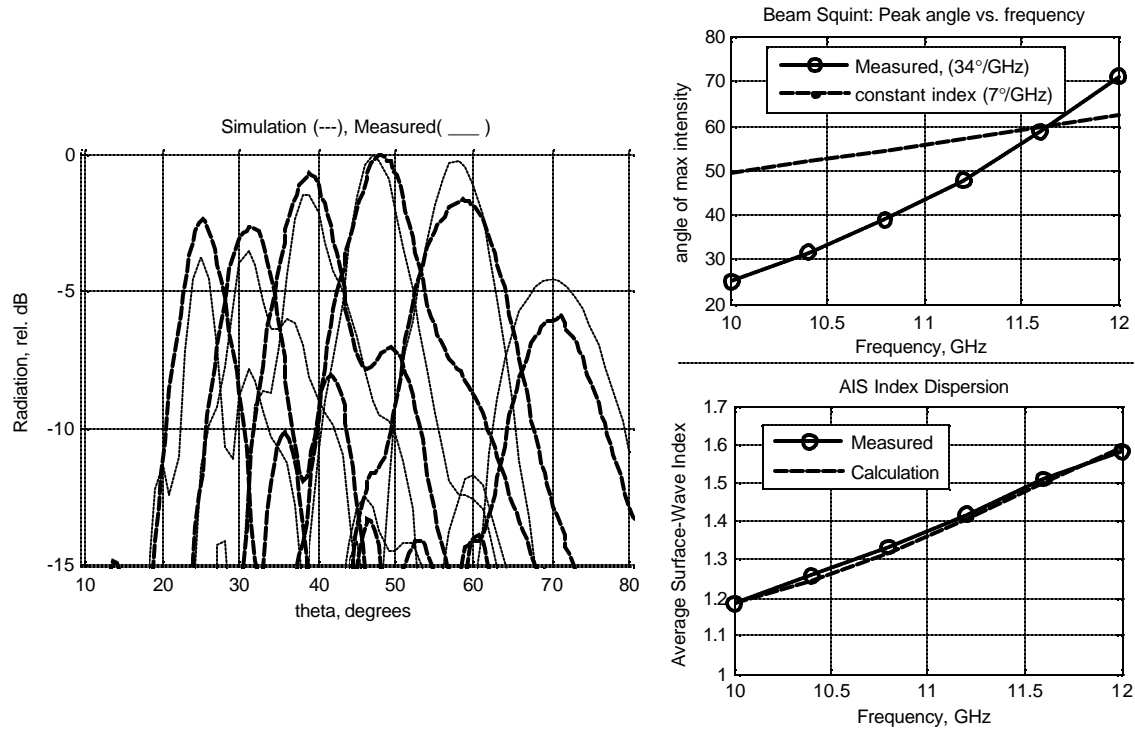


Figure 5 Radiation patterns, index dispersion and beam squint. Left: the frequency dependence of the of the AISA's radiation pattern. From left to right, the patterns are for $10.0, 10.4, 10.8, 11.2, 11.6$ and 12.0 GHz . The dashed lines are from the fast simulation method, the solid lines are measured. Top Right: The beam squint for the measured AISA is $34^\circ/\text{GHz}$, most of it being due to the AIS's index dispersion. If there is no dispersion, i.e. the AIS index is constant with frequency, then the beam squint is only $7^\circ/\text{GHz}$. Bottom Right: The AIS index dispersion is calculated according to Luukkonen [5,6]. It's compared to the index deduced from the measured peak radiation angle and Eqn. (3)

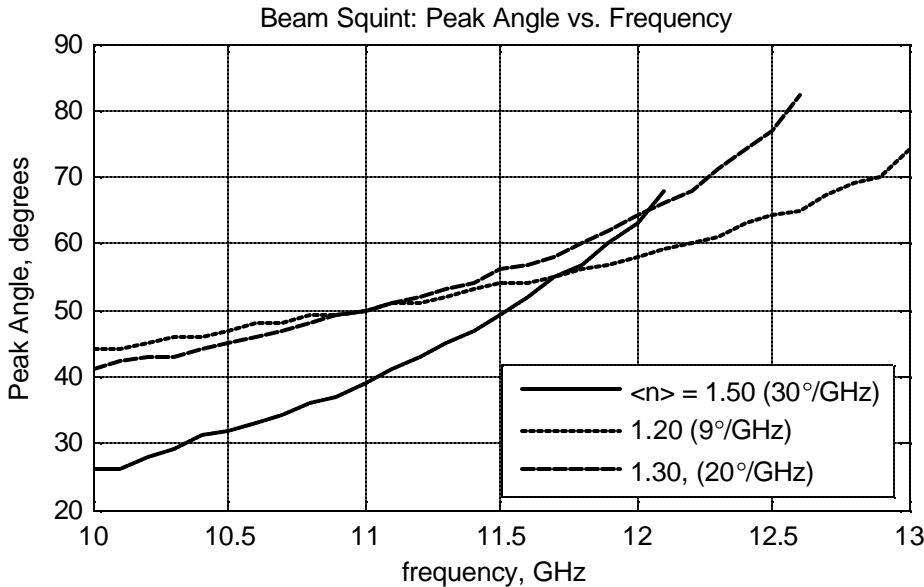


Figure 6 Peak angle vs. frequency for various values of the average index.

Measurement of three different AISAs show that decreasing the modulation's average index from 1.50 to 1.20 decreases the beam squint from 30°/GHz to 9°/GHz, in agreement with the fast approximate simulations.

The simplest way to reduce the index dispersion is by reducing n_o , the average value of the index modulation, because the dispersion is a highly nonlinear function of the index as seen in Figure 2. When the index is ~ 1.0 , the dispersion essentially vanishes. It's impossible to reduce the average index to exactly 1.0 because the index is always greater than the index of the bare grounded dielectric. For the AISAs examined here (on 50-mil thick Rogers 3010 substrates), the minimum index at 12 GHz is 1.08, therefore a reasonable minimum value for n_o is in the range between 1.2 and 1.3. The disadvantage to using low-index AIS modulation is that the number of side lobes increases as indicated in Eqn. (3).

We fabricated two low-index AISAs with reduced n_o and compared their beam squint to the AISA with $n_o = 1.50$ in Figure 6. One of the low-index AISAs has $n_o = 1.30$ with a sinusoidal modulation of ± 0.17 . Its index dispersion is $0.16/\text{GHz}$. The other AISA has $n_o = 1.2$, but with a square modulation pattern with amplitude of 0.20 and a high-index duty factor of 20%. I.e. the index is modulated such that it is at a low value of 1.12 for 80% of the time and at a high value of 1.52 for 20% of the time. The net index dispersion for this modulation is $0.082/\text{GHz}$. The $n_o = 1.50$ AISA's index dispersion is 0.238. The measured beam squint as shown in Figure 6 for these three AISAs (30°, 20°, and 9°/GHz respectively) correlate well with the calculated index dispersion.

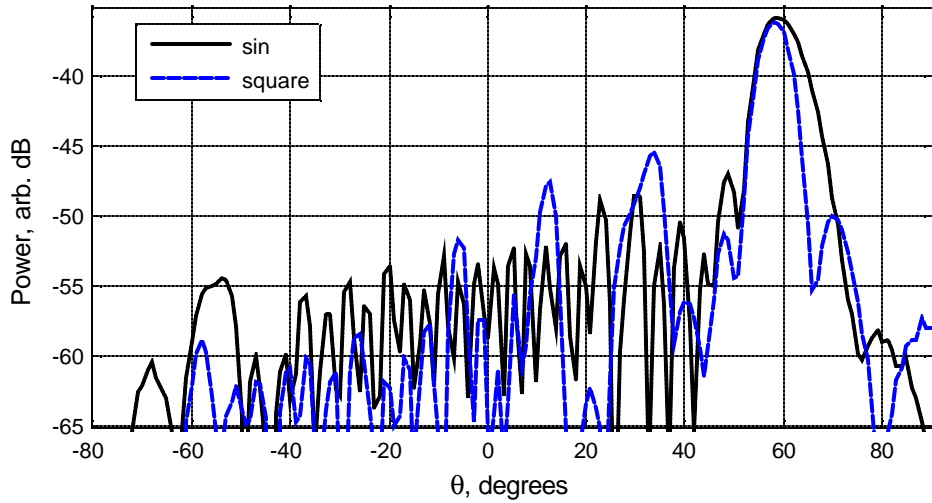


Figure 7 Measured AIS Antennas with sinusoidal and square index modulation

The square-modulation AISA minimizes the index dispersion and the beam squint. The disadvantage is its pattern has pronounced side lobes as seen in Figure 7. It's possible to cancel the side lobes with iteration to the AIS modulation that superimposes the main radiation modulation with a secondary modulation out of phase with the side lobe.

6. TE vs. TM Surface Wave Feeds

TM-mode AISAs are limited in their angular range because of the $\cos(\mathbf{q})$ term in equation (12). Conceptually, this is because each current element is a radiation dipole parallel to the surface. If the dipole lies along the radiation axis, then its contribution to the field vanishes because $\mathbf{q}=90^\circ$ and $\cos(\mathbf{q})=0$. In practice, a TM-mode AISA is limited to about $\mathbf{q} \sim 75^\circ$ maximum declination. The top left side of Figure 8 shows measured radiation patterns for an AISA radiating from 11.4 to 12.6 GHz by increments of 0.2 GHz. As the frequency is increased, the main lobe angle increases according to Eqn. (3). As the radiation angle increases beyond 75° , the main lobe power drops significantly. The bottom left of Figure 8 shows how the peak intensity drops by more than 13 dB as the main lobe shifts from 55° to 82° . The main lobe cannot be detected as it shifts beyond 82° .

One option for making an AISA that can radiate close to 90° is to design it to be fed with TE-mode surface waves. TE-mode AISAs can radiate very efficiently at high angles of declination because each current element in the integral of Eqn. (10) is perpendicular to the surface-wave propagation, and there is no \mathbf{q} dependence in Eqn. (12) for the $\hat{\mathbf{q}}$ polarization.

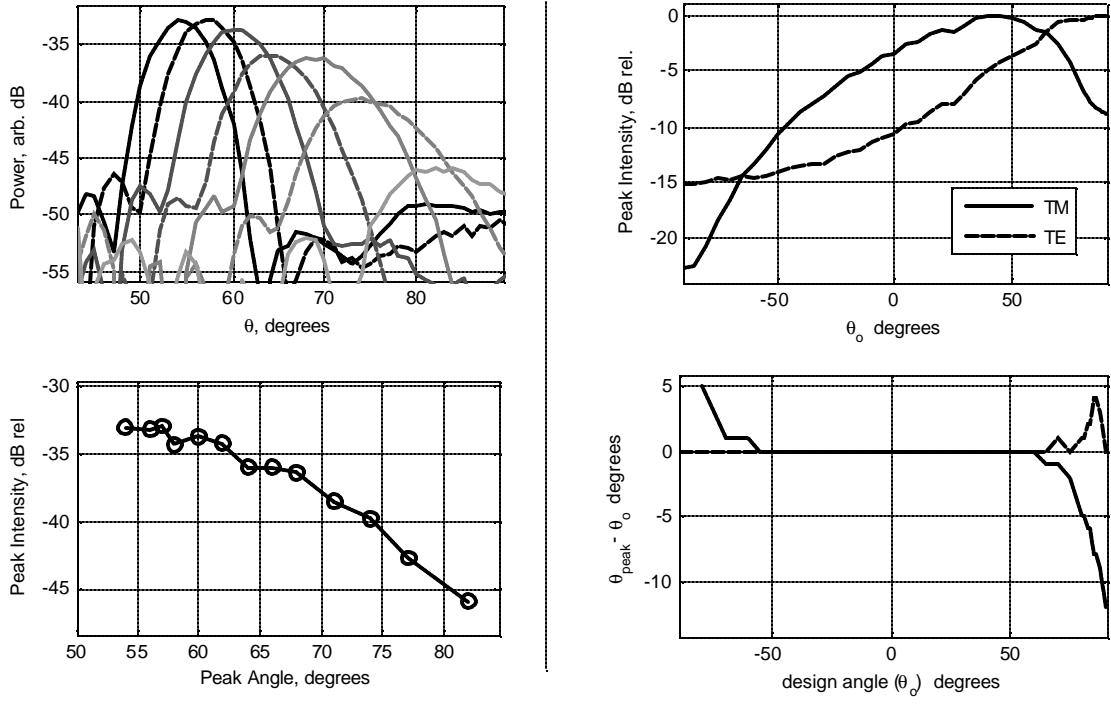


Figure 8 Variation of peak intensity with frequency and peak angle for $n_o=1.25$ AISA.

a.) Top graph: Measured radiation patterns for aTM-mode AISA from 11.4 to 12.6 GHz by 0.2 GHz. The main lobe angle increases with frequency according to Eqn. (1). Bottom graph: peak intensity decreases sharply as the lobe angle approaches 90° .

b.) Simulations comparing TE-mode to TM mode AISAs, and how the main lobe intensity changes with design angle. Top graph: intensity the man lobe vs. its angle. Bottom graph: deviation of the main lobe's angle from its design angle. Once the design angle exceeds than 60° , the main lobe fails to track it.

The right side of Figure 8 compares TM mode and TE mode AISAs designed to radiate at various angles from -90° to 90° , and how the main lobe power varies with angle. Each of the AISAs are simulated as having sinusoidal index modulation with $n_o=1.3$ and $dn=0.17$ on a 16"x10" AIS. The AISAs are fed with an idealized 12-GHz, omnidirectional surface-wave feed located at the far-left center of the AISA. A negative main lobe angle means that the AISA radiates in the direction opposite to the surface-wave propagation. The top right graph shows how the main lobe's peak intensity varies with the design angle. The TM-mode AISA's peak radiation drops abruptly as the design angle approaches 90° , while the TE-mode AISA's intensity is maximum there. It is interesting to note that the TM-mode AISA reached peak intensity for a design angle of 45° . Another important result of this study is that backward radiators, i.e. those with $q_o \neq 0^\circ$, are inherently worse antennas than forward radiators. This fact has been confirmed empirically. The bottom right graph plots how close the main lobe's angle is to the design

angle. The TM-mode AISA's main lobe deviates from the design angle when q_o approaches $\pm 90^\circ$; it never gets higher than 78° , in close agreement with the measured data in the bottom left graph. The TE mode AISA radiates at its design angle except near 90° .

7. Conclusion

We have developed a fast approximate method for simulation of artificial impedance surface antennas that can rapidly compute radiation patterns for flat and curved AISA. We have compared simulations using this tool to simulations using FastScat[©] and shown the comparison to be very favorable for main lobe calculations. We have fabricated several AIS antennas and compared their measured radiation patterns favorably to the fast approximate method. We then used the fast approximate method to study the effects of index modulation on AISA antenna patterns, showing that beam squint can be reduced with lower average index modulation. These predictions were confirmed by measurements.

8. Acknowledgements

We would like to acknowledge and thank J. J. Ottusch for showing us how to successfully use FastScat[©] to simulate AIS antennas, for guiding us on evaluating the results, and for asking the tough questions.

Thanks to John Visher for providing essential and timely FastScat[©] support.

We extend our gratitude Brian Fong for discussions on his previous work on AISA design and simulation.

9. References

- [1] Patel and Grbic, "Printed leaky Wave Antenna", 2009 IEEE
- [2] D. Sievenpiper, J. Colburn, B. Fong, J. Ottusch and J. Visher., 2005 IEEE Antennas and Prop. Symp. Digest, vol. 1B, pp. 256-259, 2005.
- [3] J. S. Colburn et al., "Scalar and Tensor Artificial Impedance Surface Conformal Antennas", 2007 Antenna Applications Symposium, pp. 526-540.
- [4] B.H. Fong et al, "Scalar and Tensor Holographic Artificial Impedance Surfaces", IEEE Trans. Antennas Propag., accepted for publication, 2010
- [5] C. Simovskii et al, "High-impedance surfaces having stable resonance with respect to polarization and incidence angle", IEEE Trans. Antennas Prop., vol. 53, 908, 2005

- [6] O. Luukkonen et al, “Simple and accurate analytical model of planar grids and high-impedance surfaces comprising metal strips or patches”, IEEE Trans. Antennas Prop., vol. 56, 1624, 2008
- [7] L. S. Canino, J. J. Ottusch, M. A. Stalzer, J. L. Visher, and S. M. Wandzura, ” Journal of Computational Physics, vol. 146, pp. 627-663, 1998.
- [8] H. Contopanagos, B. Dembart, M. Epton, J. J. Ottusch, V. Rokhlin, J. Visher, and S. Wandzura, IEEE Transactions on Antennas and Propagation, vol. 50, no. 12, pp. 1824-1830, Dec. 2002.
- [9] J.D. Jackson, “Classical Electrodynamics, 2nd Ed.”, Wiley, New York, 1975

uCAST-A NEW GENERATION UTD CODE FOR RADIATION PATTERN PREDICTIONS OF ANTENNAS ON AIRCRAFT MODELS

Çağatay Tokgöz and C. J. Reddy
Applied EM, Inc., 144 Research Drive, Hampton, VA 23666

Abstract

A new generation aircraft antenna radiation pattern prediction code has been being developed based on the application of UTD to faceted CAD models¹. A platform-independent, comprehensive and user friendly graphical user interface (GUI) has also been being developed. The code allows the user to import a faceted aircraft model and place an antenna on it. Rays that originate from the antenna, interact with the aircraft platform, and propagate in a far field direction are tracked. Geometrical parameters such as geodesic path length and radius of curvature that are required for UTD analysis are extracted from the platform model by using quadratic surface mapping. The code applies UTD solutions along the rays to find the field contribution from each ray, and the contributions from all the rays are combined to predict radiation pattern of airborne antennas. The GUI has pre-processing capabilities of showing the imported platform model and placed antenna as well as post-processing capabilities of visualizing the tracked rays and displaying radiation pattern data. The code has been validated by comparing its data with MLFMM data for a cylinder-wing configuration.

1. Introduction

Several antennas with different communication purposes are usually mounted on modern aircraft. Radiation patterns of these antennas can be significantly altered after they are mounted due to the interactions with the aircraft. Hence, prediction of radiation pattern associated with airborne antennas is very critical.

Fast and efficient low frequency techniques based on the method of moments (MoM) [1] and the finite element method (FEM) [2] become time consuming and even intractable in the analysis of platform-mounted antennas at high frequencies as the platform becomes electrically large. These techniques also do not directly provide any physical insight into the wave mechanisms involved in the analysis. In addition, high frequency techniques such as the physical optics (PO), its modifications based on the physical theory of diffraction (PTD) [3], and the shooting and bouncing ray (SBR) method [4] do not account for creeping waves resulting in inaccurate predictions of the fields in the shadow regions of antennas where these waves usually provide major contribution to the fields. As an asymptotic high frequency technique, the uniform geometrical theory of diffraction

¹ This code is being developed under a NAVAIR SBIR program (TPOC, Dr. John Asvestas and Mr. Dennis DeCarlo)

(UTD) does not suffer from the above mentioned limitations since it accounts for creeping waves and scales with frequency unlike the other techniques. There are available UTD based research codes such as NEW-AIR and NEC-BSC, which have proven to be very successful over the last two decades. However, these codes require a priori approximation of the electrically large platform in terms of canonical shapes such as elliptic cylinders, spheroids, flat plates and cone frustums, which itself is a challenging task. The absence of a UTD code that is directly applicable to platforms with arbitrary shape has led to the idea of developing a more versatile and state of the art UTD code to predict radiation pattern of antennas on faceted platforms. The authors of this paper have been working on the development of such a general purpose UTD code with a sophisticated and user friendly GUI. This new generation code is called uCAST. The development of the uCAST code is covered in this paper.

The uCAST code is based on the application of UTD to platform models represented with triangular facets. An electric or magnetic current moment, a monopole antenna with a known current distribution, or an antenna with a pre-computed radiation pattern on a perfectly conducting (PEC) infinite flat plate are available as options for a source of excitation. An antenna can be defined by choosing one of these options and it can be placed on the platform model. First-order interactions of direct propagation, reflection, edge diffraction, corner diffraction, convex surface diffraction as well as second-order interactions of convex surface diffraction followed by reflection, edge diffraction or corner diffraction can be selected to be included in ray tracking. Ray tracking algorithms have been developed and implemented into the code for these interactions. After the rays pertaining to the selected interactions are tracked, quadratic surface mapping is used to extract geometrical parameters such as geodesic path length, radius of curvature, surface torsion and divergence factor and to compute surface normal, bi-normal and tangential vectors that are needed to apply UTD solutions along the tracked rays. The field contribution from each ray is computed by applying the relevant UTD solution, and contributions from all the rays are combined to predict radiation pattern of the antenna. The code has been used to generate radiation pattern data for antennas on a cylinder-wing configuration. This data has been compared with MLFMM data for validation which suggests that the uCAST code can yield reasonably accurate data.

2. UTD Analysis of Faceted Platform Models

A flow chart for the uCAST code is shown in Figure 1. The GUI allows the user to import a platform model. A single frequency as well as a linear or logarithmic frequency range can be requested for analysis. An antenna, which can be specified as an electric or magnetic current moment, a monopole antenna or an antenna with a pre-computed radiation pattern on a PEC infinite flat plate can be defined and placed on the platform model. The mesh surface and mesh grid for the platform model as well as the placed antenna can be viewed on a three-dimensional (3-D) display window of the GUI. First-order and second-order interactions to be considered in a UTD analysis can be selected, and a radiation pattern can be requested on a two-dimensional (2-D) plane. Then, the user can perform a UTD analysis which tracks the rays pertaining to the selected interactions

first, extracts necessary geometrical parameters, applies relevant UTD solutions along the tracked rays and then combines contributions from all the rays to compute the radiation pattern of the antenna. After the UTD analysis is completed, all the tracked rays or the rays associated with the selected interactions can be displayed on the platform model. The GUI can also display a 2-D rectangular or polar plot of the total radiation pattern, or the radiation pattern for the selected interactions. In addition, a 2-D display of the total radiation pattern or the radiation pattern for the selected interactions can be generated over the platform model.

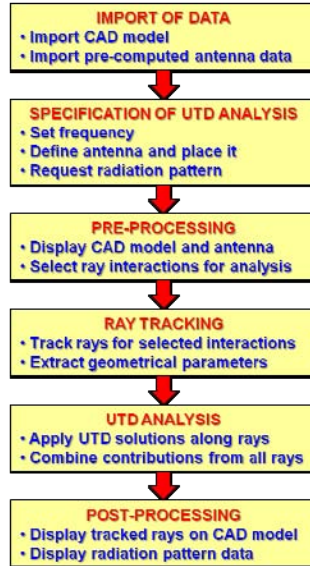


Figure 1: Flow chart for the uCAST code.

2.1. Ray Tracking

Once a platform model is imported, frequency is set, an antenna is defined and placed, and a radiation pattern is requested, the uCAST code proceeds with ray tracking. Rays that originate from the antenna, interact with the platform through various mechanisms and then propagate towards a far field direction are tracked. There are several mechanisms that could take place when rays interact with the platform. Each mechanism can be either first-order that involves only one interaction with the platform, or multiple-order that includes two or more successive interactions with the platform. Some first-order and second-order interactions that are believed to be more critical have been implemented in the uCAST code. The first-order interactions that are available in the uCAST code are the following:

- Direct ray,
- Reflected rays,
- Edge diffracted rays,
- Corner diffracted rays
- Convex surface diffracted rays.

The second-order interactions corresponding to subsequent occurrence of two first-order interactions that are available in the uCAST code are the following:

- Convex surface diffracted-reflected rays,
- Convex surface diffracted-edge diffracted rays,
- Convex surface diffracted-corner diffracted rays.

Among the first-order interactions, direct rays originate from the antenna and propagate towards a far field direction. Reflected and edge diffracted rays interact with the platform as shown in Figures 2a and 2b, respectively. If an edge diffracted ray is found, corner diffracted rays are also considered for all the corners at which the relevant edge is truncated. Convex surface diffracted rays originate from the antenna, travel over the surface and shed off the surface to propagate towards a far field direction as shown in Figure 2c. The second-order interactions of convex surface diffracted-reflected and convex surface diffracted-edge diffracted rays exist when a convex surface diffracted ray interacts with the platform as shown in Figures 2d and 2e, respectively. If a convex surface diffracted-edge diffracted ray is found, convex surface diffracted-corner diffracted rays are also considered for all the corners at which the relevant edge is truncated.

After the first-order and second-order interactions are found, a shadowing algorithm is used to determine whether they are blocked by any part of the platform. This shadowing algorithm has been accelerated by using boxing and grouping so that only the facets along a ray are searched for blockage instead searching over all the facets in the platform model. The interactions that are not blocked by any part of the platform are considered as valid interactions and the others are discarded.

The uCAST code accepts CAD models consisting of triangular facets which do not provide any curvature information and surface continuity across common edges of neighboring facets. However, curved surface representation with surface and slope continuity across common edges of neighboring facets is required for accurate tracking of surface rays and extraction of the geometrical parameters along these rays that are needed for the application of UTD solutions. Hence, quadratic surface mapping in bary-centric coordinates is used to map a quadratic surface on a triangular facet, and to achieve surface and slope continuity as shown in Figure 3 [8]. Quadratic surface mapping makes it possible to extract the geometrical parameters such as geodesic path length, radius of curvature, surface torsion and divergence factor and to compute the surface normal, bi-normal and tangential vectors that are needed to apply UTD solutions along the tracked rays.

When radiation pattern is computed for a range of angles where reflection from a convex surface of the platform model contributes to the fields for all angles, reflected rays for some angles may not be captured in the absence of quadratic surface mapping since the surface would not be continuous, which will result in discontinuity of reflected fields

across the angles. Therefore, quadratic surface mapping is used to accomplish continuity of these fields as shown in Figure 4.

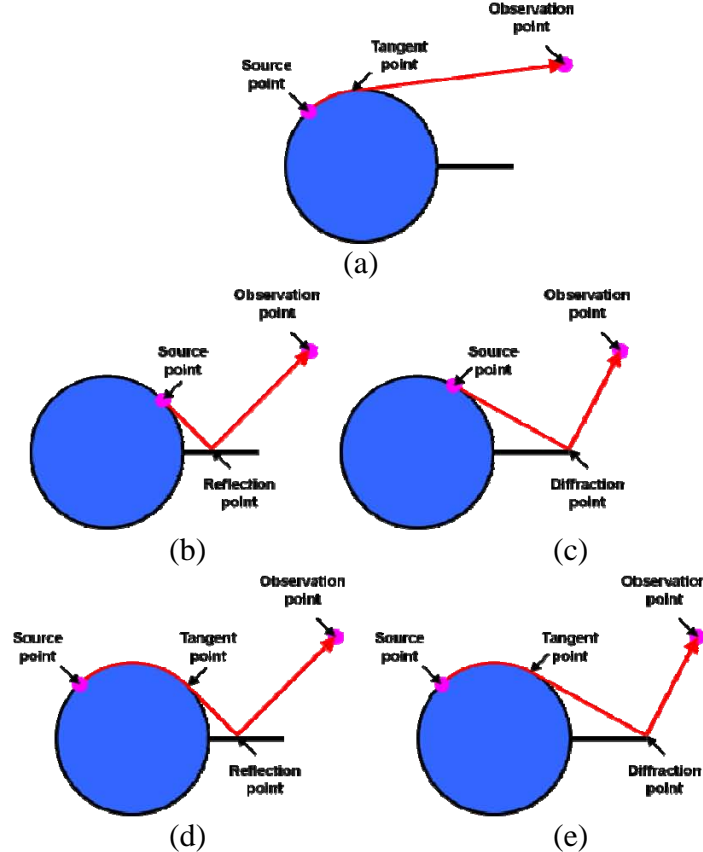


Figure 2: Some first-order and second-order interactions available in the uCAST code: a) A reflected ray. b) An edge diffracted ray. c) A convex surface diffracted ray. d) A convex surface diffracted-reflected ray. e) A convex surface diffracted-edge diffracted ray.

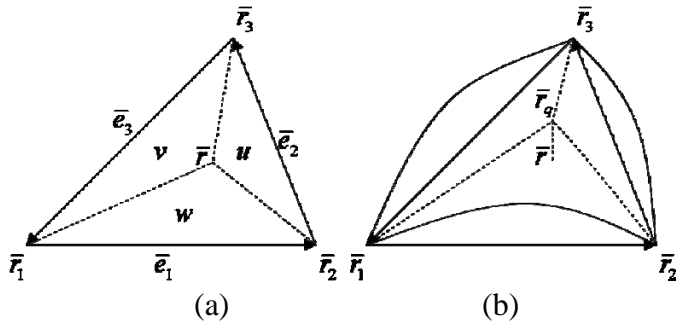


Figure 3: a) Original flat surface representation for a triangular facet. b) Quadratic surface mapping over the triangular facet where a point \bar{r} on the flat surface is mapped to a point \bar{r}_q on the quadratic surface.

2.2. Application of UTD Solutions

After ray tracking and extraction of necessary geometrical parameters, relevant UTD solutions are applied along the tracked rays. UTD solutions for PEC surfaces are available for various interactions, and they are mostly well developed and validated solutions [9], [10]. Several UTD solutions have been implemented into the uCAST code. When the antenna is on a convex surface, its radiation is modified due to the curvature of the surface and hence lit region formulation of the UTD solution for radiation from sources on a convex surface is used for direct rays [11]. The geometrical optics (GO) solution for reflection is employed to find the fields of reflected rays [9]. A UTD solution for edge diffraction has been implemented for edge diffracted rays [12]. When the fields pertaining to an edge diffracted ray are evaluated, UTD solution for corner diffraction is also applied to corner diffracted rays associated with this edge diffraction [13]. The fields contributed by convex surface diffracted rays are computed by employing the shadow region formulation of the UTD solution for radiation from sources on a convex surface [11]. The fields pertaining to convex surface diffracted-reflected, convex surface diffracted-edge diffracted and convex surface diffracted-corner diffracted rays are determined by successive application of the above mentioned shadow region formulation [11] with GO solution for reflection [9], UTD solution for edge diffraction [12] and UTD solution for corner diffraction [13], respectively. Once the fields from all the tracked rays are computed, they can be combined to determine the total field. In addition, fields from rays associated with a particular interaction can be plotted versus angle to see which interaction contributes to radiation in a given direction.

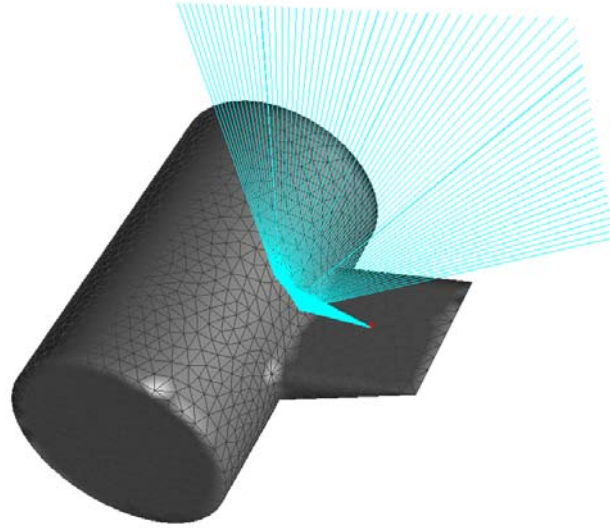


Figure 4: Continuity of reflected fields is achieved over a range of angles with quadratic surface mapping.

3. Numerical Results

The uCAST code has been used to generate numerical data for the radiation pattern of a quarter wavelength monopole antenna on a circular cylinder shown in Figure 5 at 3 GHz. The antenna is vertically placed on the surface of the cylinder at $\phi=0^\circ$. The radiation pattern has been generated in the roll plane for $\phi=0-360^\circ$. The numerical data for antenna directivity obtained from the uCAST code has been compared with the MLFMM data and they are found to compare well as shown in Figure 6. Direct and convex surface diffracted rays contribute to the radiation pattern in the lit and shadow regions of the antenna, respectively. Examples for each type of these first-order interactions are shown in Figure 7.

The uCAST code has been used to generate numerical data for the radiation pattern of a quarter wavelength monopole antenna on a cylinder-wing configuration shown in Figure 8 at 3 GHz. The antenna is vertically placed on the surface of the cylinder at $\phi=45^\circ$. The radiation pattern has been generated in the roll plane as a function of ϕ . The numerical data for antenna directivity obtained from the uCAST code agreed reasonably well with the MLFMM data as shown in Figure 9. The largest disagreement between them is observed when ϕ is between 30° and 45° . This may be due to the absence of the interaction associated with the surface rays diffracted by the root of the wing in the uCAST code. Inclusion of this mechanism may result in more accurate data. Examples are shown in Figure 10 for each type of the first-order or second-order interaction that is available.

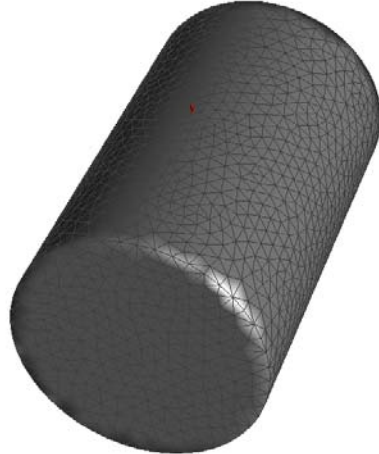


Figure 5: A quarter-wavelength monopole antenna on a circular cylinder for which radiation pattern is computed in the roll plane at 3 GHz.

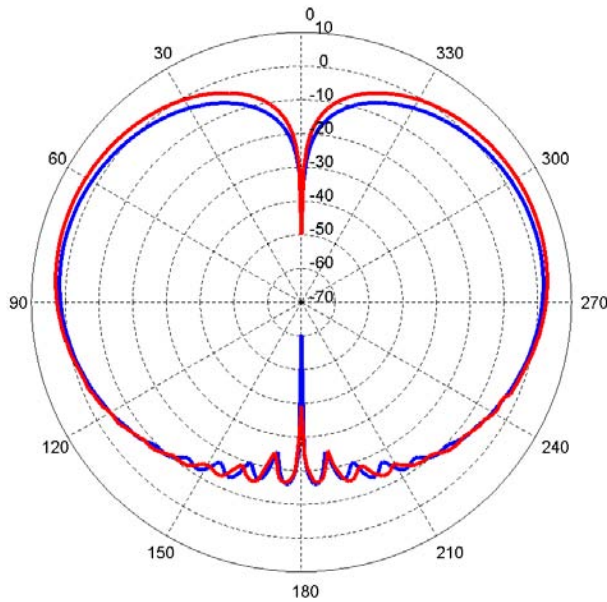


Figure 6: The numerical data for antenna directivity obtained by using the uCAST code in comparison with the MLFMM data for the monopole antenna on a circular cylinder. Directivity is plotted versus the radiation angle ϕ in degrees.

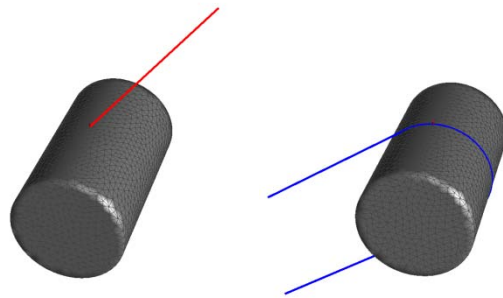


Figure 7: Examples of the tracked first-order interactions. a) A direct ray. b) A convex surface diffracted ray.

4. Conclusion

The development of the uCAST code that is based on the application of UTD to faceted platforms is presented in this paper. Radiation pattern data generated by the uCAST code for monopole antennas on a circular cylinder and a cylinder-wing configuration are compared with the MLFMM data, which suggest that the uCAST code can yield data with reasonable accuracy. Additional interactions will be added to the code to account for more mechanisms and improve accuracy.



Figure 8: A quarter-wavelength monopole antenna on a cylinder-wing configuration for which radiation pattern is computed in the roll plane at 3 GHz.

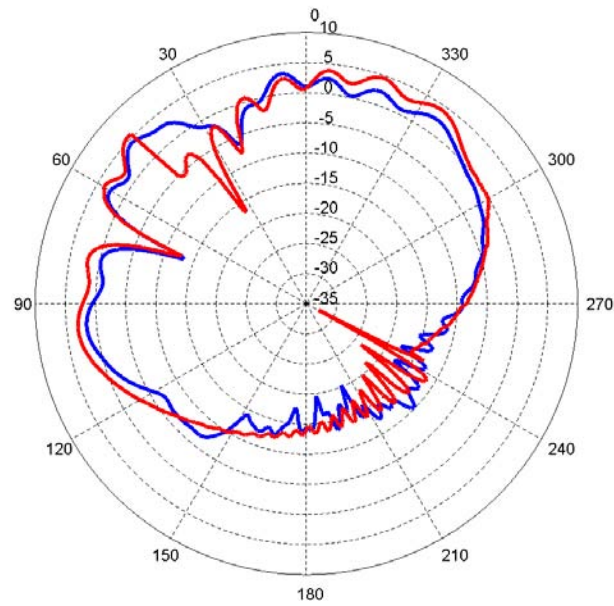


Figure 9: The numerical data for antenna directivity obtained by using the uCAST code in comparison with the MLFMM data for the monopole antenna on a cylinder-wing configuration. Directivity is plotted versus the radiation angle ϕ in degrees.

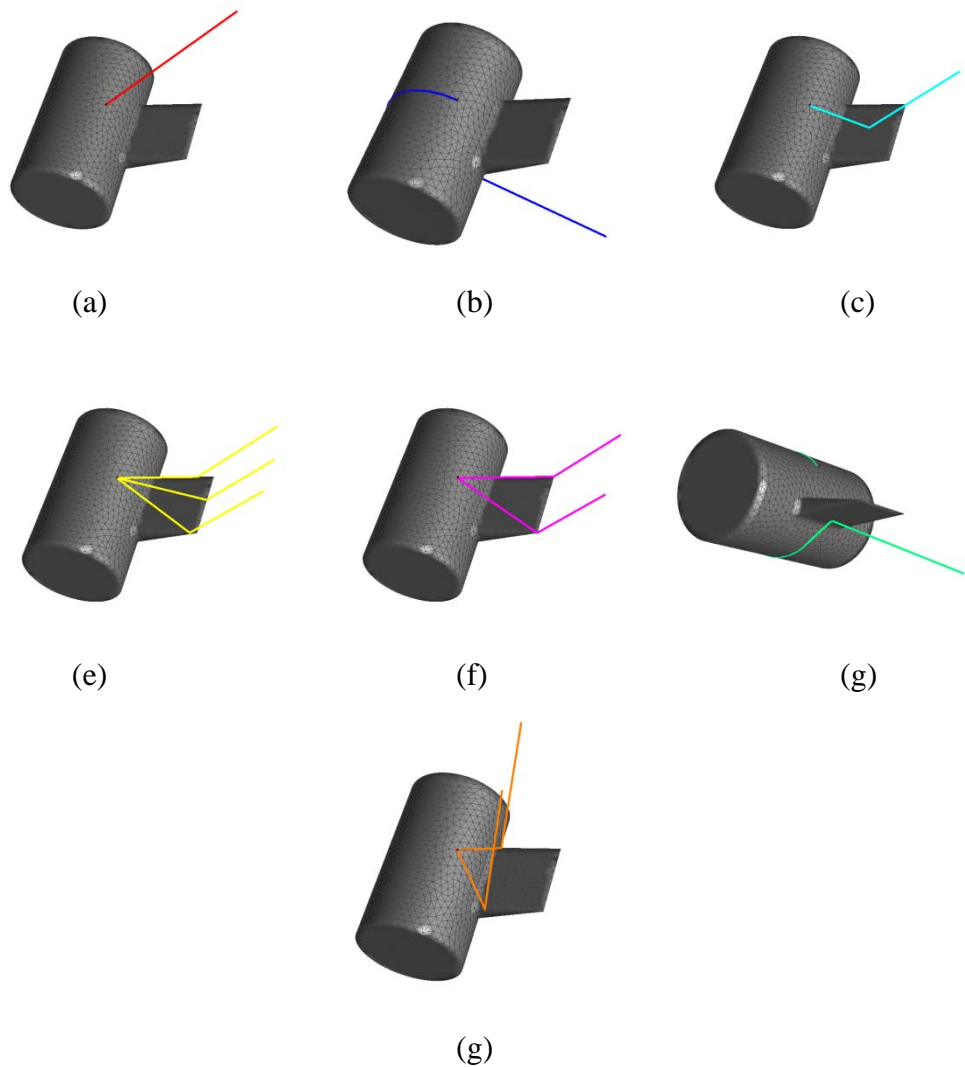


Figure 10: Examples of the tracked first-order and second-order interactions. a) A direct ray. b) A convex surface diffracted ray. c) A reflected ray. d) An edge diffracted ray. e) A corner diffracted ray. f) A convex surface diffracted-reflected ray. g) A convex surface diffracted-edge diffracted ray.

References

- [1] W. C. Chew, J-M Jin, E. Michielssen, and J. Song, *Fast and Efficient Algorithms in Computational Electromagnetics*, Norwood, MA: Artech House, 2001.
- [2] J. Jin, *The Finite Element Method in Electromagnetics*, New York, NY: John Wiley & Sons, 2002.
- [3] P. Ya Ufimtsev, “Method of edge waves in the physical theory of diffraction,” *Soviet Radio*, pp. 1-243, 1962 (Translation into English by the U.S. Air Force, Foreign Technology Division, Wright-Patterson AFB, OH, Sep. 7, 1971).

- [4] H. Ling, R.-C. Chou, and S.-W. Lee, "Shooting and bouncing rays: Calculating the RCS of an arbitrarily shaped cavity," *IEEE Trans. Antennas Propagat.*, vol. 37, pp. 194-205, Feb. 1989.
- [5] W. D. Burnside, J. J. Kim, B. Grandchamp, R. G. Rojas and P. Law, "Airborne antenna radiation pattern code user's manual," *Technical Report, The Ohio State Univ., Dept. of Electrical and Computer Eng., ElectroScience Lab.*, Columbus, OH, Sep. 1985.
- [6] R. J. Marhefka, "Numerical electromagnetic code – basic scattering code, (NEC-BSC version 4.2), user's manual," *Technical Report, The Ohio State Univ. Dept. of Electrical and Computer Eng., ElectroScience Lab.*, June 2000.
- [7] W. D. Burnside and R. J. Marhefka, "Antennas on aircraft, ships, or any large, complex environment," Chap. 20 in *Antenna Handbook: Theory, Applications, and Design*, Y. T. Lo and S.-W. Lee (Eds.), New York, NY: Van Nostrand Reinhold, 1988.
- [8] W. J. Brown and D. R. Wilton, "Singular basis functions and curvilinear triangles in the solution of the electric field integral equation," *IEEE Trans. Antennas Propagat.*, vol. 47, pp. 347-353, Feb. 1999.
- [9] P. H. Pathak, "Techniques for high-frequency problems," Chap. 4 in *Antenna Handbook, Theory, Applications, and Design*, Y. T. Lo and S.-W. Lee (Eds.), New York, NY: Van Nostrand Reinhold, 1988.
- [10] P. H. Pathak, "High frequency techniques for antenna analysis," *Proc. IEEE*, vol. 80, pp. 44-65, Jan. 1992.
- [11] P. H. Pathak, N. Wang, W. D. Burnside, and R. G. Kouyoumjian, "A uniform GTD solution for the radiation from sources on a convex surface," *IEEE Trans. Antennas Propagat.*, vol. 29, pp. 609-622, July 1981.
- [12] R. G. Kouyoumjian and P. H. Pathak, "A uniform geometrical theory of diffraction for an edge in a perfectly conducting surface," *IEEE Trans. Antennas Propagat.*, vol. 62, pp. 1448-1461, Nov. 1974.
- [13] F. A. Sikta, W. D. Burnside, T.-T. Chu, and L. Peters, Jr., "First-order equivalent current and corner diffraction scattering from flat plate structures," *IEEE Trans. Antennas Propagat.*, pp. 584-589, vol. 31, July 1983.

Electrically Small Antenna Design for Low Frequency Systems

Eric A. Richards¹, Hans G. Schantz¹, John A. Unden¹, Kurt A. von Laven², Drew Compston², and Christian Weil³

¹Q-Track Corporation, Huntsville, AL 35805
e.richards@q-track.com

²Stanford University, Stanford, CA 94305

³Georgia Institute of Technology, Atlanta, GA 30332

Abstract

There exist a wide variety of commercial RF devices ranging across the spectrum from the Low Frequency band (e.g. 125 kHz) to mm-wave (e.g. 60 GHz). “High” frequencies (which in this context mean VHF, UHF, microwaves and beyond) are well suited for data communications at high bandwidths. Where the emphasis is on signals penetration and propagation in challenging, reflective environments, however, low frequencies have substantial advantages including 1) superior penetration depth, 2) enhanced diffraction around environmental clutter including doorways and corners, 3) less vulnerability to multipath confusion, 4) long range of operation, typically 60-100 m, and 5) low probability of intercept (LPI). Low frequency systems, such as Near-Field Electromagnetic Ranging (NFER), that exploit near-field behavior to deduce location require compact antennas that are necessarily much smaller than a wavelength. Q-Track’s current transmitter design uses two orthogonally-oriented magnetic antennas to provide isotropic coverage.

We report on our design of a compact, omnidirectional transmitter that operates in the AM broadcast band (550-1710 kHz). Careful design of the magnetic antennas provides gains of -75 dBi despite being only 0.0002λ in dimension, in good agreement with theoretical predictions and FEMM simulations. Furthermore, we have developed a compact (1 m) near-field antenna testing range that allows us to characterize magnetic antennas. This transmitter has been deployed at a variety of sites, showing a tracking accuracy of 1-3 feet over areas as large as 100,000 sq. ft.

Recent work has focused on reducing the size, weight, and cost of our tag by utilizing printed circuit board (PCB) methodologies. We report on a recent breakthrough that allows us to achieve almost an order of magnitude decrease in size while retaining performance.

1. Introduction

The problem of accurate indoor positioning has received much attention, as it promises to address issues such as supply chain management, industrial safety, tactical command and control for urban military and law enforcement activities, and the lack of an alternative to GPS. Most of these Real-Time Locating Systems (RTLS) employ some flavor of RF angle of arrival, time of flight, time difference of arrival, or received signal strength indicators. These techniques almost exclusively operate at microwave frequencies and hence have several distinct disadvantages. Among these are confusion from multipath and environmental clutter, line of sight operation, need for synchronization, range restrictions, and expense. High frequencies, though well-suited for broadband and other communications applications, are a poor choice for wireless tracking.

Q-Track has chosen to approach the problem of indoor location from a different perspective, namely that of leveraging low frequency and near-field behaviors. We designed NFER¹ RTLS from the ground up with a physical layer optimized for location instead of communication. NFER systems typically operate around 1 MHz within about a quarter-wavelength of a transmitter, in the vicinity of the transition between the near- and far-field zones. Several considerations drove Q-Track to consider a low frequency alternative.

First, low frequency signals penetrate better and diffract or bend around the human body and other obstructions. As a general rule, skin depth varies as the square root of frequency, so a decrease of frequency from 6 GHz to 600 kHz (four decades) corresponds to a hundred-fold (20 dB) increase in penetration. Most importantly, low frequency signals are virtually immune from multipath. These physical advantages allow NFER RTLS to operate at relatively long range (> 30-80 m) even in cluttered propagation environments, such as industrial, office, and manufacturing buildings.

Second, conventional far-field systems are limited to measuring various combinations of amplitude and phase of two polarization components (Vertical versus Horizontal, or equivalently, Right-Hand versus Left-Hand Circular). Conventional far-field RTLS that operate at higher frequencies are limited to these four potential parameters to extract a location solution. In the near-field, there are twelve metrics by which we can solve for position. There is an additional polarization, the “radial” field, which is non-zero in the near-field. Also, the electric and magnetic fields retain separate identities in the near-field. Thus near-field location systems can measure two parameters (phase and amplitude) of each of three polarizations (vertical, horizontal, and radial) of each of two fields (electric and magnetic). These twelve parameters allow for more robust and accurate tracking than is possible with standard RTLS techniques.

¹ “NFER” is a registered trademark of the Q-Track Corporation.

A final advantage to NFER tracking is that low frequency RF hardware is inherently less expensive than microwave electronics. As a consequence of the increased range of NFER RTLS, less infrastructure is required to cover a given area. These two factors combine to make NFER RTLS more economical in large scale deployments. Typically, NFER RTLS can be installed at a cost of about \$0.50 to \$1.00 per sq. ft., about an order of magnitude less than microwave competitors. Further details on NFER RTLS are discussed elsewhere [1, 2, 3].

1.1 Near-Field Physics

An electromagnetic wave is composed of both electric and magnetic field components that oscillate perpendicular to each other and perpendicular to the direction of energy flow. In the far-field zone, many wavelengths away from a transmit antenna, this distinction is not terribly important, because the electric and magnetic waves move together with synchronized phase and amplitudes fixed by the impedance of free space, $120\pi \Omega$. In the near-field (Fresnel) zone, within about a half-wavelength from an electrically small antenna, the electric and magnetic field phases diverge. Close to an electrically small antenna, these fields are in phase quadrature, i.e., 90° out of phase.

Figure 1 shows the phase behavior around small antennas. Heinrich Hertz discovered these phase relationships, which serve as the basis of NFER technology pioneered by Q-Track [4]. Figure 1a plots these phase relationships in the near-field of a typical small antenna [5]. The green and red curves show the electric and magnetic phase relationships. The blue curve is the difference between the electric and magnetic. At a known wavelength (λ), the range (r) follows from the electric-magnetic phase difference (Δ_ϕ):

$$r = \frac{\lambda}{2\pi} \sqrt[3]{\cot \Delta_\phi} \quad (1)$$

Figure 1b plots this relationship. Q-Track's NFER works well out to about a quarter-wavelength, depending on the signal-to-noise ratio (SNR) of the link.

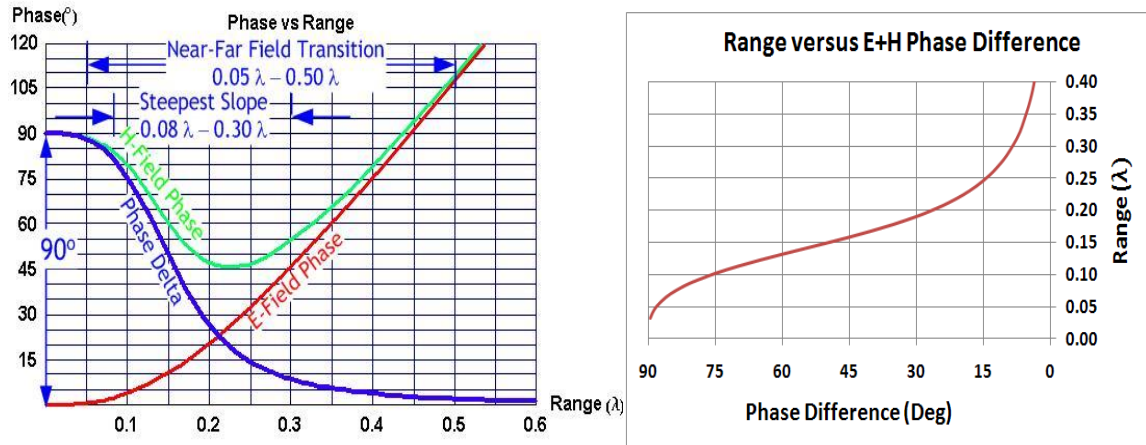


Figure 1a (left): Phase relationships around an electrically small Hertzian dipole. **Figure 1b (right):** Range versus electric-magnetic phase difference for a NFER signal.

Although we usually consider the impedance of free-space to be a fixed value of 377Ω , this is not the case in the Fresnel region where the ratio of electric to magnetic field amplitudes is a strong function of both radial distance to the source and orientation. Below we show a NEC simulation of electrically small dipoles. Our receiver array is composed of two orthogonal magnetic loops in the Vertical polarization and a V-pol electric whip. In Figure 2a we plot the impedance as a function of range for both an electric and magnetic dipole emitter. Both converge to free-space values after about a wavelength, but they have very different behaviors. In Figure 2b we show an impedance simulation from our QT-500 transmitter composed of quadrature-fed orthogonal magnetic loops. The elevation slice is taken at $\theta = 0^\circ$.

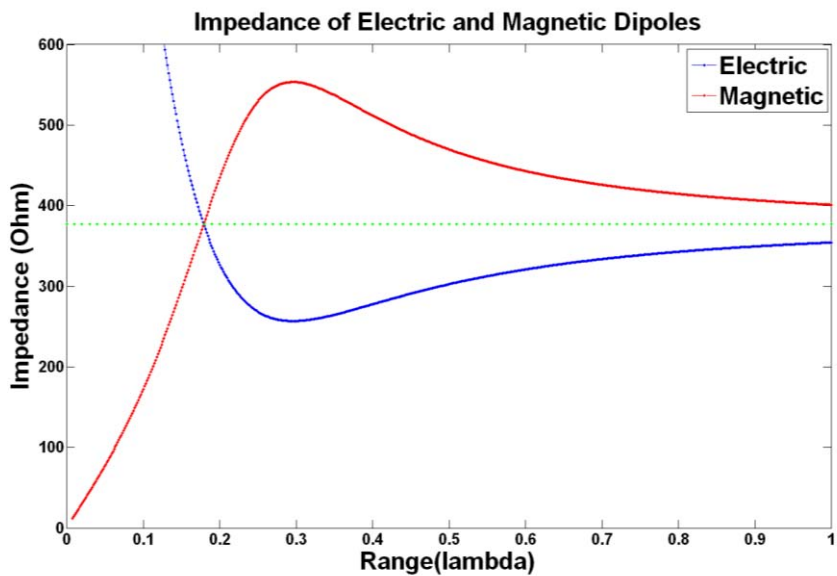


Figure 2a: Impedance is a strong function of range in the near-field of an antenna.

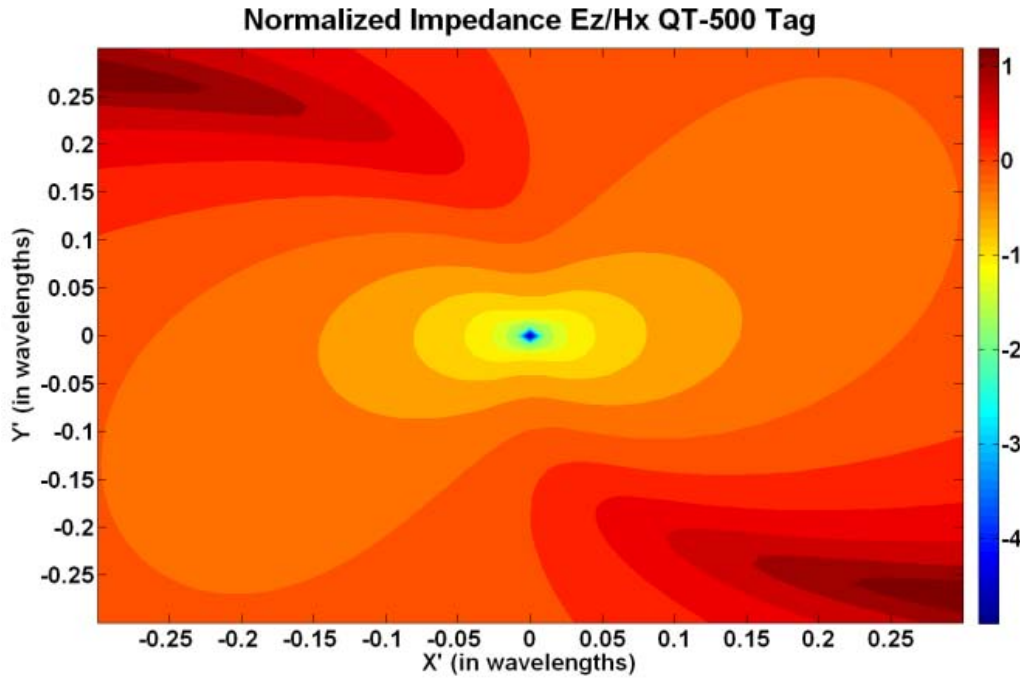


Figure 2b): Surface plot of Impedance (E_z/H_x) for a quadrature-fed magnetic loopstick array along the equatorial plane of the tag, normalized to free space.

The AM broadcast band is the optimal place for this near-field approach to RTLS. The band 0.53-1.71 MHz encompasses wavelengths of 175-566 m, enabling near-field tracking out to 44-142 m, or further at higher power levels. Also, the FCC allows 100 mW unlicensed transmitters in this band under Part 15 rules (15.219).

Within the near-field, the link law for electrically small antennas splits into two separate relations, one for like antennas (electric-electric or magnetic-magnetic) and one for unlike antennas (electric-magnetic or vice versa) [6]. The propagation relation for like antennas is:

$$\frac{P_{RX}}{P_{TX}} = \frac{G_{TX}G_{RX}}{4} \left(\frac{1}{(kr)^6} - \frac{1}{(kr)^4} + \frac{1}{(kr)^2} \right) \quad (2)$$

in which the ratio of received power (P_{RX}) to transmitted power (P_{TX}) follows from the transmit antenna gain (G_{TX}), the receive antenna gain (G_{RX}), the distance (r) between antennas, and the wave number ($k = 2\pi/\lambda$) or wavelength (λ). For like antenna links, the dominant term in the near-field is $1/r^6$, so the link rolls off with a relatively steep slope of

60dB/decade, compared to the $1/r^2$, 20dB/decade behavior of a standard far-field link. For unlike antenna links:

$$\frac{P_{RX}}{P_{TX}} = \frac{G_{TX}G_{RX}}{4} \left(\frac{1}{(kr)^4} + \frac{1}{(kr)^2} \right) \quad (3)$$

The dominant term in the near-field for unlike antenna links is $1/r^4$, so the link rolls off with a slope of 40dB/decade. It should be noted that in the limit of large separations these equations converge to the familiar Friis' free-space equation.

$$\frac{P_{RX}}{P_{TX}} = \frac{G_{TX}G_{RX}\lambda^2}{(4\pi r)^2} = \frac{G_{TX}G_{RX}}{4(kr)^2} \quad (4)$$

These relations apply for tangential field components and become slightly more complicated on inclusion of the radial field coupling [7].

A final consideration is the noise background. Potential sources of noise include dimming switches, power lines (dirty insulators), fluorescent lights (ballasts), computers, monitors, cordless phones, televisions, motors, compressors, HVACs, power supplies, and AM broadcast stations. Figure 3 presents a waterfall plot of noise for the band from 1200-1800 kHz over a five day period taken at the Q-Track lab in Huntsville, Alabama. At night, the ionosphere supports propagation from distant AM broadcast stations. Thus, around sunset, previously unoccupied channels fill with signals and noise from the interference of distant stations at the 10 kHz spacing of US broadcast stations. This background noise disappears at sunrise. To accommodate so-called “clear-channel” stations, most AM broadcast stations must decrease power to nominal levels at sunset and

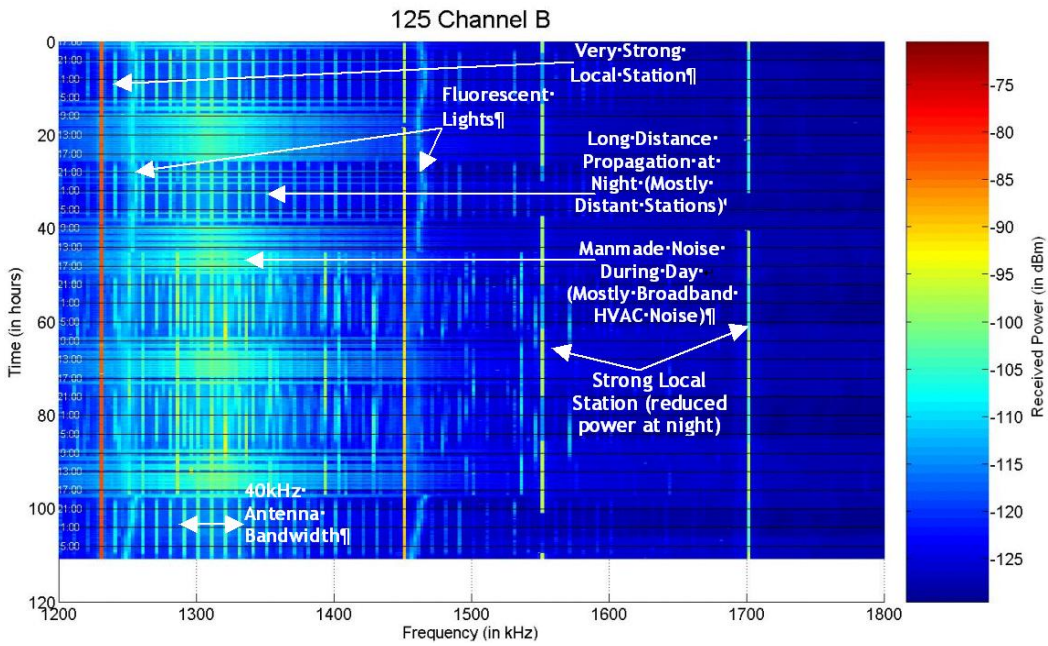


Figure 3: Waterfall plot of indoor RF noise from 1200-1800 kHz over a five day period. Understanding the noise in an operational environment is critical to making a wise choice of operational frequency.

may resume normal broadcasting at sunrise. Broadband noise shows up as horizontal lines in the temporal noise plots. Fluorescent lights show up as wavering harmonics in Figure 3.

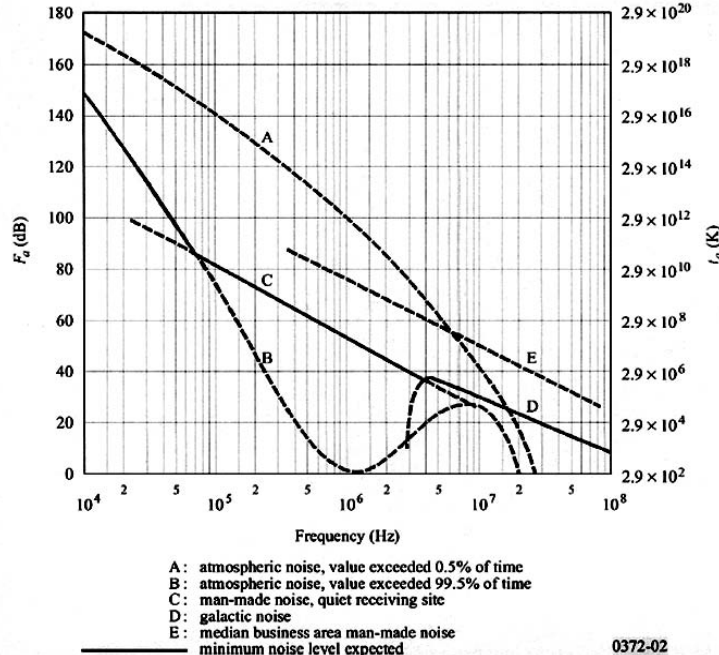


Figure 4: Typical RF natural and man-made noise levels from the VLF to VHF bands [8].

The International Telecommunications Union (ITU) has compiled characteristic noise data for various frequencies [8]. Figure 4 presents these results – typical RF natural and man-made noise levels from the VLF to VHF bands. Unlike microwave links that may be thermal noise limited, medium frequency (MF: 300 kHz–3 MHz) links must operate in the presence of substantial noise. At 500 kHz, for instance, 60 dB of RF noise over thermal is the minimum to be expected, and in a business environment, RF noise as high as 85 dB over thermal might be encountered. Although exact results will depend on the particular environment, RF noise typically decreases with increasing frequency. In any event, a more detailed understanding of how noise varies in different operational environments assists in understanding how near-field magnetic systems might be deployed.

1.2 The QT-500 NFER RTLS

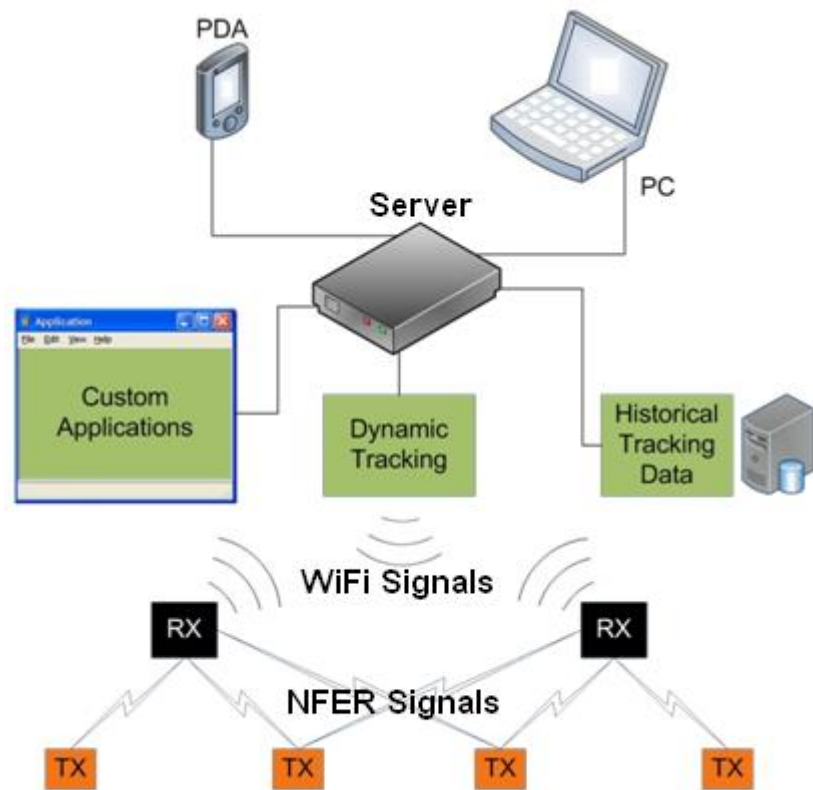


Figure 5: The QT-500 NFER RTLS architecture.

The QT-500 NFER RTLS comprises QT-500 Tag Transmitters (TX), QT-500 Locator-receivers (RX), and a QT-Server with the Q-Track Software Suite. Figure 5 shows the overall system architecture including the software structure. QT-500 Tag Transmitters emit NFER signals. QT-500 Locator-receivers detect these signals on three channels: two orthogonal magnetic channels (denoted channels A and C) and an electric

channel (denoted channel B). The Locator-receivers compare the phases between these channels and report their results to the QT-Server. The default system uses an onboard WiFi data link to the QT-Server, although hard wired Ethernet is available as an optional data link. The Dynamic Tracking module on board the QT-Server determines the tag location based on the data from the QT-500 Locator-receivers. The QT-Server writes the data to a database, makes the data available to custom applications, and can even serve it to remote PDAs or PCs through a web connection. Figure 6a shows the antenna array for a QT-550 Locator-Receiver. An electric is attached to the top of the box. Figure 6b shows the QT-500 Tag Transmitter. The Tag transmits a 100 mW signal in the AM broadcast band (530-1710 kHz) under the provisions of FCC Part 15.219.



Figure 6a (left): The antenna array for a wall-mounted QT-550 Locator-Receiver. **Figure 6b (right):** The QT-500 Tag Transmitter.

2. Electrically Small Antenna Considerations

Low frequency RTLS systems like the QT-500 require compact antennas that are necessarily much smaller than a wavelength. For example, in Q-Track's NFER system operating at 1 MHz, a quarter-wavelength is 75 m. Thus we must employ electrically small antenna techniques in order to both transmit and receive signals effectively. At Q-Track we use electrically small transmit antennas consisting of magnetic loopsticks. Our current design uses two orthogonally oriented antennas to provide isotropic coverage in the azimuthal plane (Figures 7a and 7b).

Top View; Quadrature Loopstick Array

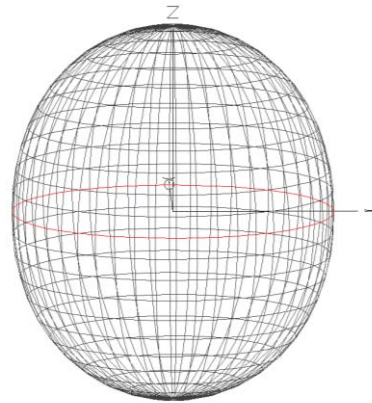
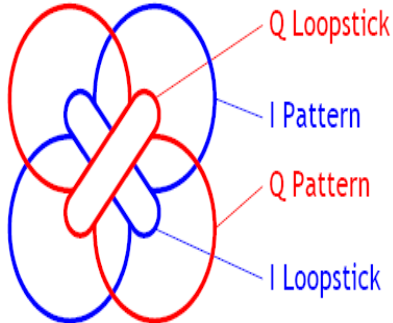


Figure 7a (left): Quadrature-fed orthogonal loopstick system to achieve isotropic pattern. **Figure 7b (right):** NEC simulation of the quadrature-fed, magnetic loops radiation pattern.

An electrically small antenna is defined as being smaller than the radiansphere, the hypothetical sphere centered on the antenna of radius $\lambda / 2\pi$ [9, 10]. It marks the transition between the near-field and far-field regions or where energy is stored and radiated around an antenna. As the size of an antenna is reduced while keeping the operating frequency constant, the bandwidth becomes narrower, and its efficiency degrades as it becomes increasingly difficult to couple energy into the radiated field. In other words the radiation resistance of the antenna diminishes, and for small antennas is often swamped by Ohmic losses.

These resistive losses directly affect the quality factor and efficiency of the antenna. In this paper we consider losses due to the skin effect (AC), proximity effect, hysteresis (in the core), and eddy currents. Typical losses for our Litz-wound transmitter antenna are about 4Ω based on our models and experimental measurements.

If we consider the magnitude of the magnetic field close to a current loop

$$H_\varphi = \frac{\mu_e NIA}{4\pi r^3} \quad (5)$$

where μ_e is the effective permeability including geometrical form factors and the coil covering factor over the ferrite core, N is the number of coil turns, A is the area of the enclosed loop, I is the current, and r is the radial distance from the antenna. From this we derive an expression for an effective magnetic moment:

$$m_e = \left(\frac{l_c}{l_r} \right)^{1/3} \left(\frac{L_c}{L_{air}} \right) N A \left(\frac{P}{R_l} \right)^{1/2} \quad (6)$$

The above expression uses l_c as the length of the wire coil, l_r as the length of the ferrite rod, L_c as the inductance of the coil with ferrite core, L_{air} as the inductance of the coil in air alone, P as the power delivered to the antenna coil, and R_l as the equivalent resistance of the magnetic loop.

By parameterizing the problem in the above form, we can disentangle the competing factors that determine the strength of the field and the efficiency of the antenna. For example, one might assume that by going to a core with a higher permeability, the field strength will increase commensurately. This is not necessarily the case as the length to diameter ratio of the core largely sets the effective permeability for a given material [11].

Furthermore, if we consider the covering factor of the coil over the wire, we might expect the magnetic moment to be maximized when the entire coil covers the core. However, the flux density of the electric field is not uniform over the individual turns of the solenoid. In particular, near the ends of the solenoid we can have fringing where the electric field penetrates into the wire turns, thus increasing resistive losses.

As a final example, consider the number of turns a loopstick antenna might have. If we increase the number of turns, this suggests the spacing between the wires must decrease for a fixed covering factor. But this dramatically increases the power dissipated through resistive losses via the proximity effect. These effects entangle in complex ways. In order to determine the optimal configuration, we turn to numerical simulation utilizing Finite Element Method Magnetics (FEMM) [12].

FEMM can solve low frequency electromagnetic problems involving axis symmetric domains. Our simulations provide a numerical solution using a fine spatial mesh ($< 0.05"$) where the proximity and skin effects in the wire, DC losses, magnetic ferrite losses, and eddy current losses are represented. The material properties of the ferromagnetic cores were obtained from Fair-Rite Corporation courtesy of Jan van der Poel. The following parameters were used in modeling the ferromagnetic material, coercivity, permeability, loss factor, and BH curves. The coercivity is equal to 144 A/m, the initial permeability is equal to 125, and the loss tangent is equal to 0.2149° for mix 61.

Although the FEMM code has been validated by a number of authors, we made experimental comparisons with a prototype loopstick antenna to demonstrate agreement. For a one-inch coil of 45 turns on a mix 61 ferrite, we found measured values of $L_{exp} = 101 \mu\text{H}$ and $Q_{exp} = 165$, in reasonable agreement with FEMM simulated values of $L_{sim} = 120. \mu\text{H}$ and $Q_{sim} = 139$. Here L refers to inductance and Q to the antennas quality factor.

Thus we proceeded to evaluate a number of trade-offs, such as type of ferrite, form factor, coil covering factor, number of turns, wire gauge, wire spacing, and gap between coil and ferrite. For the simulations reported on here, we considered the following matrix parameters as shown in Table 1.

Parameter	FEMM Values
Mix	33, 43, 52, 61, 67
Type	Solid, hollow
Form Factor	1, 4, 8, 16
Covering factor	0.3, 0.6, 0.9
Wire Gauge	16-30
Spacing	0, 1, 3
Gap	0, 2

Table 1: Parameters used in FEMM Modeling.

The magnetic data for the ferrite mixes were taken from the Fair-Rite Catalog [13]. Form factor is the rod length to diameter ratio with a set 2-inch length, except for the form factor 1, where we considered a 1-inch by 1-inch ferrite. The dimensions of the hollow-core simulations were taken as 0.5 inch outer diameter by 0.4 inch inner diameter. The covering factor is the fraction of the rod covered by the coil. Wire spacings of zero, one, and three wire diameters were used between each winding. Finally, we simulated a gap of zero (i.e., flush to rod) and two wire diameters between the coil and the core. We automated the above simulations using the LUA scripting language. The simulations suggest the smallest wire diameter yields the highest antenna efficiency in terms of magnetic moment. Adding a small gap between the rod and coil changed the magnetic moment by less than 1%. At our field strengths and frequency of interest, we found that type 61 material composed of NiZn mix provided the best performance. One conclusion was that the bulk of the losses appear in the coil itself. This led us to consider employing Litz wire as it offers the advantage of reducing the skin and proximity effect losses by smoothing the current distribution along a strand bundle. Representative simulations are shown in Figures 8a and 8b.

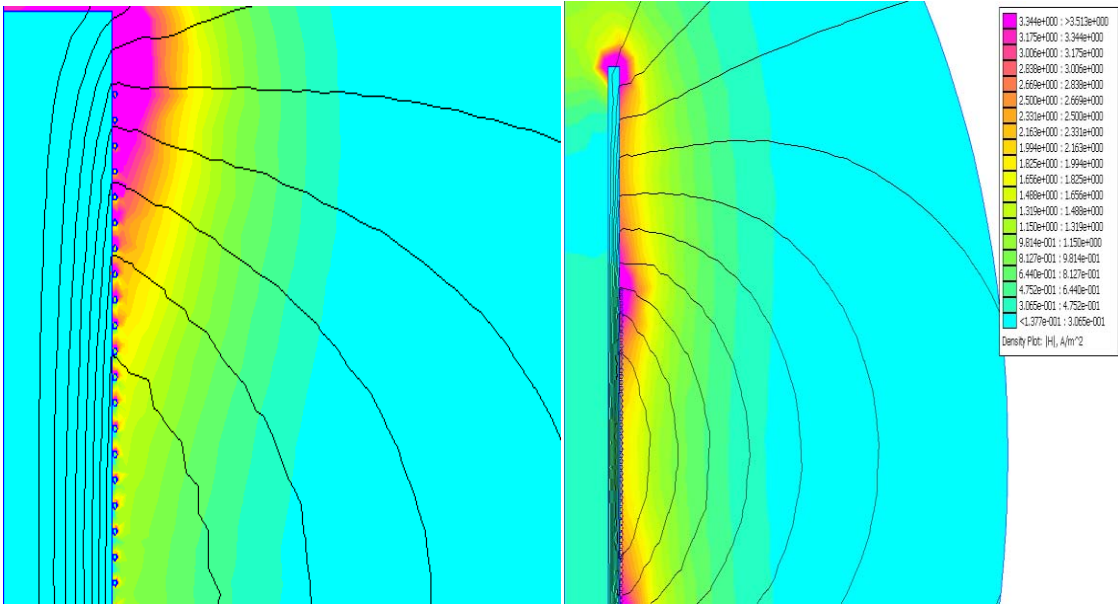


Figure 8a (left): FEMM simulation of prototype antenna using solid wire, type 61 ferrite, and 45 windings of AWG 24 wire with a spacing of 3 wire diameters. **Figure 8b (right):** Simulation of H-fields for our hollow-core, mix 61, Litz wrapped design.

3. Antenna Testing/Near-Field Link and Gain Extraction

NFER antennas operate within the AM broadcast band under Federal Communications Commission (FCC) Part 15.219 over the range 510-1705 kHz. The wavelengths involved are several hundreds of meters, making standard far-field antenna gain measurements impractical. We have therefore constructed a near-field antenna testing range using a two-port HP vector network analyzer (VNA), the HP 8753D. We use the complex reflection coefficients from the VNA together with relations for the near-field link equation to solve for the absolute gain of the antenna under test (AUT). We have validated our approach with an independently calibrated reference antenna (Empire LP-105).

The impedance of a transmission line (Z_0) is the ratio of the electric to magnetic fields of an electromagnetic signal propagating along the line. The impedance of an antenna is the ratio (Z_A) of the electric to magnetic fields at the antenna's terminals. If the transmission-line impedance ($Z_0 = R_0$; assumed real and typically 50Ω) and the antenna impedance are not identical, then there will be a mismatch at the antenna terminals, and some of the incident signal will be reflected back to the source. This reflection is characterized by a reflection coefficient (Γ_{11}), which is the ratio of the reflected voltage (V_0^-) to the transmitted voltage (V_0^+):

$$\Gamma_{II} = \frac{V_o^-}{V_o^+} = \frac{Z_A - Z_0}{Z_A + Z_0} = \frac{(R_A - R_0) + jX_A}{(R_A + R_0) + jX_A} = \Gamma_{IIR} + j\Gamma_{III} \quad (7)$$

This reflection coefficient is typically a complex valued quantity since the transmitted and reflected voltages are not necessarily in phase. The equation above provides an illustration of the quantities involved in the reflection coefficient. The S_{11} VNA measurement is typically expressed in terms of complex reflection coefficients: $\Gamma_{11} = \Gamma_{IIR} + j\Gamma_{III}$. Solving the S_{11} reflection coefficient (1) for the antenna impedance yields:

$$Z_A = R_A + jX_A = \frac{1 - \Gamma_{IIR}^2 - \Gamma_{III}^2 + j2\Gamma_{III}R_0}{(1 - \Gamma_{IIR})^2 - \Gamma_{III}^2} R_0 \quad (8)$$

under the assumption that the reference impedance is strictly real, or $Z_0 = R_0$. Then:

$$R_A = RE \left[\frac{1 - \Gamma_{IIR}^2 - \Gamma_{III}^2 + j2\Gamma_{III}}{(1 - \Gamma_{IIR})^2 - \Gamma_{III}^2} R_0 \right] = \frac{1 - \Gamma_{IIR}^2 - \Gamma_{III}^2}{(1 - \Gamma_{IIR})^2 - \Gamma_{III}^2} R_0 \quad (9)$$

$$X_A = IM \left[\frac{1 - \Gamma_{IIR}^2 - \Gamma_{III}^2 + j2\Gamma_{III}}{(1 - \Gamma_{IIR})^2 - \Gamma_{III}^2} R_0 \right] = \frac{2\Gamma_{III}}{(1 - \Gamma_{IIR})^2 - \Gamma_{III}^2} R_0 \quad (10)$$

The Voltage Standing Wave Ratio (VSWR) with respect to 50Ω is:

$$VSWR = \frac{1 + |\Gamma_{II}|^2}{1 - |\Gamma_{II}|^2} = \frac{1 + \sqrt{\Gamma_{IIR}^2 + \Gamma_{III}^2}}{1 - \sqrt{\Gamma_{IIR}^2 + \Gamma_{III}^2}} \quad (11)$$

The return loss with respect to 50Ω is:

$$RL = |\Gamma_{11}|^2 = \Gamma_{11r}^2 + \Gamma_{11i}^2 \quad (12)$$

i.e., $RL = 0$ for perfect match, $RL = 1$ for open or short. The return loss (in dB) with respect to 50Ω is:

$$RL = LogMag|S_{11}| = 20\log|S_{11}| = 20\log\left|\sqrt{\Gamma_{11r}^2 + \Gamma_{11i}^2}\right| \quad (13)$$

The mismatch power loss with respect to 50Ω is:

$$PL = 1 - |\Gamma_{11}|^2 = 1 - (\Gamma_{11r}^2 + \Gamma_{11i}^2) \quad (14)$$

i.e., $PL = 1$ for perfect match, $PL = 0$ for open or short. We assume the AUT is connected to port 1. The gain of the AUT (G_{AUT}), as referenced to the VNA's 50Ω impedance is:

$$G_{AUT} = \frac{4(kr^6)|S_{12}|^2}{G_{REF}} = \frac{4(kr^6)}{G_{REF}}(\Gamma_{12r}^2 + \Gamma_{12i}^2) \quad (15)$$

where G_{REF} is the gain of the reference antenna (in our case, the Empire loop), k is the wave number ($k = 2\pi/\lambda$), and r is the range (in our case, typically $3\text{ft} = 0.9142 \text{ m}$).

If we remove the power loss due to the mismatch with respect to 50Ω , the ideal gain of the antenna is:

$$G_{AUT}^* = \frac{4(kr)^6|S_{12}|^2}{G_{REF}PL} = \frac{4(kr)^6}{G_{REF}} \frac{(\Gamma_{12r}^2 + \Gamma_{12i}^2)}{1 - (\Gamma_{11r}^2 + \Gamma_{11i}^2)} \quad (16)$$

Figure 9 shows Q-Track's near-field antenna testing range.

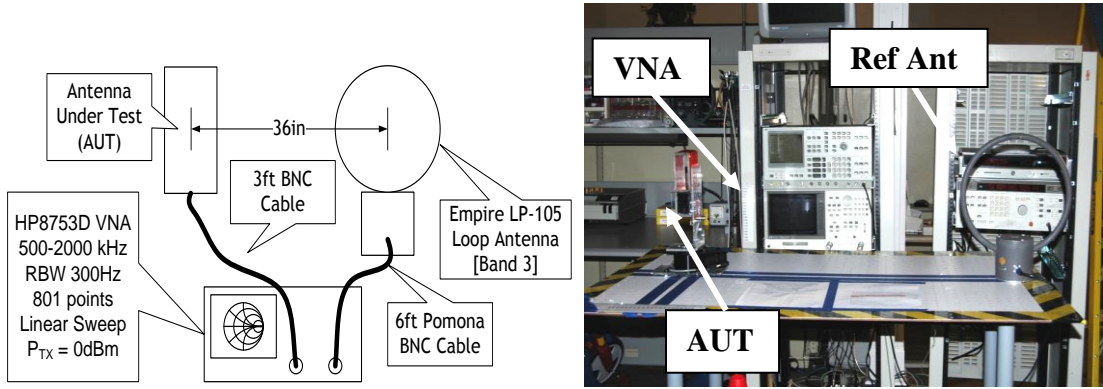


Figure 9a (left): Schematic showing our set-up for near-field testing. **Figure 9b (right):** Antenna Testing Range

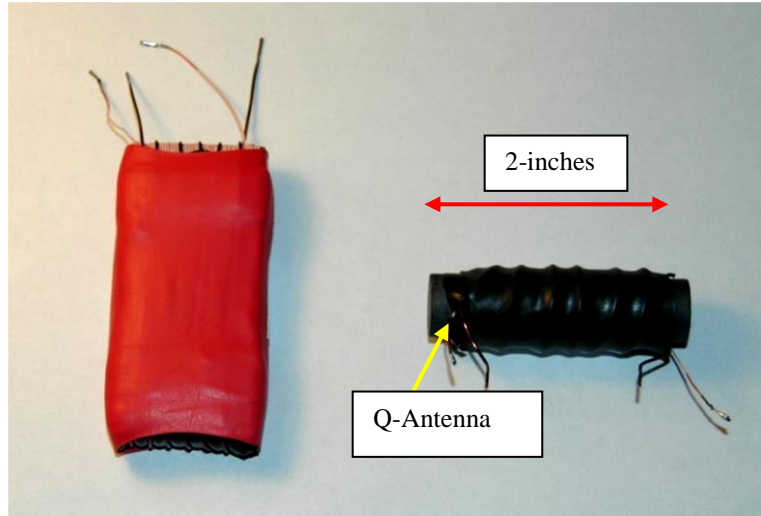


Figure 10: Magnetic Loopsticks for channels I and Q in QT-500 transmitter. The Q-antenna on the right is a hollow ferrite rod wound with 45 strands of Litz wire. Coupling is achieved through 6 turns of magnetic #24 wire.

The Q-channel of our QT-500 transmitter tag, shown in Figure 10, is a custom designed ferrite loopstick, composed of 55 turns of Type 1 Litz 40/44 wire on a hollow 2-inch-long rod. Measured values of inductance and Q are $150 \mu\text{H}$ and 300, respectively. We characterized the QT-500 Q-channel antenna according to the antenna testing procedure described above. One variable under examination was the number of coupling turns used to actively link RF power into the transmit antenna. Figures 11a and b show the summary data from our antenna analysis. In general, increased coupling turns results in a

higher gain. For our QT-500 NFER system, we have used 6 coupling turns, which at 1000 kHz results in an antenna impedance of 1300Ω and a gain of -74 dBi. These results were collected *in situ* within the tag enclosure and in the close proximity to the tag motherboard and associated battery pack.

It is instructive to understand how our experimental results compare to theory. Using the definition of antenna gain we find $G = kD$, where for a magnetic dipole the directivity, $D = 1.5$. The antenna efficiency (k) can be calculated by considering the ratio of radiation resistance (R_r) to total losses (R_l) in the antenna:

$$k = \frac{R_r}{R_r + R_l} \quad (17)$$

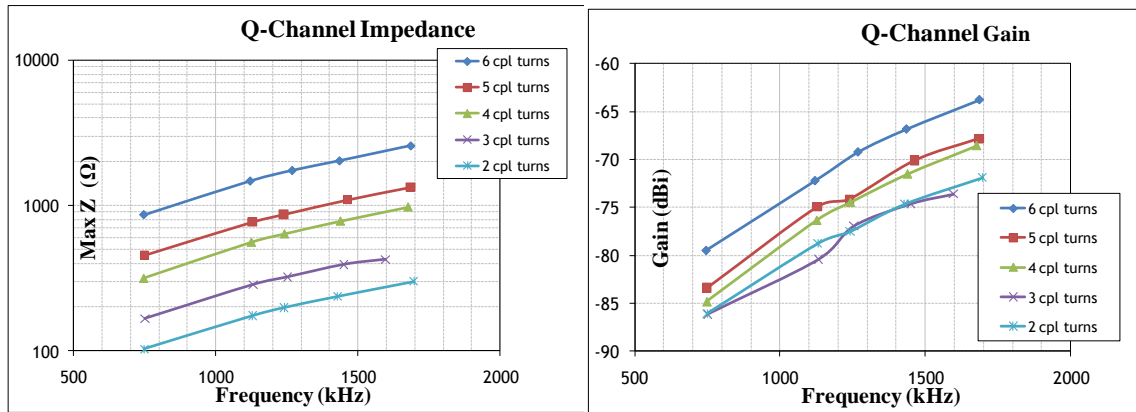


Figure 11a (left): Antenna impedance as a function of coupling turns and frequency across the AM band.

Figure 11b (right): Antenna gain as a function of coupling turns and frequency across the AM band.

Using both FEMM and unloaded Q measurements, we find R_l is 4.3Ω . Kraus gives the radiation resistance of a ferrite loaded coil as [14]:

$$R_r = 31,200 \mu_e^2 n^2 \left(\frac{A}{\lambda^2} \right)^2 \quad (18)$$

Here μ_e is the effective permeability of the ferrite, 17 for our choice of Type 61 and form factor, n is the number of turns, 55, A is the cross sectional area, $1.27E-4 \text{ m}^2$, and λ is

the wavelength. Once the radiation resistance is known, calculation of the gain is straightforward; results are provided in Figure 12. For comparative purposes, we also calculate the gain of a short electric dipole of length 2 inches. As can be seen, the theoretical gain for our loopstick under test is about -77 dBi, in good agreement with our measured value of -74 dBi.

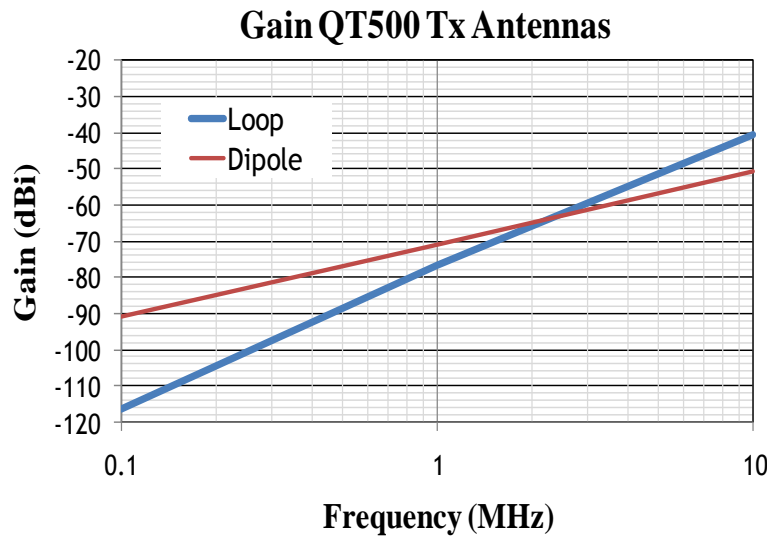


Figure 12: Theoretical gain for both a magnetic loopstick and small electric dipole (2-inch).

4. PCB Antenna Modeling and Prototyping

In order to reduce the form factor of our tag, we have been exploring Printed Circuit Board (PCB) implementations of our magnetic transmitter. The goal is to reproduce a magnetic loop antenna with gain comparable to our current generation QT-500 antennas in a PCB. The concept is depicted in Figure 13.

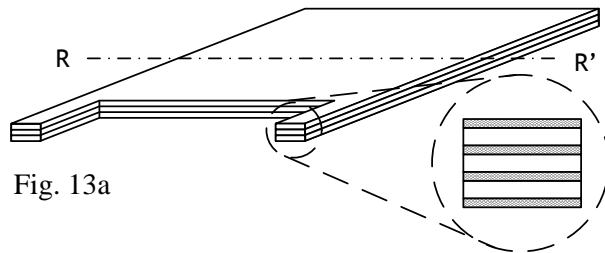


Fig. 13a

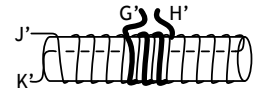


Fig 13b

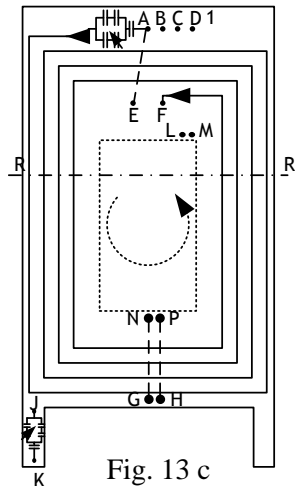


Fig. 13 c

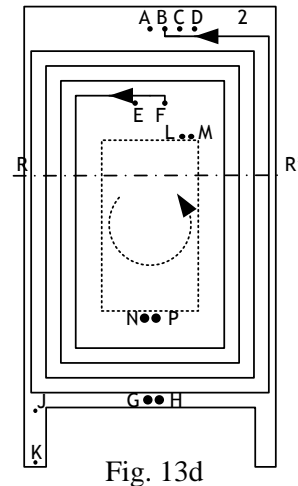


Fig. 13d

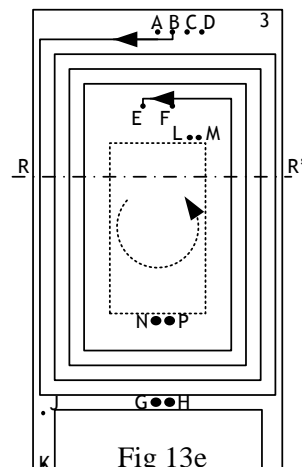


Fig 13e

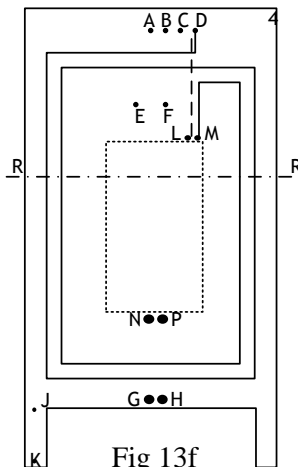


Fig 13f

Fig. 13a: Multiple winding layers may be implemented through PCB traces. **Fig. 13b:** A standard loopstick is inserted into the PCB slot to produce an orthogonal magnetic antenna. **Fig. 13c:** The top layer of the PCB containing a tuning circuit. Current is carried counter-clockwise through multiple turns outside to inside until ending at point F. **Fig. 13d-e:** Traces conduct current in the same counter-clockwise fashion originating at point F, moving inward to outward. Point B conducts current to additional layers before and vice-versa until ending at Point E. Point E is then shorted to Point A which closes the circuit loop. **Fig. 13f:** The bottom layer of the board contains the inductive coupling turns. Point D is ground while Point M is the source.

We considered a number of tradeoffs, including the width and thickness of individual traces, spacing between traces, proximity of ground plane, total number of traces, and number of traces per layer. Using FEMM we examined how these various parameters would affect the inductance, losses, Q, and gain of our PCB antenna. Figure 14 shows sample results.

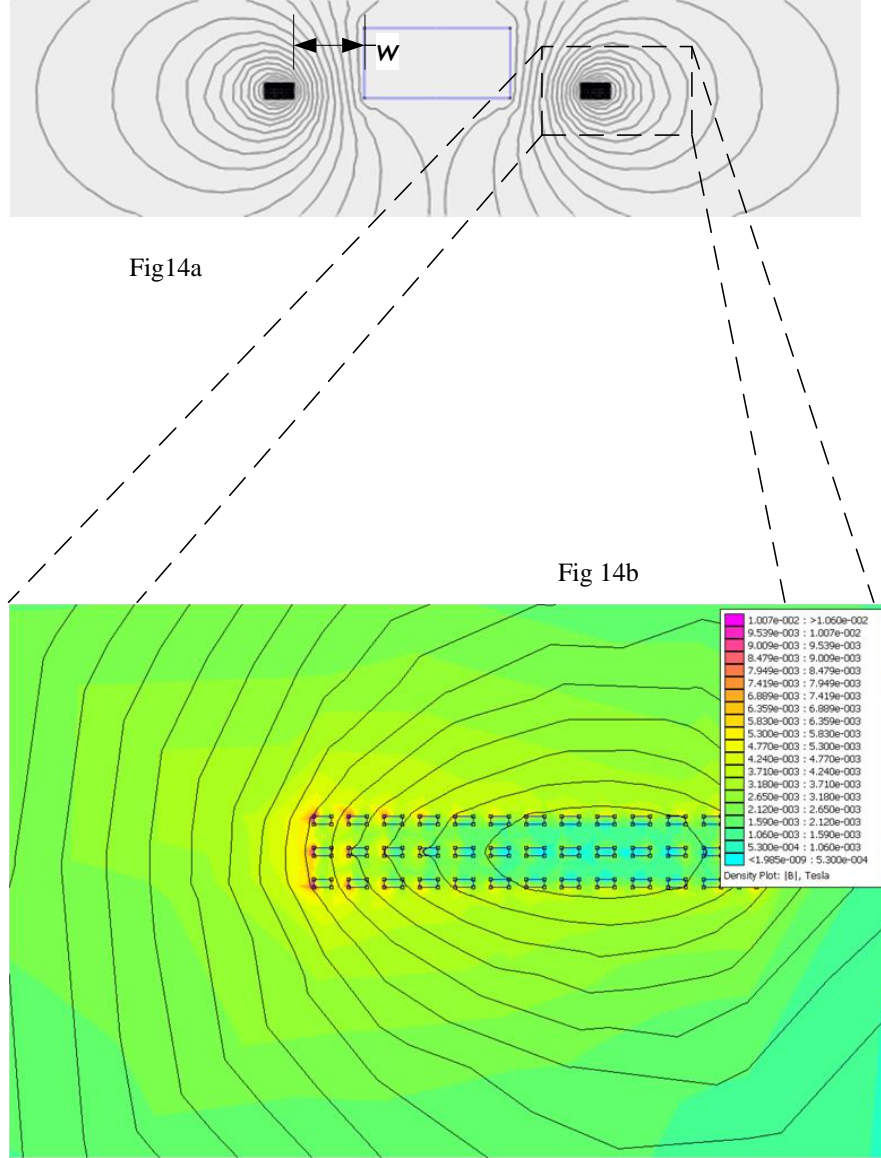


Figure 14a (top): FEMM simulation of PCB antenna with flux lines shown. The exclusion zone in the center represents the battery and circuitry. **Fig. 14b (bottom):** Close-up view of the individual traces. The areas nearest the exclusion zone to the left correspond to traces with dominant losses as the flux lines are compressed together.

After careful consideration of the various parameters, we have settled on a design using 3 layers composed of 13 traces each with 1.4 mil thick (1 oz.) copper for a total of 39 turns to our primary I-channel antenna. The width of these traces is 6 mil with a trace-to-trace spacing of 6 mil. The overall thickness of the PCB board is 60 mil. We use 9 traces to inductively couple into the antenna as this provides a good compromise between the strength of primary to secondary coupling and impedance. Using FEMM we simulate several parameters such as inductance, AC losses, and Q. FEMM predicts an inductance, $L = 197 \mu\text{H}$, DCR = 46.3Ω , ACR = 49.4Ω , and Q = 25. These values compare favorably with measured lab values. The measured gain results on the PCB tag antenna are shown in Figure 15b.

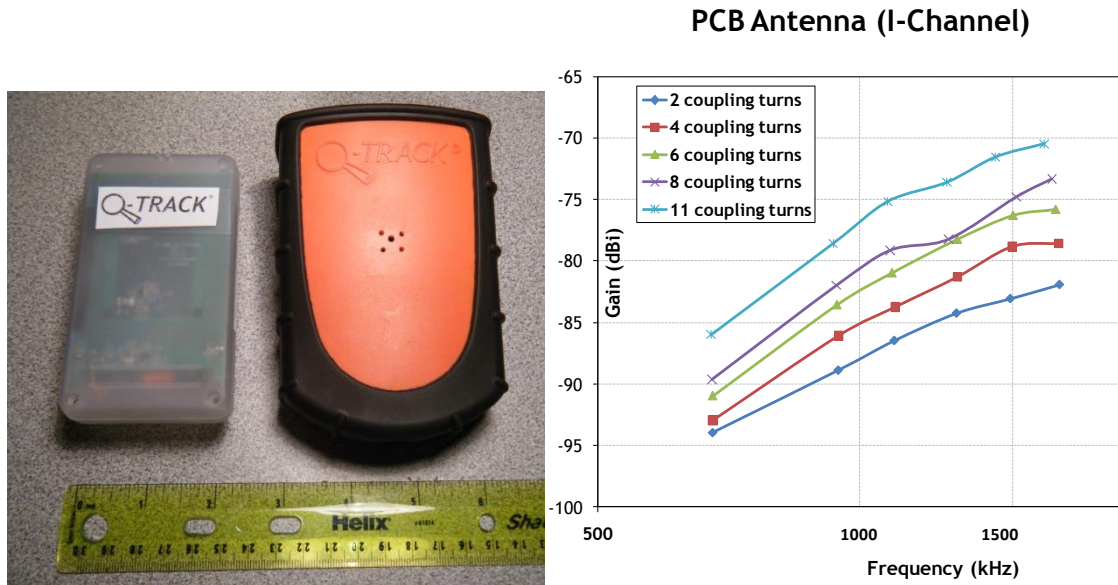


Figure 15a (left): Comparison of QT-500 tag and PCB-based tag under investigation. **Fig. 15b (right):** Measured gain of PCB antenna matching the performance of our larger loopstick array used in the QT-500.

Our analysis suggests a number of best practices to optimize PCB magnetic antenna performance including:

- 1) Increasing the thickness of the traces improves performance. Because the skin depth is on the order of 1 mil, we would expect a decrease in loss with a heavier weight trace. Although FEMM simulations indicate this is indeed the case, we have not been able to demonstrate improved antenna performance with thicker traces.
- 2) Increasing the spacing beyond about one trace width does not improve overall performance. Although it decreases the AC losses via the proximity effect, it does so at the cost of diminishing the enclosed area and thus reducing the inductance and magnetic moment.

3) Increasing the number of interior rows improves antenna performance. Because there is significant flux penetration near the perimeter of the antenna, a non-uniform spacing scheme should decrease resistive losses.

5. Location Error Analysis

In order to characterize the robustness of the QT-500 NFER based RTLS, we conducted an objective study within Q-Track's RF laboratory over an extent of 16 m x 36 m. We recorded the errors of individual location solutions from each of the five Locator- Receivers at each of the 82 measurement points. This resulted in a total of 410 individual measurements of location error.

Table 2 presents the average error for range and transverse components for each of the five receivers. When averaged by receiver, range error varied from 23.4 cm to 43.0 cm. When averaged by receiver, transverse error varied from 21.6 cm to 44.2 cm. The average error for all receivers was 34.0 cm in the radial direction and 35.5 cm in the transverse direction for a total average error of 55.1 cm.

RX	Range (cm)	Transverse (cm)	Total (cm)
B7	25.2	21.6	36.3
22	23.4	33.5	44.5
61	37.3	34.8	55.0
BE	41.1	43.0	68.8
52	<u>43.0</u>	<u>44.2</u>	<u>69.8</u>
Average	34.0	35.5	55.1

Table 2: Average location error broken down into range (i.e., radial) component, transverse component, and total location error for each of five NFER Locator- Receivers.

These systematic errors include precision in calibration, repeatability of our return to the calibration point to assess error, anisotropies in the transmit tags' phase response, and the like. Because power levels roll off so sharply in the near-field, typically as r^{-6} or r^{-4} , we expect excellent phase accuracy and low error. We presume that if we were to have extended our data collection past 25 m, we soon would have reached a point where low SNR seriously would have impacted phase accuracy, error would have increased significantly, and the system rapidly would have become unusable.

Figure 16 shows the error distribution for all receivers. Several features are immediately evident. First, the range and the transverse errors are closely related. In other words, the system is well balanced between the range or radial component of the error and the transverse or angular component of the error. Second, we have an almost

exponential fall-off of error with a relatively modest tail of outliers. About 50% of all location measurements are within 38 cm, 67% are within 56 cm, and 83% are within 1 m. Only 3% of all location measurements are more than 2 m in error. Full results and data for our error analysis are available. [15]

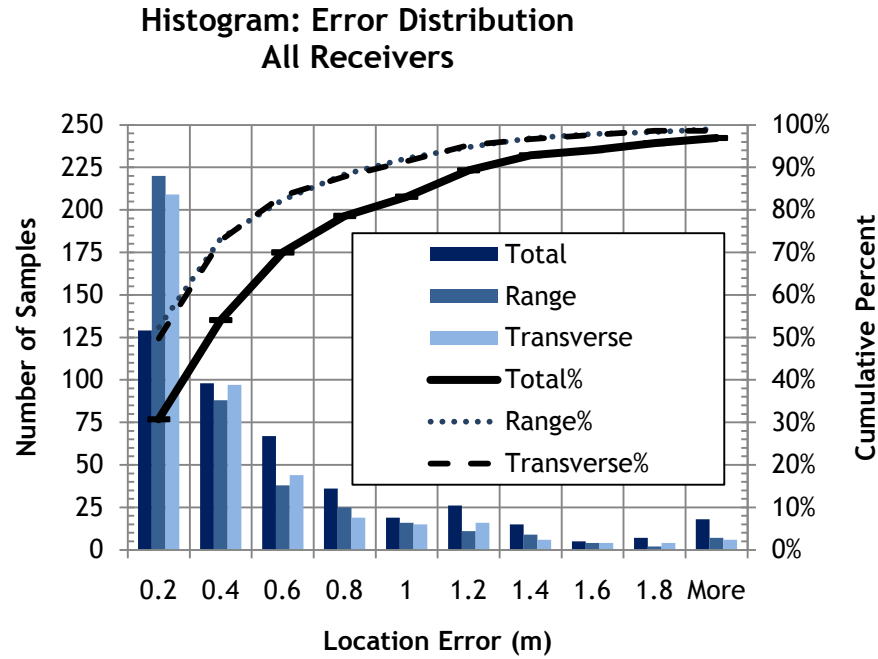


Figure 16: Histogram of error distribution for all receivers.

6. Conclusions

We have instantiated a number of best practices in small magnetic antenna design, including optimizing ferrite performance, wire type and gauge, winding technique, and inductive coupling. The need for a magnetic antenna with minimal environmental capacitive coupling and an omnidirectional radiation pattern motivated our choice of quadrature-driven loopsticks. A few direct results of our parametric study are:

1. Ferrite material 61 is superior near 1 MHz to the types tested here: 33, 43, 52, and 67.
2. Resistive losses in the coil of the loopstick antenna dominate those in the ferrite core. For our prototype Q-channel antenna, the model suggests 5% of the losses are associated with the core and 95% with the solenoid.
3. Litz wire provides a ready means for reducing these Ohmic losses, and consequently increasing antenna gain.

4. Multiple-layer PCB methods can be used to implement small loops of reasonable gain matching the performance of larger ferrite loaded loopsticks.

Furthermore, we have developed a compact (1 m) near-field antenna testing range that allows us to characterize magnetic antennas despite having operating wavelengths on the order of 300 m. Our results have been validated with independently calibrated antennas. Our procedure provides a powerful platform from which to develop electrically small antennas in support of our NFER-RTLS system.

NFER-RTLS promises to deliver accurate location information through walls in difficult, non-line-of-sight office and industrial environments. The results of the present study validate that an individual NFER Locator-Receiver yields an accurate location to within 1 m 83% of the time. We found an average range error of 34.0 cm, an average transverse error of 35.5 cm, and a corresponding total location error of 55.1 cm. Overall system accuracy should improve roughly as $1/\sqrt{N}$ for an NFER RTLS with N receivers simultaneously tracking a tag.

[1] H. Schantz and R. DePierre, "System and Method for Near Field Electromagnetic Ranging", U.S. Patent 6,963,301, November 2005.

[2] H. Schantz, "A real-time location system using near-field electromagnetic ranging", 2007 IEEE Antennas and Propagation International Symposium, pp. 3792-3795, June 2007. See: <http://www.q-track.com/phocadownload/IEEE-APS-2007-.pdf>.

[3] A variety of technical papers may be accessed at: <http://www.q-track.com/index.php/location-innovation/technical-papers>.

[4] H. Hertz, Electric Waves, pp. 152, London: Macmillan and Company, 1893.

[5] Schantz, "Near Field Phase Relationships", IEEE APS Conference, July 2005. Reprint available at <http://www.q-track.com>. The discussion of this section is excerpted in part from this paper.

[6] H. Schantz, "A Near-Field Propagation Law & A Novel Fundamental Limit to Antenna Gain Versus Size", 2005 IEEE Antenna and Propagation Society International Symposium, vol. 3A, pp. 237-240, July 2005.

[7] A. Compston, et al., "A Fundamental Limit on Antenna Gain for Electrically Small Antennas", 2008 IEEE Sarnoff Symposium, Princeton, NJ, April 2008.

[8] International Telecommunication Union, Recommendation ITU-R P.372-8: Radio noise, 2003, as cited in NATO RTO Technical Report, "HF Interference, Procedures, and Tools", pp. 2-11 to 2-12, RTO-TR-IST-050, June 2007. See: [http://ftp.rta.nato.int/public/PubFullText/RTO/TR/RTO-TR-IST-050/\\$\\$TR-IST-050-ALL.pdf](http://ftp.rta.nato.int/public/PubFullText/RTO/TR/RTO-TR-IST-050/$$TR-IST-050-ALL.pdf).

[9] H. A. Wheeler, "Fundamental Limitations on Small Antennas", Proceedings of the IRE, vol. 35, pp. 1479-1484, December 1947.

[10] H. A. Wheeler, "The Radiansphere Around a Small Antenna", Proceedings of the IRE, vol. 47, pp. 1325-1331, August 1959.

[11] M.F. DeMaw, Ferromagnetic Core Design & Application Handbook, 1st ed., pp. 41, MFJ Publishing, Starkville, MS, 1996.

[12] D. C. Meeker, Finite Element Method Magnetics, Version 4.2, <http://femm.foster-miller.net>, 2009.

[13] Fair-Rite Products Corporation Soft Ferrites, 15th Ed., 2009.

[14] J. D. Kraus, R. J. Marhefka and A. S. Khan, Antennas for All Applications, 3rd Ed., pp. 220, Tata McGraw-Hill, India, 2008.

[15] Schantz, Hans Gregory; Weil, Christian; Unden, Alfred Hans Radio and Wireless Symposium (submitted), 2011 IEEE 16-20 Jan., 2011 (preprint can be accessed at: <http://www.q-track.com/index.php/location-innovation/technical-papers>).

SUPER-RESOLVING BIOMIMETIC ELECTRICALLY SMALL ANTENNAS AND THEIR APPLICATIONS

Nader Behdad and Mudar A. Al-Joumayly
Department of Electrical and Computer Engineering
University of Wisconsin-Madison,
1415 Engineering Drive, Madison, WI 53706, U. S. A.
email: behdad@wisc.edu

ABSTRACT: Many small animals possess acute directional hearing capabilities and are able to localize a sound source of interest with an astonishing degree of precision. An analogy can be drawn between the hearing mechanisms of these small animals and electrically small antenna arrays, composed of isotropic receiving elements, that are capable of resolving the direction of arrival of an electromagnetic wave with a fine angular resolution. Inspired by this analogy between these acoustical biological devices and electrically small antenna arrays, we introduce the concept of biomimetic, super-resolving electrically small antennas in this paper. The paper also describes potential applications of these devices and the new capabilities that they offer. A method for designing such electrically small antenna arrays as well as simulated and measured results of a fabricated prototype are also presented and discussed in this paper. These biomimetic antenna arrays could be used in numerous applications ranging from miniaturized RF sensors and direction finding systems to small aperture, high-resolution microwave imaging systems and radars.

1. INTRODUCTION

Electrically small antennas have been the subject of many studies over the past few decades. In particular, a number of theoretical studies have examined the relationship between the electrical dimensions (physical dimensions normalized to the wavelength) of an antenna and its radiation characteristics including gain, radiation efficiency, bandwidth, and directional characteristics [1-9]. All of these studies point to a set of either *fundamental* or *practical limitations* that govern the performance of such antennas. In particular, as the electrical dimensions of an antenna are decreased, its radiation efficiency and bandwidth also decrease [1-3]. These studies propose a set of *fundamental limits* that predict the upper bounds of these radiation parameters as demonstrated by the famous Chu limit [1] and its subsequent variations. Similar theoretical studies have been carried out to investigate the relationship between the directionality of an antenna array or continuous aperture [3-9] and its electrical size. The results show that, in theory, achieving superdirective is possible from an antenna array or a continuous aperture. In principle, such super-directive arrays could be used to precisely resolve the direction of arrival of an EM wave. In this regard, a super-directive antenna array composed of

isotropic receiving elements can be used to resolve the direction of arrival of an electromagnetic (EM) wave. However, when the overall electrical dimensions of the antenna array decrease, the nearby elements of the array must be excited with significantly oscillatory and widely varying excitation coefficients to achieve super-directional characteristics [8, 9]. While mathematically possible, the realization of such excitation coefficients is not practical for small antenna arrays due to problems such as mutual coupling between the elements and tolerances in device design and fabrication. This presents a set of *practical limitations* in the path of using highly-directional, electrically small antennas to obtain super-resolving capabilities. While we have not yet been able to overcome these problems, nature provides us with examples of biological organisms that have addressed similar problems.

The biological organisms' ability to evolve in response to environmental changes and the hyperacute sensing capabilities that some organisms have evolved point to an interesting question: *How would a biological entity evolve the capability to receive and transmit electromagnetic waves if an evolutionary environment was present in which it would have needed this capability to survive?* The answer to this question could reveal new methodologies and concepts for designing small antenna systems that work within the bounds set by the laws of physics but deliver performance levels that have not been achieved to date. A good starting point for answering this question is to investigate biological organisms that already possess similar capabilities. Among a plethora of organisms that could be studied, insects are the most magnificent and inspiring subjects, since many insect species have hyperacute and extremely efficient sensing capabilities in ultra-small packages. In particular, the sense of directional hearing in certain insect species [10-14] and small vertebrates [15-17] is most germane to the problem of super-resolving electrically small antenna arrays. Many animals use sound waves for communication and sensing. The auditory system of such creatures have evolved and adapted to be able to detect the sound waves of interest and identify and localize their sources. To achieve this, most animals use two ears, which act as pressure sensitive receivers excited by the pressure of an incoming sound wave. Based on its direction of incidence, the sound wave arrives at one ear earlier than the other. Additionally, the amplitude of the vibrations at the two ears are generally different due to the scattering caused by the animal's body. These differences in the time of arrival and the amplitude of the two received signals are the main cues used by the auditory system of most animals to determine the location of the emitting source. In large animals and humans, the separation between the two ears is physically large and significant scattering of sound is created by the large head separating the two ears. This results in large interaural time differences (ITDs) and interaural intensity differences (IIDs) between the two received signals that can be easily detected by the animal's central nervous system. As the size of the animals decrease, however, these differences become smaller and smaller. Therefore, one would think that smaller animals and especially insects are inherently at a disadvantage when it comes to directional hearing. However, surprisingly, many small animals demonstrate hyperacute directional hearing capabilities. In the insect world, various species of cicadas [10], crickets [11], parasitoid flies [12-13], and grasshoppers

have acute directional hearing capabilities. Similar characteristics are also found among small vertebrates in various species of frogs [15-16], reptiles [17], and birds [18]. In all of these examples, the auditory organ of the animal is composed of two ears separated by a very small distance from each other (compared to the wavelength of sound). Due to this small separation and the small size of the animals' heads (or insects' bodies), there is little or no intensity difference between the level of sound that arrives at the two ears. Therefore, the only cues available are the small differences in the time of arrival of the sound between the two ears. The auditory systems of these organisms amplify these minute differences in the time of arrival of sound and increase them to detectable levels. In this paper, we will demonstrate how the sense of directional hearing in insects can be used to develop super-resolving electrically small antennas and present preliminary results of these biomimetic antennas and discuss the potential applications of the proposed biomimetic antenna arrays.



Fig. 1. Photograph of the parasitoid fly *Ormia Ochracea*. The fly has two ears that are separated from one another by 500 μm . The entire body length of the fly is almost 1 cm long. Photo courtesy of Prof. William H. Cade from University of Lethbridge, Lethbridge AB, Canada. Used with permission.

2. BACKGROUND AND THE PROPOSED CONCEPT

An example of an insect which possesses an astonishing directional hearing capability is the parasitoid fly *Ormia Ochracea* shown in Fig. 1. Female *Ormia Ochracea* flies rely on live field crickets to reproduce [12]. They locate their hosts at night relying only on auditory cues from the male crickets' mating calls, which have peaks at 4.8 kHz with a free space sound wavelength, λ_{s0} , of 7 cm. The separation between the two ears of the fly is approximately 500 μm or equivalently $\lambda_{s0}/140$. Additionally, the fly's body size of 1 cm is significantly smaller than the wavelength and does not cause considerable scattering of the sound wave. Yet the fly is capable of discriminating the direction of arrival of the cricket's mating call with a precision of 1°-2° [14]. The details of the auditory organ of this insect have been analyzed in a number of publications. It has been demonstrated that the amazing directional hearing capabilities of this and other small animals are in part due to the presence of a set of coupled ears, which act as pressure difference receivers [19-20]. This is in sharp contrast to larger animals and humans that have isolated ears acting as pressure receivers. In *Ormia Ochracea* the separation between the two ears is so small that they are physically connected together using a flexible mechanical lever as shown in Fig. 2. This coupled ear mechanism enhances the

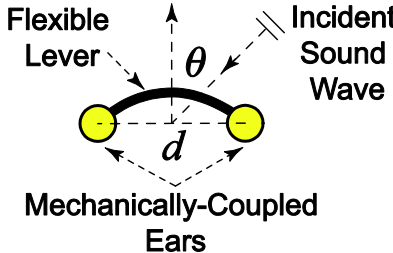


Fig. 2. Schematic of the mechanically-coupled ears of *Ormia Ochracea*. The hearing system of this fly consist of two tympanal membranes located within 500 μm of each other and connected together using a flexible mechanical lever.

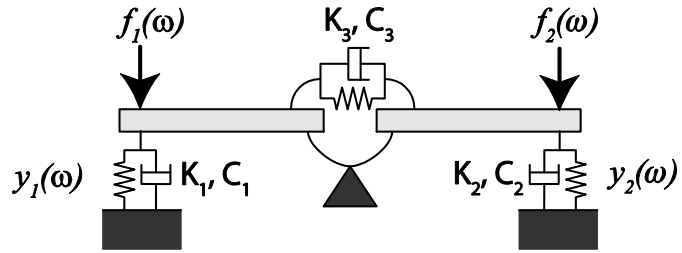


Fig. 3. Mechanical system modeling the performance of the *Ormia Ochracea*'s hearing mechanism [19]. This model is shown to predict the measured frequency response of *Ormia Ochracea*'s hearing mechanism with a reasonable degree of accuracy [19].

minute difference in the time of arrival of the sound wave between the two ears and amplifies it to a level that is detectable by the fly's simple nervous system.

Various mechanical models for the coupled ears of small animals have been proposed over the years. A simplified mechanical model of the fly's ear, proposed in [19], is shown in Fig. 3. This model is shown to be capable of predicting the measured frequency response of the fly's ear with a reasonable degree of accuracy [19]. A close examination of this model reveals that this is a second-order coupled resonator mechanical system with two inputs, $f_1(\omega)$ and $f_2(\omega)$, and two outputs, $y_1(\omega)$ and $y_2(\omega)$. They respectively represent the forces exerted on each tympanal membrane and the vibration amplitudes of each tympanal membrane. We can use the equivalency between the basic mechanical elements (mass, damper, and spring) and electrical circuit elements (inductor, capacitor, resistor) to derive two *electrical* equivalent circuit models of *Ormia Ochracea*'s ear as shown in Fig. 4. Fig. 4(a) shows a second-order coupled resonator network with two inputs, $v_1(\omega)$ and $v_2(\omega)$, and two outputs, $i_1(\omega)$ and $i_2(\omega)$. Fig. 4(b) shows the dual of this circuit, which is also a coupled-resonator circuit with two inputs, $i_1(\omega)$ and $i_2(\omega)$, and two outputs $v_1(\omega)$ and $v_2(\omega)$. Since the two inputs of these circuits represent the input signals at each ear, under sinusoidal excitation, they will have the same magnitude and only a small phase difference between them caused by the difference in time of arrival of sound between the two ears. This phase difference can be expressed as $\Phi_{\text{in}}(\theta) = 2\pi d \sin \theta / \lambda_{s0}$, where $d \ll \lambda_{s0}$ is the spacing between the two ears, and θ is the incidence angle (see Fig. 2). Analysis of this circuit reveals that by properly choosing the element values (R_1, L_1, C_1, \dots), it can be designed to increase the phase difference between the two output signals, even though the two input signals are almost identical. Assuming that the two inputs are represented as $v_1 = 1$ and $v_2 = e^{-j\Phi_{\text{in}}(\theta)}$, the outputs can be represented as $i_1 = A(\theta)e^{j\phi_1(\theta)}$ and $i_2 = B(\theta)e^{j\phi_2(\theta)}$, where $A(\theta)$ and $B(\theta)$ represent the output amplitudes and $\phi_1(\theta)$ and $\phi_2(\theta)$ represent their phases. We define the output phase difference as $\Phi_{\text{out}}(\theta) = \phi_1(\theta) - \phi_2(\theta)$. *Ormia Ochracea*'s

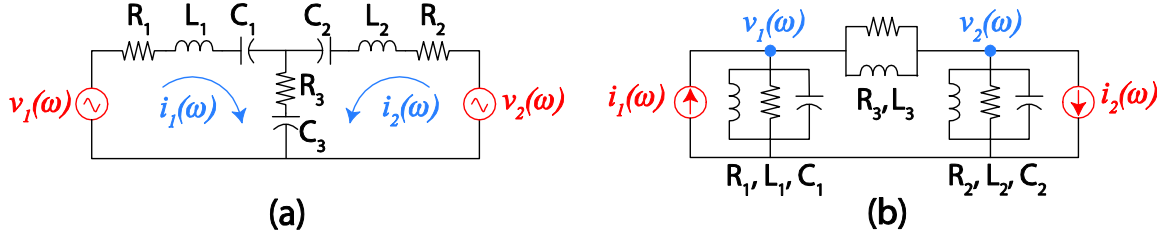


Fig. 4. The equivalent circuit models for the ear of parasitoid fly *Ormia Ochracea*. The circuit model of part (a) is obtained when considering force in a mechanical system to be analogous to voltage in an electric circuit and velocity to current. The dual of this circuit depicted in part (b) is obtained when choosing force to be analogous to current and velocity to voltage.

mechanically coupled ears significantly increase the output phase difference $\Phi_{\text{out}}(\theta)$ with respect to $\Phi_{\text{in}}(\theta)$ over a frequency range containing the peak intensity of the male cricket's mating calls. This allows the fly to precisely determine the direction of arrival of the incoming sound and localize the location of its host.

3. BIOMIMETIC ELECTRICALLY SMALL ANTENNAS

We can draw an analogy between the hearing mechanism of *Ormia Ochracea* and a simple two element antenna array. Figure 5 shows the comparison between a regular two-element antenna array and a biomimetic antenna array (BMAA) based on *Ormia Ochracea*'s hearing mechanism. Assuming that the two elements of the array are separated by a distance of $d \ll \lambda_0$ (λ_0 is the free space wavelength of the EM wave) and the array is illuminated with an incident plane EM wave, the outputs of the two antenna elements of the regular array will have the same magnitude and a phase difference of $\Phi_{\text{in}}(\theta) = kd \sin \theta$, $k = 2\pi/\lambda_0$. On the other hand, in a properly designed BMAA, the phase difference between two outputs, $\Phi_{\text{out}}(\theta)$, can be significantly larger than $\Phi_{\text{in}}(\theta)$. To quantify this, we can define a dimensionless quantity called Sensitivity Factor (SF) for the two antenna arrays as:

$$SF_{RA}(\theta) = |1 + x_1/x_2|^2 = |1 + e^{-j\Phi_{\text{in}}(\theta)}|^2 \quad (1)$$

$$SF_{BMAA}(\theta) = |1 + y_1/y_2|^2 = |1 + A(\theta)/B(\theta)e^{-j\Phi_{\text{out}}(\theta)}|^2 \quad (2)$$

where SF_{RA} and SF_{BMAA} refer respectively to the sensitivity factors of the regular array and that of the BMAA. The angular variations of sensitivity factor are henceforth referred to as the sensitivity pattern. The sensitivity pattern is a dimensionless quantity, which can be used as a measure for quantifying the capability of a receiving array, composed of two closely spaced isotropic antennas, in determining the direction of arrival of an incoming EM wave. For the BMAA, this sensitivity factor is in fact the ratio of the power of two signals, $y_1(\theta) + y_2(\theta)$ and $y_2(\theta)$, i.e.:

$$SF_{BMAA}(\theta)|_{dB} = 10 \log(|y_1 + y_2|^2 / |y_2|^2) \quad (3)$$

where $y_1(\theta)$ and $y_2(\theta)$ are the outputs of the BMAA circuit shown in Fig. 5(b). Therefore, its value can be determined using two simple power measurements. The sensitivity pattern is different from the traditional array factor, which is an indication of the amount of power received by the array. For the regular array shown in Fig. 5(a), the sensitivity pattern and the normalized array factor have the same angular dependency. On the other hand, as will be shown later, the angular variations of the sensitivity pattern of the BMAA are considerably different from those of its array factor. Comparison of (1) and (2) reveals that if $\Phi_{out}(\theta)$ can be approximated as a linear function of $\Phi_{in}(\theta)$ with a slope of $m > 1$, then the sensitivity pattern of the two-element biomimetic array is equivalent to that of a regular two-element array with a spacing of $m \times d$ between the two elements. In other words, as far as spatial resolving capabilities of a receiving array are concerned, the effective aperture size of the two-element biomimetic array is m times its maximum physical size, d . However, as is shown below, due to the nonlinear relationship between $\Phi_{out}(\theta)$ and $\Phi_{in}(\theta)$, this virtual aperture amplification is even more significant allowing a simple two-element BMAA to have a sensitivity pattern equivalent to a multi-element array with significantly larger aperture dimensions and half-wavelength spacing between the elements.

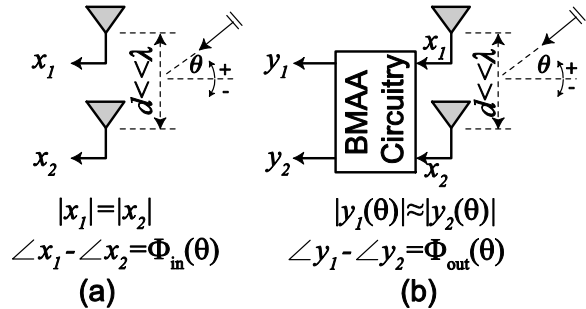


Fig. 5. (a) A two-element regular antenna array (RA) illuminated with an incident plane EM wave. (b) A two-element biomimetic antenna array (BMAA) based on the hearing mechanism of *O. Orchacrea* illuminated with a plane EM wave.

To demonstrate this, a BMAA composed of two isotropic receiving elements spaced $0.05\lambda_0$ apart and a regular two-element array with the same element type and spacing are analyzed. This BMAA is utilizing an equivalent circuit model similar to the one shown in Fig. 4(a). The values of the BMAA equivalent circuit model are $R_1=R_2=1.1 \Omega$, $C_1=C_2=1.75 \text{ pF}$, $L_1-L_2=82 \text{ nH}$, and $R_3=0 \Omega$. The values of the coupling capacitor C_3 are varied to study the effect of this parameter on the output phase difference between the two ports of the antenna. Fig. 6(a) shows the calculated $\Phi_{out}(\theta)$ as a function of θ for the regular array and the BMAA with various values of C_3 . In this case, the BMAA circuitry is designed to ensure that $A(\theta) = B(\theta)$ (see (2)). For a small value of $d = 0.05\lambda_0$, the phase difference between the two outputs of the regular array remains very small as θ changes. However, the biomimetic array can provide a significantly larger output phase difference; Using (1) and (2), the corresponding sensitivity patterns of the two arrays are also calculated and shown in Fig. 6(b). Because the spacing between the two elements is extremely small, the regular array behaves almost similar to an isotropic receiver as seen from Fig. 6(b). On the other hand, the phase difference between the two outputs of the

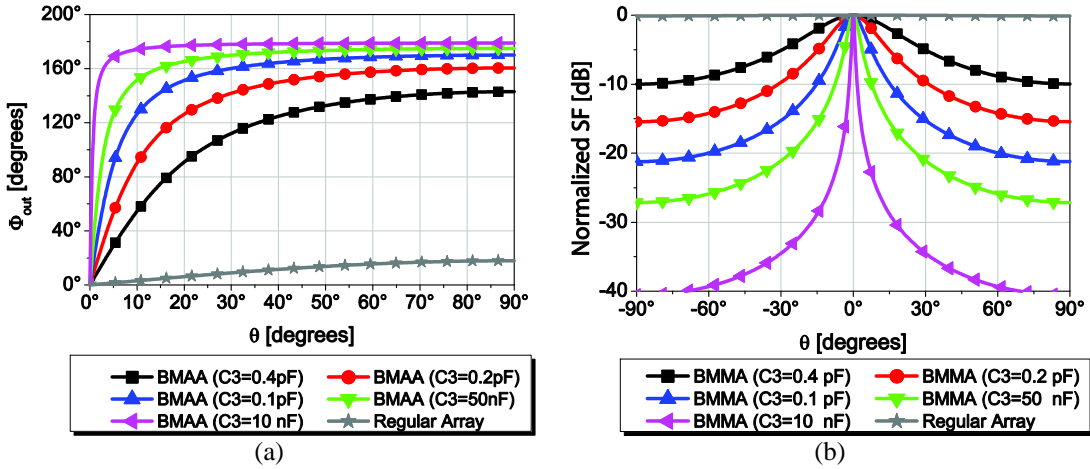


Fig. 6. (a) Variations of $\Phi_{\text{out}}(\theta)$ vs. incidence angle, θ , for the regular array and BMAA shown in Fig. 5. The two outputs of the biomimetic array have a significantly larger phase difference compared to the regular array. (b) Normalized sensitivity factors of the regular array and the BMAAs with various phase responses shown in part (a). The capacitance values in the legend refer to the value of C3 in Fig. 4.

biomimetic array is significantly larger than that of the input phase difference. More importantly, the phase difference varies as a function θ and rapidly saturates to a level close to 180° as θ increases. This results in the sensitivity pattern of the biomimetic array to become significantly more directional than that of the regular array. Also, as observed from Fig. 6 and expected from (2), sharper variations of $\Phi_{\text{out}}(\theta)$ vs. θ result in sharper sensitivity patterns. Achieving the same 3 dB sensitivity beam widths from regular arrays is only possible if a densely populated array with a significantly larger aperture size is used. For example, the sensitivity pattern achieved from a BMAA with $C_3=10 \text{ nF}$ can be achieved from a regular antenna array with 100 elements and $\lambda/2$ spacing between the elements.

4. EXPERIMENTAL VALIDATION

To experimentally verify the theoretical results discussed in Section 3, a prototype of the two-element BMAA is designed, fabricated, and tested at 300 MHz. Figure 7 shows the topology of this antenna array. The structure is composed of two electrically small monopole antennas separated by a distance

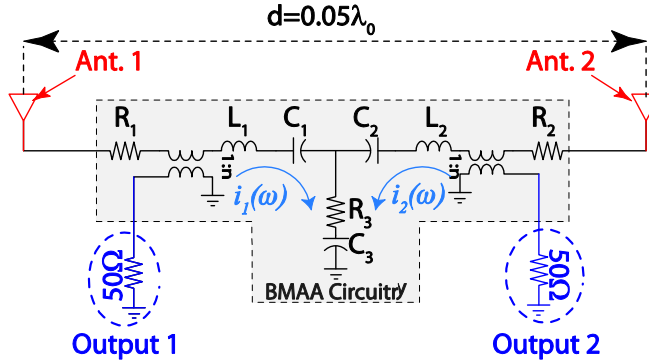


Fig. 7. Schematic of a two-element, electrically small biomimetic antenna array designed to mimic the performance of *Ormia Ochracea*'s hearing mechanism. The antennas are omni-directional electrically small monopoles. The shaded region in the circuit is the BMAA circuitry depicted as a black box in Fig. 3. R_1 and R_2 model the radiation resistance of the two monopole antennas and $R_3=0 \Omega$.

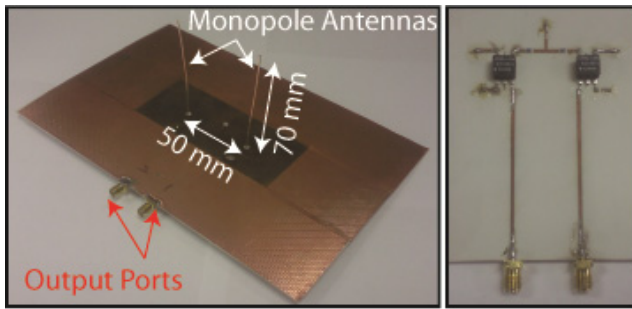


Fig. 8. Photograph of the fabricated prototype. Top view (left) shows the two electrically short monopole antennas constituting the BMAA and bottom view (right) shows the circuit elements.

50Ω output ports. A photograph of the fabricated prototype is shown in Fig. 8. Two short wire sections are used to implement monopoles. The antennas are located on top of a ground plane with finite dimensions. A thin dielectric substrate with dielectric constant of 3.4 and thickness of 500 μm covers the bottom side of the ground plane. On the bottom side of this dielectric substrate, the BMAA circuit elements are located and connected to each other and to the monopole antennas using simple 50Ω microstrip transmission lines. The connection between the monopole antennas and the transmission lines is achieved using simple through hole vias. The outputs of the two transformers are connected to the output ports of the antenna using two identical 50Ω lines. In this BMAA, the values of the resistors, R_1 and R_2 , and capacitors, C_1 and C_2 , are determined from the input impedance of the two electrically small monopoles. Therefore, the only external circuit elements utilized are two inductors, L_1 and L_2 , one capacitor, C_3 , and two transformers that are used to convert the output loop currents into output port voltages that could be

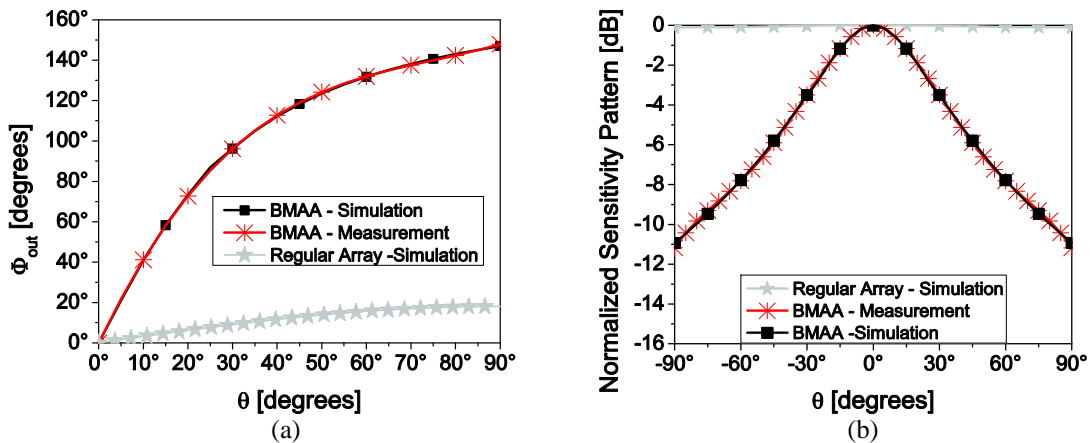


Fig. 9. (a) Measured and simulated phase responses of the biomimetic array shown in Fig. 7 and those of a regular array with identical elements and spacing (but without the BMAA circuitry). (b) Measured and simulated sensitivity patterns of the two arrays.

of $0.05\lambda_0$ (5 cm at 300 MHz) and a coupled resonator circuit similar to the one shown in Fig. 4(a). The series resistors, R_1 and R_2 , represent the radiation resistances of the two monopoles and C_1 and C_2 model the reactive part of their input impedances. In a plane normal to their axes, the monopoles are omnidirectional antennas. To simplify the measurement process, the output loop currents are sampled with two series transformers and converted to output voltages measured at two

output ports. The fabricated prototype is shown in Fig. 8. Two short wire sections are used to implement monopoles. The antennas are located on top of a ground plane with finite dimensions. A thin dielectric substrate with dielectric constant of 3.4 and thickness of 500 μm covers the bottom side of the ground plane. On the bottom side of this dielectric substrate, the BMAA circuit elements are located and connected to each other and to the monopole antennas using simple 50Ω microstrip transmission lines. The connection between the monopole antennas and the transmission lines is achieved using simple through hole vias. The outputs of the two transformers are connected to the output ports of the antenna using two identical 50Ω lines. In this BMAA, the values of the resistors, R_1 and R_2 , and capacitors, C_1 and C_2 , are determined from the input impedance of the two electrically small monopoles. Therefore, the only external circuit elements utilized are two inductors, L_1 and L_2 , one capacitor, C_3 , and two transformers that are used to convert the output loop currents into output port voltages that could be

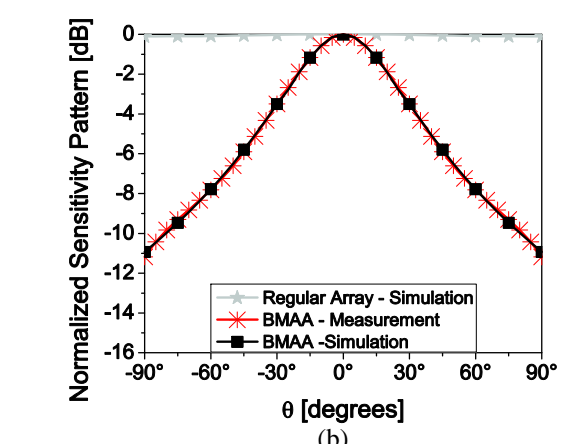


Fig. 9. (a) Measured and simulated phase responses of the biomimetic array shown in Fig. 7 and those of a regular array with identical elements and spacing (but without the BMAA circuitry). (b) Measured and simulated sensitivity patterns of the two arrays.

easily measured using a vector network analyzer (VNA).

The fabricated prototype is characterized by illuminating the BMAA with a plane wave from various incidence angles and measuring the two output signals. Figure 9(a) shows the phase difference between the two outputs of the biomimetic array and those of the regular array. The measured results agree very well with the theoretically predicted ones and confirm that the output phase difference of the BMAA is indeed enhanced compared to that of the regular array. Additionally, the measured sensitivity pattern of the BMAA is shown in Fig. 9(b) and compared to that of the regular array. As expected from (1)-(2), despite its extremely small aperture dimensions, the BMAA's sensitivity pattern is more directional compared to that of the regular array.

5. DISCUSSION AND POTENTIAL APPLICATIONS

In the most general case, one can envision three different outputs for the BMAA shown in Fig. 7. These include the loop currents i_1 and i_2 and the branch current flowing in the parallel branch $i_1 + i_2$. Denoting these three outputs as y_1 , y_2 , and y_3 respectively, we can obtain the following expression for $y_3 = i_3$ assuming the simplified equivalent circuit model shown in Fig. 4(a) and that $R_1=R_2$, $C_1=C_2$, and $L_1=L_2$:

$$y_3(\omega, \theta) = \frac{v_1(\omega, \theta) + v_2(\omega, \theta)}{Z_s + 2Z_p} \quad (4)$$

where $Z_s = R_1 + j\omega L_1 + (j\omega C_1)^{-1}$ and $Z_p = R_3 + (j\omega C_3)^{-1}$. For an electrically small receiving antenna with $d \ll \lambda$, $v_2(\omega, \theta) = v_1(\omega, \theta)e^{-jkd \sin \theta}$. Therefore, the angular dependency of y_3 vs. θ is in the form of:

$$y_3(\omega, \theta) \propto 1 + e^{-jkd \sin \theta} \quad (5)$$

which is the conventional definition of array factor and the same as the sensitivity pattern of the regular array. Therefore, in such a two-element BMAA, the angular variation of the signal $y_1 + y_2$ follows the angular variation of the regular array. Such a two-element BMAA with three different outputs and an electrically small aperture dimension acts as an omni-directional receiving antenna with the capability of resolving the direction of arrival of an incoming wave. This can be done using either a coherent system or an incoherent system. In a coherent measurement system, by measuring the phase difference between the two signals y_1 and y_2 , the phase profiles shown in Fig. 6(a) can be derived. This output phase difference can be related to the input phase difference and the direction of arrival of the incoming EM wave. In this case, the BMAA enhances the output phase difference over the input phase difference. This makes detection of small phase differences easier and enhances the angular resolution of such a direction finding system.

Such a BMAA can also be used in conjunction with more advanced direction finding algorithms as well.

By examining (2) and considering that in this two-element BMAA, $|y_1(\theta)| \approx |y_2(\theta)|$, we can easily see that the maximum value of the sensitivity function is known a priori. Furthermore, the absolute value of this sensitivity pattern is only a function of direction of incidence of an EM wave and not of its power density. This concept can be used to design direction finding systems without the need for using coherent measurements. The sensitivity pattern of the BMAA can also be measured using simple power measurement as indicated in (3). Since the maximum value of the sensitivity factor is known a priori, measuring the sensitivity factor of the BMAA and comparing the value with the a priori known maximum value of the function can be used as a means of determining whether the signal is arriving from the direction of maximum sensitivity or not. Therefore, a system composed of a BMAA with electronically tunable sensitivity patterns and simple power detectors and comparators can be used as a basic direction finding system with electrically small dimensions.

The above discussions illustrate the possibility of using a BMAA composed of two closely spaced isotropic radiators ($d \ll \lambda_0$) to precisely resolve the direction of arrival of an incoming EM wave with an angular resolution that is only available from significantly larger antenna arrays. While this two-element BMAA has a significantly higher resolving capability compared to a regular array, this pattern does not translate to a higher directivity or gain for the BMAA. In other words, the maximum power that this array can collect is still limited by the physical size of its aperture. This is caused by the fact that the amplitudes of the two outputs of the BMAA, y_1 and y_2 in Fig. 5 vary as a function of θ . As described before, for a BMAA designed to have $|y_1(\theta)| \approx |y_2(\theta)|$, this amplitude variation is such that when $y_1(\theta)$ and $y_2(\theta)$ are coherently added together, i.e. $y_3(\theta) = y_1(\theta) + y_2(\theta)$ (the conventional array factor), the variations of y_3 vs. θ can be expressed using (1). Therefore, the conventional array factor and the directivity of this two-element BMAA are the same as those of a regular two-element array. Consequently, the highly directional sensitivity patterns of the array do not translate to higher received power or directivity compared to the regular array. *This also makes sense biologically, since insects can hear sounds arriving from almost any direction (low directivity) but can precisely resolve their directions of arrival to within 1°-2° angular resolution (highly directional sensitivity patterns).* Therefore, the term "directional hearing" which is commonly used to refer to the ability of a biological hearing mechanism in resolving the direction of arrival of a sound wave should not be mistaken with the concept of directionality in antenna theory which does indicate more received power.

The maximum gain of the BMAA prototype discussed in the previous section was also measured and found to be approximately 2 dB lower than the measured maximum gain of the regular array composed of the same receiving antennas but without the BMAA circuitry. This is attributed to the losses of the transformers, inductors, and capacitor used in the BMAA circuitry, which are not present in the regular array. In this prototype the

value of R_3 is chosen to be 0Ω and no external resistors is used. Our measurement results suggest that the reactive elements used in this BMAA circuitry do not noticeably increase the noise temperature of the antenna. Thus, it is expected that the output signal to noise ratio (SNR) of this BMAA is mainly determined by the available power at the antenna outputs. While such BMAs do not offer higher directivity compared to their regular array counterparts, their directional sensitivity patterns could prove to be extremely useful in certain applications. Examples of these applications include small aperture radar systems, imaging systems, and RF sensors and will be discussed in the symposium.

6. CONCLUSIONS

A new concept for designing electrically small antenna arrays is proposed in this paper. This concept could lead to advancements in designing electrically small antenna arrays with capabilities that are not achievable from conventional antenna arrays with similar aperture dimensions. A biomimetic, electrically small antenna array modeled based on the hearing mechanism of a parasitoid fly was also demonstrated both theoretically and experimentally. It was shown that such antenna arrays demonstrate the resolving capabilities that are commonly seen in larger arrays. This concept could be beneficial in a wide range of application areas including miniature direction finding systems, high-resolution small aperture radar, miniaturized radio-frequency sensors, and high-resolution microwave imaging systems with small apertures.

REFERENCES

- [1] L. J. Chu, "Physical Limitations of Omni-directional Antennas", *Journal of Applied Physics*, Vol. 19, pp. 1163-1175, Dec. 1948.
- [2] H. A. Wheeler, "Fundamental Limitations of Small Antennas," *Proceedings of the IRE*, Vol. 35, No. 12, pp. 479 - 1484, Dec. 1947.
- [3] R. C. Hansen, *Electrically Small, Superdirective, and Superconducting Antennas*, Wiley, NY, 2006.
- [4] S. A. Shelkunoff, "A Mathematical Theory of Linear Arrays," *The Bell Systems Technical Journal*, Vol. 22, pp. 80-107, 1943
- [5] C. L. Dolph, "A Current Distribution for Broadside Array which Optimizes the Relationship Between Beamwidth and Sidelobe Level," *Proc. IRE*, Vol. 34, No. 6, p. 335, 1946.
- [6] A. Bloch *et al.*, "Superdirective," *Proc. IRE*, Vol. 48, pp. 1164, 1960.
- [7] R. Benjamin, "Optimum Use of Fully Populated, Over Populated and Sparsely Filled Antenna Apertures," *IEE Proceedings, Part H - Microwaves, Optics and Antennas*, Vol. 127, pt. H, No. 3, pp. 117-120, June 1980.

- [8] P. M. Woodward and J. P. Lawson, "The Theoretical Precision With Which An Arbitrary Radiation Pattern May Be Obtained From A Source Of Finite Size", *Proc. IEEE*, Vol. 95, pp. 120–126, 1948
- [9] D. G. Tucker, "Superdirective Arrays: The Use of Decoupling Between Elements to Ease Design and Increase Bandwidth," *Radio and Electronic Engineer*, Vol. 34, p. 251-256, 1967.
- [10] D. Young and K.G. Hill, "Structure and Function of the Auditory System of the Cicada, *Cystosoma Saundersii*," *Journal of Comparative Physiology- A*, Vol. 117, pp. 23-45, 1977.
- [11] A. Michelsen, A.V. Popov and B. Lewis, "Physics of Directional Hearing in the Cricket *Gryllus Bimaculatus*," *J Comp Physiol A* , Vol. 175, pp. 153-164, 1994.
- [12] W. Cade, "Acoustically Orienting Parasitoids: Fly Phonotaxis to Cricket Song," *Science*, Vol. 190, Issue 4221, pp. 190-191, 1975.
- [13] U. Kohler and R. Lakes-Harlan, "Auditory Behavior of a Parasitoid Fly (*Emblemasoma Auditrix*, Sarcophagidae, Diptera)," *J. Comp. Physiol. A*, Vol. 187, pp. 581-587, 2001.
- [14] A. C. Mason, M. L. Oshinsky, and Ron R. Hoy, "Hyperacute Directional Hearing in a Microscale Auditory System," *Nature*, Vol. 410, pp. 686-690, 5 April 2001.
- [15] A. S. Feng, "Directional Characteristics of the Acoustic Receiver of the Leopard Frog (*Rana pipiens*): A Study of Eight Nerve Auditory Responses," *J. Acoust. Soc. Am.*, Vol. 68, pp. 1107-1114, 1980.
- [16] H. C. Gerhardt and J. Rheinlaender, "Accuracy of Sound Localization in a Miniature Dendrobatid Frog," *Naturwissenschaften*, Vol. 67, pp. 362-363, 1980.
- [17] J. Christensen-Dalsgaard and G. A. Manley, "Directionality of the Lizard Ear," *J. Experiment. Biol.*, Vol. 208, pp. 1209-1217, 2005.
- [18] O. N. Larsen, R. J. Dooling and A. Michelsen, "The Role of Pressure Difference Reception in the Directional Hearing of Budgerigars (*Melopsittacus Undulatus*)," *J Comp Physiol A*, Vol. 192, pp. 1063–1072, 2006.
- [19] R. N. Miles, D. Robert and R. R. Hoy, "Mechanically Coupled Ears for Directional Hearing in the Parasitoid Fly *Ormia Ochracea*," *J. Acoust. Soc. Am.*, Vol. 98, pp. 3059-3070, Dec. 1995.
- [20] D. Robert, R. N. Miles, and R. R. Hoy, "Directional Hearing by Mechanical Coupling in the Parasitoid Fly *Ormia Ochracea*," *J Comp. Physiol. A*, Vol. 179, pp. 29-44, July 1996.

Compact Multiband Planar Mobile Antenna Operating Over LTE, GSM, WLAN and WiMAX Bands

M.R. Khan, M. Morsy, D.W. Addison, F.J. Harackiewicz,

Department of Electrical and Computer Engineering

Southern Illinois University Carbondale, IL 62901-6603

Abstract: This paper describes an internal multiband mobile antenna proposed for covering the LTE (746 – 806 MHz), GSM850 (824 – 894MHz), GSM900 (880 – 960 MHz), PCS1900 (1850 – 1990MHz), WiMAX (3.4 – 3.6 GHz) and WLAN (5.15 – 5.85 GHz) frequency bands. Simulations were carried out using two electromagnetic codes: HFSS (Ansoft, Inc.) and CST Microwave Studio. The proposed antenna was fabricated on an FR4 substrate with 4.4 dielectric constant and overall size of 50x35x1.5 mm³. At the higher frequency range between the 5GHz and 6GHz, it has a measured impedance bandwidth of 18.18% and peak simulated gain of 3.44 dBi.

1. Introduction

The transition of the TV broadcasting service from analog to digital is complete and according to the FCC, the 700 MHz band (698-806), which was used till recently by TV broadcasters, can be used for commercial communication [1]. Long term evolution is one of the mobile communication technologies that are targeting the 700MHz band. The LTE service is expected to provide better communication quality than the existing services, such as GSM850 (824-894), GSM900 (880-960), DCS1800 (1710-1880 MHz) and PCS (1850-1990 MHz) [2]. However, mobile phones are desired to be able to cover at least a few of the existing service bands and LTE bands at the same time, especially before LTE services are widespread. Printed antennas with a uniplanar and compact structure are very attractive for slim mobile phone applications, mainly because they can be directly printed on the system circuit board of the mobile phone at

low cost and their antenna height above the circuit board can generally be ignored [3]. In this paper, a novel internal uniplanar printed microstrip fed antenna with a small size of $50 \times 35 \text{ mm}^2$ is presented. The proposed antenna is suitable to be directly printed on the system circuit board of a mobile phone making it easy to fabricate at low cost and attractive for slim mobile phone applications.

Table 1 Target bands

Long Term Evolution (LTE)	(747-807) MHz
GSM850	(824-894) MHz
GSM900	(880-960) MHz
DCS1800	(1710-1880)MHz
PCS 1900	(1850-1990)MHz
UMTS	2100 MHz
WLAN	(5.15-5.35)GHz
WLAN	(5.725-5.825)GHz
WiMAX	(5.24-5.85)GHz

2. Proposed Antenna:

Figure 1 shows the geometry of the proposed microstrip-fed printed antenna for the LTE/ GSM/ UMTS/ WiMAX and WLAN bands.

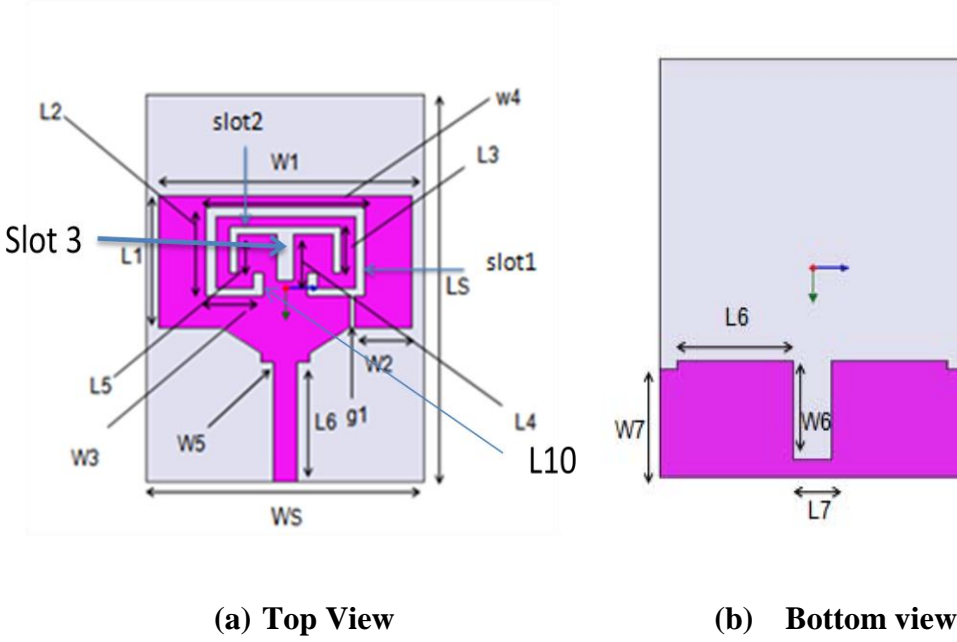


Fig .1 Geometry of the proposed antenna

The proposed antenna is a printed monopole with an inverted U-shaped slot and a slit in the corner, a modified T-slot inside of that, and a notch in the ground plane behind the feed line. The antenna is placed on an FR4 substrate ($\epsilon_r=4.4$) with 1.5mm thickness, which is commonly used as the system circuit board of the mobile phone. The overall size of the antenna is $35 \times 50 \times 1.5\text{mm}^3$. The detailed dimensions of the structure are listed in Table 2.

Table 2 list of the parameters of the dimensions of the antenna (units: mm)

L1	17	L5	5	Width of slot 3	2
L2	11.5	L6	15.5	Horizontal length of slot 2	16
L3	6	L7	6.5	L10	4
L4	6	g1	0.25		
W1	32	W5	1.5		
W2	7.3125	W6	11.8		
W3	6	W7	13		
W4	20	WS x LS	35×50		
Width of slot 1	1	Width of slot 2	2		

Table 3 Proposed Antenna Specifications

Structure	Uniplanar
Feeding Technique	Microstrip line
S ₁₁ Requirement	Less than -6 dB for LTE and GSM bands Less than -10 dB for UMTS,WLAN and WiMAX bands
Physical Dimension	50x35x1.5mm ³ (Including Ground Plane)
Target Application	Mobile Communication (Smart Phones)
Wireless Technologies Supported	LTE,GSM,UMTS,WIMAX,WLAN
Frequency bands supported	LTE(747-807) MHz, GSM850 (824-894) MHz GSM900 (880-960) MHz, DCS1800, (1710-1880)MHz, PCS 1900(1850-1990)MHz, UMTS 2100 MHz, WLAN(5.15-5.35)GHz, WLAN(5.725-5.825)GHz, WiMAX(5.24-5.85)GHz
Gain	3.44dBi in (5-6) GHz Band -1.5 dBi for DCS PCS and UMTS band -9dBi for LTE band
Nominal Impedance	50 ohms

3 Design Methodology:

Parametric studies are conducted to arrive at the desired performance. The outer dimension of the patch is obtained using standard design expressions for width and length with some preselected specifications.

Table 4 Specification for determination of the outer parameters of the patch

Parameter	Specification
Thickness of dielectric substrate (h)	1.5 mm
Operating frequency	Resonance frequency of choice
Dielectric Material	FR4 ($\epsilon_r = 4.4$)

The antenna is fed by 50 Ω microstrip line. This feeding technique is selected to ease integration and fabrication. The advantage of this technique is that both of the feed and the patch lie on the surface of the substrate. This technique is efficient for thin substrates [4]. The patch itself

provides a resonant frequency and in addition to other factors determines the outer dimensions of the patch. The design procedure followed the following steps: First, an approximate equation is used to determine the initial patch width and length [5] based on the center frequency of 2.4GHz.

$$W = \frac{C}{2f_0\sqrt{\epsilon_r+1}/2} = \frac{3 \times 10^{10}}{2 \times 2.4 \times 10^9 \sqrt{(4.4+1)/2}} = 3.7\text{cm}=37\text{mm}$$

$$L \approx 0.49\lambda d = \frac{\lambda_0}{\sqrt{\epsilon_r}} = 28\text{mm}$$

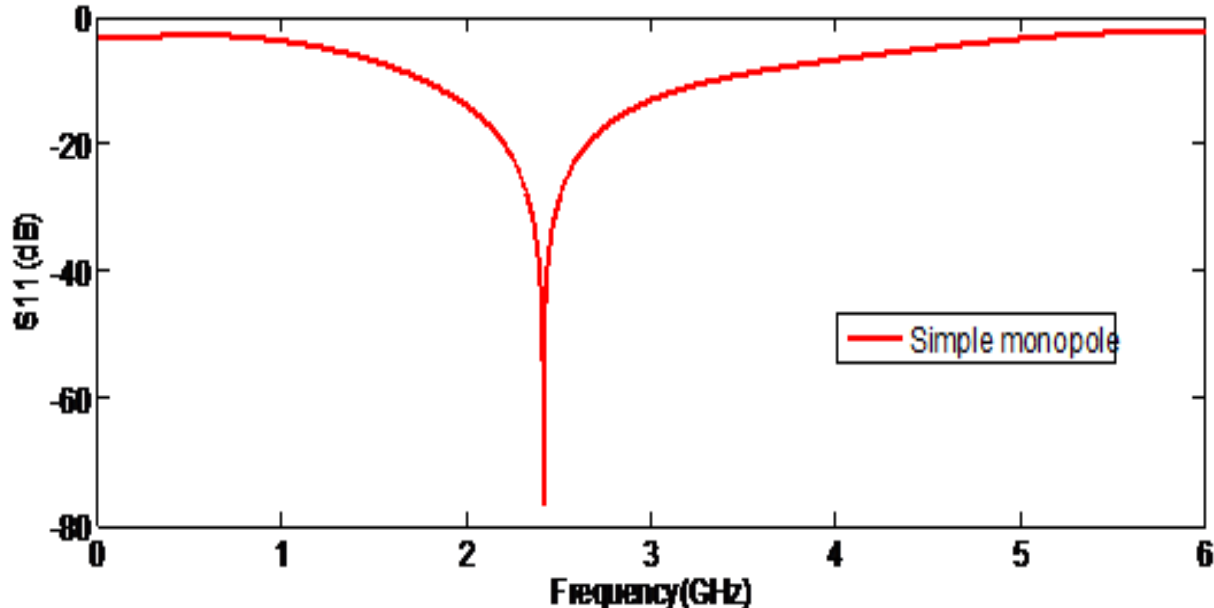


Fig .2 simulated $|S_{11}|$ in dB versus frequency in GHz of a simple monopole

Parameters of the patch are determined by the basic set of above equations that involves length, width dielectric constant of the material and resonant frequency. Second, a parametric analysis is used to optimize the above dimension. Multiband operation of patch antenna is not uncommon. By loading the patch with slots one not only can enhance the bandwidth by adding another resonant mode near the TM_{10} resonance frequency of the unslotted rectangular antenna but can

also help in achieving multiband operation. The response of the slot depends on its width and length. A typical U shaped slot is used for antennas operating at high frequency range (>3GHz).

a) Contribution of outer slot and slit in Patch:

A slot perturbs the current distribution on the patch surface and consequently modifies the fundamental mode of the rectangular microstrip patch antenna. In addition the slot introduces another mode which results in multiband operation of the patch. The U shaped slot essentially forces current to flow in a different path on the patch .Once the equivalent current –flow path is determined ,it can be easily converted back to the resonant frequency based on its length [6].

The multiband characteristic of the proposed antenna is achieved by incorporating a U-shaped slots and a slit. The resonance at the 750 MHz LTE band is achieved by simultaneous use of the slit and outer slot. The slit and slot together form a monopole element. The approximate, physical length of a printed quarter-wave monopole antenna is $L = 400\text{mm} / 4 = 100\text{mm}$.

b) Notch in the ground plane:

The notch in ground plane under the microstrip feed line forces the antenna to be resonant for the DCS, PCS and WLAN and WiMAX bands. It is evident from S11 curve in Fig 3 that without the notch in the ground plane proposed antenna will not be able to support PCS, DCS, WLAN and WiMAX bands.

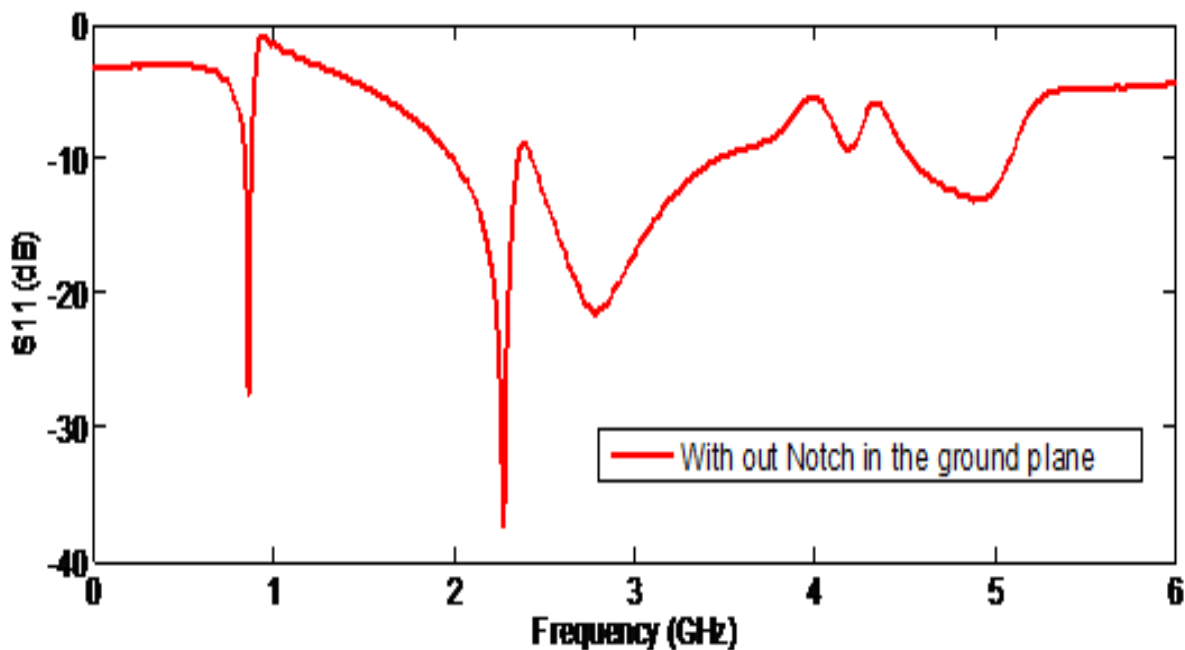


Fig .3 simulated $|S_{11}|$ of proposed antenna without notch in the ground plane

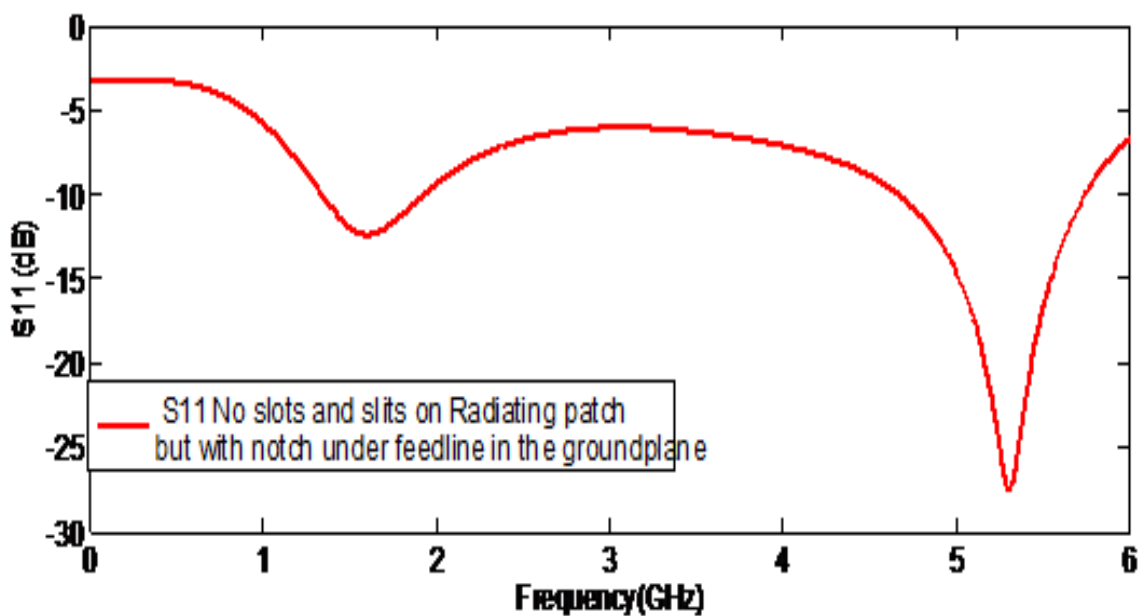


Fig .4 simulated $|S_{11}|$ of proposed antenna with notch in the ground plane

The S₁₁ curves in Figs 3 and 4 identify different parts of the patch antenna that support different bands. The notch in the ground plane behind the feeding line forces the antenna to support the WLAN and WiMAX bands as well as the PCS and DCS bands. Also the antenna supports the LTE and GSM bands because the outer slot and slit together form a monopole element.

4 Simulation and Fabrication:

The proposed antenna was fabricated and measured. Fig 2 shows the measured and simulated return loss for the fabricated prototype. The simulated results obtained using Ansoft HFSS are similar to the measured data in the bands of interest which are LTE700, GSM 850, GSM900, PCS1800 DCS1900 UMTS 2000 ,WLAN (5.15-5.35) (5.725-5.825)GHz and WiMAX (5.25-5.85)GHz.

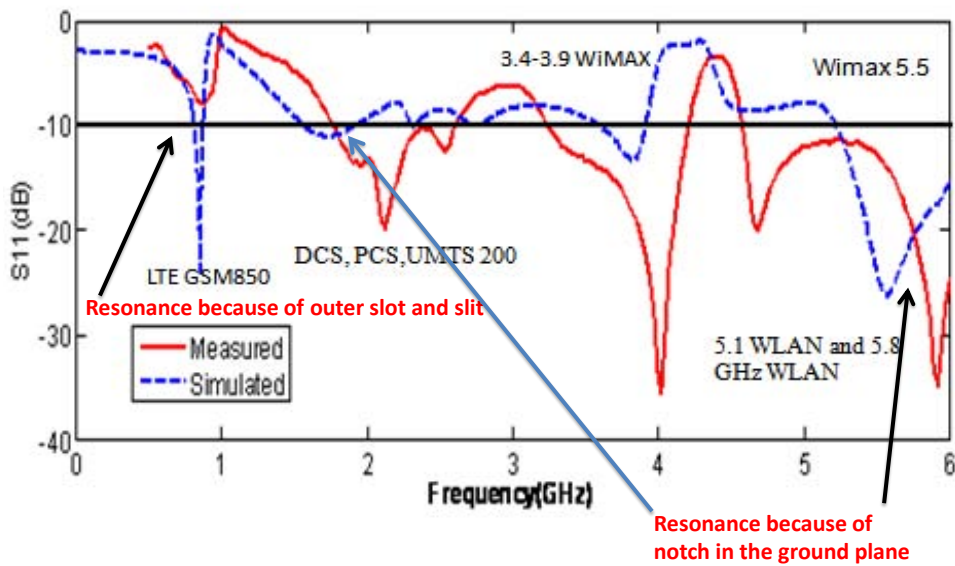


Fig .5 Measured and simulated |S₁₁| in dB versus frequency in GHz

In Figure 5 is presented the variation of the amplitude of S_{11} in the frequency range of 0.5GHz-6GHz. It is observed that the return loss from simulation results through Ansoft HFSS and from network analyzer has reasonable agreement. Figures 6, 7, and 8 show the simulated 3D radiation patterns at 5.5GHz, 2GHz and 0.75GHz respectively and that the best gain is at the higher frequency. The peak gain at these three frequency points is shown in Table 3. The gain is highest 3.44dBi in the frequency range of (5-6) GHz. The antenna demonstrates an omnidirectional radiation pattern in this range and supports all of the WLAN and WiMAX bands.

Table 3 Gain Vs frequency

Frequency (GHz)	Peak Gain (Absolute)	Phi Component	Theta Component
5.5	3.44dBi	3.42dBi	-0.11dBi
2	-1.53 dBi	-1.53dBi	-1.53dBi
0.75	-9.03dBi	-9.06dBi	-9.4dBi

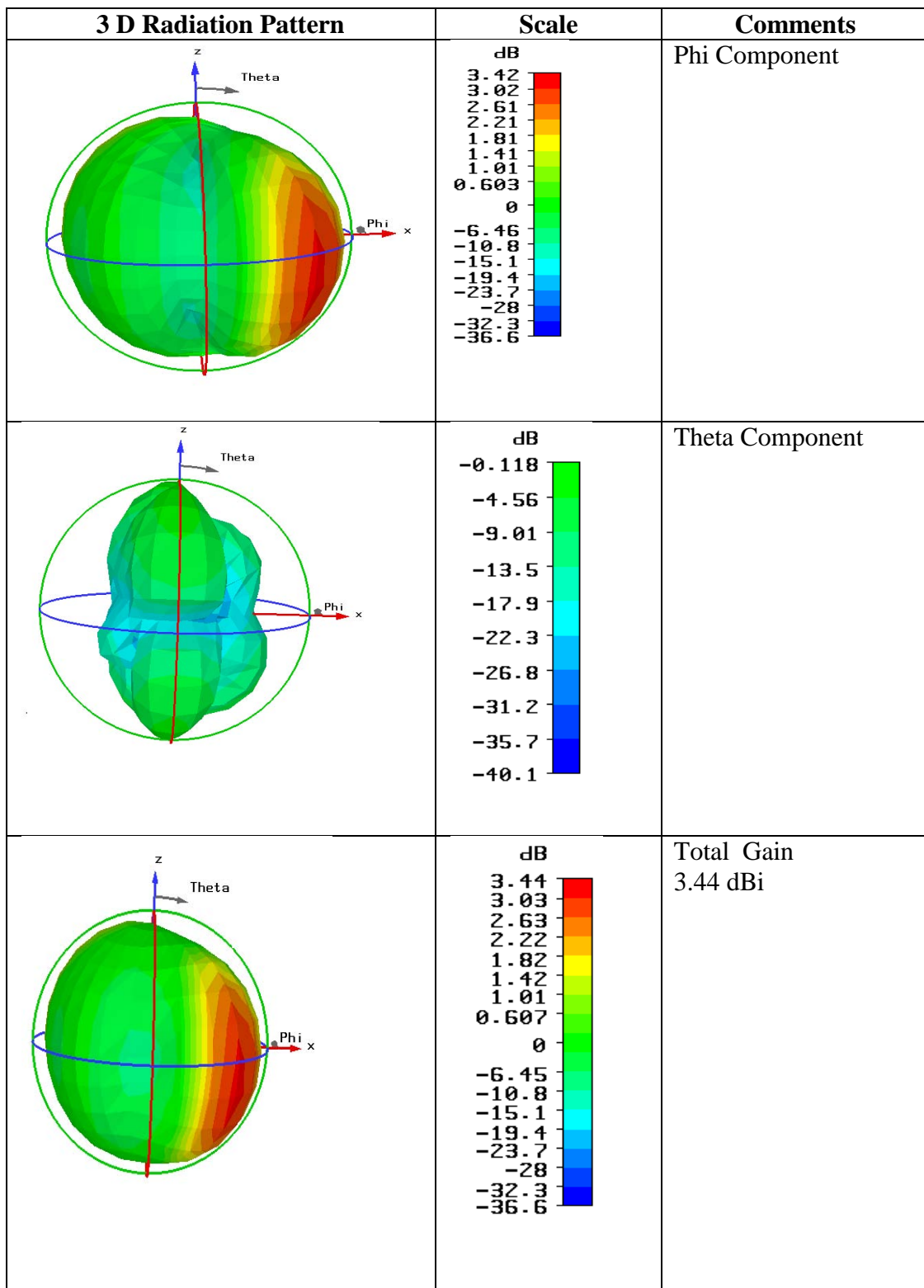


Figure 6 - Simulated Radiation Pattern at 5.5 GHz

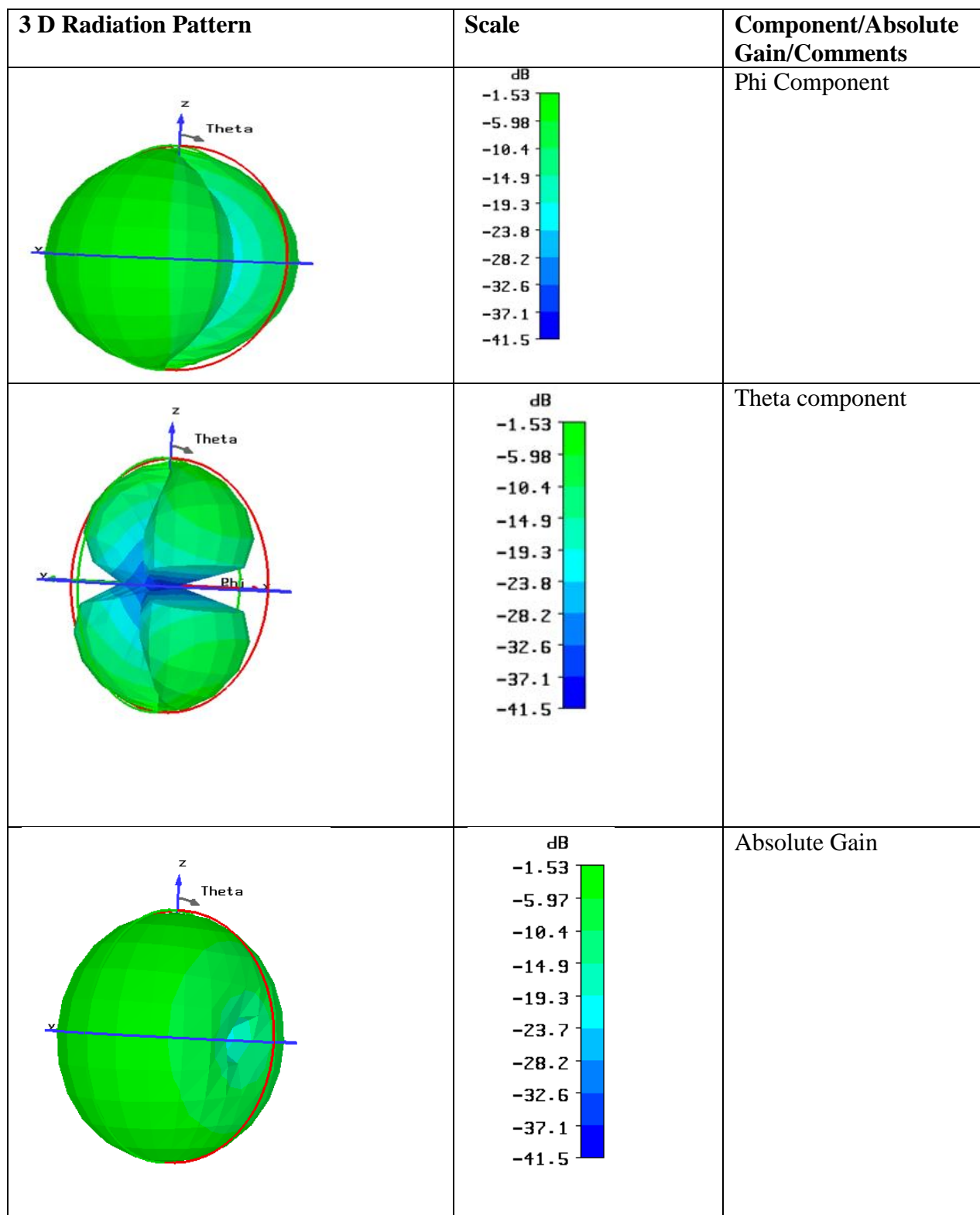


Figure 7 Simulated Radiation Pattern at 2 GHz

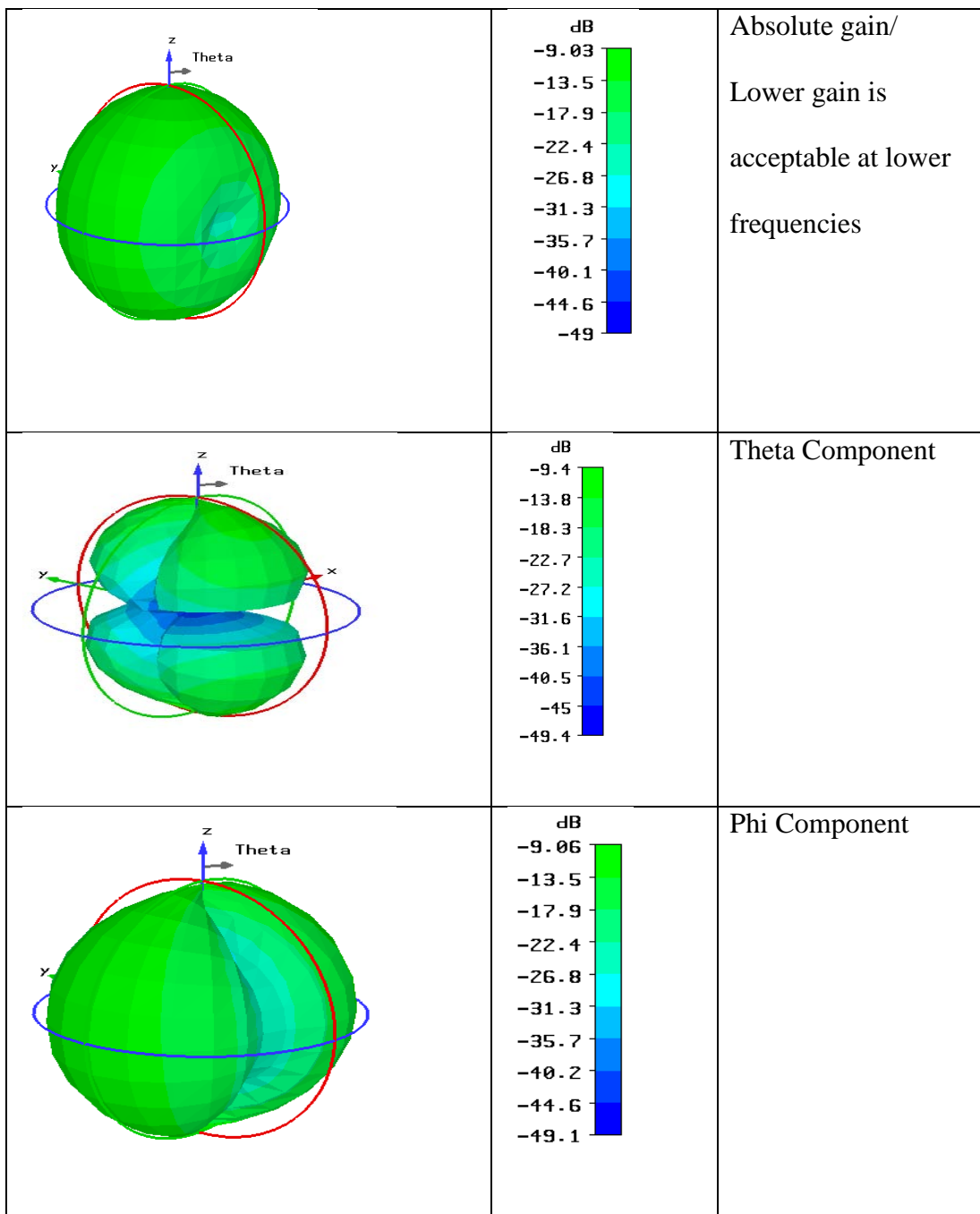


Figure 8 Simulated Radiation Pattern at 0.75 GHz

5. Results:

The measured VSWR is compared with the simulated in Table 4. The 5-6 GHz bandwidth and the 747-960MHz bandwidth both have good agreement between simulation and measurement. The bandwidth beginning at 1710MHz shows a much better simulated bandwidth than measured.

Table 4 Simulated and Measured Impedance Bandwidth

Frequency Band	Simulated 2:1 VSWR BW	Measured 2:1 VSWR	Simulated 3:1 VSWR	Measured 3:1 VSWR BW
(5-6)GHz	18.18%	18.18%		
(747-960) MHz			24.95%	25%
(1710-2100)MHz		20.47%		
(1710-4000)MHz	80%			

The gain for the lower band is low but it is still in acceptable range. Acceptable $|S_{11}|$ is less than -6dB, for GSM and LTE band. For practical applications for these bands the bandwidth is defined by 3:1 VSWR [7].

Proposed antenna is a compact antenna ($50 \times 35 \text{ mm}^2$) with a simpler structure as compared to [7]. In [7], a PIFA and monopole are used together to support the bands of LTE, GSM, PCS and DCS. In [7], the structure is 3D with two ground planes ($40 \times 80 \text{ mm}^2$) and ($40 \times 70 \text{ mm}^2$). In [1], the overall size of the antenna without ground is $40 \times 100 \times 5 \text{ mm}^3$ which is a rather large 3D structure for the latest small phone applications.

6. Parametric Analysis:

To improve the impedance matching of the antenna, parametric studies were carried out by simulating the antenna with one geometry dimension slightly changed from the reference design while all other parameters are fixed. The best dimensions were used for the proposed antenna. All the simulations are carried out using CST Microwave studio. Some parameters like L2, width of slot 1, width of slot 2, gap g, and width of notch in the ground plane are set as variable and

their effects on the impedance bandwidth are studied. It is found that the reflection coefficient is very sensitive to some of these parameters as compared to the others.

Table 5 Fixed and Variable Parameters of Proposed antenna

Fixed Parameters (mm)	Variable parameters(mm)
Width of microstrip line =3mm	L2=Length of slot L2
Substrate dimensions ($L_S \times W_S$)	Width of slot 1
Substrate Thickness=1.5mm	Width of Slot 2
	Width of Notch =L7 in the ground plane
	Length of Slot 3

In the above table the variable parameters were found to be the parameters that most affected the impedance bandwidth of the proposed antenna. This parametric analysis of the proposed antenna is not focused on any single band but on all the bands supported by the designed antenna.

In planar slot antennas, the wider slot gives more bandwidth, and the optimum feed structure gives good impedance matching. There are three parameters to characterize the slots, namely slot length, slot position, and slot width. The width of the slot is changed and its impact on the magnitude of S_{11} is recorded and compared with the different width of the same slot while keeping other parameters constant.

It is evident in Fig. 9 that the resonant frequency shifts slightly lower as the length of the slot (L2) is increased from 10.5mm to 12.5mm. As L2 increases, the upper and lower resonant frequencies shift downward. The optimum length for L2 is 12.5 mm as it decreases the first resonant frequency and thus covers the LTE band more effectively. Also the -10 dB $|S_{11}|$ bandwidth increases from 16.16% to 22% and thus can support the DCS (1800 MHz) cellular band in addition to the PCS (1900) and UMTS (2000MHz) bands.

The width of slot 1 is increased by an increment of 0.5mm while keeping the slot length constant and in Fig. 10 the resulting magnitude of S_{11} curves are depicted. Matching is improved as the slot width is decreased from 2mm to 0.5mm in the frequency range of 2 to 3 GHz.

Figures 11 and 12 show that the first, second and the highest resonant frequency of the proposed antenna do not change by changing the widths of slot 2 and slot 3. It is evident that there is no significant variation of S_{11} magnitude in the upper and lower resonant frequencies. Varying widths of slot 3 does not change S_{11} in the upper and lower resonant frequencies but has some impact where the antenna is not resonating. The slot width of 2mm is fabricated.

Figure 13 shows the $|S_{11}|$ versus frequency as the length of the substrate is varied from 50 mm to 40mm. It is seen that varying the length of the substrate over this range has no significant impact on the return loss of the proposed antenna. LS is the length of substrate which has been varied over a maximum range. The antenna is fabricated with LS of 50mm.

Figure 14 depicts the return loss versus frequency for different notch widths (L7) in the ground plane. The notch width affects the overall performance of antenna from frequencies of about 2GHz and higher. For L7 =5.5mm, the antenna demonstrates wideband performance in the upper bands and also the upper resonant frequency decreases as the width of the notch is decreased from 8.5 mm to 5.5 mm.

Figure 15 shows variation of the magnitude of S_{11} curves with the width of the slit in the patch. This gap (g) is varied in four steps and changes the resonances of the antenna in upper bands it is supporting.

Based on the parametric analysis optimized dimensions are given in Table 6.

Table 6 Optimal parameter values of the antenna.

Ls	L7	Slot1 (width)	L2 (Length)	Slot3 (width)	Gap (g)
40mm	6.5mm	2mm	12.5mm	0.5mm	0.25

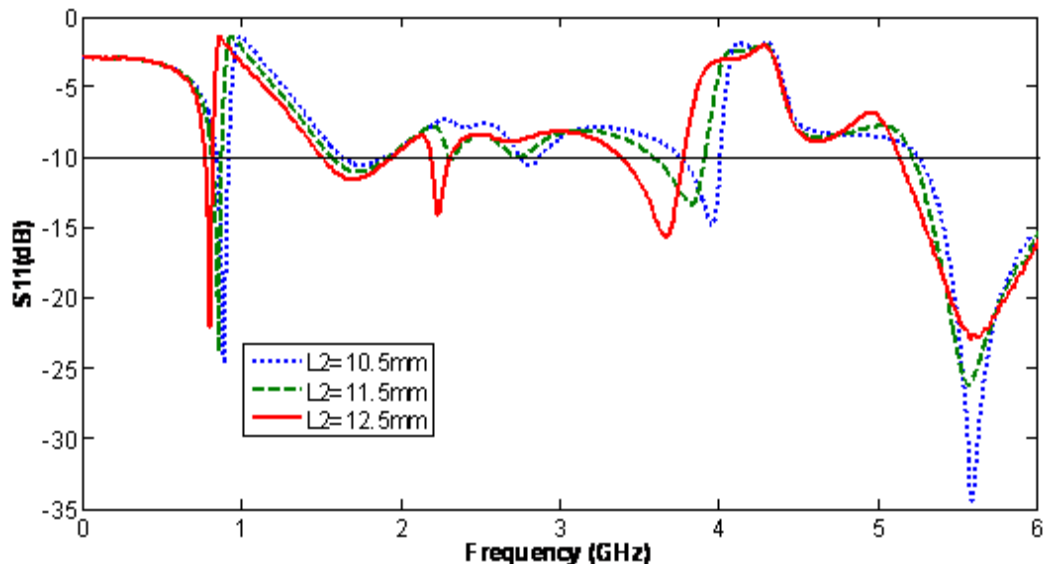


Figure 9 Simulated $|S_{11}|$ curves for different values of the vertical slot length L2

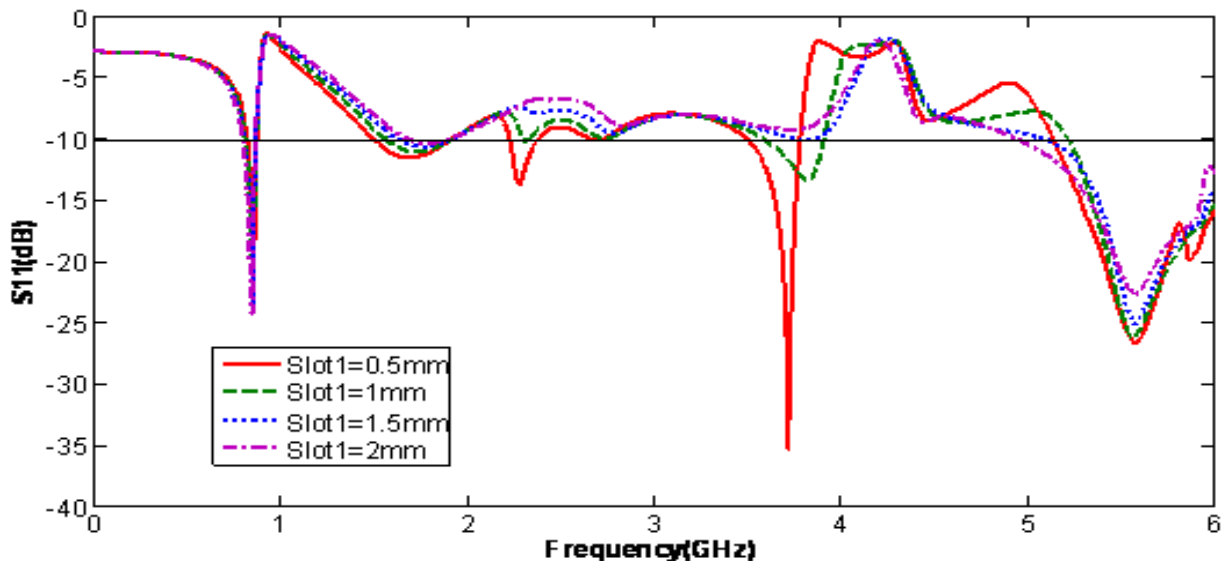


Figure 10 Simulated $|S_{11}|$ curves for different values of width of Slot1

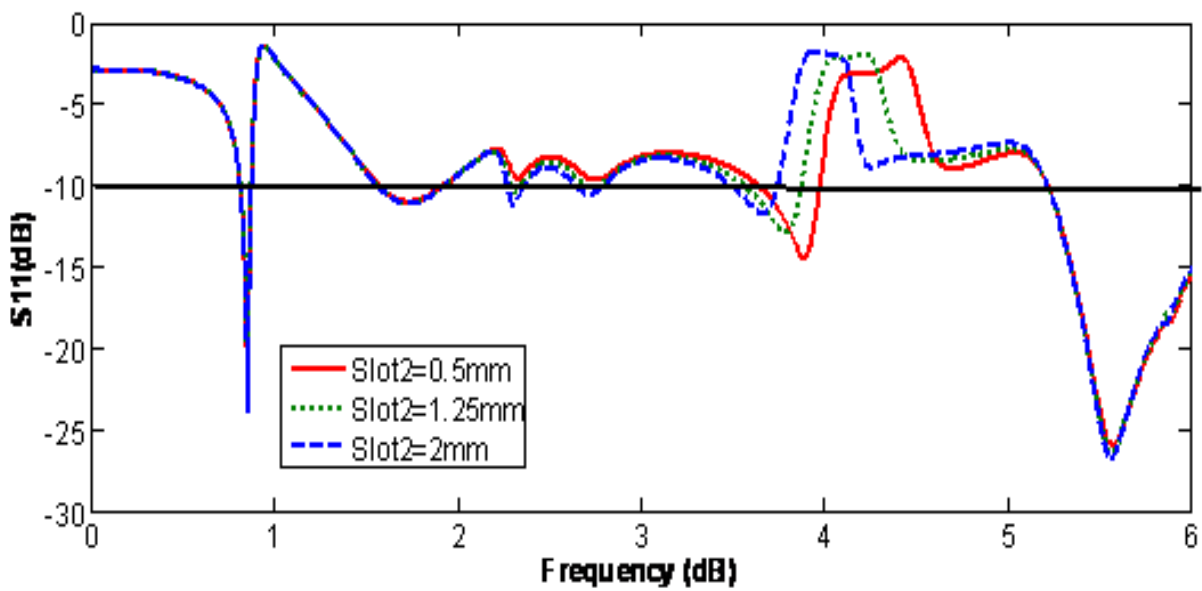


Figure 11 Simulated $|S_{11}|$ for various widths of Slot2.

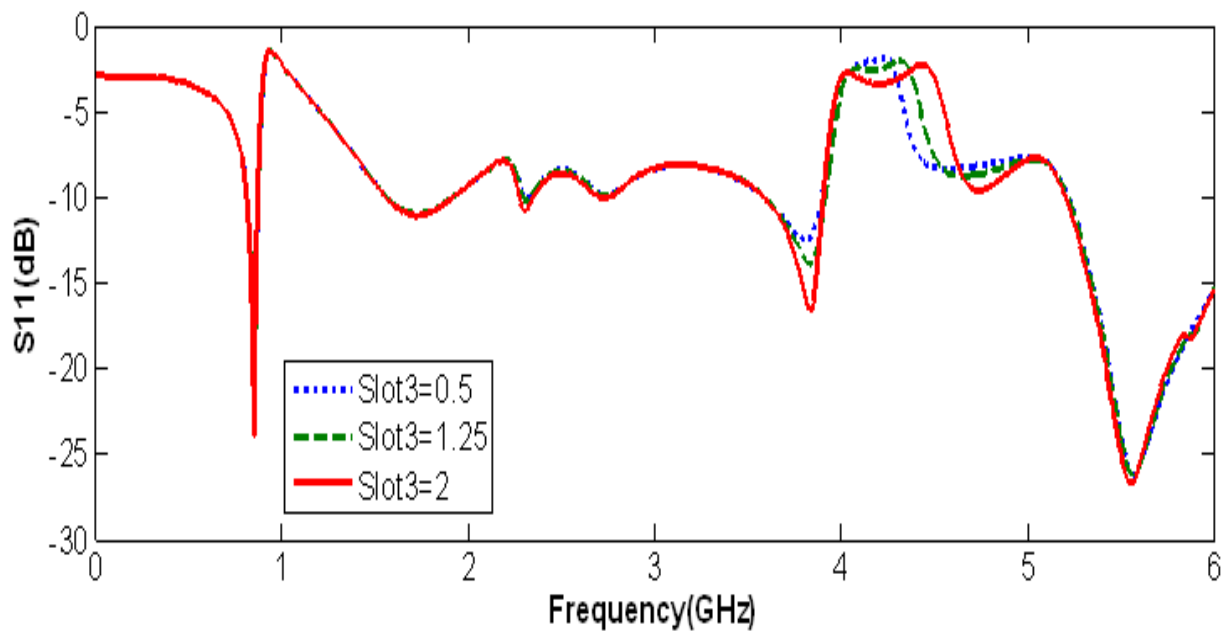


Figure 12 Simulated $|S_{11}|$ for various widths of Slot3

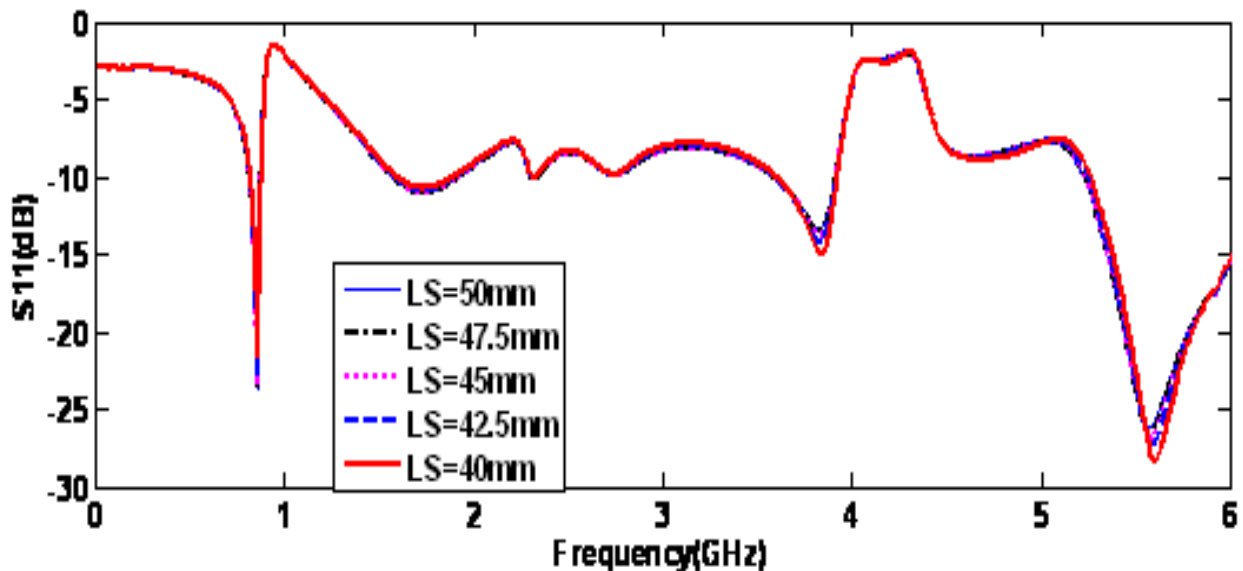


Figure 13 Simulated $|S_{11}|$ for various lengths of substrate.

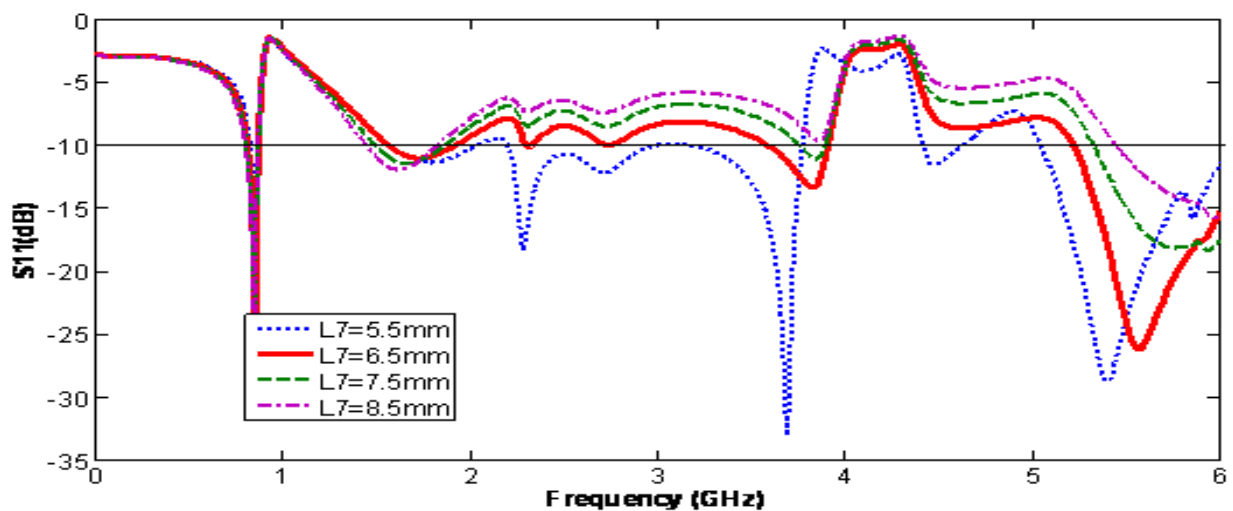


Figure 14 Simulated $|S_{11}|$ for various widths of notch in the Ground plane

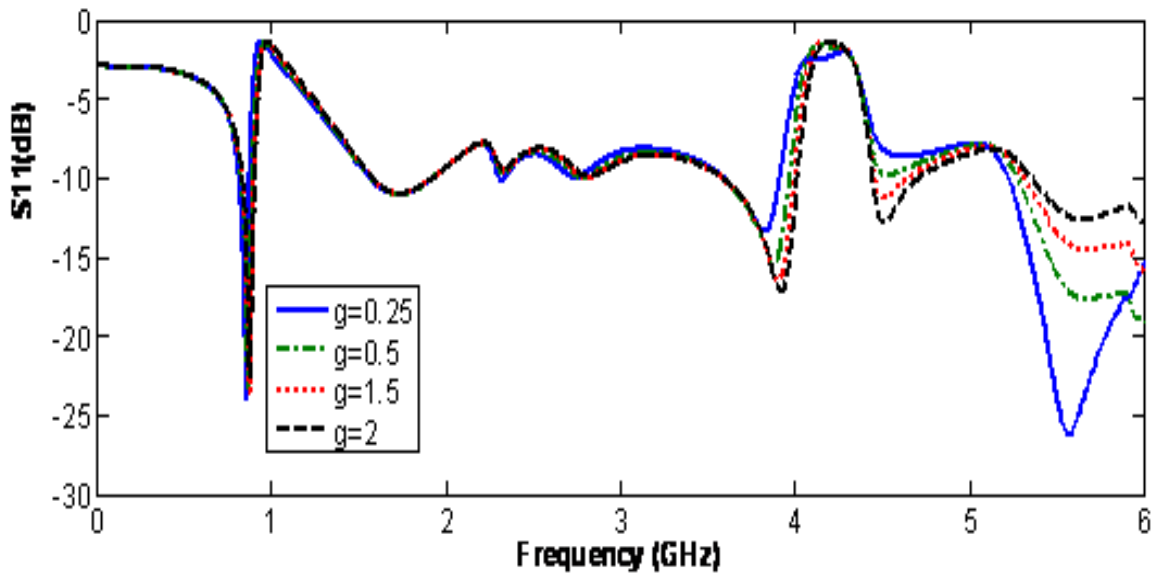


Figure 15 – Simulated $|S_{11}|$ for various dimension of gap g in mm

Conclusion:

In this paper, a novel printed monopole antenna with multi-resonance performance is proposed. In this design, the proposed antenna can support LTE 700, GSM850, GSM900 with $S_{11} < -6$ dB and PCS 1800, DCS1900 and UMTS, 5.1 GHz and 5.8 GHz WLAN and 5.5 GHz WiMAX bands with $S_{11} < -10$ dB.

References:

- [1] Youn Suk Jeong, Sang Heun Lee, Ji Hwan Yoon, Won Yong Lee, Woo Young Choi and Young Joong Yoon “Internal Mobile Antenna for LTE/GSM850/GSM900 / PCS1900 / WiMAX / WLAN,” *Radio and Wireless Symposium (RWS)*, 2010 IEEE, 10-14 Jan. 2010, New Orleans, LA, pp. 559 – 562.,
- [2] Jeongsam Cho Kangwook Kim “A Frequency-reconfigurable Multi-port Antenna Operating over LTE, GSM, DCS, and PCS Bands” *Antennas and Propagation Society International Symposium, 2009. APSURSI '09*, 1-5 June 2009, Charleston, SC, pp. 1 – 4.
- [3] Kin-Lu Wong , Wei-Yu Chen “Small-size printed loop-type Antenna integrated with two Stacked coupled-fed shorted Strip monopoles for eight-band LTE/GSM/UMTS operation in the Mobile phone” *Microwave and Optical Technology Letters*, Vol 52, no 7, April 2010

[4] J. Uddin1, M. B. I. Reaz1, M. A. Hasan, A. N. Nordin, M. I. Ibrahimy, M. A. M. Ali “UHF RFID antenna architectures and applications” *Scientific Research and Essays*, Vol. 5(10), pp. 1033-1051, 18 May 2010.

[5] www.orbanmicrowave.com/The_Basics_Of_Patch_Antennas.pdf

[6] Shun-Yun Lin; Hong-Ren Huang; Cing-Wei Guan; Shu-Ani Yeh; “A novel compact slot antenna for ultra-wideband communications,” *Antennas and Propagation Society International Symposium 2007*, 2007 IEEE, 9-15 June 2007 Honolulu, HI, pp. 5123 – 5126.

[7] Jeongsam Cho, Kangwook Kim “A Frequency –reconfigurable Multi-port Antenna Operating over LTE, GSM, DCS, and PCS Bands” *Antennas and Propagation Society International Symposium, 2009.APSURSI '09*.

EFFICIENCY IMPROVEMENTS OF A DIRECTLY-DRIVEN ANTENNA-BASED AM TRANSMITTER OVER THE AM FREQUENCY BAND

Olusola O. Olaode¹, William T. Joines¹, and W. Devereux Palmer²

¹Department of Electrical and Computer Engineering,

Duke University, Durham NC 27708

²US Army Research Office, Durham NC 27703

Abstract- Operation across a wide frequency bandwidth and high power efficiency are important goals of radio transmitter design. Conventional radio transmitters have a narrow bandwidth, primarily limited by the bandwidth of the impedance matching network between the power amplifier and transmit antenna. The Directly-Driven Antenna (DDA) architecture has the potential to eliminate this limitation, as without the frequency constraints imposed by the conjugate impedance matching network, it may be possible to couple power to a transmit antenna efficiently across a very wide bandwidth. Previous work suggested that the DDA architecture can produce an improvement of a factor of 10 in the radiated power using an electrically-small antenna when compared to conventional transmitter architecture. Results obtained over the past year, incorporating suggested changes to the DDA circuit and measurement techniques reported previously, indicate that the radiated power improvement is still closer to a factor of 10 at ~1 MHz but changes with frequency. This presentation will discuss the refinements made to the circuit design, measurement technique and results, and will show data demonstrating operation of a DDA transmitter across the AM broadcast band.

1. Introduction

Modern wireless systems increasingly require more compact, portable, wide-band, and efficient transmitter architectures. In conditions where depletable power supply sources are used to power mobile devices, it is especially important that they are efficient. The research described in this paper is oriented towards the investigation of alternative transmitter architectures for US Army ground mobile wireless communications. Therefore, it is our expectation that the integration of this technology into actual Army

radios, prove to be more efficient than the existing radios. Since 80% of the Army's ground mobile wireless communication is conducted in the HF to VHF bands, the focus of this work, which is to improve the efficiency of the transmitter architecture, will center on the AM band where commercial components are readily available. A block diagram of a simple amplitude modulation (AM) transmitter is shown in the upper half of Figure 1.

The most notable in terms of efficiency and cost are the power amplifier and matching stages. Conventional AM transmitters have often employed class A, B, or AB linear amplifiers in the output stage, all of which are known to draw significant bias current to or from the load; thus, producing considerable power loss in the output power amplifier. In order to mitigate these losses, designers of wireless transmission systems have explored the use of higher-efficiency class-D amplifiers to replace the PA component in the traditional architecture shown in the upper half of Figure 1.

In comparison to class A (efficiency: 25% [1]) or class B (efficiency: 78.5% [1]), class D amplifiers can theoretically provide an efficiency of unity. Due to the non-linearity of the class-D amplifier, it is expected to yield a higher Total Harmonic Distortion (THD) compared with their linear counterparts. However, when designed carefully, an output filter improves the THD to <1% [1]. Therefore, the class D amplifier provides the optimum compromise between THD and efficiency.

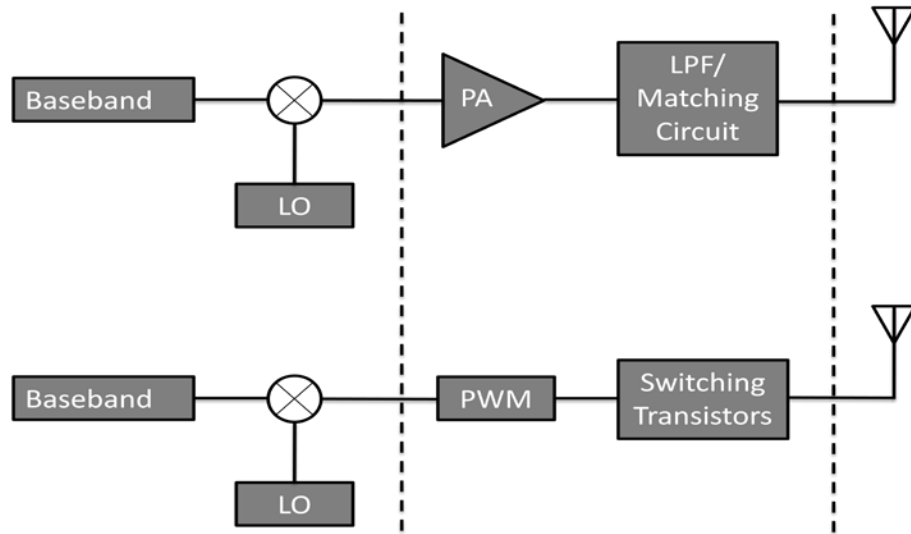


Figure 1. Block diagram showing the architectures of the (upper) conventional and (lower) digitally-driven antenna (DDA) AM transmitters. Glossary of terms - LO: Local Oscillator, PA: Power Amplifier, PWM: Pulse-Width Modulator, LPF: Low-Pass Filter.

Another approach taken by some researchers in improving the efficiency of a wireless transmitter circuit is to use a filter-less class D amplifier. Muggler et al. were able to obtain 86% power efficiency with their filter-free design [3]. However, in that application, the full-bridge configuration of the class D amplifier was used to differentially power the output speaker. This approach required pulse-width generation for each half-circuit of the H-bridge class D amplifier and pre-amplifier stage.

A dramatically different approach was proposed by Joseph T. Merenda (formerly of Hazeltine Corporation). Merenda (Patent # 5,402,133) proposed a system in which a radio signal can be digitized through a pulse width modulator and used to control the switching rate of a pair of complimentary transistors in a class D amplifier configuration. The signal is subsequently radiated by electrically small antenna systems (antennas whose physical sizes are small relative to excitation wavelength [2]). This approach was proven to result in improved bandwidth and efficiency in getting signals to the antenna and forms the basis of the work described in this report.

The lower block diagram in Figure 1 shows the architecture of the DDA system. Modulation of an information signal is performed in an identical manner in both the DDA and the conventional systems except that the power amplifier and low-pass filter/matching network stages in the conventional architecture are replaced with a pulse-width modulator and complimentary switching transistors in the DDA architecture. Details on the contributions of the PWM/switching transistor networks combinations are to be presented later in the paper.

2. Digitally Driven Antenna Circuit Design and Architecture

2.1 Pulse Width Modulator

The Pulse Width Modulation (PWM) in the DDA architecture is performed by a comparator amplifier as shown in Figure 2. An audio signal that has been modulated with a high-frequency local oscillator (Modulated Carrier, V_{MC}) is driven into the positive terminal of the comparator and sampled through a much-higher frequency sawtooth waveform (Reference, V_{REF}). The output of the comparator is low when the magnitude of the reference exceeds the baseband and high otherwise; hence resulting in the pulse-width modulation. For a given input level, the sawtooth frequency determines the frequency of the comparator's output [1] while the baseband frequency determines its duty cycle. Therefore, for an accurate signal reconstruction, the frequency of the reference waveform should be at least ten times that of the baseband [1].

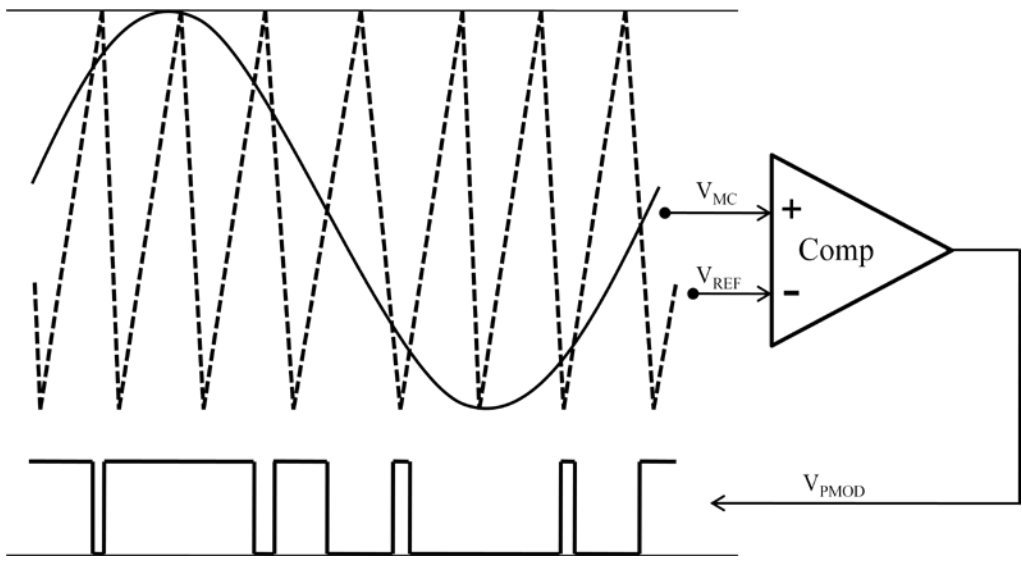


Figure 2. Pulse Width Modulation stage. *Glossary of terms* - Comp: Comparator

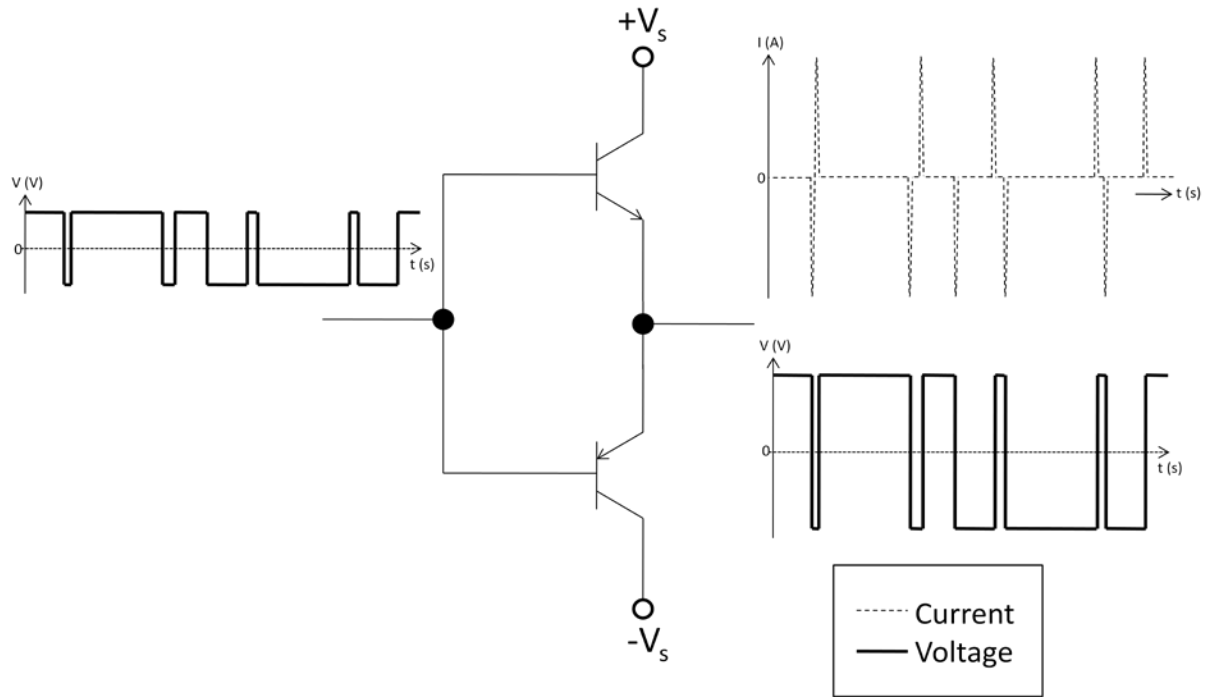


Figure 3. Class D amplifier switching amplifier stage.

2.2 Switching Transistor Network

The digitized version of the modulated carrier signal from the PWM stage discussed in the previous section is driven directly into a class D amplifier shown in Figure 3. The class D amplifier used in this study comprises of a pair of complimentary bipolar junction transistors driven either in cutoff or saturation. Therefore, the output is a copy of the input pulse train but at a higher current level, oscillating between the amplifier's rail voltages ($+V_S$ and $-V_S$). Furthermore, current spikes are generated only during the transition times of the voltage signal. The information contained in the modulated carrier signal and encoded in the separation of the current spikes is converted to analog by the antenna reactance, radiated and recovered at the receiver end. Because current flows to the antenna only in very short bursts, the power efficiency of the transmitter output stage may be increased.

2.3 Transmit and Receive Antenna Selection

This section covers both the dipole antenna used as a transmitter and a ferrite rod loop antenna used as a receiver. Geometrically small and portable radios require electrically small antennas. A half-wavelength dipole antenna at resonance was used for this study (see Figure 5). The electrical length was $\lambda/3300$ at 1MHz carrier frequency. Such dipole antennas can be represented by resonant RLC circuits [4], [5], [6], [7]. For example, [7] suggested that a dipole antenna can be represented with a four-element equivalent circuit in Figure 4. Calculation of the equivalent impedance seen looking in Figure 4 suggests a much higher capacitive component and a very small radiation resistance, which is expected in electrically small antennas.

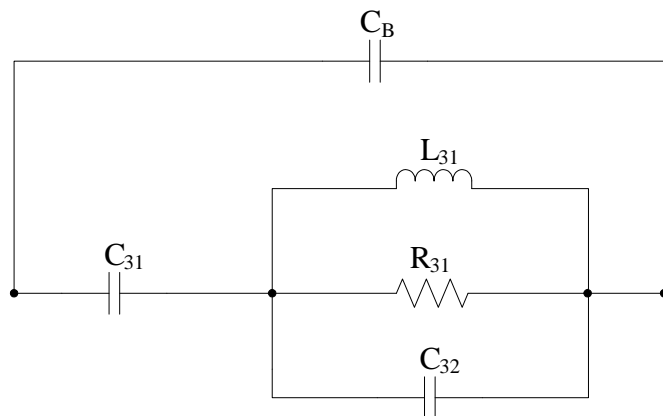


Figure 4. R-L-C representation of a Dipole Antenna. Adapted from [7].

Based on the equations provided in [7] and reproduced here for convenience, theoretical values of C₃₁, L₃₁, R₃₁, C₃₂ were calculated and are shown below.

$$C_{31} = \left\{ \frac{12.0674 h}{\log\left(\frac{2h}{c}\right) - 0.7245} \right\} pF \quad (1a)$$

$$C_{32} = 2h \left\{ \frac{0.89075}{[\log(2h/c)]^{0.8006} - 0.861} - 0.02541 \right\} pF \quad (1b)$$

$$L_{31} = 0.2h \{ [1.4813 \log(2h/c)]^{1.012} - 0.6188 \} \mu H \quad (1c)$$

$$R_{31} = \{ 0.41288 [\log(2h/c)]^2 + 7.40754 (2h/c)^{-0.02389} - 7.27408 \} k\Omega \quad (1d)$$

$$C_{31} = 0.5468 pF \quad (2a)$$

$$C_{32} = 0.115 pF \quad (2b)$$

$$L_{31} = 0.0179 \mu H \quad (2c)$$

$$R_{31} = 0.6952 k\Omega \quad (2d)$$

Analysis of the total impedance of the circuit in Figure 4 using the theoretical values of C₃₁, L₃₁, R₃₁, C₃₂ obtained in equations (2a)-(2d) suggests C₃₁ as dominant. Hence, L₃₁, R₃₁, C₃₂ can be ignored. The capacitance introduced by the balun is estimated as that of two concentric hollow cylinders 8cm in length and with 0.55cm radius and 0.17cm thickness, as calculated in equation (3).

$$C_B = \frac{2\pi\varepsilon_0}{\ln\left(\frac{a}{c}\right)} \cdot b = \frac{2\pi \cdot 8.854 \cdot 10^{-12}}{\ln\left(\frac{0.0055}{0.0017}\right)} \cdot 0.08 = 3.8 pF \quad (3)$$

For the receive antenna, we used a 470μH antenna. Therefore, a combination of both transmit (0.5468pF capacitor) and receive (470μH inductor) antennas constitutes a filter; albeit the first few harmonics are still permitted and a dedicated filter may be necessary based on the application environment.

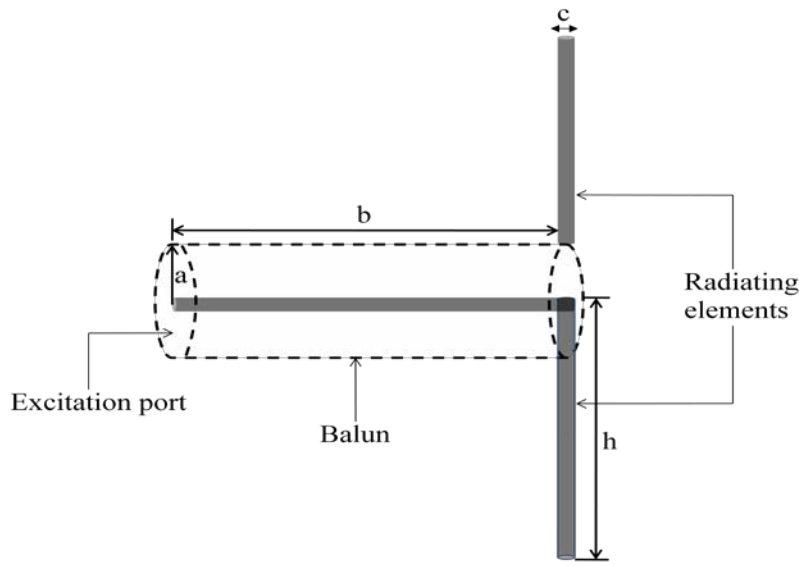


Figure 5. 3-D sketch of the Dipole Antenna used for this study. $h = 4.55\text{cm}$, $c = 0.17\text{cm}$, $a = 0.55\text{cm}$, $b = 8\text{cm}$. Radiating elements and balun are made of copper. SMA connector at the excitation port facilitates interfacing to circuit.

3. Measurement Setup

As indicated earlier, the goal of the work described in this report is to investigate potential efficiency improvement of the DDA over conventional transmitter architectures. Therefore, it is important that both architectures are kept identical except in the output stage, and that measurements are made under the same conditions. Figures 6 and 7 depict the two architectures. In both cases, an audio signal with bandwidth approximately 20 kHz is coupled from a music player in to an AM transmitter kit, manufactured by Ramsey Electronics, LLC. The transmitter circuit is optimized to produce an amplitude-modulated carrier sine wave at 570 kHz, 950 kHz and 1430/1440 kHz. A copy of the schematic has been provided in Figure 9 for reference purposes.

In the conventional AM transmitter circuit (upper half of Figure 8), the carrier-modulated sine wave is amplified with a low-power audio amplifier (LM386) commonly employed in commercially-available AM radios and transmitted to a low pass filter prior to propagation by the transmit dipole antenna. The low pass filter facilitates a further suppression of spurious content in the received frequency spectrum. A highly-inductive receive antenna ($470\mu\text{F}$) commonly in use in commercial AM radios was placed at a

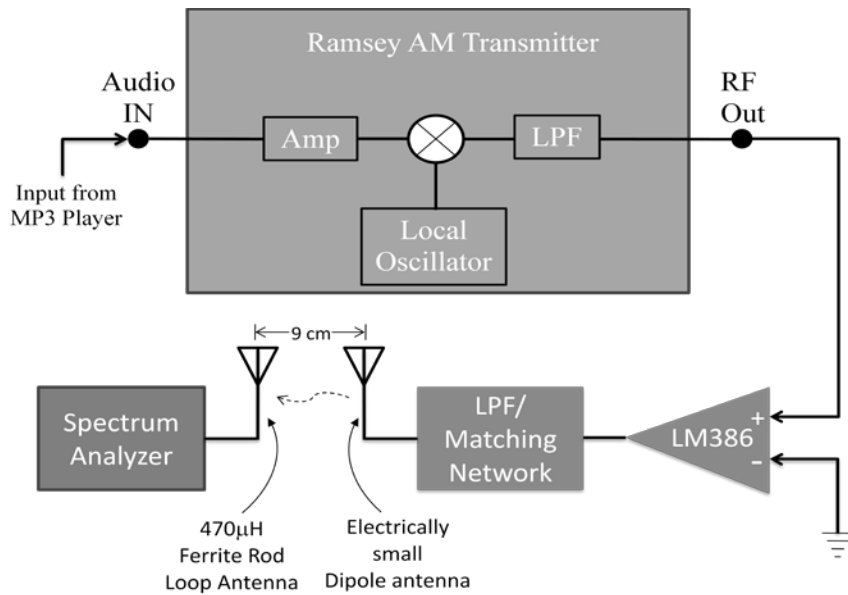


Figure 6. Measurement setup of the Conventional AM transmitter architecture. *Glossary of terms* – LPF: Low Pass Filter, Amp: Amplifier. Ramsey AM Transmitter refers to the AM1C AM transmitter kit produced by Ramsey Electronics.

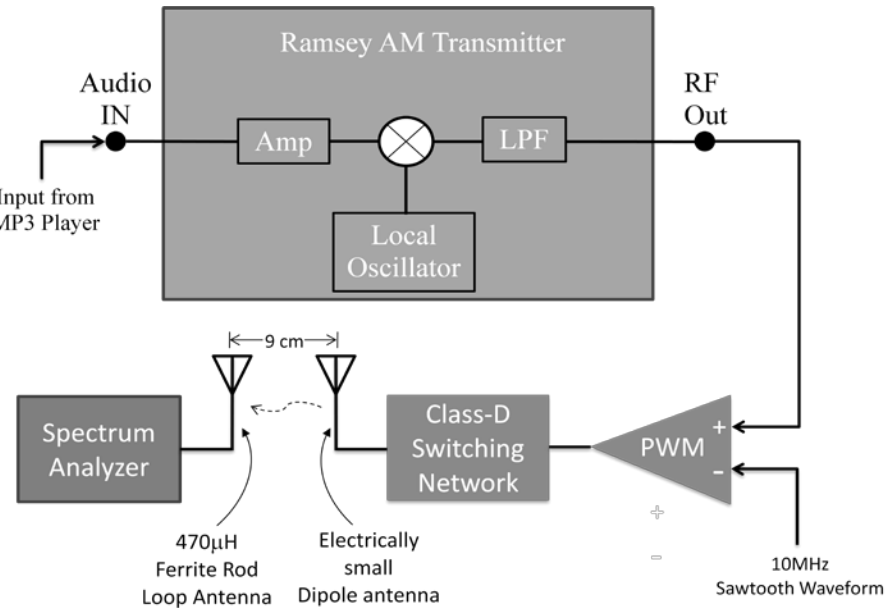


Figure 7. Measurement setup of the DDA AM transmitter architecture. *Glossary of terms* – LPF: Low Pass Filter, Amp: Amplifier. Ramsey AM Transmitter refers to the AM1C AM transmitter kit produced by Ramsey Electronics.

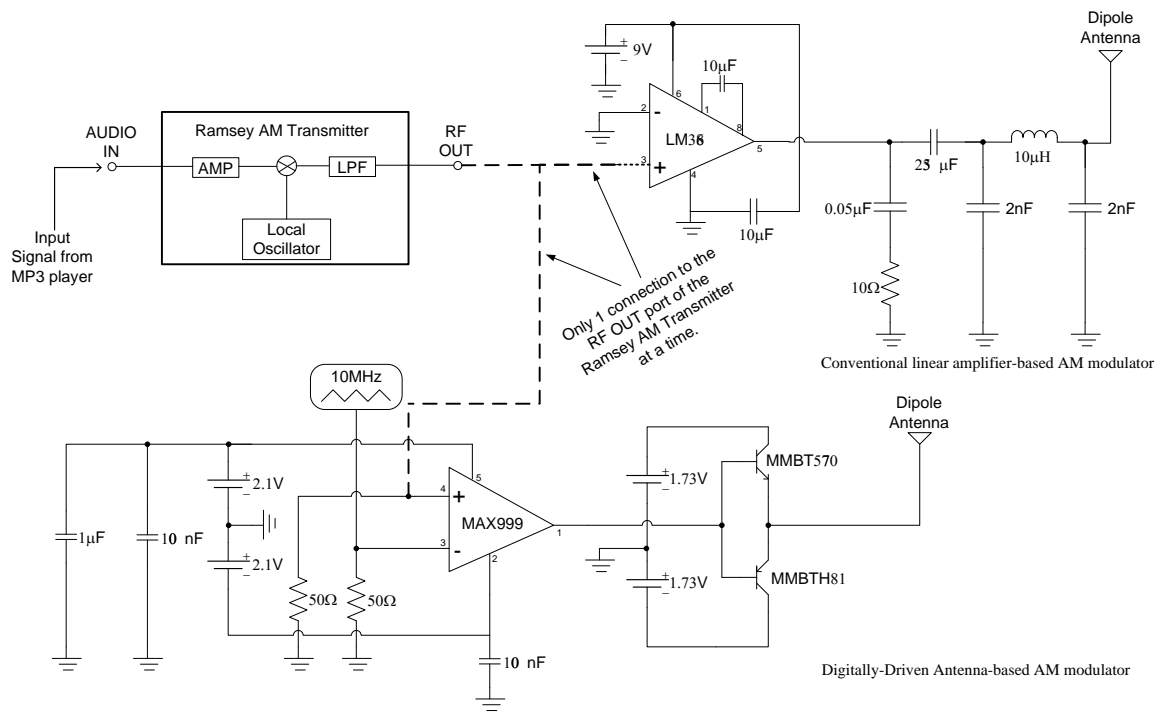


Figure 8. Schematic-level representation of Figures 6 and 7. Ramsey AM Transmitter refers to the AM1C AM transmitter kit produced by Ramsey Electronics.

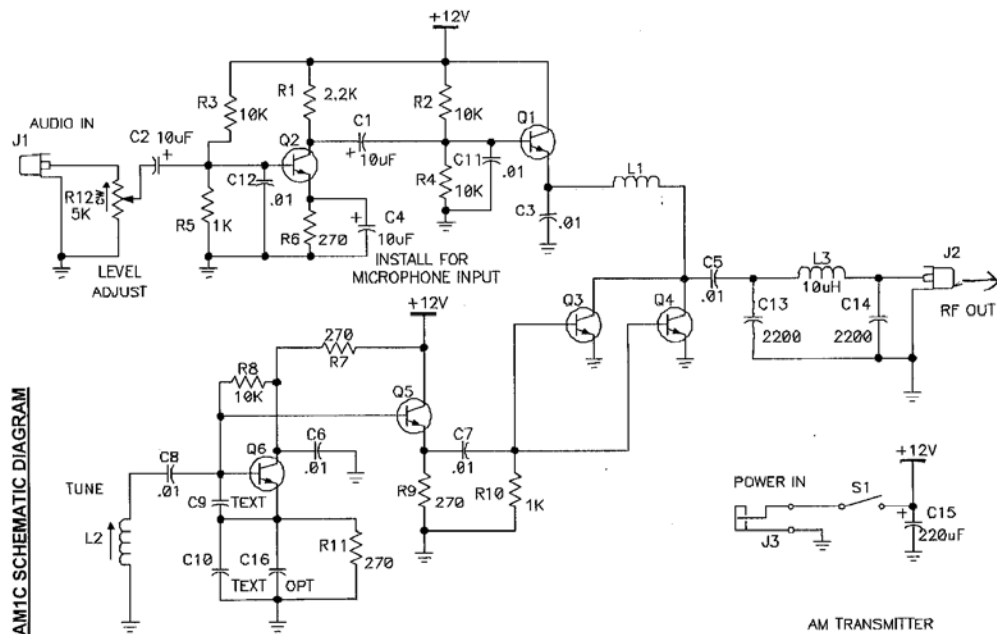


Figure 9. Schematic of the Ramsey AM Transmitter. Courtesy: Ramsey Electronics, LLC.

distance of 9cm for both transmit architectures. Following our report on the previous work presented at the 2009 Allerton Antenna Symposium, several structural changes were made to the test environment and circuits under test, in accordance with recommendations found in the ARRL Handbook [11], and feedback from the audience. To minimize the effect of electromagnetic interference from unwanted sources, circuit boards were enclosed in Diecast Aluminum enclosures, interconnects shortened, regular vector boards were substituted for prototyping boards, ground loops minimized, and potentially radiating cables and wires were isolated as much as possible. See Figure 10 for the laboratory setup.

The scope of the work described in this report was expanded to cover the entire AM frequency band. We decided to investigate potential efficiency gains (or losses) of the DDA architecture at the following frequencies: 570 kHz, 950 kHz, and 1430 kHz. The measurement results are discussed in the following section.

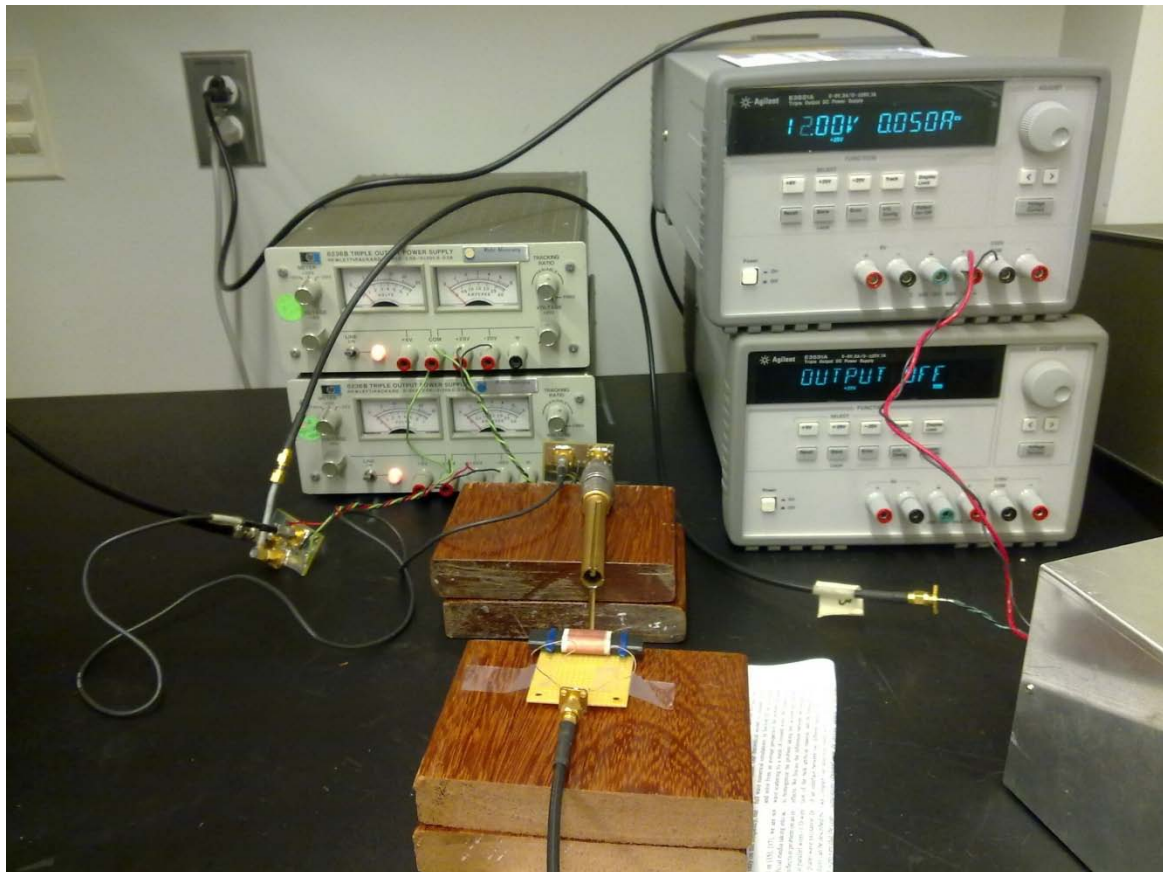


Figure 10. Laboratory Environment Setup

4. Results

To qualitatively compare the performance of the two AM transmitter architectures, the modulated 1MHz carrier signal was set to a given power level and the signal received on the portable tabletop AM radio receiver was tuned to the carrier frequency. The AM radio was gradually moved away from the dipole (transmit) antenna along the plane of the peak broadside radiation pattern. It is noteworthy to mention that both transmitters reproduced the signal from the music player in a clear, recognizable way although the DDA-based transmitter yielded a much higher-fidelity reproduction of the original signal despite the fact that the DDA architecture does not include an explicit filtering mechanism on the output. In addition, the broadcast signal still could be heard a few feet beyond where the signal produced by the conventional transmitter architecture became unintelligible. Given that the testing conditions for the two architectures were otherwise identical, the observation described above signifies that more of the modulated carrier signal power is radiated in the DDA case than in the conventional circuit case. Therefore, these qualitative observations strongly suggest that the DDA transmitter produces a more efficient coupling of the signal to the electrically-small transmit antenna.

To quantify the relative performance, the radiated frequency spectrum was measured at the receive antenna end placed at a distance of 9 cm using each architecture. The distance of 9 cm while arbitrary, is well in the far field region of the transmit antenna as estimated by Equation 4 [10] and also minimizes interference from the test equipment and active transmission lines. Under identical testing conditions outlined earlier, the power magnitudes in the received waveforms were measured at the following carrier frequencies: 570 kHz, 950 kHz, and \sim 1430 kHz, for both architectures (DDA and conventional AM transmitters). The results are summarized in Table 1. In each case, care was taken to ensure that the same amount of power, 1.2mW was delivered from the power supplies to the dipole transmit antenna. Therefore, the received power gains recorded for the DDA case were a function of the electronics in its architecture. Note: in Figure 16, the frequency scale was adjusted to observe the harmonics generated from the mixture of the carrier frequency and the frequency of the sawtooth wave (reference) waveform. As a result, the received power at 1440 kHz was recorded, instead of 1430 kHz. For each of the DDA measurements, the sawtooth wave frequency is always ten times the selected carrier frequency.

Carrier Frequency (kHz)	Transmit Architecture			
	Conventional AM		DDA	
	(dBm)	(pW)	(dBm)	(pW)
570	-89.331	1.167	-88.440	1.432
950	-91.866	0.651	-82.007	6.299
1430(Conv. AM) / 1440 (DDA)	-90.740	0.843	-87.563	1.753

Table 1: Summary of received power results

$$r_{ff} = \frac{2D^2}{\lambda} \quad (4)$$

Where r_{ff} is radial distance from the dipole antenna, D is the largest dimension of the antenna and λ is the smallest wavelength radiated.

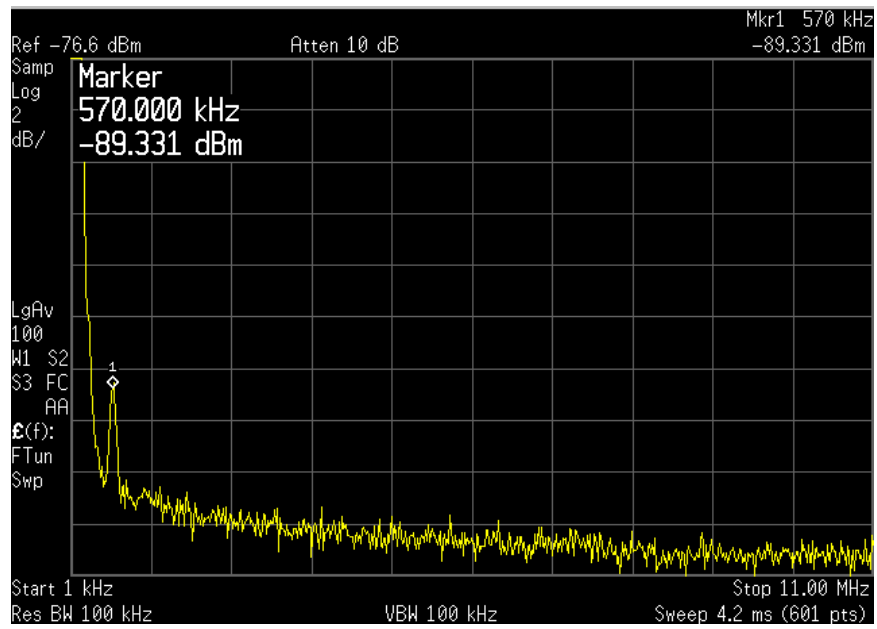


Figure 11. Radiated frequency spectrum observed at 9 cm from the transmit dipole antenna using the conventional AM circuit architecture at 570kHz

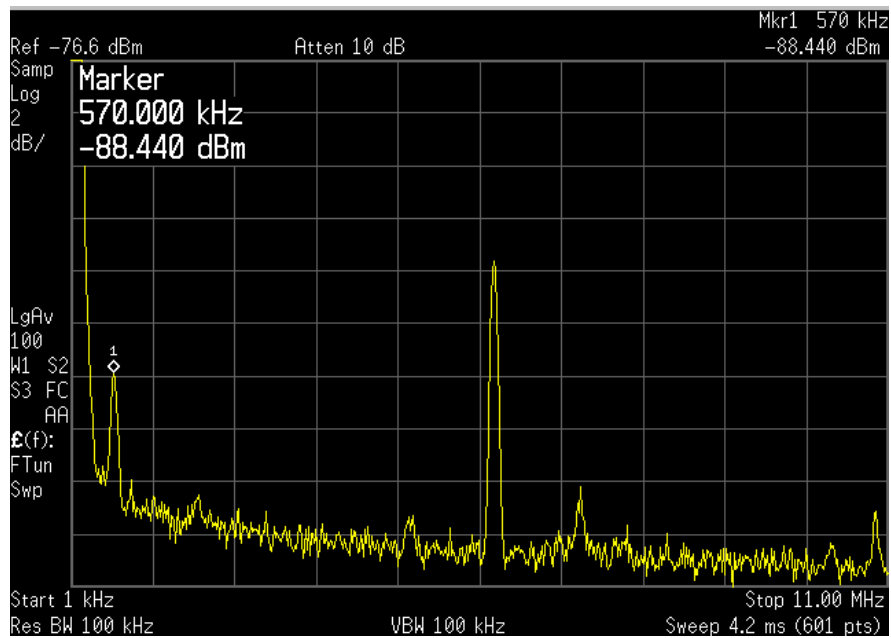


Figure 12. Radiated frequency spectrum observed at 9 cm from the transmit dipole antenna using the DDA architecture at 570kHz

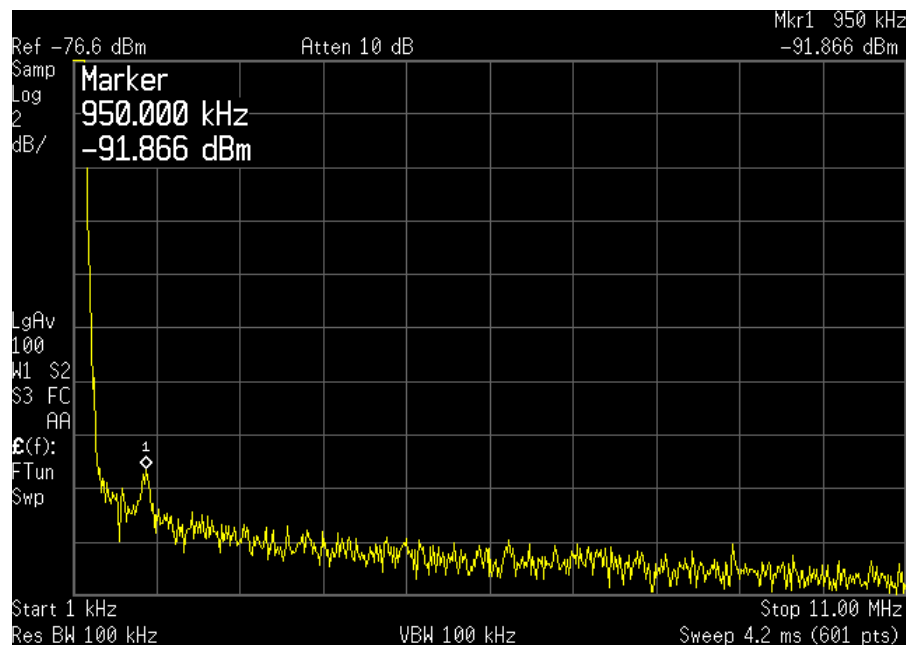


Figure 13. Radiated frequency spectrum observed at 9 cm from the transmit dipole antenna using the conventional AM circuit architecture at 950kHz

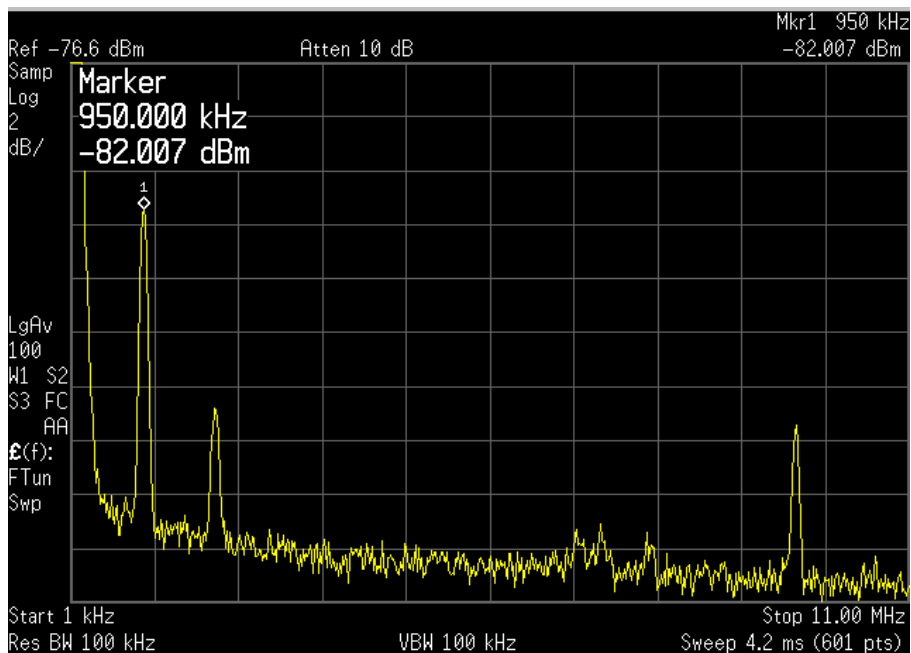


Figure 14. Radiated frequency spectrum observed at 9 cm from the transmit dipole antenna using the DDA circuit architecture at 950kHz

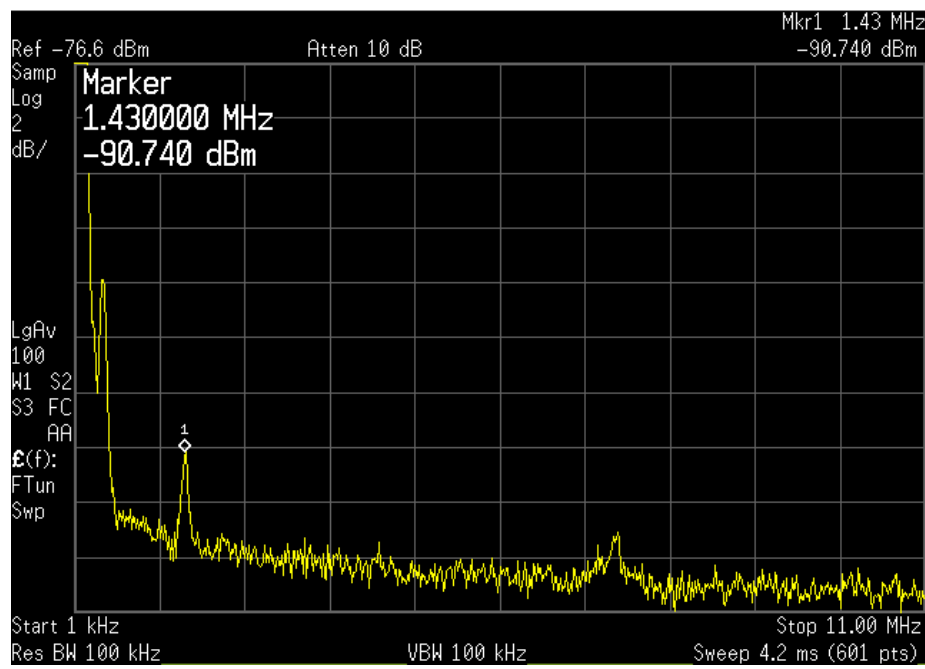


Figure 15. Radiated frequency spectrum observed at 9 cm from the transmit dipole antenna using the conventional AM circuit architecture at 1430kHz

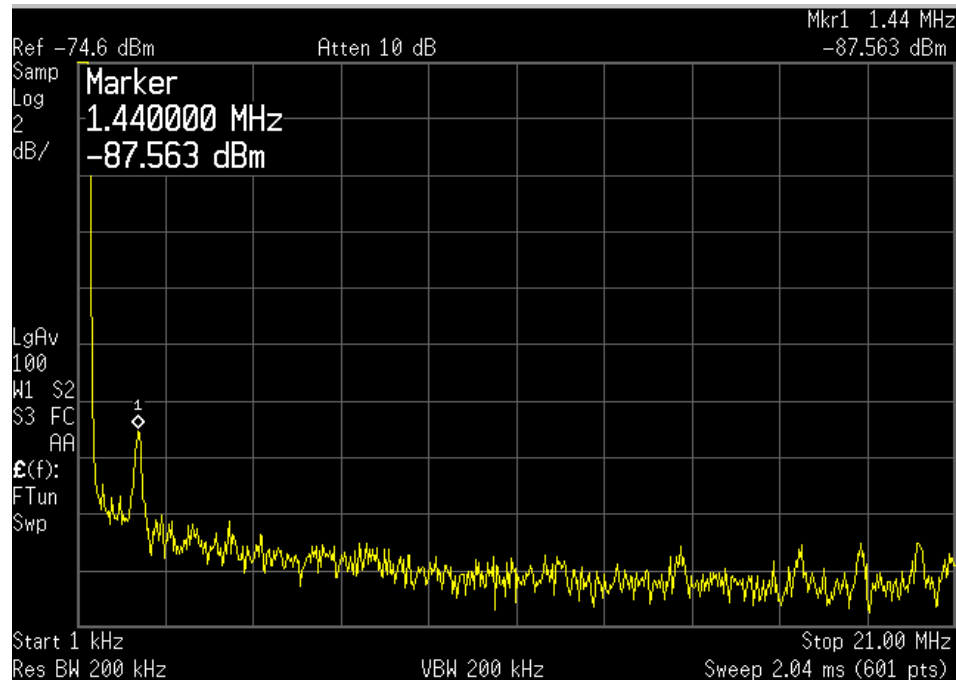


Figure 16. Radiated frequency spectrum observed at 9 cm from the transmit dipole antenna using the DDA circuit architecture at 1440kHz

5. Conclusion and Future Research

The potential for the DDA architecture to break the performance bounds of the traditional transmitter architecture make it an attractive research area for potential use in US Army ground mobile wireless communications. According to Table 1, the DDA architecture showed minimal gains at 570 kHz and 1430/1440 kHz, but a much higher gain (9.6X) at 950 kHz. Therefore, it can be concluded that the gain improvement realizable by the DDA technique is carrier-frequency dependent and is largest around 1 MHz. In addition, the results suggested that the DDA architecture produces more efficient coupling of the modulated carrier to an electrically-small transmit antenna. In cases where minimal improvements were recorded, the DDA is still the more versatile transmitter approach in that, the fundamental requirement for a matching circuit is bypassed. Many research questions remain, including analysis and control of the spectral content of the radiated signal, comparison of the relative efficiency, size, and cost of the DDA and conventional architectures, PWM clock rate and stability requirements as a function of modulation complexity, and the effect of the transmit antenna design on the filtering properties of the DDA architecture. The DDA architecture also introduces more fundamental questions, potentially requiring new definitions for standard antenna terms such as “match” and “near field” in the DDA context where the assumptions used in analysis of steady state operation no longer apply. The scope of the study described in this report is to be expanded to other digital modulation techniques and at other frequency regimes.

6. Acknowledgement

This work was supported in part by the US Army Research Laboratory and the US Army Research Office under Agreement Number W911NF-04-D-0001, Delivery Order 0003.

7. References

- [1] *Class D Audio Amplifiers Save Battery Life*, Maxim Integrated Products, Sunnyvale, CA, AN1760, 2002.
- [2] J.T. Merenda, “Synthesizer Radiating Systems and Methods,” U.S. Patent 5 402 133, March 28, 1995.
- [3] P. Muggler, W. Chen, C. Jones, P. Dagli, and N. Yadzi, “A Filter Free Class D Audio Amplifier with 86% Power Efficiency,” *IEEE Symposium on Circuits and Systems*, vol. 1, pp. 1036-1039, May 2004.

[4] R. G. Brown, R. A. Sharpe, W. L. Hughes and R. E. Post, *Lines, Waves, and Antennas*, New York: Wiley, 1973, pp. 339-346.

[5] H. Jasik, *Antenna Engineering Handbook*, New York: McGraw-Hill, 1961, pp. 2-11.

[6] R. W. P. King, *The Theory of Linear Antennas*, Cambridge: Harvard University Press, 1956, p. 176.

[7] T. G. Tang, Q. M. Tieng, and M. W. Gunn, “Equivalent circuit of a dipole antenna using frequency-independent lumped elements,” *IEEE Trans. Antennas and Propagation*, vol. 41, no. 1, pp. 100–103, January 1993.

[8] S. B. Wang, A. M. Niknejad, and R. W. Brodersen, “Modeling omnidirectional small antennas for uwb applications,” in *Conf. Rec. IEEE Antennas and Propagation International Symposium*, 2004.

[9] W.D. Palmer, W.T. Joines, and S.D. Keller. “Transmission of a 1 MHz Signal Using a Directly Driven Antenna System,” *Antenna Applications Symposium at Allerton*, Monticello IL, September 16-18, 2008.

[10] W. L. Stutzman, G. A. Thiele, *Antenna Theory and Design*, New York: John Wiley & Sons, Inc, 1998, p. 413.

[11] M. J. Wilson, *The ARRL Handbook for Radio Communications* (86th edition), ARRL – The National Association for Amateur Radio, 2009.

DEVELOPMENT OF CONFORMAL SPACE SUIT ANTENNAS FOR ENHANCED EVA COMMUNICATIONS AND WEARABLE COMPUTER APPLICATIONS

T. G. Campbell, Christian W. Hearn, and C. J. Reddy

Applied EM, Inc., 144 Research Drive, Hampton, VA 23666

Robert C. Boyd

Unitech, LLC, 228-B Patterson Avenue, Hampton, VA 23669

Taeyoung Yang and W. A. Davis

Virginia Polytechnic Institute and State University, Blacksburg, VA

Adam Persans and Stephen Scarborough

ILC Dover, Inc., One Moonwalker Road, Frederica, DE 19946-2080

ABSTRACT

As NASA plans future space missions, it is anticipated that astronauts will always conduct space walks (or Extra Vehicular Activities (EVA)) and be more exposed to the hazards of EVA operations. Providing reliable communications is imperative during all space missions and especially during servicing missions for the International Space Station (ISS). Communications during EVA relays progress and the health and ability of the astronaut to perform in hazardous environments. Therefore, in order to improve communications between the astronaut and ISS and ground tracking stations as well as to improve the astronaut's mobility in space, Applied EM, Inc. has developed new conformal, flexible, body-worn antenna designs that can be integrated into the current EMU space suit configurations. The new space suit antenna designs have been simulated and RF tested in full EMU suit configurations. Test results demonstrate improved performance over the current UHF antenna used during EVA operations. In addition, the new antenna designs enable multi-frequency capabilities that could support wireless bio-med telemetry for wearable computer applications during space operations. The results of this research contributes to NASA's efforts to develop new space suit designs which will improve the astronaut's mobility, efficiency, and safety during long periods of EVA operations.

1.0 *Introduction*

As NASA prepares for future manned and unmanned space explorations, Extra-Vehicular Activities (EVA) by the astronauts will be required and there will be more time exposed to the hazards of EVA operations. EVA's can be characterized as planned, unplanned, contingency or unexpected for crew safety. Complex EVA's require both specialized tools and extended duration or unrestrained translations. Providing reliable communications is imperative during

current EMU/ISS operations as well as future space exploration missions. Voice communications, telemetry, and bio-med data using wireless links during EVA relays progress as well as monitoring the health and ability of the astronaut while in hazardous environments.

The antenna system currently used during EVA operations, shown in Figure 1, is located on top of the Primary Life Support System (PLSS). In order to improve space to space communications and information transfer during EVA operations, Applied EM has been sponsored by a NASA SBIR [1] project to develop conformal, body-wearable antennas that are integrated into space suits to improve communications and will enable wearable computer networks. A body-worn, conformal antenna has been designed to overcome the communications limitations imposed previously on astronauts during EVA space operations. The new antenna designs use flexible polymer substrate materials and highly conductive coatings that were developed during Applied EM's Conformal Antenna Materials Technology program sponsored by the Air Force Research Laboratory (Hanscom) [2]. During this research program, polymer antenna coatings were developed using patented dielectric and conductive Unishield [3] coatings developed by Unitech, LLC. Applied EM's team for developing new space suit antennas included Unitech, LLC, Virginia Tech, ILC-Dover, and Hamilton-Sundstrand.

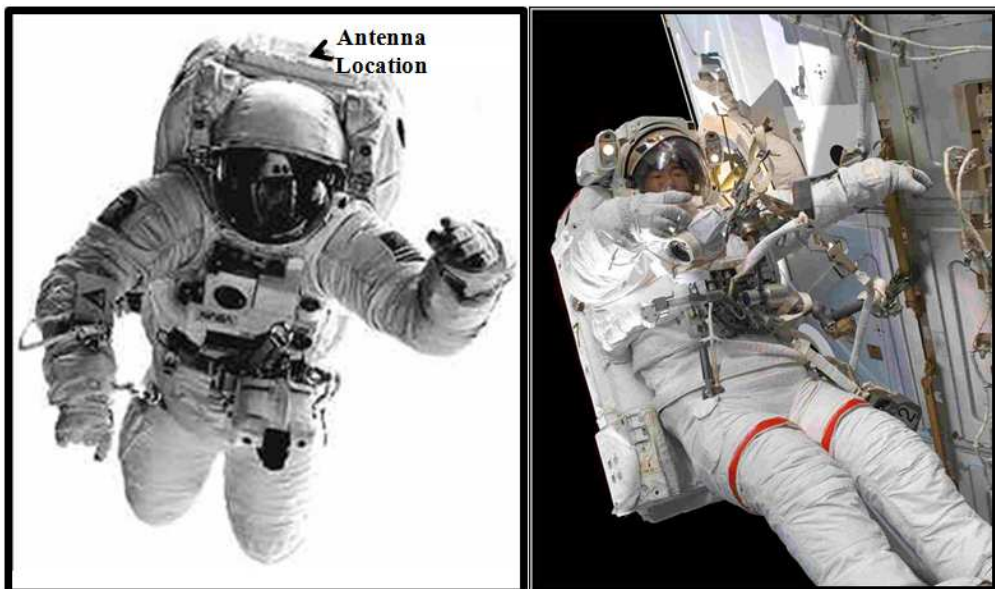


Figure 1 – Photographs of astronaut during EVA and with EMU and tool belt.

In particular, highly flexible, low-mass, advanced spacesuit antennas are needed for future space explorations as well as new space suit designs. Therefore, Applied EM has developed and demonstrated conformal, flexible, body-worn antenna designs for multi-frequency operations. The new, flexible antenna designs can be integrated into the upper torso region of the space suit or in the outer cover materials or on the Primary Life Support System (PLSS). The capability for multi-frequency antenna design enables wireless bio-med telemetry for wearable computer

applications during space operations. In addition, computational electromagnetic modeling of space suit was developed that was used to simulate the integration of the antenna into the suit and to predict the spherical radiation coverage of the antenna at different locations as well as during animated space operations. This research not only provides innovative antenna concepts for new space suits, but it also responds to NASA's need for advanced antenna concepts that can be used in different applications such as planetary surface vehicles, habitats, and robotic missions; all requiring good communications.

2.0 Research Requirements

The antenna research requirements for the conformal antenna research program are based on referenced NASA documents [4] and the performance requirements for the current UHF (413-418 MHz) communications antenna. The research requirements were prepared and documented and they were used to guide the engineering tasks especially in regard to the selection of space qualified materials, and environmental qualification and acceptance test procedures. The electrical specifications for the current antenna were reviewed especially in regard to operating frequency (415 MHz), VSWR, gain, spherical coverage, size, weight, integration, and test methods. For reference purposes, the basic operational specifications for the current UHF EVA communications antenna are summarized in table 1.

Table 1 – Specifications for Current UHF Communications Antenna for EVA

Topic	Specification	Comment
Operating Frequency	414.2 MHz, primary 417.1 MHz, back-up	
Gain, Spherical Coverage	90% coverage @ -15.8 dBi	See discussion below
Impedance/VSWR	50 ohms, 2.0 (413-418 MHz)	
Dimensions	10.23in. x 3.5in. x 0.75in.	Excluding SMA connector
Antenna Weight	1.5 lbs.	
Kick-Load Impact	125 lbs.	Force over 0.50-inch circular area, 2-ft. per sec. impact without loss of performance.
Temperature	+ 170° F to - 65°F; VSWR 6.0 allowed	
Shock/Acceleration	20 g peak, 11 milliseconds +/- 5g's, 5 minutes	20 g landing emergency landing impact
Antenna Mounting	Velcro strips	
Power Handling	2.0 watts	
Shelf Life	25 years; 10 yr. lifetime	Certified for 50 missions

The antenna gain required for EVA operations is at least 90% spherical coverage at a gain of -15.8 dBi. The radiation distribution data for the current EVA antenna qualification unit was

obtained during RF tests using on a full scale “astronaut” model which resulted in 91.9% spherical coverage at -14 dBi, and 99.4% at -20 dBi.

Space qualified materials are required and conformal, flexible antennas must satisfy the electrical requirements as well as the environmental requirements for space mission applications. ILC-Dover and Unitech, LLC supported Applied EM, Inc. on all materials selected for the conformal antenna as well as assurances that selected antenna materials are space qualified and would satisfy the environmental specifications for space applications. These environmental specifications include temperature, vibration, shock, kick-load, and humidity. Due to resource limitations, environmental tests could not be conducted to demonstrate compliance with NASA acceptance criteria with the exception of the kick-load force impact test. Since the conformal body-worn antenna consists of a flexible substrate material with coaxial cable connections, it was imperative that this kick-load test be conducted to prove that the antenna can withstand rough handling during space operations.

Current Antenna Space Suit Integration

The initial challenge in the design of new space suit antennas was regarding the complexity of the suit garment and the number of layers involved that could affect antenna design and integration. These layers include outside pressurized layers that are between outer Thermal Micro Meteoroid Garment (TMG) layer (Ortho-Fabric) and scrim reinforced aluminized Mylar plies. Figure 2 shows a photograph of the multiple layers used in the current space suit.

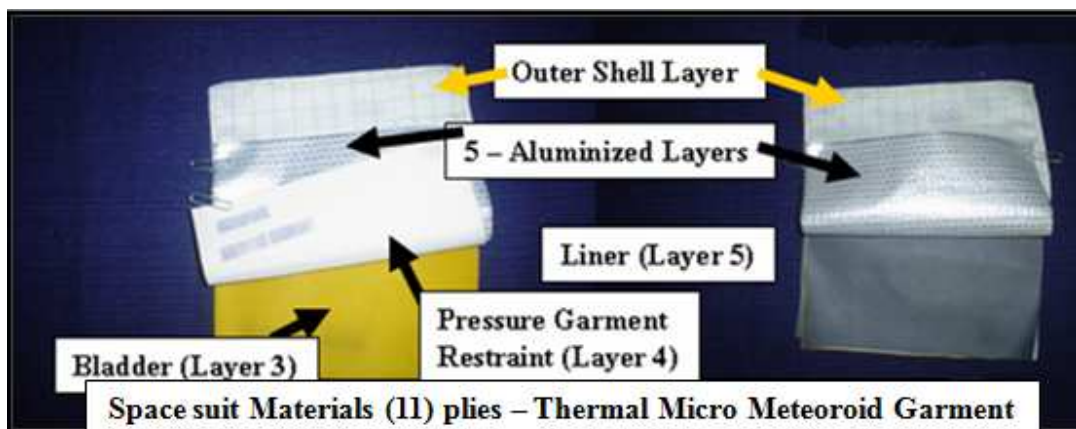


Figure 2 – Multiple material layers used in the current space suits.

The current EVA antenna is integrated into the space suit as shown in Figure 3 and the attachment method uses elastomeric materials, Nomex pads, Velcro hook and pile attachment methods. The white TMG garment shell covers the entire assembly. Since these materials are currently being used (and space qualified), they were considered candidate materials for new antenna designs but using conformal “paint-on” antenna techniques. The current antenna is mounted on padding by way of Velcro hook and loop fasteners and is essentially insulated from

the aluminized Mylar layers of the PLSS TMG. The antenna is connector to the EVA UHF radio which is located directly beneath the antenna by a coaxial cable with SMA connectors.

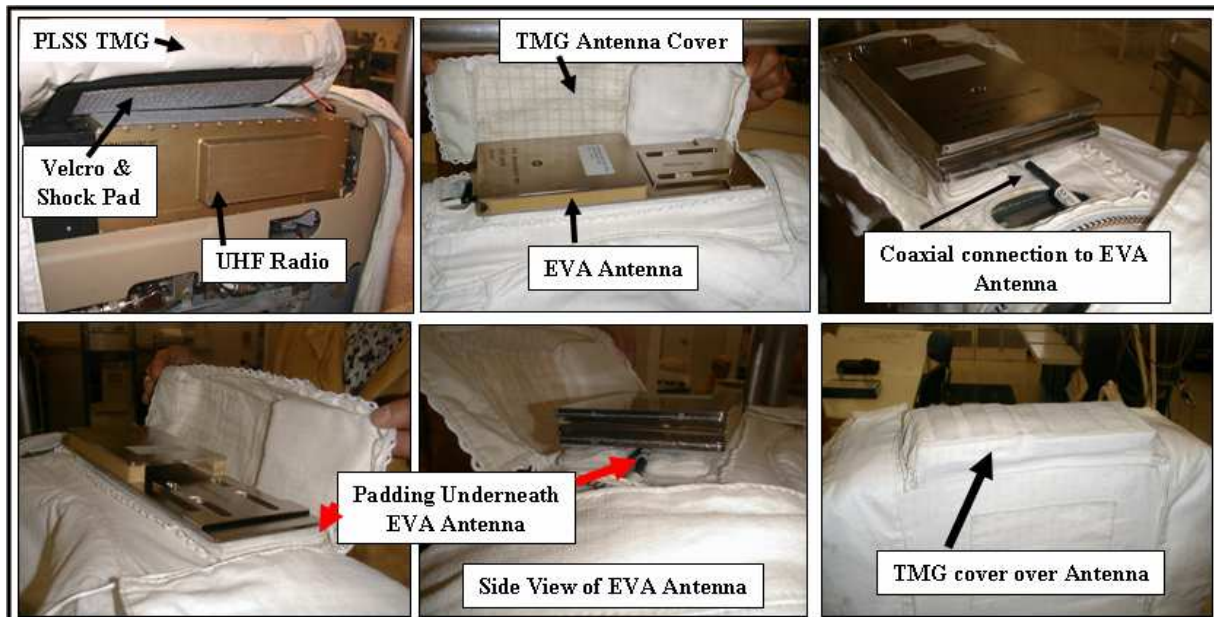


Figure 3 – Photographs of the installation and RF coaxial connection for the existing UHF antenna to the radio installed on the PLSS.

Since the current antenna is located on top of the PLSS, this location was selected as well for performance comparison purposes.

3.0 Antenna Design Trade Study

Since the objective of this research is to design new flexible and conformal antennas, a design trade study was conducted to determine the best approach for space suit applications. Three antenna concepts were down selected since they exhibited the potential for conformal design applications. These concepts are (1) fundamental bow tie and (2) planar inverted F-antenna (PIFA). These design configurations are presented in Figure 4 and they could be designed for space suit applications, particularly thin and flexible designs.

Reference [5] describes conventional microstrip elements constructed with e-textiles. It was concluded that e-textile antenna designs for higher frequency microstrip antennas are indeed feasible, but this approach was not selected for UHF (415 MHz) space suit designs because they would be larger and more difficult to position antennas sewn at fixed locations in the suit. Therefore, the new UHF antenna design will require the use of elastomeric flexible substrate materials with conformal conductive coatings as well as ways to co-locate multiple antenna elements at a single location on the space suit.



(a) Bow tie element

(b) PIFA element

Figure 4 – Preliminary antenna design concepts selected for EM analysis.

Bow Tie Element Analysis and Simulations

Since the operating wavelength in free space for the UHF antenna design is 28.4-inches (72.1 cm), the PLSS dimensions (30.5-in. x 23.0-in. x 7.0) are equivalent to the operating wavelength. Therefore, this geometry has a direct effect on the radiation pattern of an antenna attached to it. Depending upon the type of antenna chosen, the PLSS configuration and subsequently the astronaut space suit (which is assumed to electrically conducting) will affect the impedance and the radiation patterns of the antenna. Since the TMG covering materials include aluminized mylar thermal layers, it was initially assumed that the PLSS geometry forms a conducting ground plane for the antenna elements. Omni-directional pattern coverage is achieved using the vector sum of vertical and horizontal polarizations.

A bow tie antenna (21-in. x 6-in.) was positioned 0.20-wavelength (approximately 1.4-inch) over the PLSS simulated configuration to investigate the radiation patterns and interactions with the finite (PLSS) ground plane. Radiation patterns (shown in Figure 5) were calculated using a FEKO EM model of the antenna elements indicated that omni-directional patterns can be achieved about the PLSS geometry configuration. But, coupling to the PLSS geometry indicated that two dominant frequencies occurred with the antenna in that position; essentially a fundamental and harmonic frequencies at 415 MHz and 287 MHz respectively.

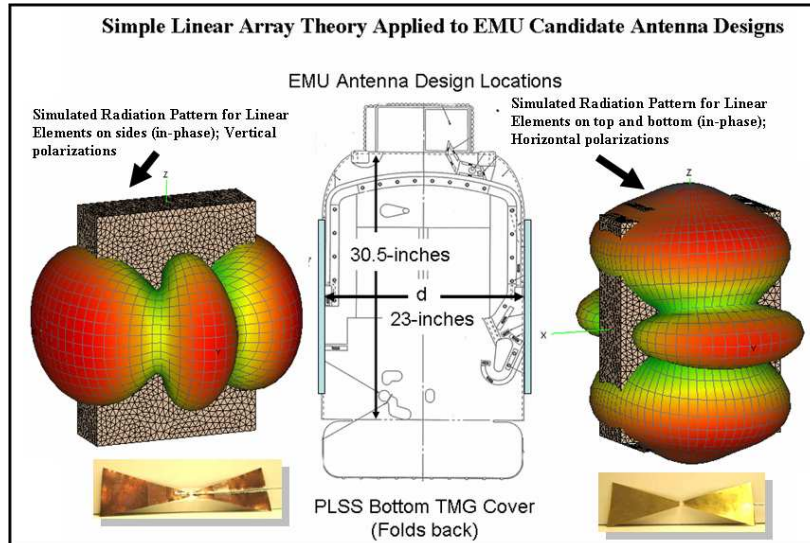


Figure 5 – Preliminary radiation patterns analyzed using bow tie elements on four panels of the PLSS geometry (assuming conductive surfaces).

After achieving a reasonable impedance match at 415 MHz (and with a corresponding match at 287 MHz), radiation patterns were calculated at both frequencies to determine the effect of the PLSS geometry. These results are presented in Figures 6(a) and 6(b). The coupling effects observed at 415 and 287 MHz respectively are caused by the (simulated) PLSS “scattering edges.” The electrical length from the top bow tie element (feedpoint) to the bottom scattering edges of the PLSS is approximately 1.0λ at 287.0 MHz and 1.5λ at 415 MHz. These distances cause the pattern reflections to be in phase at 287 MHz and out of phase at 415 MHz which causes the radiation patterns to be reversed as the electrical distance (in wavelengths for each frequency) are multiples of 0.5-wavelengths from the bow tie element to scattering edges of the PLSS.

These simulation results emphasized that coupling to the PLSS (and to the space suit) must be reduced to the fullest extent so that variations in the space suit configurations and on-orbit operations would not grossly affect the radiation pattern performance of the antenna system. This is especially important because the space suit consists of multiple layers of aluminized Mylar that shields the astronaut from UV and cosmic radiation. The PLSS covering materials could serve as “ground planes” for the conformal antenna elements integrated in the space suit system.

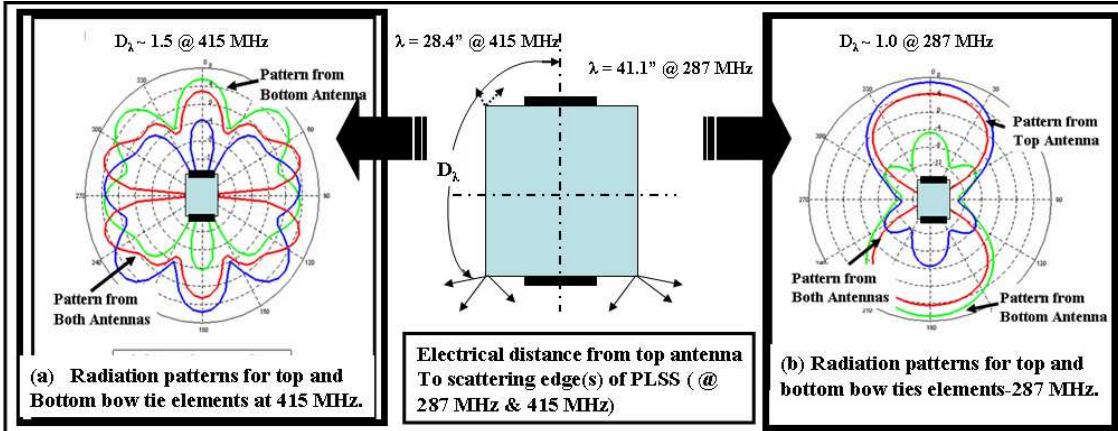


Figure 6 – Results of EM simulations of fundamental bow tie antenna elements for impedance matched conditions and resulting radiation patterns on the PLSS.

To further demonstrate the extended PLSS ‘ground plane’ effect, additional EM simulations were conducted with the low profile bow tie positioned on the long side of the PLSS. All dimensions and impedance loading parameters were identical to the previous case but with the element on the top and bottom of the PLSS. The results are presented in Figure 7 and using the same explanation as before, the electrical distance to the opposite scattering edges is effectively less than 1.5λ ; so, the resulting peak amplitude of the pattern is off the same side as the element.

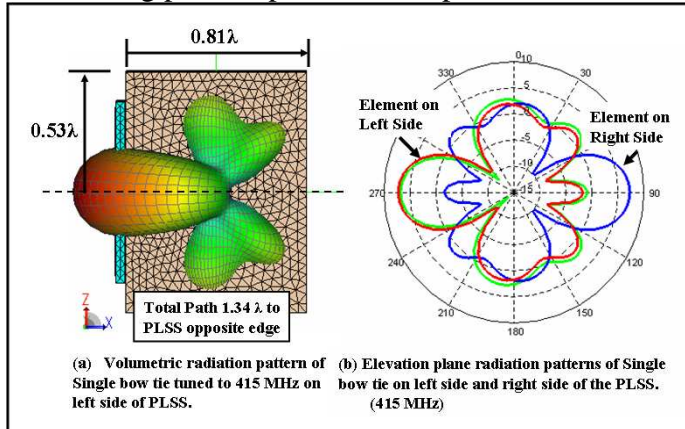


Figure 7 – Radiation patterns for the case when the low profile bow tie is positioned on the long side of the PLSS extended ground plane.

To briefly summarize, the initial low profile bow tie simulations demonstrated the following pattern interaction effects with the PLSS geometry:

- The fundamental resonant frequency of the antenna element design must operate at 415 MHz in order to optimize electrical performance.
- Coupling effects of the antenna with the PLSS and other parts of the space suit system must be considered.
- The Conformal EVA Antenna design must be integrated with the PLSS and other space

suit systems and exhibit minimal coupling effects due to the proximity of the PLSS and Astronaut “attachments.”

Planar Inverted ‘F’ Antenna (PIFA)

In addition to improving the UHF communications during EVA, developing a multi-function antenna capability would also be desired that could operate at several frequencies including wireless (ISM) communications (2.4 GHz.). A planar inverted ‘F’ antenna (PIFA) was designed by Cummings [5] (Virginia Tech Antenna Group) and this concept demonstrated how two antennas could be integrated for GPS and Cellular operations respectively. Hence, this concept was a hybrid design that consisted of two collocated antennas operating at two different bands. Based on the merits of this design, this concept was selected for the space suit design because it embodied the potential for a conformal, flexible “body worn” antenna design and also the optional capability to include ISM wireless antenna elements. A sketch of the Cummings low profile antenna concept is presented in Figure 8. In order to evaluate the PIFA design concept to this application, EM simulations were conducted by altering the dimensions, the substrate, and feed line designs to make it compatible for conformal ‘body-worn’ applications.

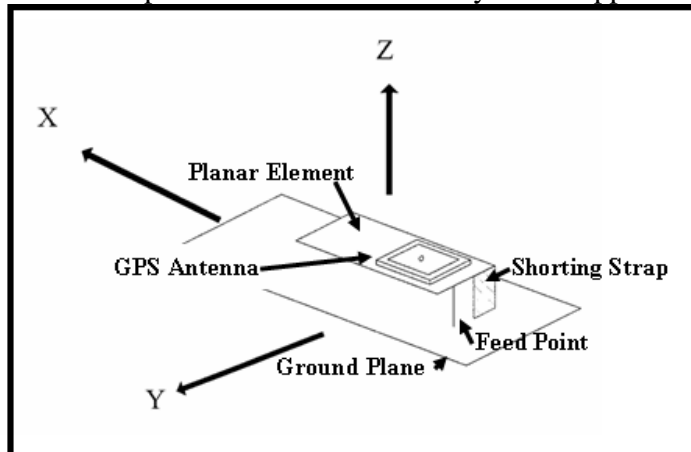


Figure 8 – Low profile integrated GPS and Cellular Telephone Antenna design configuration.

4.0 PIFA Space Suit Antenna Designs

Since the PIFA design concept was selected for the space suit antenna development, detailed EM simulations and design optimization tasks were initiated by the Virginia Tech Antenna Group and these details are discussed by Yang et al in reference [7]. Therefore, this report discusses some of the engineering development tasks associated with the PIFA antenna and less on the design optimization. As described by Yang, two PIFA antennas were designed, narrow band and wide bandwidth configurations since it was deemed important that design options are available depending upon the performance results during space suit integration and the subsequent antenna tolerances to detuning effects. For reference purposes, the basic (narrow bandwidth) PIFA configuration for UHF operations is shown in Figure 9 and the design parameters are listed in

table 2. Yang used a genetic algorithm and the commercial electromagnetic simulation code (FEKO, [8]) in all of the simulations. The structure was optimized at 415 MHz as a function of substrate thickness (H , see table 2).

The fractional bandwidth becomes larger as the substrate height increases and/or dielectric loss increases, which is predicted by the fundamental-limit theory [9]. At the same time, the gain decreases as substrate height decreases and/or dielectric loss increases. Thus, antenna size (height), bandwidth, and gain (or efficiency) are trade-offs. Parametric study plots were used to select a substrate thickness and a dielectric loss range to meet the given performance specifications. Since the antenna must be conformal and flexible, the thickness of the antenna was selected to be approximately 0.5692" ($H / \lambda_0 = 0.020$) which was based on previous flexure tests using elastomer substrate materials. All other dimensions were optimized accordingly as described by Yang.

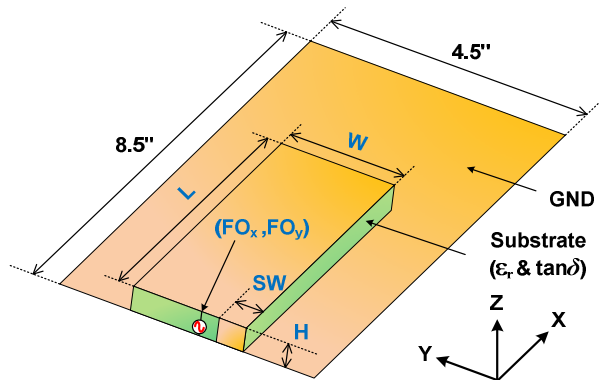


Figure 9 - Geometry and parameters of the PIFA used for parametric study.

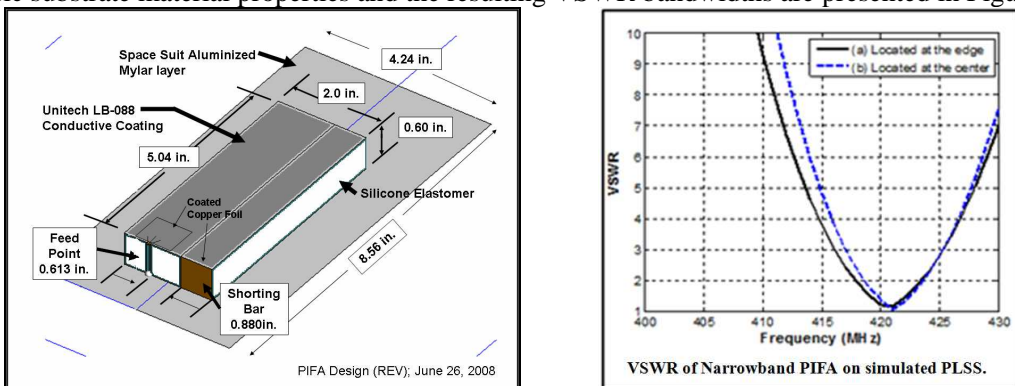
Table 2 - Optimization parameters and their descriptions

Parameters	Description
L	Strip length of PIFA
W	Strip width of PIFA
H	Substrate height
SW	Shorting strip width
FO_x	Position of Feed offset in x-direction (set to zero)
FO_y	Position of Feed offset in y-direction
ε_r	Dielectric constant of substrate material
tanδ	Loss tangent of substrate material

$H / \lambda_0 @ 415 \text{ MHz}$	Physical dimension
0.005	0.1423"
0.010	0.2846"
0.015	0.4269"
0.020	0.5692"
0.025	0.7115"

Parameters	Assigned Value
L	5.51"
W	2.15"
SW	0.65"
H	0.7115" ($H / \lambda_0 @ 415 \text{ MHz} = 0.025$)
ϵ_r	2.5
$\tan\delta$	0.006

The EM performance of the PIFA antenna design shown in Figure 10(a) was simulated using assumed dielectric substrate material properties and the resulting VSWR bandwidths are presented in Figure 10(b).



(a) – PIFA point design configuration.

(b) – VSWR for PIFA design.

Figure 10 – Antenna “point design” selected during Phase-I for the conformal space suit antenna design application.

Since the optimization results discussed by Yang [6] indicated the need for additional resiliency to lateral and longitudinal deformations, a wider bandwidth antenna was designed to reduce detuning effects caused by flexing the antenna in the space suit. The wide bandwidth PIFA design configuration and parameters are presented in Figure 11 and table 3 respectively.

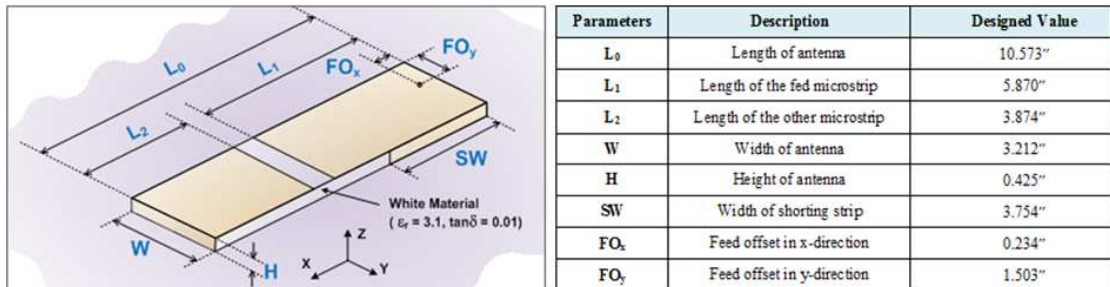


Figure 11 – Wide bandwidth PIFA configuration. Table 3 – Design parameters for WB PIFA.

The VSWR and bandwidth characteristics for the wide bandwidth PIFA design are presented in Figure 12 and can be compared to the narrow bandwidth PIFA (note Figure 10(b)).

The corresponding bandwidths (at VSWR = 2.0) for the narrowband and wideband PIFA's are 1.2% and 4.8% respectively. Since the overall space suit antenna performance must be evaluated based on numerous factors such as; spherical gain coverage, impedance, bandwidth, and detuning effects, etc., it was decided to develop, test, and evaluate both antennas for possible use in the space suit.

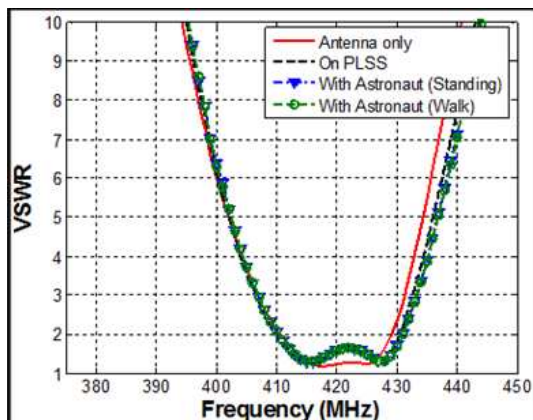


Figure 12 – VSWB characteristics of the wide bandwidth PIFA design for space suit applications.

5.0 Antenna Materials Development

Dielectric Substrate Material Selection

Flexible dielectric and conductive materials were developed that could be used in the design of the conformal “paint-on” UHF antenna. It was also necessary to characterize the RF properties of the space suit materials such as the TMG garment fabric material for possible interactions with the antenna. The TMG material was measured and it was found that it exhibits low (<1dB) RF loss characteristics (at these frequencies of interest). Experiments were also conducted with

TMG material using Unishield 12447 highly flexible and conductive coatings that can form antenna circuits. In addition, ILC-Dover provided a list of (space qualified) fabrics that could be considered for a “fabric laminated” antenna design concepts as well. It was concluded that Unishield 12447 could adhere properly to TMG to form an antenna if desired, but, this was not pursued.

Two candidate foam materials were considered for the dielectric core for the PIFA antenna. These candidates were Poron polyurethane elastomer foam and the Bisco silicone elastomer foam. Both foams had desirable electronic properties and thereby useful for fabricating the PIFA design antenna. But, another fabrication issue was confronted using the foams in that the flexible conductive coating exhibited poor adhesion qualities with the silicone elastomer foam. This issue led to another investigation involving the use of metalized fabrics to possibly replace the conductive coating as the conductive surfaces for the PIFA antenna. Woven and non-woven Nickel/Copper Polyester fabrics are highly conductive metals and provide excellent surface conductivity, and corrosion resistance. The approach was to laminate the conductive fabric to the silicone elastomer foam and then solder the coaxial feed line directly to the material. But, it was determined that this combination of the fabric over foam would de-laminate during impact; so, this approach failed initial testing.

Therefore, a more durable substrate material was required for the center core of the PIFA antenna. Silicone rubber elastomers such as room temperature vulcanized (RTV) silicone rubber instead of foams were investigated. They were found to be compatible with the conductive coating applications and are pourable rubber bases that become firm, flexible silicone rubber when cured. The cured rubbers exhibit good dielectric properties and various combinations of base and catalyst allow a wide range of working times and curing rates that can satisfy most potting, coating and mold making needs.

Following the selection of the RTV silicone rubber materials, it was necessary that the dielectric constant and loss tangent RF properties were measured and characterized for antenna design applications. In addition, a conductive coating is also required for the antenna design, and a brief summary of tests regarding the conductivity of this flexible coating is discussed as well.

Dielectric Material Properties

The dielectric properties of the RTV substrate materials were determined using the airline network analyzer setup shown in Figure 13. RTV dielectric specimens were formed to be inserted into the airline with an inside diameter of 3mm, an outside diameter of 7mm and a thickness of 0.60 mils. Later, it was determined that the dielectric test specimens should be in the range of 1.0 inches in thickness to improve the accuracy of the measurement. A casting technique was used to form a tube with extending the length to 1 inch with the outside diameter of 7mm. The tube mold was fitted with a 3mm center pin to form the center hole for the specimens. The RTV silicone liquid was cast into the molds and allowed to cure, then demolded. It was found that casting these tubes was again very difficult to keep consistent shape throughout

the entire length. In the measurement of the 1 inch specimens, the fit of the specimen was suspect and there were some questions as to the validity of the measurement.



Figure 13 – Network analyzer and airline coax for measuring the dielectric properties of material specimens.

It was then determined that to get an exact fit, the RTV silicone material (3110) would have to be cast directly into the airline test fixture with the center pin in place. This would insure a perfect fit inside the tube and around the center pin. Figure 14 shows the specimen of the RTV silicone material produced from casting in the air line test fixture.

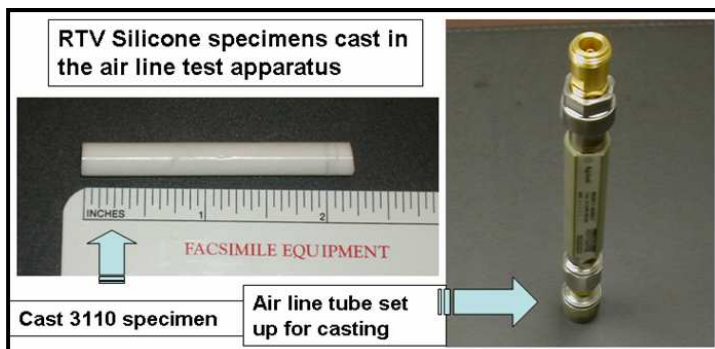


Figure 14 - Casting of the RTV Silicone 3110 in the Air Line Test Specimen

The RTV Silicone casting and the airline assembly was setup to measure the dielectric constant and loss tangent properties. The results of those measurements are presented in Figure 15 and the values at 417 MHz are 2.98 and 0.006 respectively.

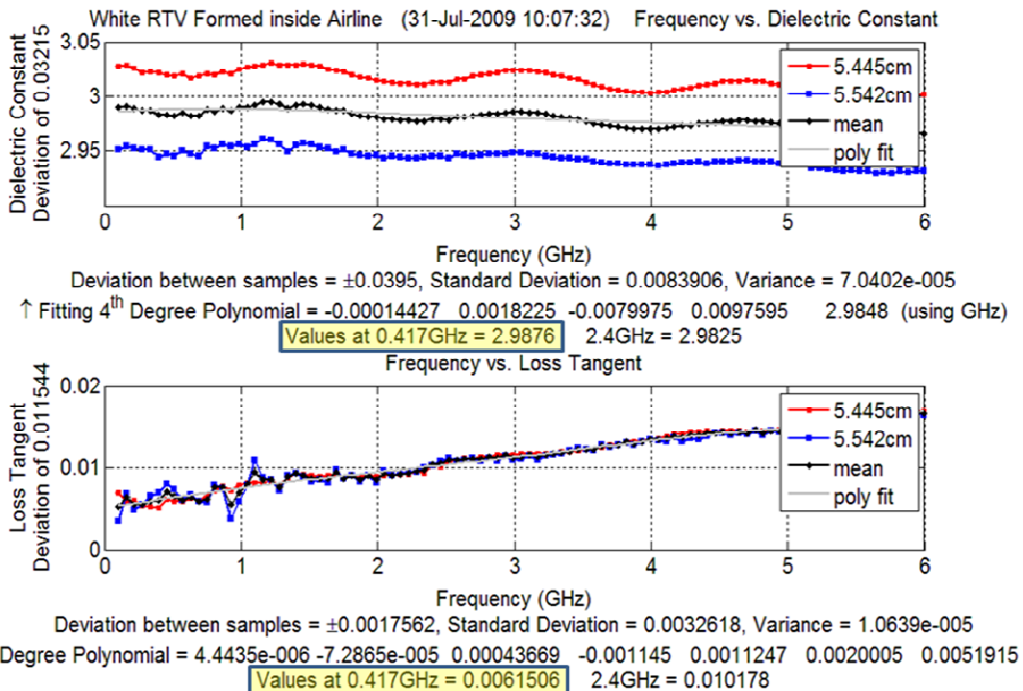
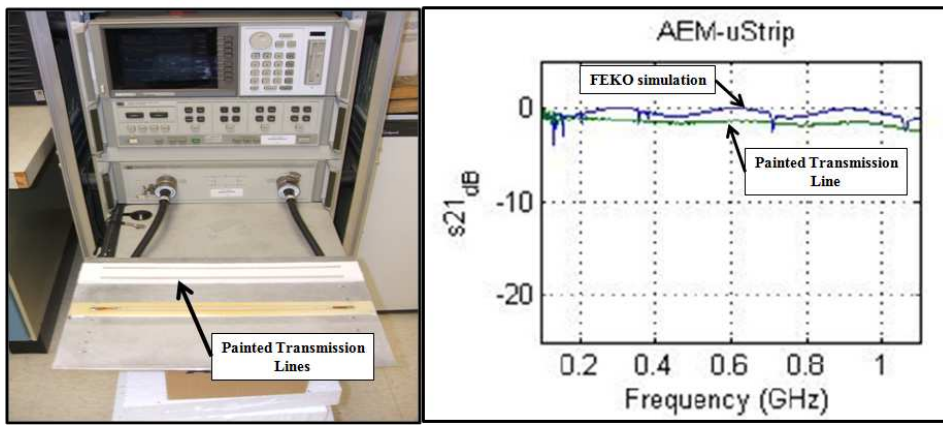


Figure 15 – Dielectric constant and loss tangent of RTV Silicone 3110 specimen for antenna design applications.

The next task was to evaluate the RF loss characteristics of Unishield 12447 flexible conductive coatings for the antenna design. The Unishield 12447 is a flexible electrically conductive silicone coating suitable for spray applications. It demonstrates excellent adhesion and peel strength to silicone polymer systems. A number of RF tests were conducted to measure the insertion loss versus frequency which included transmission line and antenna gain measurements using this material. A microstrip transmission line was fabricated using the 3110 dielectric substrate (0.062-inch thick) and a conductor was painted onto the substrate using 12447 conductive coating. Network analyzer tests, shown in Figure 16(a), were conducted and FEKO simulations of the line predicted the S21 insertion loss versus frequency. The measured S21 results compared to the FEKO simulations are presented in Figure 16(b). It can be seen that reasonable loss characteristics were obtained for the Unishield 12447 coating.

The Unishield 12447 is very resistant to flexing and creasing and typical cured properties are listed below:

Crease Resistance:	Excellent
Surface resistivity:	0.01 to 0.008 Ω/sq
Solderable:	No
Hydrolytic Stability:	Excellent
Temperature Range:	-70C to 260C, -94 to 450F



(a) Network analyzer setup.

(b) S21 results for 12447.

Figure 16 – Network analyzer measurement setup for measuring Unishield 12447 and S21 results.

6. Development of PIFA Space Suit Antennas

The next task was to develop prototype PIFA antennas using the fabrication methods for 3110 dielectric substrate material and 12447 conductive coatings. The narrow band and wide band PIFA designs were selected for prototyping, tests, and evaluations. Blocks of 3110 dielectric substrate material were fabricated by casting. The fabrication involved casting the RTV dielectric substrate, integration of copper tabs as solder points for the feed and a copper shorting bar, soldering the feed point, and coating the ground plane and antenna element area with the Unishield 12447. The fabrication of each antenna is discussed next.

Narrow Bandwidth PIFA Fabrication

The fabrication of the prototype narrow band PIFA antenna began with the casting of the 3110 RTV silicone block. A casting was made in a 6" x 6" tooling mold at 0.55" thickness. After full cure the casting was de-molded and cut down to a 2.0" x 5.0" block for the base of the PIFA antenna. The Unishield 12247 was then applied to the entire bottom of the casting and to 3.50" across the top of the PIFA antenna. The next step in fabrication was bonding on copper shim stock for soldering points for the coaxial SMA type connector. Copper shim stock with a thickness of 0.005" was used in place of copper foil in order to form a more rugged solder point for the antenna feed. The copper shim stock was bonded in place with Unishield 12447 coating and allowed to cure for 24 hours. An SMA connector was then soldered in place. These fabrication steps are presented in the photographs in Figure 17.

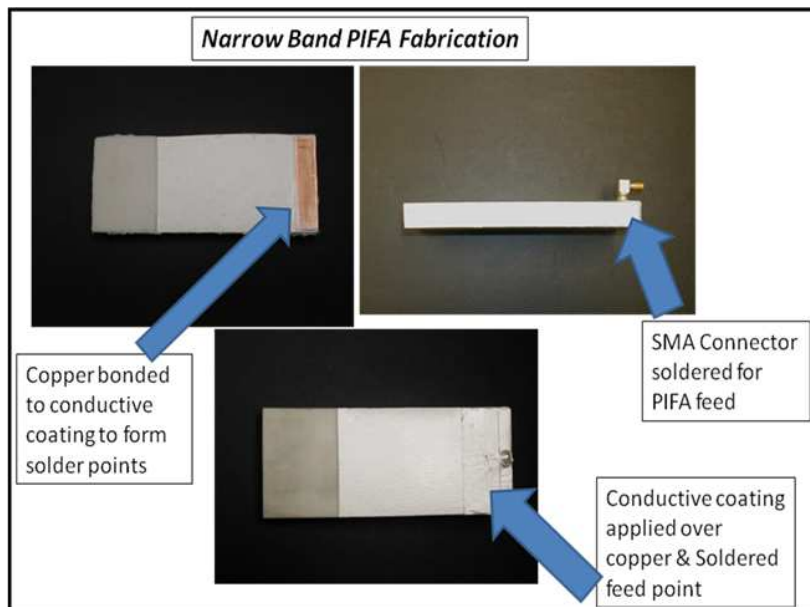


Figure 17 – Narrow band PIFA fabrication process showing addition of SMA connector replacement of soldered coaxial cable connections.

As a result of the preliminary PIFA fabrication, it was determined that a better transition was required from the copper shim stock to the conductive coating on the surface of the RTV silicone block. After the connections were soldered, copper foil tape was applied over the transition point between the copper shim stock and the Unishield 12447 on the both the bottom ground plane side and the top element side of the antenna. Unishield 12447 conductive coating was applied to the bottom of the PIFA, coating over the copper shim stock and taped transition and the soldered connection for the coaxial shield. The conductive coating was applied to the entire 2.0" x 5.0" area. After fully curing the application to the bottom of the PIFA, the Unishield 12447 was applied to an area of 2.0" x 3.50" on the top of the PIFA again coating over the copper shim stock, copper tape transition and the soldered feed point connection. This completed the fabrication of the antenna.

Wide Bandwidth PIFA Fabrication

Similarly, the fabrication of the prototype wide band PIFA antenna began with the casting of the 3110 RTV silicone block. A casting was made in an adjustable tooling mold to the specific antenna dimensions of 7.66" x 3.91" and at 0.55" thick. After cure for 48 hours at ambient conditions the casting was de-molded and allowed to cure for an additional 48 hours. The cast block for the base of the PIFA antenna. The Unishield 12247 was then applied to the entire bottom of the casting. The Unishield 12447 was cured at 302°F for 1 hour. The next step in fabrication was bonding on copper shim stock for soldering points for the coaxial SMA type connector. Copper shim stock with a thickness of 0.005" was used in place of copper foil in order to form a more rugged solder point for the antenna feed. The copper shim stock was bonded in place with Unishield 12447 adhesive and was forced cured for 1 hour at 302°F Then ambient cure for 24 hours. The SMA connector was then soldered in place. After curing the application to the bottom of the PIFA, the Unishield 12447 was applied to the antenna element area on the

top of the PIFA again coating over the copper shim stock and the soldered feed point connection. The antenna received a final cure for 1 hour at 302°F. Figure 18 shows the completed initial prototype for the Optimized wideband PIFA.

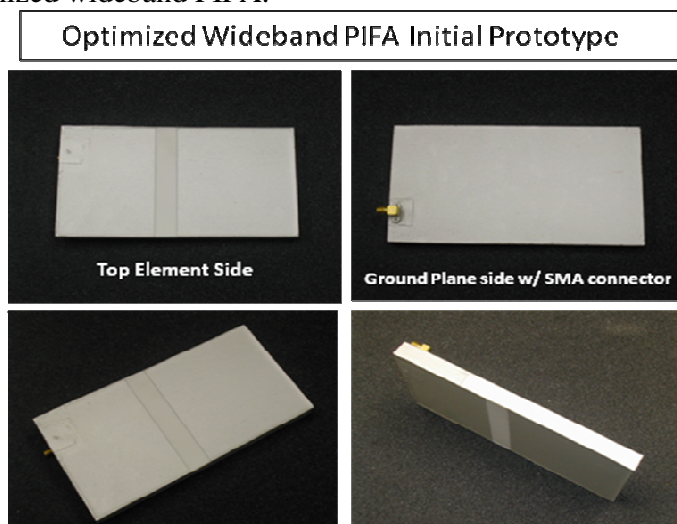


Figure 18 – Fabricated wideband PIFA UHF antenna prototype.

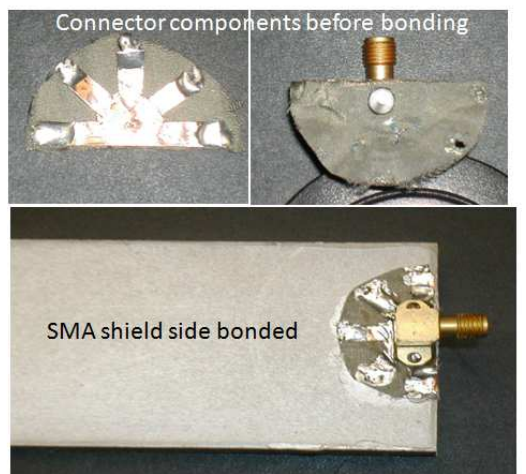
Unitech has also fabricated 3110 materials for a protective covering for the PIFA antennas. The process consisted of 1/8" sheet material cut to form layers around the four sides and top of the antenna. The objective is to determine the de-tuning effects of the covering material. The final antenna models will be overcast the RTV silicone to form a 1/8" thick covering for the top and four sides.

Improved RF Connection to Flexible Substrate

After fabricating several narrowband (NB) and wideband (WB) antennas, it was determined that a better method was needed for attaching the RF coaxial connector to the conductive coating and to the flexible silicone substrate material. Essentially, the adhesion between the connector and the conductive coating had to be improved especially if the connector was impacted or flexed during normal operations. It was decided to incorporate the features developed during Applied EM's SBIR Phase II- Conformal Antenna Materials Technology Project which provided good electrical connections from an RF connector to a "painted" conductive antenna surface. But, the challenge here was to achieve a good electrical connection to a "flexible" substrate. Therefore, this design objective was to demonstrate that the antenna will maintain the desired electrical characteristics (VSWR, center frequency, etc.) before and after flexing the antenna as well as after severe impacts such as with the specified kick load impact requirements.

In the earlier experiments, the connection approach involved bonding copper shim stock to the Unishield 12447 coated RTV silicone substrate with a conductive adhesive. The bonds were stable unless they were subjected to excessive flexing. Some corners of the shim stock started showing signs of de-bonding. To eliminate this problem, a solid square of shim stock, a

“flowered” approach was fabricated. The shim stock was cut to a flowered design to give better stress relief when flexing the antenna. This design is presented in Figure 19 and was implemented by soldering copper strips to the flange of the SMA connector and then these strips are “sweat” soldered to the small semi-circular patch of conductive fabric. After the RF connectors are prepared, they were bonded to the silicone substrate using flexible conductive adhesives. After curing, another layer of conductive paint coating is applied over the connector/fabric and the entire assembly is post cured. This method for connecting the RF connector to the flexible substrate has been incorporated into the final PIFA antenna designs.



Pre-cut and soldered connection system for SMA connector

Figure 19 - New design connector fabrication and installation.

Kick Load Impact Antenna Tests using Fabricated NB and WB Antennas

The latest fabricated NB and WB antennas were used for kick load force impact tests and they were subjected to a 125 inch/lb load over a $\frac{1}{2}$ inch diameter area. Impact areas were marked to identify impact points to evaluate any change in antenna performance after each impact. Also, we incorporated the new soldering procedures for attaching the RF SMA connector to the flexible antenna substrate. The setup used to conduct the kick load tests is shown in Figure 20(a) and 20(b). Essentially, the antenna was placed at the bottom of the pipe and the weight was inserted at the top of the pipe that guides the weight to the impact point. The antenna is re-positioned after each strike. The VSWR measurement setup is shown in Figure 20(d) and the antenna is placed on the PLSS mockup before and after each impact to determine damage to the antenna by measuring any frequency shifts and/or VSWR effects.

The Narrowband PIFA was subjected to 3 impacts (shown in Figure 20(c)), starting at the center, second impact near the feed point and the third on the opposite end from the feed point. There was no apparent damage to the antenna substrate after the impacts. The antenna frequency and VSWR were measured after each impact and recorded.

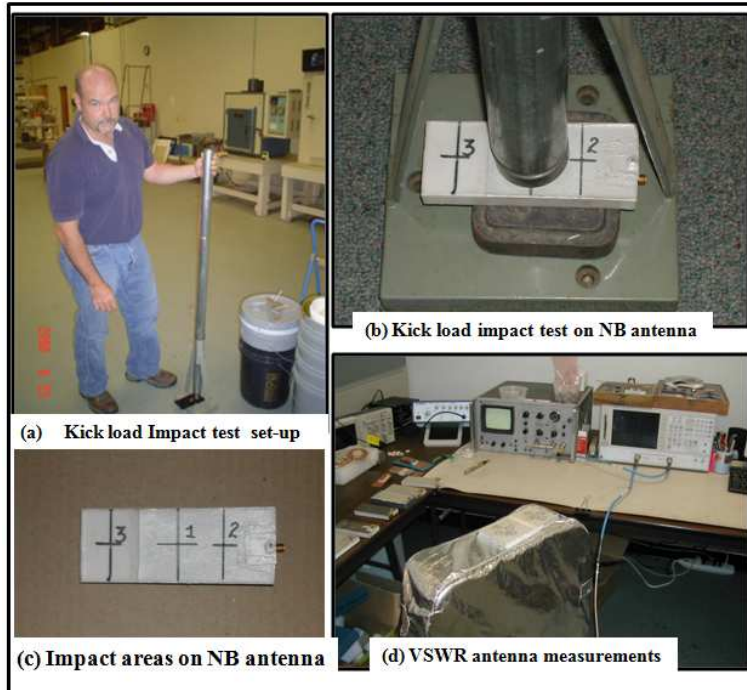


Figure 20 – Setup for antenna kick load force impact testing on the NB and WB antennas showing VSWR measurement setup before and after impact tests on each antenna.

The VSWR test results, shown in Figure 21, reveal that the NB antenna was only slightly detuned after the three impacts and there was no major damage to the antenna substrate due to the impact. This was a very successful test result as the 3110 RTV substrate material demonstrated the ability to withstand impact and return to the designed shape. Also, since minor antenna detuning occurred, the dielectric properties of the 3110 substrate and the 12447 conductive coating were not severely affected.

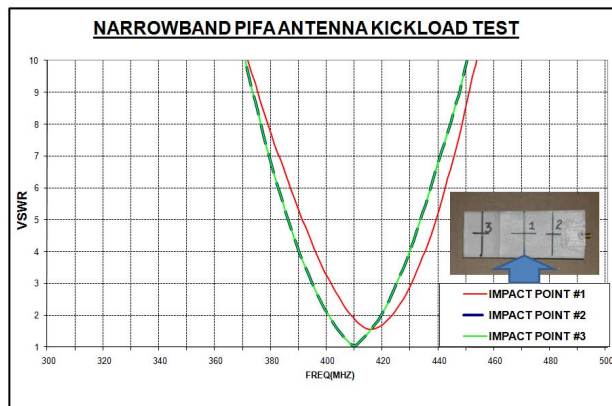


Figure 21 – VSWR measurement results on the NB antenna before and after (3) kick load force impact tests.

The Wideband PIFA was subjected to a total of nine impacts and the VSWR measurement setup and procedures were identical to the NB antenna using the PLSS mockup. Four impacts were directed to the microstrip section and five on the PIFA section of the antenna. VSWR results after impacts are presented in Figure 22 (a) and Figure 22 (b) for each section of the antenna. As indicated in Figure 22(a), minimal detuning resulted after the four impacts on the coupled microstrip section of the WB antenna. But, as shown in Figure 22(b), significant detuning did result after the five impacts on the PIFA section of the antenna.

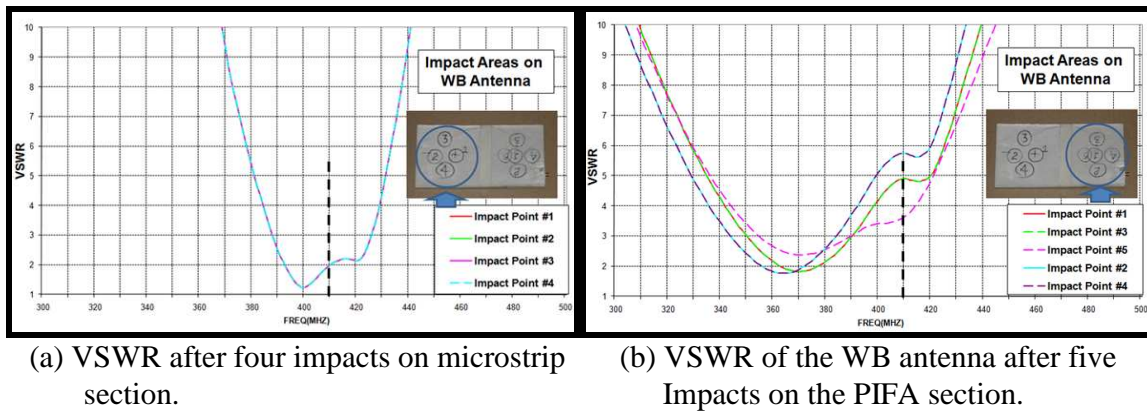


Figure 22 – VSWR of the WB antenna after four and five impacts on the different sections of the antenna.

After the first of five impacts on the PIFA section of the WB antenna, the antenna center frequency shifted to approximately 370 MHz and the VSWR increased to about 5.8 at 415 MHz. After the fifth and last impact, the VSWR improved slightly to about 3.7. Upon closer inspection of the damage done to the antenna at each point of impact, it was observed that the edge of the impacting weight cylinder cut into the conductive coating and created voids in the antenna surface. These voids in the conductive surface contributed to the shift in the tuned frequency and impedance and VSWR changes in the antenna. It is anticipated that the layer of 3110 protection will resolve this problem and prevent any impact damage to the 12447 conductive coating on the antenna. Tests will be conducted in the future to verify this condition.

7.0 Space Suit Antenna Integration and Testing

New PLSS Shielded Jacket Design

Since the results of earlier investigations indicated that antennas on the PLSS are affected by the shape and size of the PLSS, it was also determined that good electrical connections to a ‘stable’ ground plane are required for optimum antenna performance. The “ground plane” of the PLSS does affect the input impedance and the surface currents on the outer surface of the PLSS jacket affect the radiation characteristics of the antenna. Upon closer inspection of the aluminized Mylar layers of the TMG PLSS cover, it was determined that they are not electrically connected from

one section to another through the zippers. In addition, the Mylar coating is on the outside surface of the shielded layer and, thereby, would insulate the antenna from the ‘ground plane’ surface of the TMG.

Therefore, as a result of this investigation, a new ‘experimental’ conductive ‘sleeve’ was designed and fabricated by ILC-Dover. The new conductive sleeve exhibited improved RF shielding characteristics throughout the PLSS covering and provided a stable ground plane for the UHF antenna. The antenna is attached to the sleeve using conductive tape and positioned over the PLSS as indicated in Figure 23.

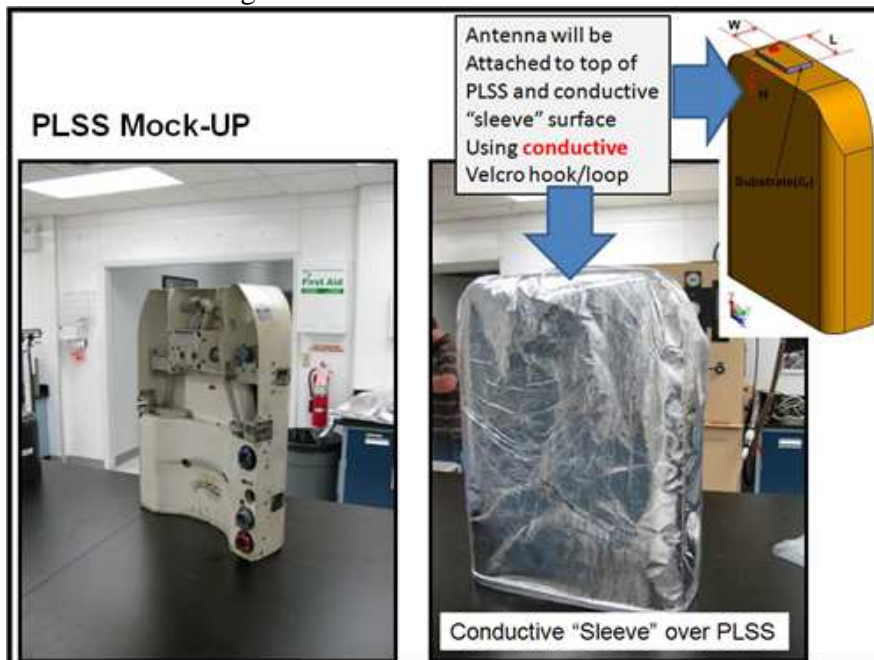


Figure 23 – PLSS mockup and conductive sleeve that will have the antenna attached and the It is
Antenna-Space Suit Integration and Impedance Tests

The current TMG PLSS cover has numerous cutouts to facilitate attaching the PLSS to the astronaut, a conductive sleeve was modified and tests were planned at ILC to determine any antenna impedance problems with the integrated setup. Since these cut-outs could potentially affect the impedance (and tuning) of the UHF antenna, S11 return loss measurements were conducted on narrow band and wide band PIFA antennas in a full scale space suit test configuration. PLSS mounted antennas were attached to the hard upper torso (HUT) and the astronaut’s helmet with the conductive visor and antenna VSWR measurements were conducted during the buildup stages. Photographs of the sequence of antenna-space suit impedance and fit checks are presented in Figure 24.

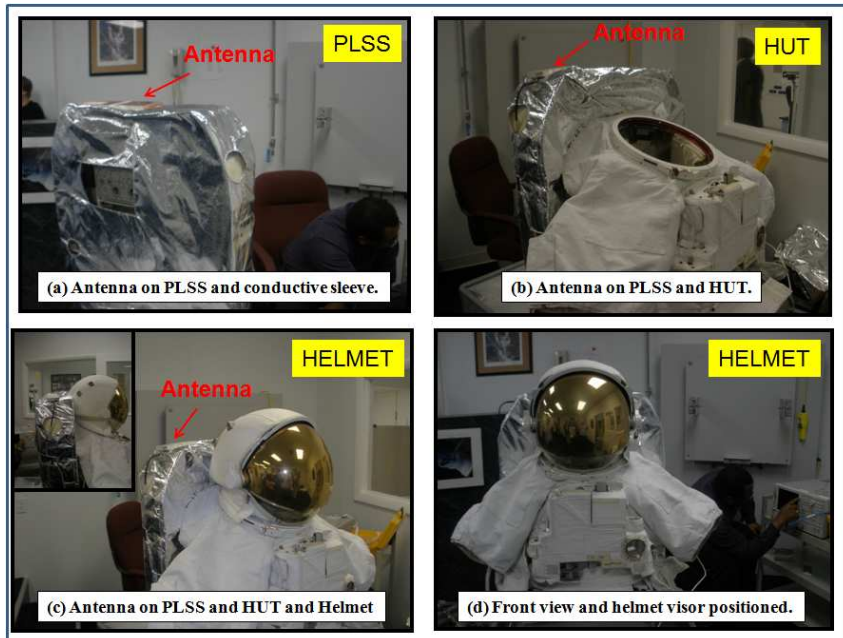


Figure 24 – Sequence of antenna-space suit impedance and fit-checks with EMU space suit (PLSS-HUT-Helmet).

These tests were conducted using the PLSS conductive sleeve with cut-outs that are required for mounting the PLSS to the HUT. Each narrow band and wide band UHF antennas were tested separately using conductive pressure sensitive tape to attach the antennas to the PLSS conductive sleeve. The sleeve cut-outs were provided to the size required to make the connections as well as for non-assisted astronaut assembly of the PLSS to the HUT. The VSWR results for each antenna are presented in Figure 25 and it can be seen that no major impedance detuning occurred for either antenna configuration.

Even though the impedance tests indicated no major detuning and proximity effects during the space suit integration tests, full-scale radiation pattern and gain performance tests are planned.

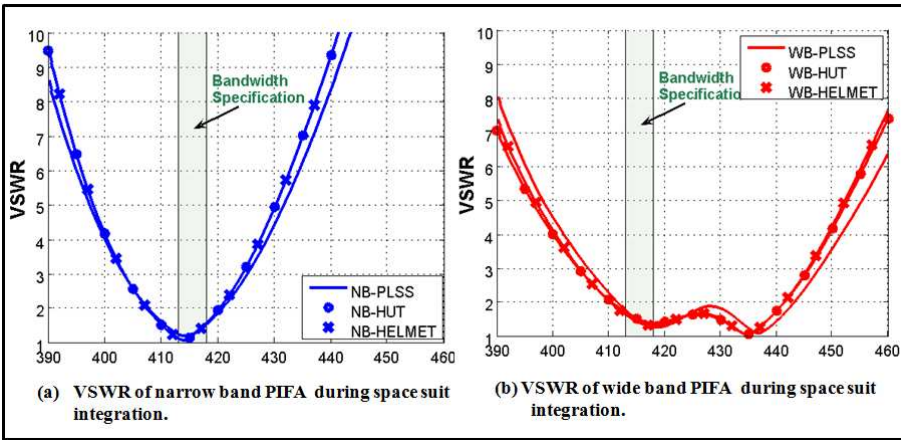


Figure 25 – VSWR measurement results for the narrow band PIFA and wide band PIFA during space suit integration tests.

Alternate Space Suit Antenna Positions – Sleeve Mounted Antennas

Additional embodiments of our conformal, body-worn antenna designs include the capability to ‘flex’ the antennas into different locations in the space suit and maintain acceptable EM performance. The PLSS-mounted antenna location was selected because that is the location for the current legacy antenna and it is a somewhat benign location for the antenna in terms of flexing and possible deformations. The effects of lateral and longitudinal deformations on antenna performance have been investigated and the PIFA antenna designs can be ‘flexed’ and installed at different locations in the suit.

8.0 Space Suit Antenna Spherical Coverage Analysis

A very important task in the development of space suit antennas is the development of a computer simulation model of the entire space suit that can be used in antenna design and performance predictions. Since a CAD model of the existing EMU suit was not available, Applied EM [8] developed a CADFEKO model using Pro-E CAD model of the Mark III space suit that was provided by NASA-JSC. The availability of the Pro-E CAD model of the Mark III suit was vitally important in developing Applied EM’s EM simulation model. It is important that the EM simulation space suit model exhibit the accuracy and sufficient details so that the performance simulations are effective. The dimensions especially around the top of the PLSS and in the area around the helmet are important. In addition, ILC-Dover developed a limited solid works (SW) model of the upper torso section of the current EMU space suit and this model was used to clarify the structural differences between the EMU and Mark III suits (as shown in Figure 26). Since the SW model did not include the entire suit, it could not be used in the volumetric radiation pattern analysis of the space suit antenna.

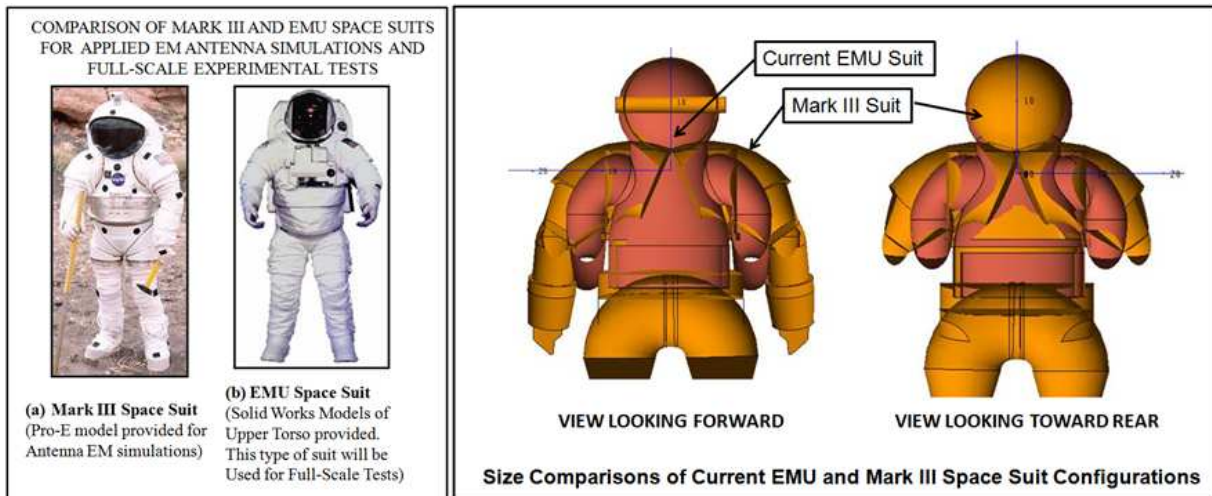


Figure 26 – Comparisons of the Mark III and EMU space suit configurations for EM simulations.

Therefore, Applied EM's space suit antenna model (based on the Mark III suit) was used to predict the radiation patterns of the antenna at different locations in the suit as well as the spherical coverage gain predictions. All of the volumetric radiation pattern coverage simulations used a CADFEKO model based on the Pro-E model of the Mark III suit (Figure 27). Using Applied EM's space suit CADFEKO model, simulations of the PIFA were conducted that included both the PLSS and astronaut models. Spherical gain coverage for the PIFA antennas was analyzed at various installation locations, orientations, and astronaut motion shapes (in symmetric and an asymmetric motion).

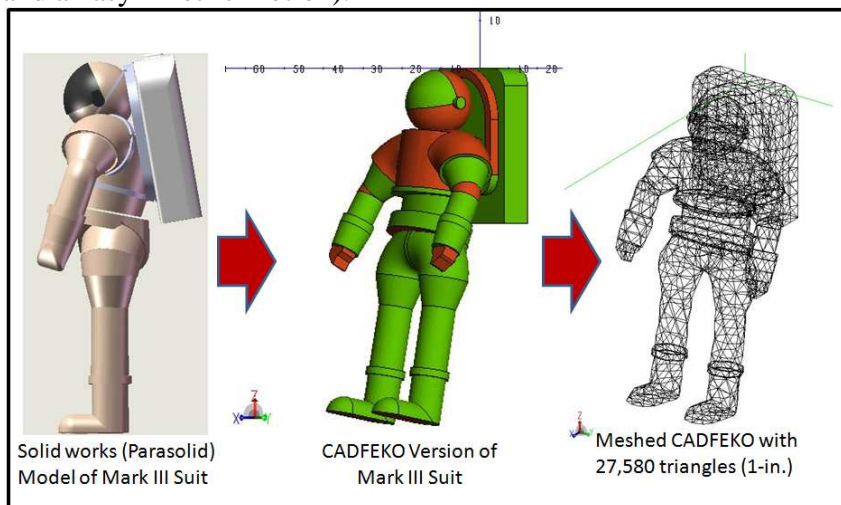


Figure 27 – Development stages for a meshed CADFEKO model of the PLSS and space suit for antenna coverage analysis.

An example of the spherical coverage analysis results is presented in Figure 28. The results when the ‘astronaut’ is attached to the simulated PLSS, the proximity effects on the radiation

patterns are not as severe and 3-D spherical coverage is acceptable (but with some pattern nulls). As compared to the current UHF antenna, all of the cases considered outperformed the current EMU. However, the spherical coverage analysis was based on a total gain. Thus, this is a very optimistic result. The spherical coverage results showed that the PIFA located at the edge of the PLSS outperformed the other cases considered in this memo, though the predicted absolute coverage values are optimistic due to the estimation from a total gain.

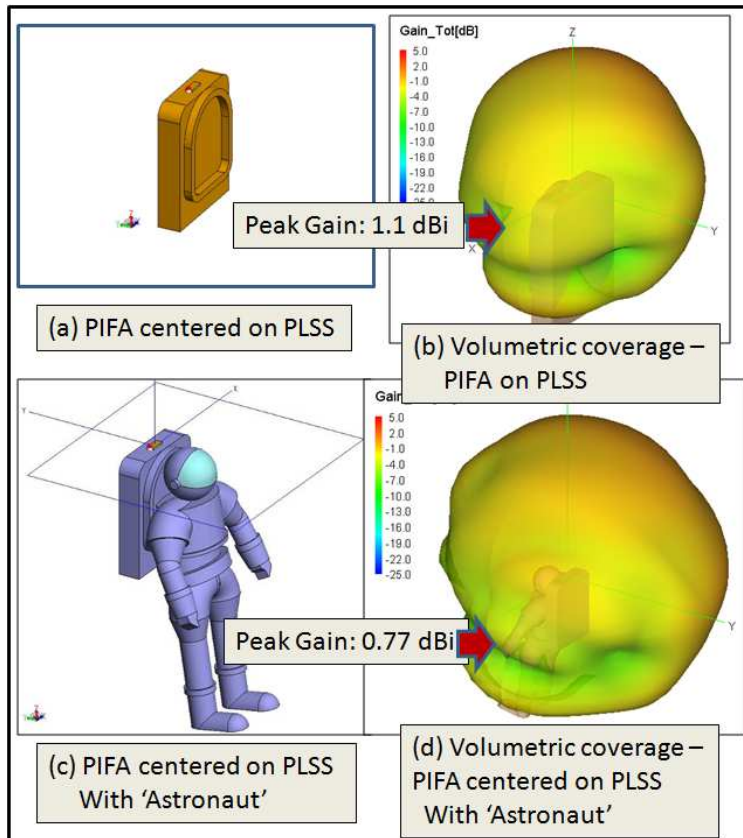


Figure 28 – Spherical gain patterns of the PIFA centered on the PLSS without and with the astronaut.

In the final analysis, however, the overall accuracy predicting the final antenna's performance is in doubt and will be evaluated when the full scale antenna data has been obtained. Full scale antenna radiation pattern tests will be conducted using an actual EMU suit that will be provided by ILC and Hamilton Sundstrand.

Comparison of Simulated Astronaut Space Suit Antenna Performance with Full-Scale PLSS Antenna Test Results

Since full scale space suit antenna test data is not yet available, full scale PLSS mockup antenna

test data was available; so, it is important to compare the spherical gain test results using the recent PLSS (mock-up) antenna test data with the spherical gain simulations for the full astronaut space suit (with motion). So, these comparative results are presented in Figure 29 and it can be noted that there is about 1 dB difference (at the 90% coverage level) between the full suit antenna simulations and the full scale PLSS antenna test results. It is important to point out that the space suit antenna simulations are based on MARK III suit configuration and not for the EMU suit. As discussed previously, there are significant physical differences between the MARK III and EMU suits not only dimensionally but in suit configurations. Therefore, it is anticipated that these some of these differences will be resolved when the full scale space suit antenna data is available.

Comparison of EM simulations with Experimental Measurements Full Suit (Simulations) vs. PLSS only (Measurements)

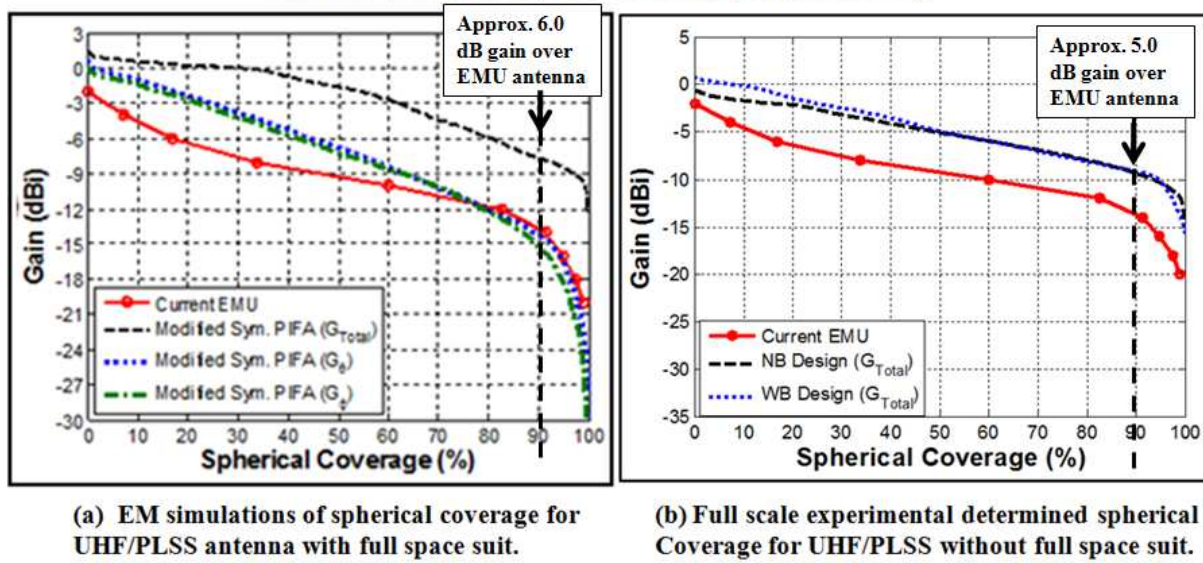


Figure 29 – Comparison of EM simulations of full suit with PLSS only antenna pattern measurements.

Full-Scale Space Suit Antenna Radiation Pattern Tests

Applied EM prepared a test plan for the full-suit antenna tests and provided that to ILC-Dover for issuing an RFQ to Satimo, Inc. ILC/HSSI will provide the EMU suit and Applied EM and Unitech will provide the antennas for testing. The plan includes testing each NB and WB antennas located on top of the PLSS. Currently, the tests will be conducted August 10-12, 2010. A photograph of the Satimo (SG-64) test facility that includes a rendering of the proposed setup for the full scale space suit antenna tests is presented in Figure 30.

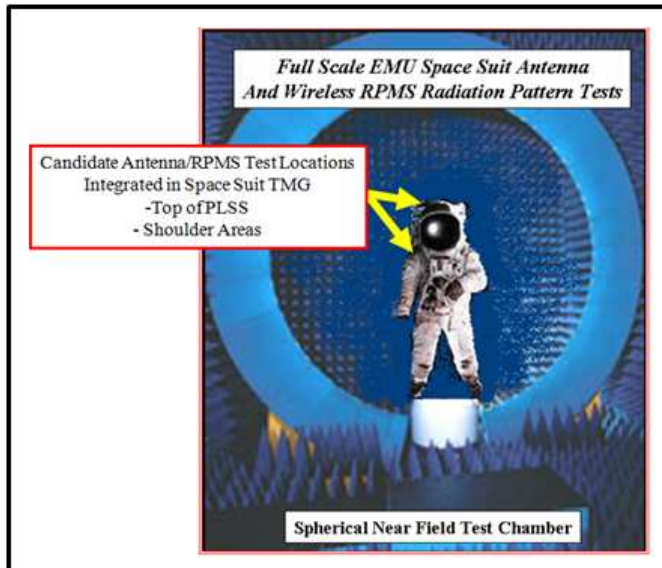


Figure 30 – Satimo SG-64 Spherical Near Field Measurement System proposed for Applied EM’s Space Suit antenna tests.

9.0 Summary

Applied EM, Inc. has developed new conformal, flexible, body-worn antenna designs that can be integrated into the current EMU space suit configurations. The new space suit antenna designs have been simulated and RF tested in full EMU suit configurations. Test results demonstrate improved performance over the current UHF antenna used during EVA operations. In addition, the new antenna designs enable multi-frequency capabilities that could support wireless bio-med telemetry for wearable computer applications during space operations. The results of this research contributes to NASA’s efforts to develop new space suit designs which will improve the astronaut’s mobility, efficiency, and safety during long periods of EVA operations.

10.0 Acknowledgements

The outstanding support from Mr. Andrew Chu, Technical Monitor, and Mr. Terry Hill of NASA-JSC is especially acknowledged. Also, from Applied EM’s Ms Dalia Elsherbeni and Mr. Ron Buckles for their support conducting material property measurements of the polymer substrates is deeply appreciated. Also, the support of Mr. Buckles in the development of the FEKO space suit simulation model that was used in antenna gain performances is also deeply appreciated. Also, from ILC-Dover, for the support from Ms Jinny Firl and Mr. Stan Bauman is deeply appreciated. We appreciate the support from Mr. John Estrada, Benjamin Ballart, and Rhett Burrell from Satimo USA during space suit antenna testing.

11.0 References

[1] Contract No. NNX09CA94C for NASA – Lyndon B. Johnson Space Center, 2101 Parkway,

Houston, TX, 77058-3696; Technical Monitor/COTR: Andrew Chu

[2] Thomas G. Campbell, C. J. Reddy, and Robert Boyd; “Development of Conformal Antenna Materials Technology to Enable “Paint-On” Antenna Arrays for Air Force Aerospace Applications,” paper presented at Antenna Applications Symposium (AAS), Champagne-Urbanna, ILL, September, 2006.

[3] www.unishield.com

[4] JSC26640

[5] Timothy F. Kennedy, Patrick W. Fink, Andrew W. Chu, Nathan J. Champagne, II, Gregory Y. Lin, and Michael A. Khayat; “Body-Worn E-Textile Antennas: The Good, the Low Mass, and the Conformal” IEEE-APS, Vol 57, April 2009.

[6] Nathan P. Cummings; Low Profile Integrated GPS and Cellular Antenna, Thesis submitted for the degree of Master of Science in Electrical Engineering, Virginia Polytechnic Institute and State University, October 31, 2001.

[7] Taeyoung Yang, W. A. Davis, T. G. Campbell, and C. J. Reddy; Design Optimization of Antenna Concepts for Conformal Space Suit Antenna and Wearable Applications; paper presented at Antenna Application Symposium, September 21-23, 2010.

[8] FEKO Suite 5.4, <http://www.feko.info>

[9] L. J. Chu, “Physical limitations on omni-directional antennas” J. Appl. Phys., vol. 19, pp. 1163 – 1175, December 1948.

[10] Applied EM CADFEKO model prepared by Mr. Ron Buckles, Research Engineer.

A LOW-PROFILE ANTENNA DESIGN APPROACH FOR CONFORMAL SPACE SUIT AND OTHER WEARABLE APPLICATIONS

Taeyoung Yang¹, William A. Davis¹, Thomas G. Campbell² and C. J. Reddy²

¹Virginia Tech antenna Group, Blacksburg, VA 24061

²Applied EM, Inc., 144 Research Drive, Hampton, VA 23666

ABSTRACT

This paper describes a design approach of a planar inverted-F antenna (PIFA) design with an extremely-low profile specification. The antenna was built with an elastomer substrate for space suit and other wearable applications. Low-profile wideband planar antennas in the literature are reviewed, but demonstrating miniaturization and broadband techniques are not effective because of the extremely low-profile requirement (0.5 inch height, approximately 0.02 wavelength). In this case, adding resistive loss to the antenna is effective to obtain broad impedance bandwidth, but the resultant radiation efficiency (or gain) is reduced. This trade-off is explained by reviewing the classic fundamental-limit theory on antenna size and performance. As an alternative approach to the resistive loading, a continuous broadband technique was designed by introducing parasitic elements. A polymer substrate material was characterized through measurements before starting the actual design process. Simulation results using a commercial hybrid MoM + FEM code (FEKOTM) and a genetic algorithm showed that a fractional bandwidth of 3 ~ 4% was required when a minor shape deformation is considered and approximately 10% was required for a severe shape deformation. The simulation results also predicted that a PIFA antenna at the selected location shows a better spherical coverage as compared to the legacy antenna. The demonstrated design process and concepts for the extremely-low profile wearable antenna can be applied to other platforms including hats, gloves, vests, and shoes.

1. Introduction

Wearable antennas can find a wide range of potential applications due to light weight, invisibility, flexibility and user mobility. For example, wearable computing / monitoring devices can exchange information through a body-centric wireless network using a wearable antenna [1]. A military-based wearable antenna provides the radio operator a low visual signature and enhances mobility [2, 3]. In addition, damage from the obstacles in an urban environment is reduced, compared to conventional antennas often used. Another application of a wearable antenna is for a space suit. As NASA prepares for the Constellation Space Missions and Extra-Vehicular Activity (EVA) on the moon in the future, astronauts will be required to spend more time exposed to the hazards of EVA operations [4, 5]. Communications during EVA is required to relay progress regarding the task and to monitor the health and ability of the astronaut to perform in hazardous environments. Reliable communications is imperative during the operations and missions. Wearable antennas meet the need to provide astronaut mobility and reliable space communications.

In this paper, we consider a design approach for low-profile, planar, wearable antennas for space suits as well as commercial and military applications. The target maximum height of the antenna is less than 0.5". An elastomer is used for a substrate material. The desired operational frequency range is 413 – 418 MHz, corresponding to approximately 1.2 % fractional bandwidth. If a potential antenna shape deformation and environmental proximity effects are considered, we may need to design an antenna with a wider bandwidth than the specification in order to prevent the antenna detuning effects. In addition, the height of the antenna is about $0.018 \lambda_0$ at the lowest operational frequency, which is an extremely low profile. Then, a question is how much antenna impedance bandwidth is necessary to provide reliable communications when shape deformation is considered. The other question is what antenna type or configuration can meet the necessary impedance bandwidth. In following sections, we address these questions and provide an antenna design meeting the needs.

2. Preliminary Antenna Design Studies

Since the size specification requires an antenna form factor having an extremely low-profile, the corresponding antenna bandwidth and radiation efficiency will be limited by physics, not technology. As the classic fundamental-limit theory on antenna size and performance [6] implies, the antenna size, bandwidth, and radiation efficiency (or gain) are in the trade-off relationship that only two of them can be achieved close to the theoretical limit. Typically, radiation quality factor (Q_{rad}) has been used as a metric of the limit theory, the factor being defined by [6]

$$Q_{rad} = e_r \frac{W_{non-radiating}}{P_{rad} / \omega} \quad (1)$$

where $W_{non-radiating}$ is the average non-radiating energy, P_{rad} is the average radiated power, and e_r is the radiation efficiency of the antenna. For example, Chu's radiation- Q limit is given as [6]

$$Q_{rad, Chu} = e_r \frac{1+2k^2a^2}{(k^3a^3)(1+k^2a^2)} \quad (2)$$

where k is the wave number and a is a radius of the sphere just enclosing the antenna (antenna sphere). The theoretical limit of the minimum radiation- Q varies with different solution approaches [7], but converges to $1/(k^3a^3)$ as the electrical size of the antenna becomes smaller. In addition, it is well known for small antennas that the radiation Q is inversely proportional to 3-dB fractional, instantaneous impedance bandwidth, i.e.

$$Q_{rad} = \frac{f_c}{BW_{3dB}} \quad (3)$$

where f_c is a center frequency.

Figure 1 shows that the typical radiation Q of various antennas, comparing to the theoretical limit. Most of antennas in Figure 1 are not even close to the theoretical minimum Q . Particularly, the legacy performance line connecting from a dipole to a spiral antenna seems almost shifted from the limit curve. That is because those antennas do not use the volume of the antenna sphere efficiently, compared to the folded hemisphere and Goubau antennas. Typical low-profile, planar antennas, such as microstrip and planar inverted-F antennas (PIFA), have a high non-radiating energy due to the strong coupling between the planar antenna structure and the ground plane as well as inefficient usage of the antenna sphere. As a result, typical low-profile planar antennas have a high radiation Q as seen in the Figure 1. If the antenna uses a lossy material in the metallic structure or the substrate, the radiation Q can be lowered due to the reduced radiation efficiency.

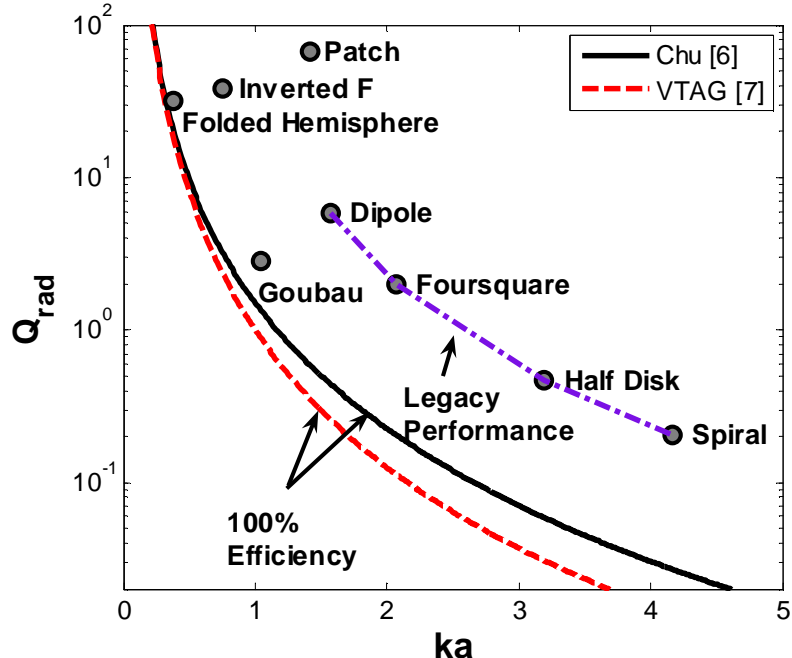


Figure 1. Radiation Q of various antennas, compared to theoretical minimum radiation- Q versus ka [8].

In our design problem, the radiation Q for the required operational bandwidth is approximately 83.33, which suggests that the minimum diameter of the antenna sphere, based on Eq. (2), is approximately 5.34 cm. Since planar antennas do not use the volume of the antenna sphere efficiently, the required minimum radiation Q and the size would be higher than the initial calculations.

In order to have a more concrete idea in terms of size, gain, and bandwidth of a planar antenna, a parametric study was carried out for a planar inverted-F antenna (PIFA). The basic geometry of a PIFA used in the parametric study is shown in Figure 2. The feed and the shorting strip are located in the same vertical plane of the substrate. A commercial hybrid code (method of moment + finite element method) [9] was used for simulations. The feed location, shorting-strip width, size of the antenna, and material property of the substrate were considered as variables (see Table 1). These variables were optimized with a function of substrate thickness (H , see Table 2) through the genetic algorithm to make the antenna tuned at 415 MHz. All the metals were assumed to be a copper ($\sigma = 5.8e7$ S/m). Note that running an optimization does not guarantee the design will be any closer to the theoretical limit curve.

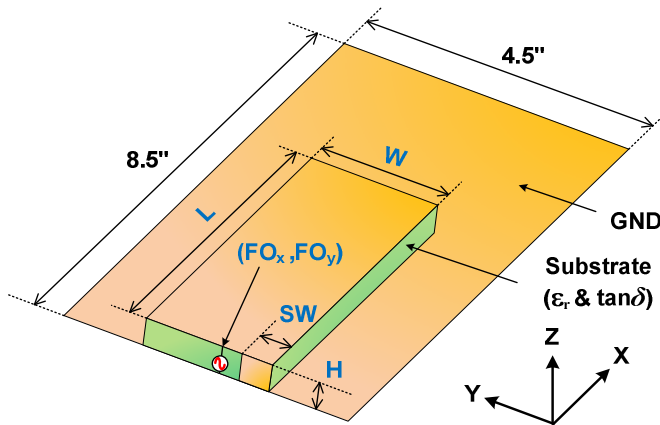


Figure 2. Geometry and parameters of the PIFA used for a parametric study.

Table 1. Optimization parameters and their descriptions

Parameters	Description
L	Strip length of PIFA
W	Strip width of PIFA
H	Substrate height
SW	Shorting strip width
FO_x	Position of Feed offset in x-direction (set to zero)
FO_y	Position of Feed offset in y-direction
ε_r	Dielectric constant of substrate material
Tanδ	Loss tangent of substrate material

Table 2. PIFA height variation factor and its physical dimension

H / λ₀ @ 415 MHz	Physical dimension
0.005	0.1423"
0.010	0.2846"
0.015	0.4269"
0.020	0.5692"
0.025	0.7115"

The results of parametric study for variations of dielectric constant, dielectric loss, and antenna height are depicted in from Figure 3 through Figure 5. The fractional bandwidth becomes larger as the substrate height increases and/or dielectric loss increases, which is well known. At the same time, the gain decreases as substrate height decreases and/or dielectric loss increases. Notice that the fractional bandwidth of the dielectric-loaded cases (Figure 3) is smaller than that of loss tangent variation cases (Figure 4). Thus, antenna size (height), bandwidth, and gain (or efficiency) are trade-offs as the fundamental-limit theory suggested.

Another observation out of the parametric study is that the fractional bandwidth increases almost linearly for the given range of antenna height change. The same trend was also observed in the parametric study of the wideband U-slot patch [10] and the conventional patch antenna [11]. Other wideband planar antennas shown in the literature were reviewed, but the bandwidth performance of the wideband planar antennas was almost the same as a narrowband patch antenna if the height of the planar antenna is limited to a low profile ($< 0.05 \lambda_0$). In this sense, we can choose a simple planar antenna like a PIFA as an initial design candidate. If a wider bandwidth is necessary, adding a loss to the antenna structure is an effective solution, which is basically suggested in the classic fundamental-limit theory.

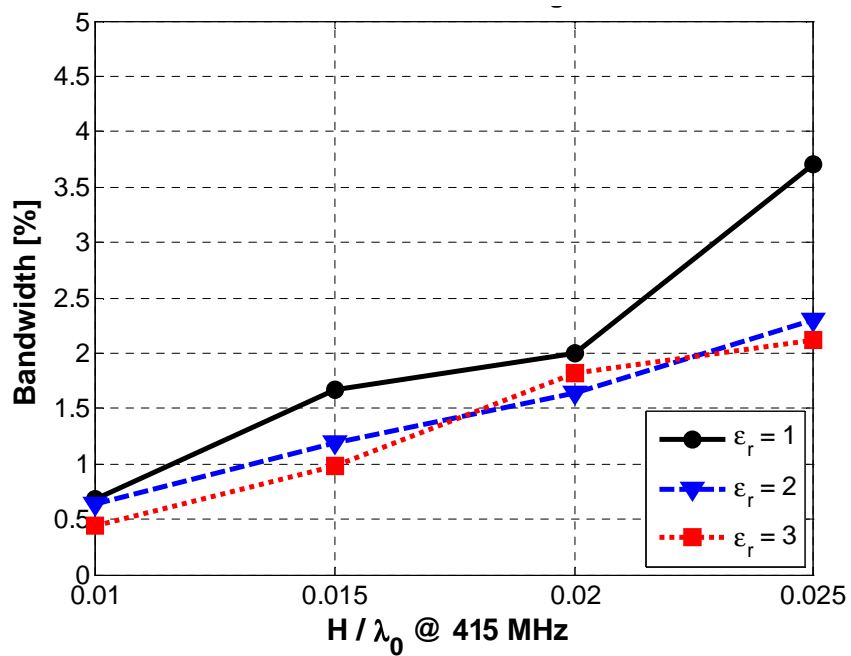


Figure 3. Fractional impedance bandwidth versus PIFA height for various dielectric constants ($\tan\delta = 0$).

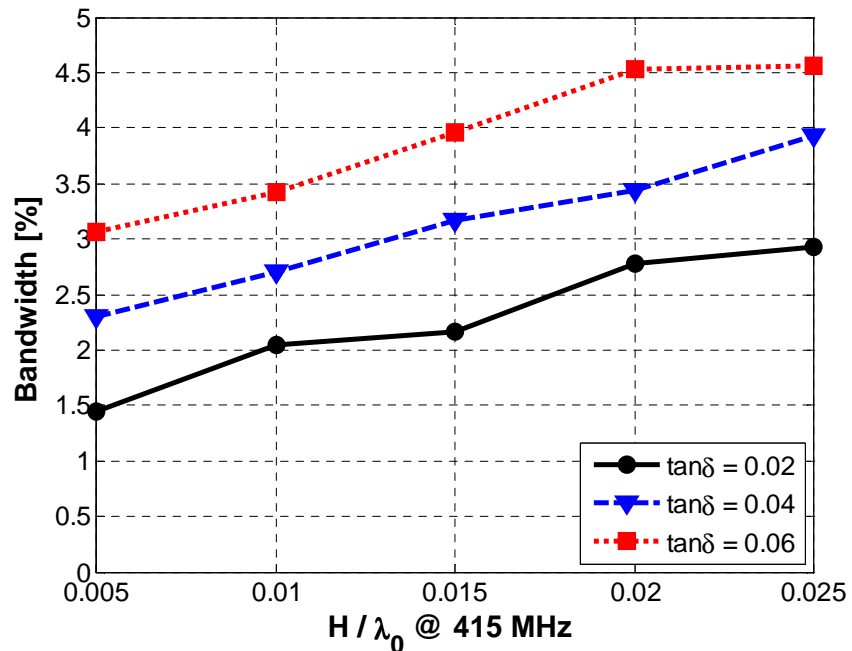


Figure 4. Fractional impedance bandwidth versus PIFA height for various loss tangents ($\epsilon_r = 1$).

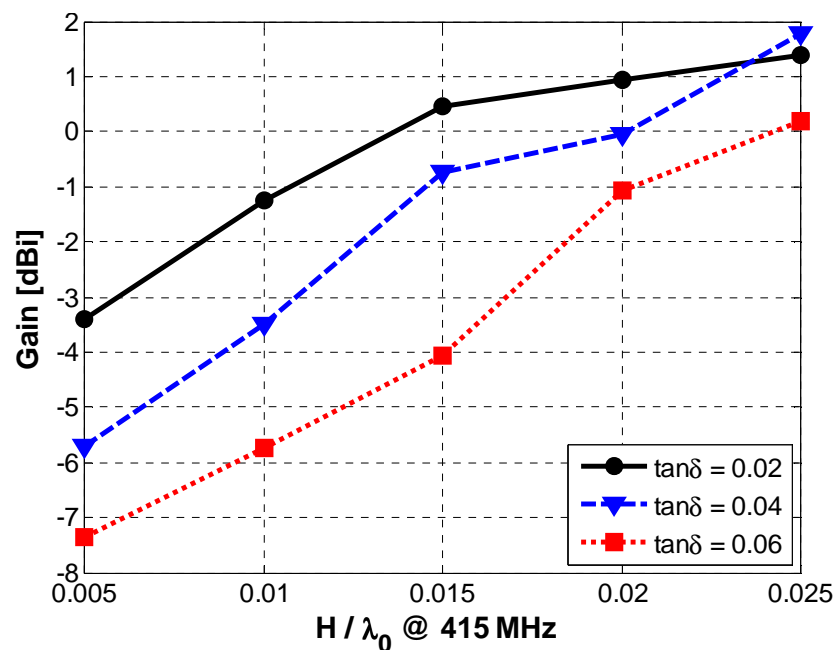


Figure 5. Gain versus PIFA height for various loss tangents ($\epsilon_r = 1$).

3. Shape Deformation Study with Conventional PIFA

Based on the parametric study results in the previous section, it seemed possible to design an antenna meeting the given antenna height (0.5") and the impedance bandwidth (1.2%) specifications. However, we may need more bandwidth than the original bandwidth specification if we consider the detuning effects due to the shape deformation in order to provide reliable communications. The required bandwidth considering shape deformation is investigated in this section.

The considered PIFA geometry and the assigned parameter values for the shape deformation test are depicted in Figure 6 and Table 3. Notice that the antenna height was not restricted to 0.5" for this study. Both lateral and longitudinal variations are investigated through simulations. The considered deformed shapes are shown in Figure 8.

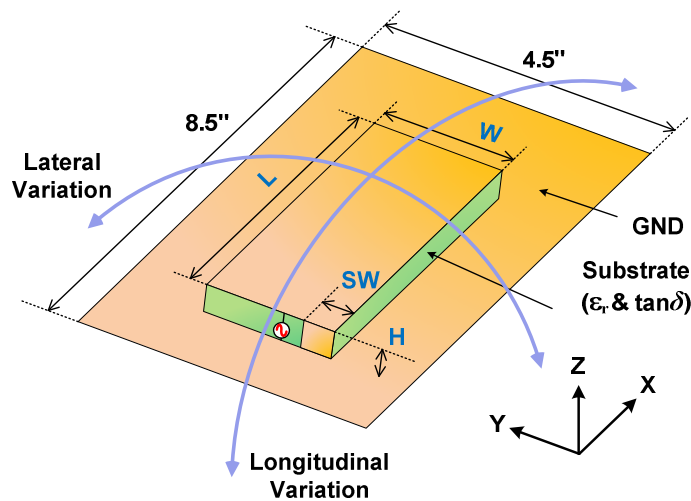


Figure 6. Geometry of the reference PIFA design. Note that the PIFA is located at the center of the ground plane.

Table 3. Parameters and assigned values for the reference flat design.

Parameters	Assigned Value
L	5.51"
W	2.15"
SW	0.65"
H	0.7115" ($H / \lambda_0 @ 415 \text{ MHz} = 0.025$)
ϵ_r	1
$\tan\delta$	0.006

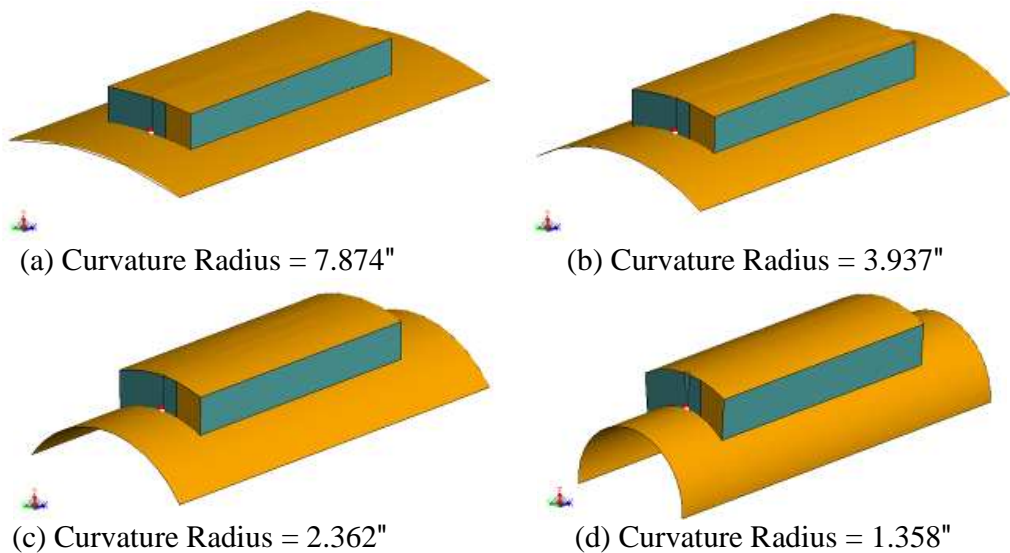


Figure 7. Deformed PIFA in a lateral direction.

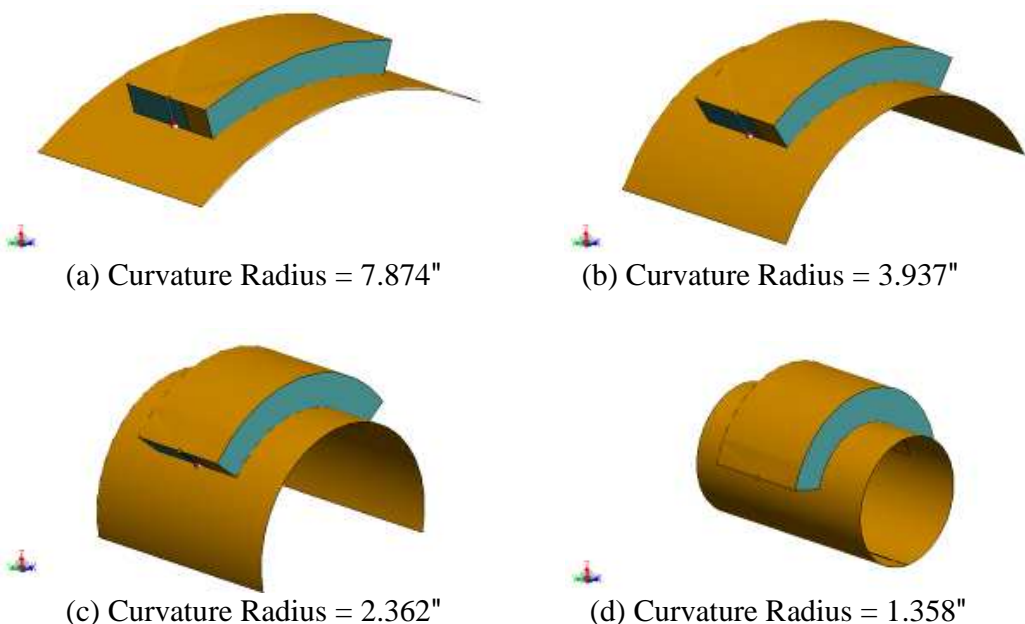


Figure 8. Deformed PIFA in a longitudinal direction.

The simulation results in Figure 9 show that the shape deformation in a lateral direction caused a minor frequency detuning at lower frequencies (approximately 2.4 %), as the curvature radius decreases. On the other hand, a noticeable detuning (approximately 9.6%) occurred at higher frequencies for the shape deformation in a longitudinal direction, as the curvature radius decreases. However, it was observed that the impedance bandwidth does not change significantly for both lateral and curvature cases (see Figure 10 and Figure 11). Thus, if the PIFA has a $3 \sim 4$ % fractional bandwidth, the detuning effects of the lateral shape deformation may be prevented. For a longitudinal variation approaching the extreme case of $R_{\text{Curvature}} = 1.358"$ is concerned, we may need to have a PIFA with approximately 10 % fractional bandwidth.

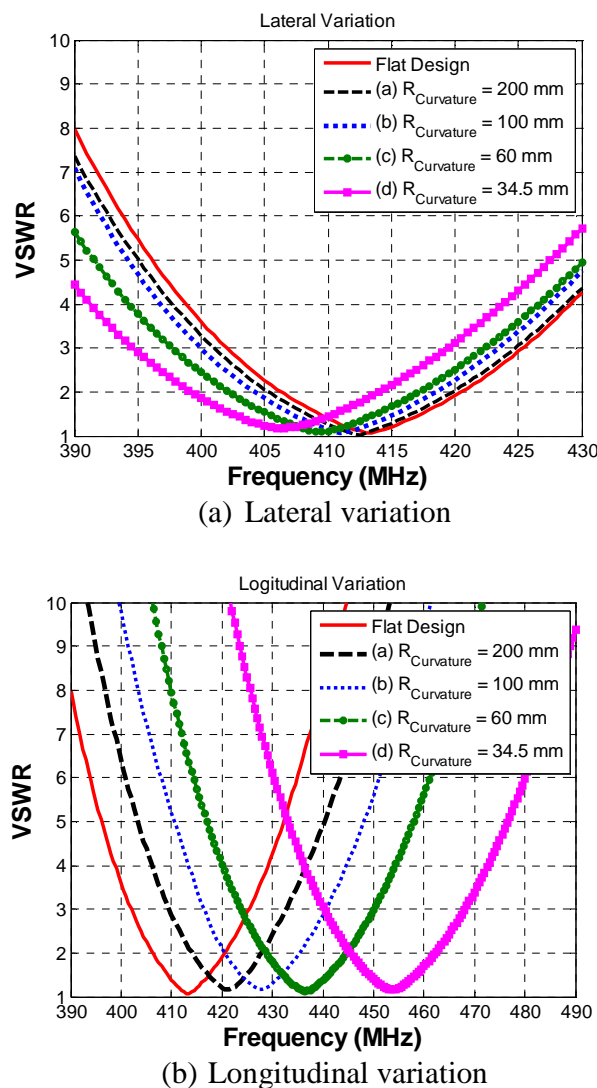


Figure 9. Simulated VSWR comparison for deformed PIFA in a lateral and a longitudinal direction.

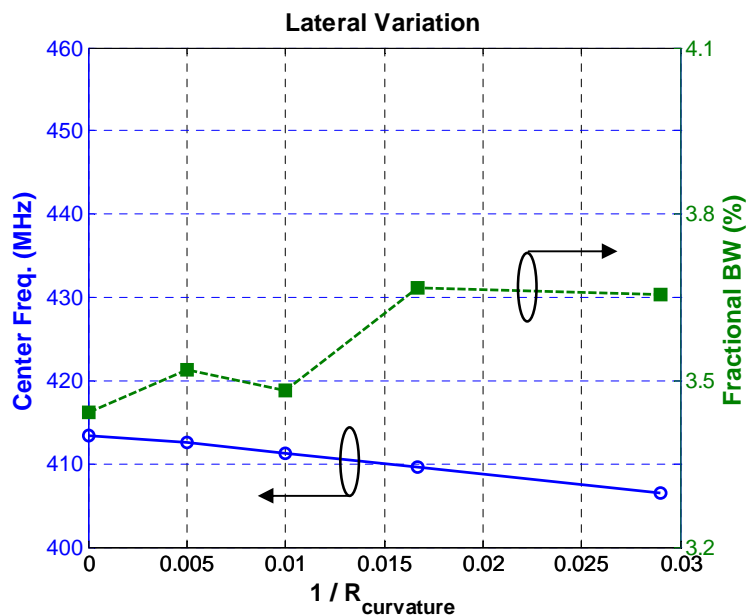


Figure 10. Center frequency and fractional bandwidth versus $1/R_{\text{curvature}}$ for variations in a lateral direction.

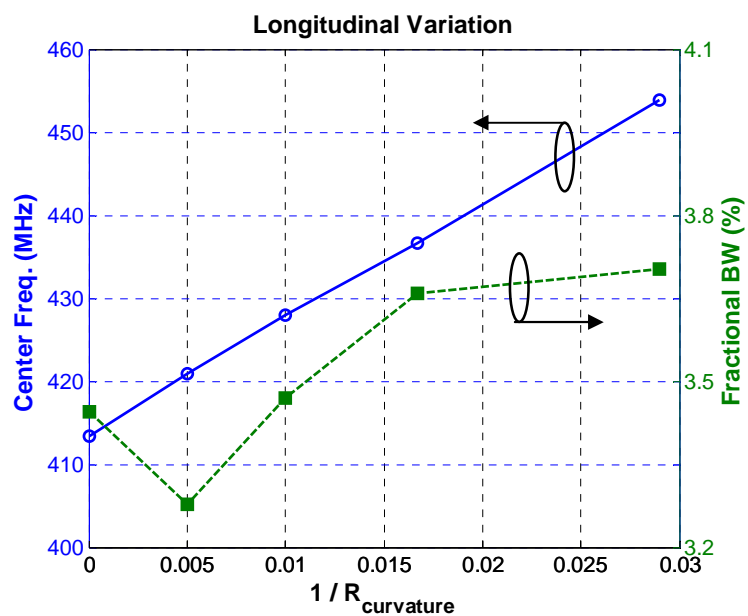


Figure 11. Center frequency and fractional bandwidth versus $1/R_{\text{curvature}}$ for variations in a longitudinal direction.

4. A Wideband PIFA Design Approach

Based on the shape deformation test, the bandwidth of a conventional PIFA design using a lossy substrate (3 – 4 % fractional bandwidth, see Figure 4) may be enough to prevent minor detuning due to the shape deformation in both a lateral and longitudinal direction. For severe detuning cases, we may increase the loss in the substrate to obtain a larger impedance bandwidth. However, the resulting radiation efficiency will suffer (see Figure 5). In addition, as explained in the preliminary design study in Section 2, many wideband planar antennas in the literature show almost the same bandwidth performance as a conventional microstrip antenna if the antenna height is restricted in an extremely-low profile.

In order to find out an alternative solution other than adding a loss, we may look at the basic assumptions made in the classical fundamental-limit theory [6]. The implicit assumption in the limit theory is that the transfer function of the ideal antenna meeting the performance and size limit is passive, linear, and time-invariant. Therefore, the phase response of the antenna transfer function should be linear. The corresponding group delay over the entire operating frequency is constant for typical ultra-wideband antennas. Such antennas do not have resonances other than the frequency near the lowest operational frequency, but in practice one can observe weak resonances in the band. Thus, the bandwidth implied in the classical limit theory is an instantaneous bandwidth. A typical return loss performance of the antenna with an ultra-wideband instantaneous bandwidth is shown in Figure 9a, a challenging goal in a compact form. However, if the phase linearity condition is relaxed, we can consider an antenna with multiple resonances in the band as shown in Figure 9b. The resulting phase response around the midpoint of the adjacent resonant frequencies may show a non-linear phase behavior. If the frequency ratio between adjacent resonant frequencies is small, the non-linearity may be minor. Frequency independent antennas, such as equiangular spirals and log-periodic antennas, are examples for this case.

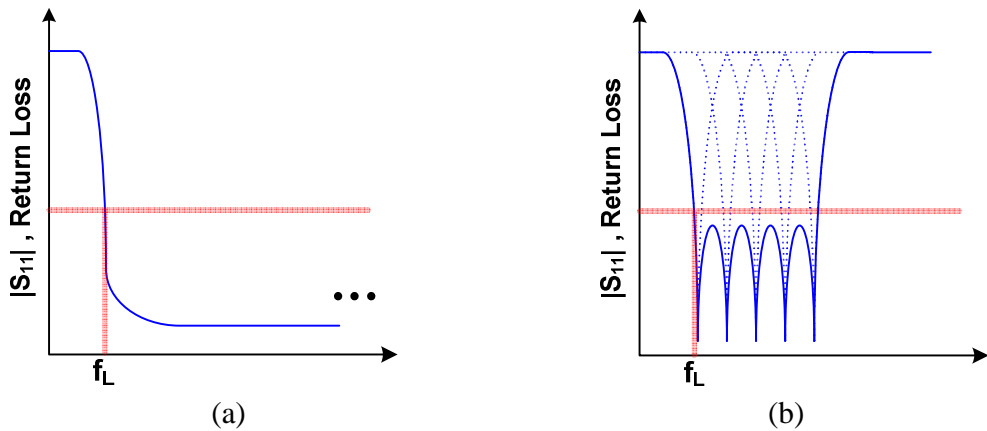


Figure 9. Illustration of types of impedance bandwidth – (a) Instantaneous bandwidth resonances and (b) Continuous wide bandwidth with multiple resonances [12].

If we consider a two-element, log-periodic PIFA without a corporate feed, the resulting PIFA structure will look like a PIFA with a parasitic element. The parasitic element can be excited through capacitive coupling from the main PIFA structure. In many cases of wearable antenna design, the low-profile requirement is emphasized over the size of the antenna foot print. Thus, adding a parasitic element to the antenna design can be a simple, but effective solution to increase the impedance bandwidth.

In order to obtain an initial wideband PIFA design, we first characterized the dielectric property of the given elastomer substrate. A 50Ω , 7mm coaxial air line was prepared. The annular ring shape of the test material was loaded inside the air line as shown in Figure 12. Two-port scattering parameters were measured with a HP 8510C vector network analyzer. The complex permittivity was obtained by using the reflection and transmission coefficient approach [13, 14], based on the analytic model of the coaxial air line and the measured scattering parameters. The estimated material properties at 415 MHz are listed in Table 4.

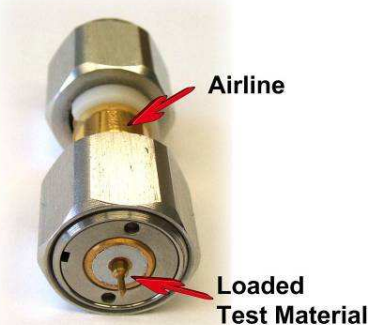


Figure 12. Picture of the 7 mm coaxial air line loaded with a material under test.

Table 4. Estimated property of the elastomer substrate material at 415 MHz.

Frequency	Dielectric Constant (ϵ_r)	Loss Tangent ($\tan\delta$)
415 MHz	≈ 3.1	≈ 0.01

Based on the characterized material properties of the elastomer substrate, a PIFA with a parasitic element was designed. The overall geometry is shown in Figure 13. The main PIFA structure have a shorting strip on the side of the antenna, compared to the conventional PIFA (see Figure 2). One side of the parasitic element was also shorted to the ground plane. The initial design values were obtained by using a generic algorithm to maximize the impedance bandwidth, which is summarized in Table 5.

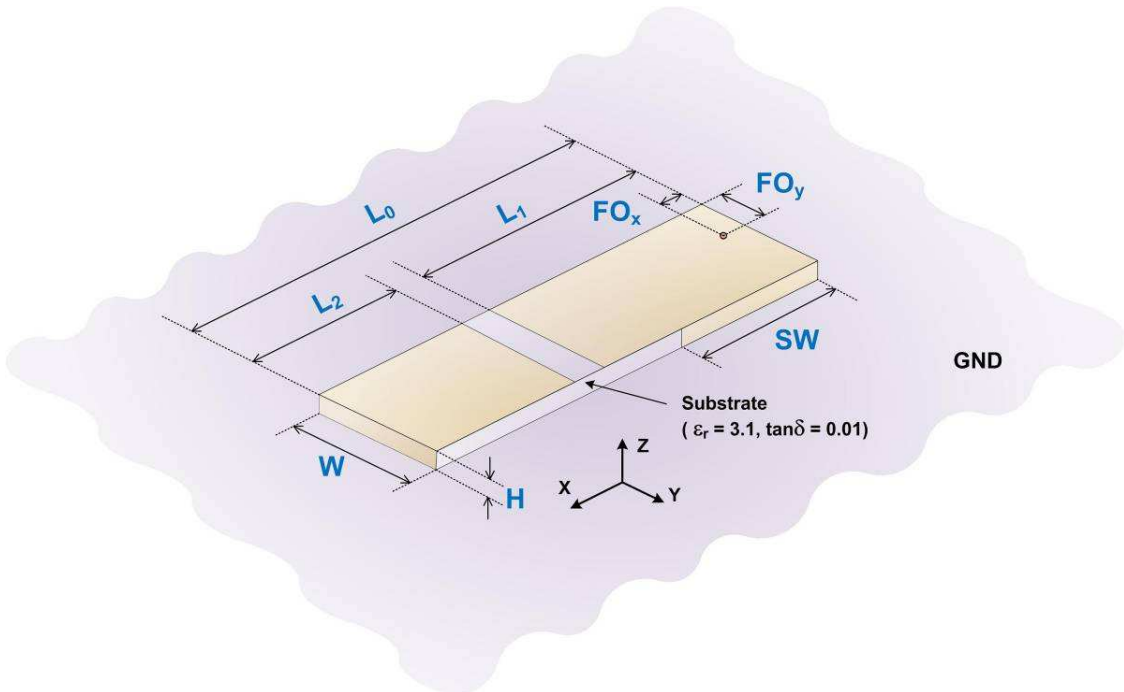


Figure 13. Geometry of a wideband PIFA with a parasitic element.

Table 5. Design parameters of the wideband design.

Parameters	Description	Designed Value
L₀	Length of antenna	10.573"
L₁	Length of the fed patch	5.870"
L₂	Length of the parasitic element	3.874"
W	Width of antenna	3.212"
H	Height of antenna	0.425"
SW	Width of shorting strip	3.754"
FO_x	Feed offset in x-direction	0.234"
FO_y	Feed offset in y-direction	1.503"

In order to observe the detuning effects on the wideband PIFA design, the wideband design on curved surfaces with lateral or longitudinal variations was considered. The detailed deformed shapes are depicted in Figure 14 and Figure 15. The simulation results of the VSWR variation versus the curvature radius are plotted in Figure 16 and Figure 17 for the lateral and longitudinal cases respectively. As the curvature radius decreases for the lateral case, a minor frequency detuning occurs toward a lower frequency, which is similar to the case for the conventional PIFA. The corresponding impedance bandwidth becomes wider with a minor impedance mismatch. Notice that the required impedance bandwidth (413 – 418 MHz) is preserved for the deformed shapes with the lateral variation. For the longitudinal case, as the curvature radius decreases, frequency detuning occurs toward a lower frequency, which is opposite to the case for the conventional PIFA. Other than the extreme case ($R_{\text{curvature}} = 72.77$ mm), the desired impedance bandwidth is preserved with an acceptable VSWR. Therefore, the simulation results suggested that the wideband PIFA antenna is expected to have good tolerance for shape deformation except for some extreme cases.

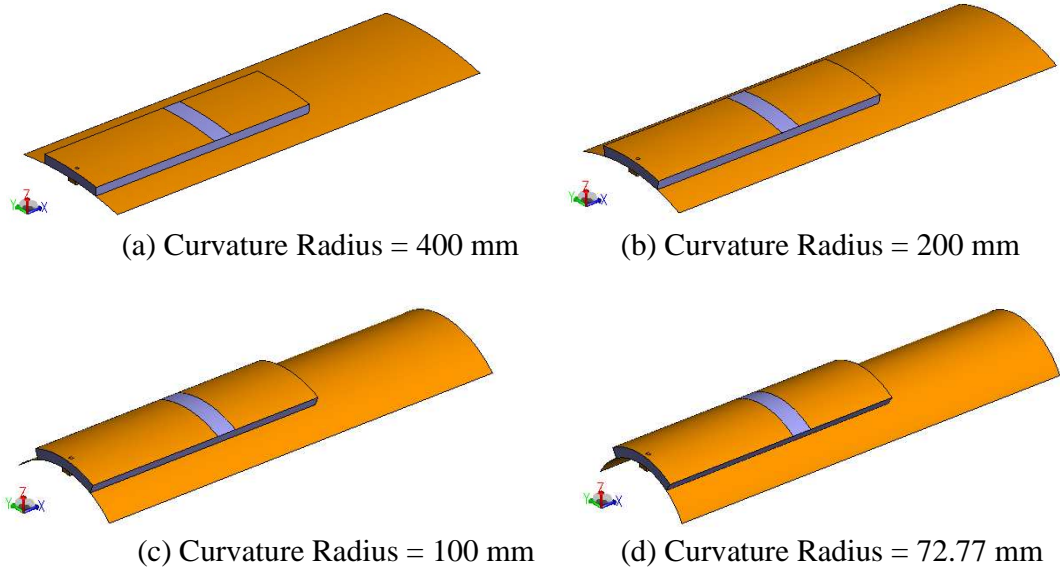


Figure 14. Wideband design on a curved surface with a lateral variation.

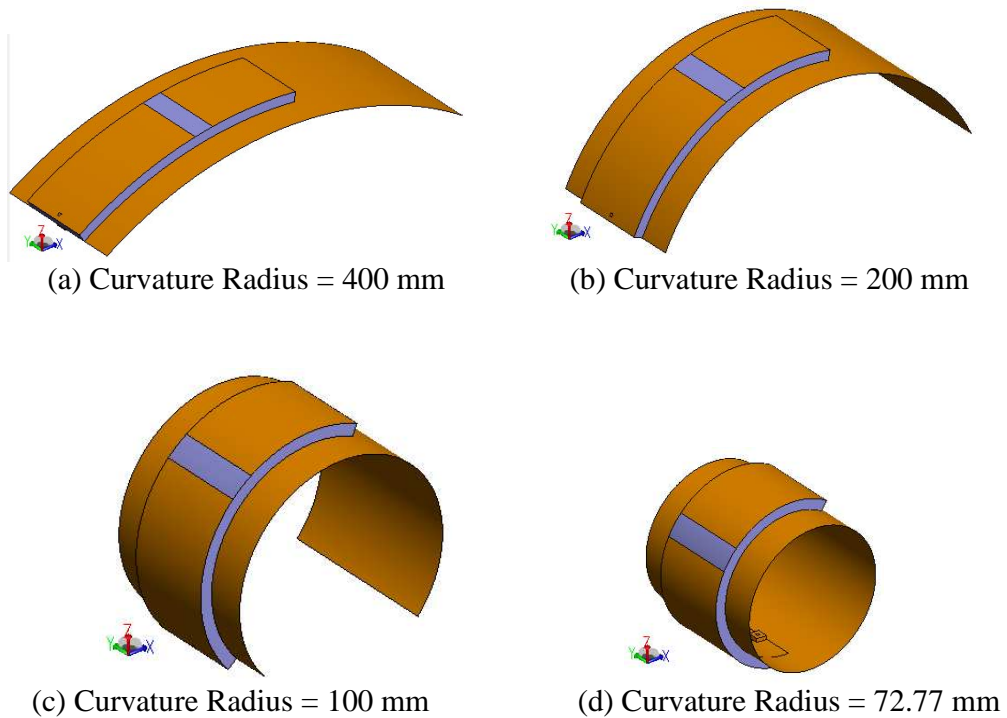


Figure 15. Wideband design on a curved surface with a longitudinal variation.

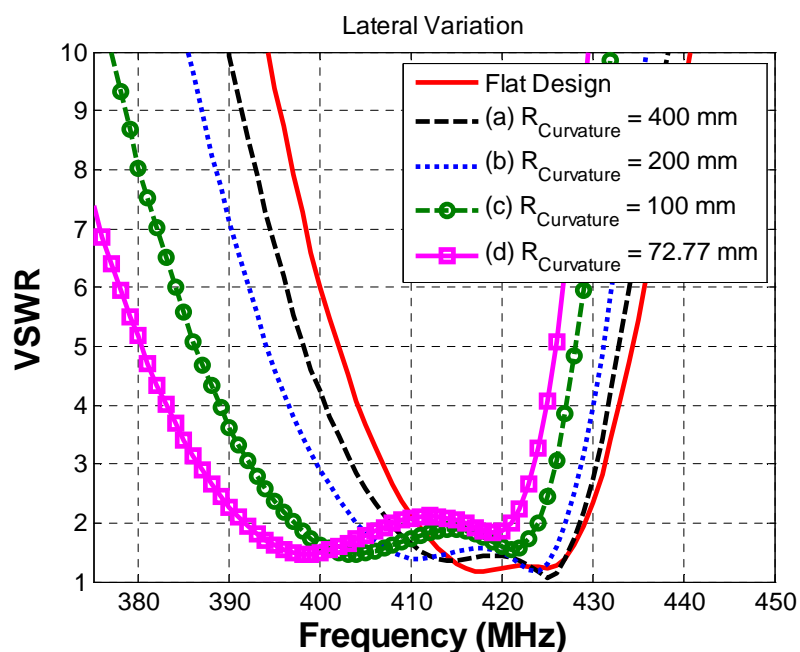


Figure 16. VSWR versus curvature radius of the test antenna on a curved surface with a lateral variation.

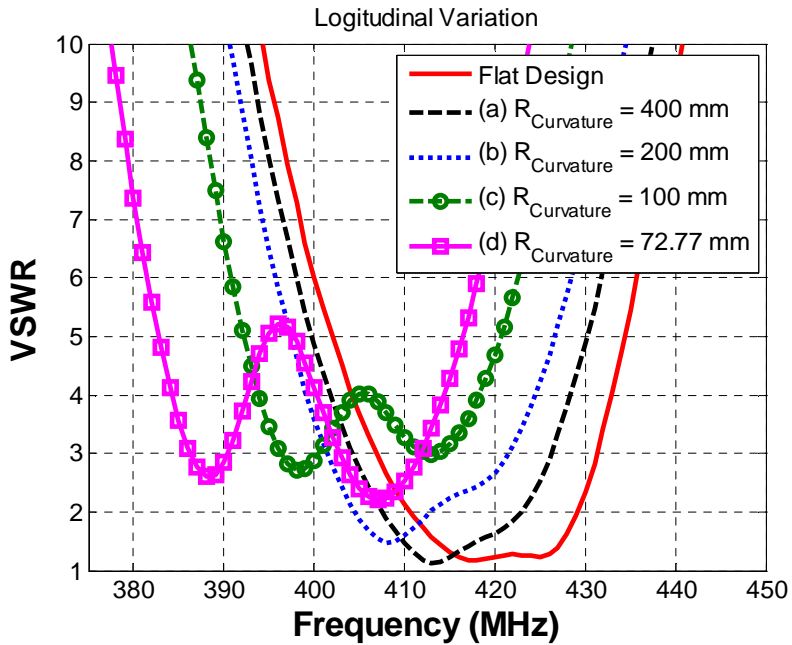


Figure 17. VSWR versus curvature radius of the test antenna on a curved surface with a longitudinal variation.

Another interesting shape deformation of the antenna would be on a human shoulder. As illustrated in Figure 18, the shape deformation will happen in both lateral and longitudinal directions at the same time. As observed in the deforming test for the wideband design, the frequency shift for lateral and longitudinal directions happens in an opposite direction, i.e. toward lower or higher frequencies. Therefore, if both lateral and longitudinal deformations happen at the same time, one may expect that there will be minor detuning effects because the detuning effects from both directions would compensate each other. In order to investigate this aspect, we consider the case of the wideband PIFA design on a human shoulder with different curvature radius, as shown in Figure 19. The simulation results in Figure 20 show that the wideband PIFA design on a human shoulder retain the desired operational bandwidth, even with the bandwidth split in two distinctive parts. Therefore, the human shoulders seem to be a good place to mitigate severe detuning effects.

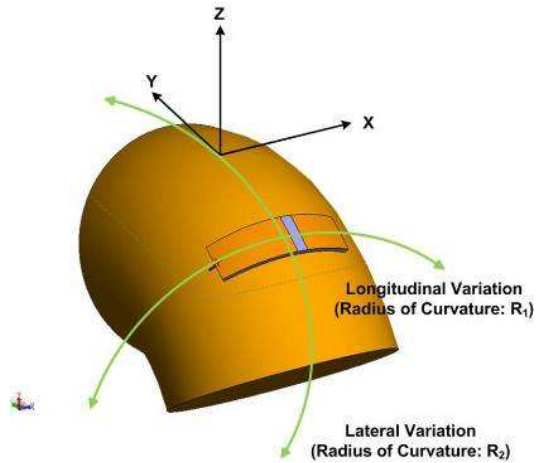


Figure 18. Geometry of the wideband PIFA design on a human shoulder.

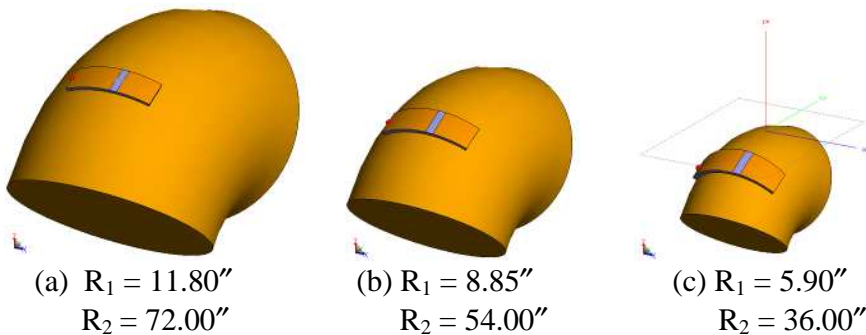


Figure 19. Wideband PIFA on a shoulder with various curvature radii.

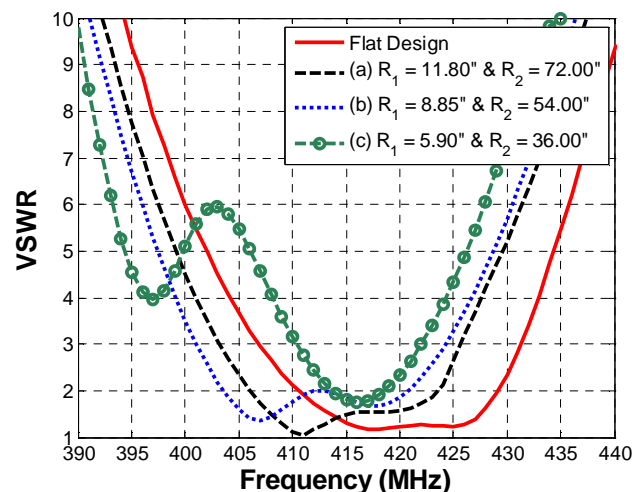


Figure 20. VSWR versus curvature radius for the test antenna on the surface of a human shoulder.

5. Experimental Results

Through the design evolution, both narrowband PIFA (conventional PIFA without a parasitic element) and wideband PIFA designs meeting the given specifications (maximum 0.5" height and frequency coverage of 413 – 418 MHz) were obtained for a primary life support system (PLSS) platform, the backpack of astronaut [15]. As shown as in Figure 21, the fabricated PIFAs were mounted on a PLSS mockup. The return loss and the radiation patters were measured inside the anechoic chamber of the Virginia Tech Antenna Group. Styrofoam was used to support the test antenna. The scanned near-field radiation gain pattern data was transformed to a far-field pattern by using spherical mode decomposition.

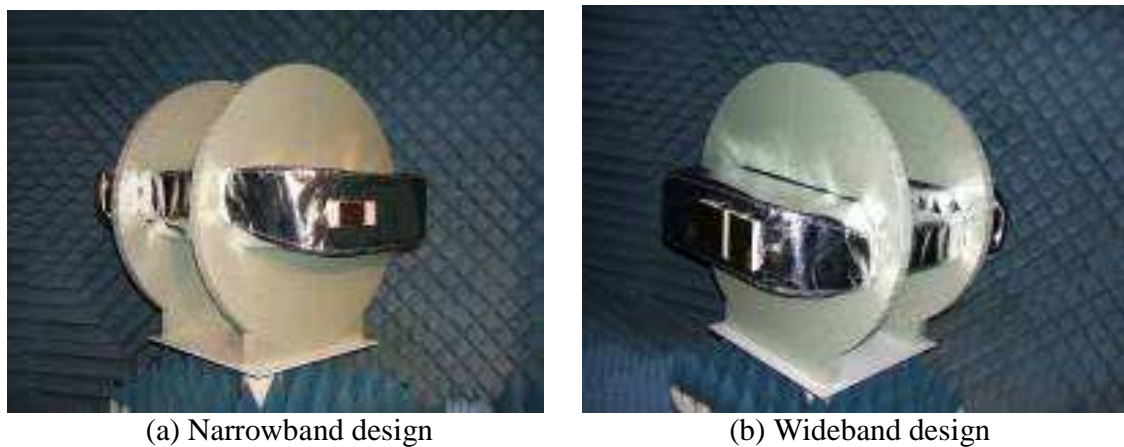


Figure 21. Picture of the measurement setup in Virginia Tech anechoic chamber – (a) Narrowband PIFA (conventional PIFA without a parasitic element) and (b) Wideband PIFA design.

The measured return loss, 2-D radiation gain pattern at principle cuts, and 3-D radiation gain pattern for the narrow and wideband designs are shown from Figure 22 through Figure 25. The fractional impedance bandwidth of narrow and wideband designs was approximately 2.5 % and 7 % respectively. The 3-D patterns between simulations and measurements agreed well. It appears that the overall gain performance of the wideband design slightly outperformed the gain of the narrowband design, but not significantly.

Finally, a spherical coverage analysis was performed for the wideband design case, based on the measured 3-D pattern data. The result in Figure 26 shows that the expected minimum gain of the antenna with vertical polarization (G_0) is approximately -5 dBi if a 50 % spherical coverage is desired. So, the spherical coverage analysis is useful when link budget estimation is necessary to support reliable communications. It also turned out that the spherical coverage of the wideband design outperforms the legacy antenna, but this result is not included in this paper.

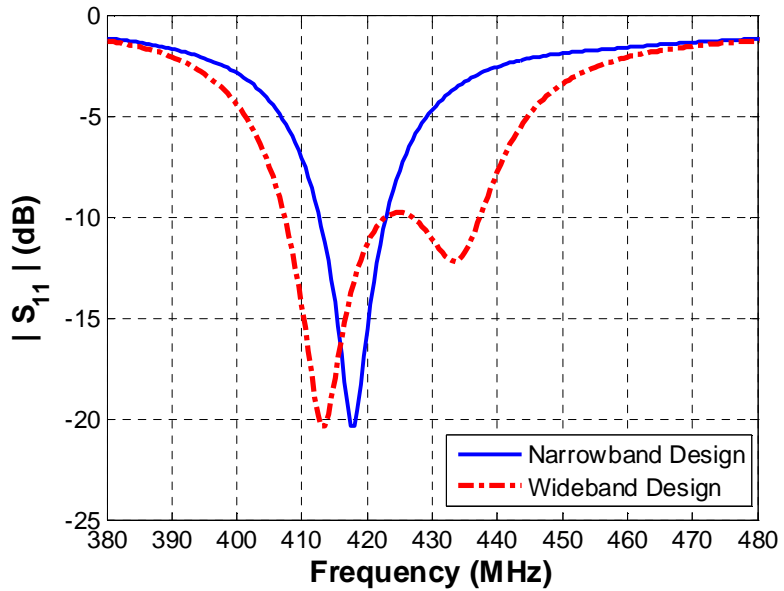


Figure 22. Measured return loss comparison between narrow and wideband designs.

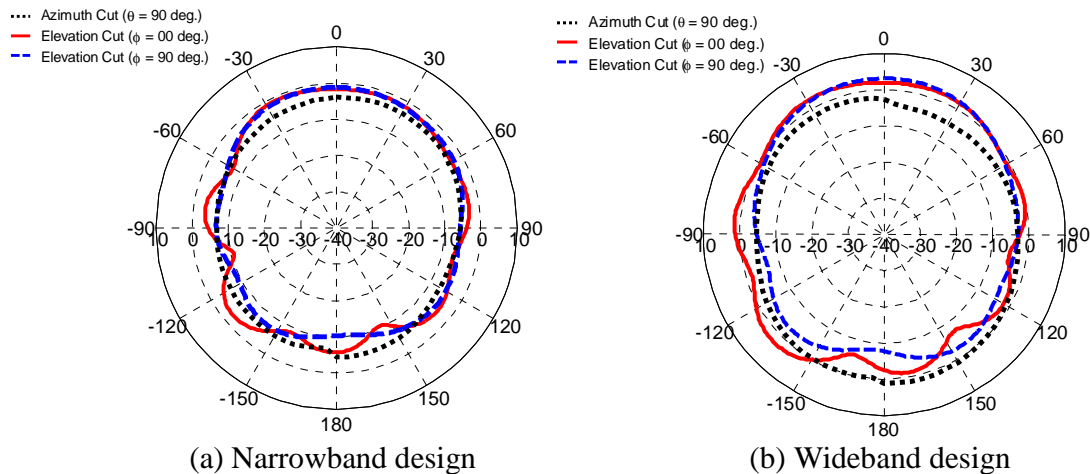


Figure 23. Comparison of principal cuts of measured radiation gain patterns for narrow and wide band PIFA designs at 415 MHz.

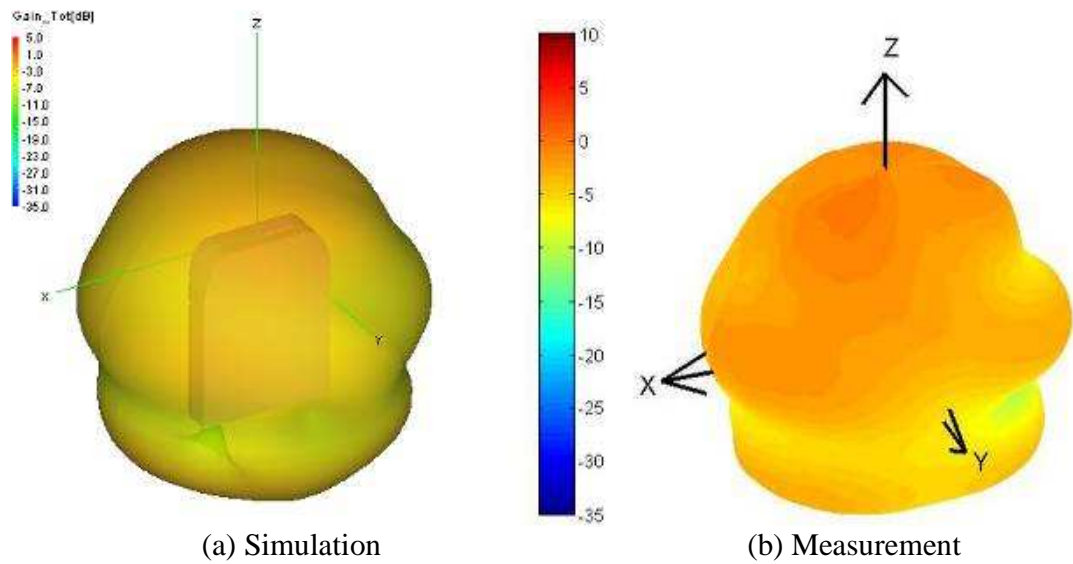


Figure 24. Simulated and measured 3-D gain pattern of narrowband PIFA design (conventional PIFA without a parasitic element) at 415 MHz.

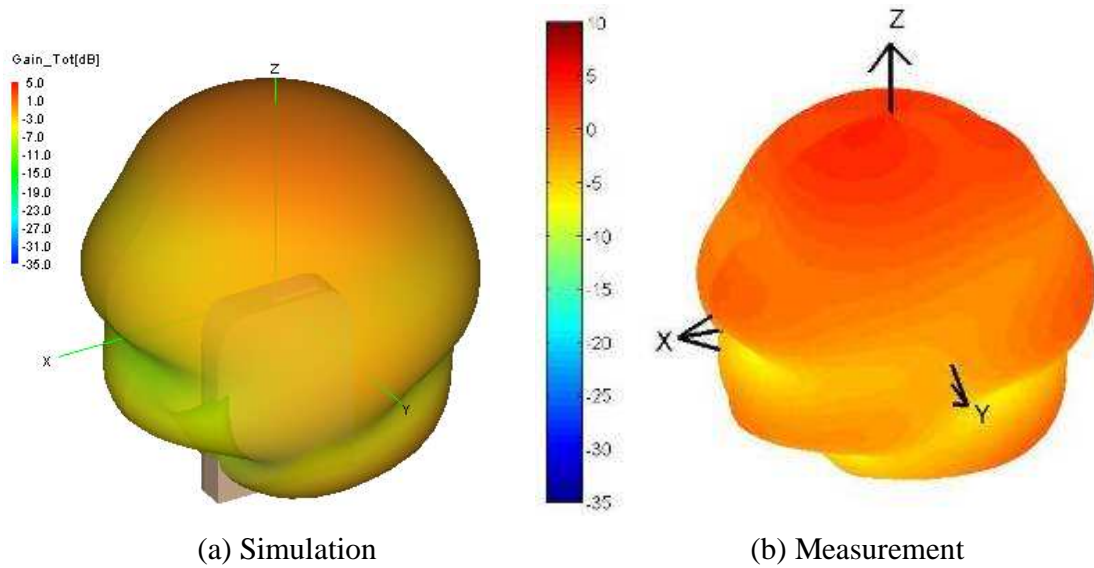


Figure 25. Simulated and measured 3-D gain pattern of wideband PIFA design at 415 MHz.

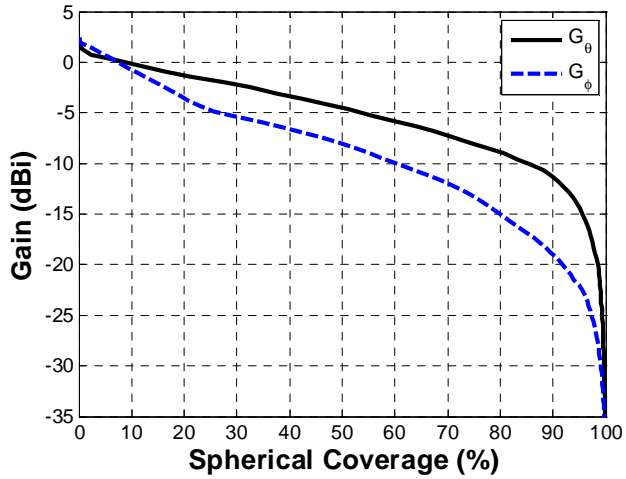


Figure 26. Spherical coverage versus gain for wideband PIFA design.

6. Summary and Conclusions

In this study, a design approach for a wearable antenna with an extremely-low profile (0.5" height, approximately 0.02 wavelength at the center frequency 415 MHz) was investigated.

It was observed that the miniaturization and broadband techniques shown in the literature were not effective because of the desired, extremely low-profile specification. A parametric study using a conventional planar inverted-F antenna led us to the same conclusion. In this case, it was explained that adding resistive loss to the antenna is effective in obtaining the broad impedance bandwidth, rather than tweaking the antenna shape. However, the resultant radiation efficiency (or gain) is reduced. This trade-off was explained by reviewing the classic fundamental-limit theory on antenna size and performance. As an alternative approach to the resistive loading, a continuous broadband approach was discussed by introducing parasitic elements for the case that the size of the antenna footprint is not restricted. The shape deformation studies indicated that the wideband design will be less sensitive to detuning effects due to either lateral or longitudinal shape deformation, compared to the narrowband design. Additional shape deformation tests for the case of the wideband PIFA on a human shoulder indicated that the shoulder may be a good place to mitigate the detuning effects. After characterizing the given elastomer substrate, both narrowband and wideband designs were obtained through design evolutions for the primary life support system of astronauts. The measured fractional bandwidth of the narrow and wideband designs were 2.5% and 7%. The peak gain for a vertical linear polarization was approximately -0.9 dBi and 2 dBi for the narrow and wideband design respectively. A spherical coverage analysis was performed for the wideband design to help link budget estimation. The resulting spherical coverage was found to outperform legacy antennas.

The demonstrated design process and concepts for the extremely-low profile wearable antenna can be applied to other platforms including hats, gloves, vests, and shoes.

Acknowledgements

This work was supported and funded through NASA SBIR Phase II Contract#NNX09CA94C. The efforts of Mr. Robert Boyd and Mr. Christian Hearn to fabricate and characterize the elastomer substrate are gratefully acknowledged.

References

- [1] I. Khan and P. S. Hall, "Multiple Antenna Reception at 5.8 and 10 GHz for Body-Centric Wireless Communication Channels", *IEEE Trans. Ant. And Propagat.*, vol. 57, pp. 248 – 255, 2009.
- [2] J. E. Lebaric *et al.*, "Ultra-wideband, zero visual signature RF vest antenna for man-portable radios", *Proc. MILCOM*, vol. 2, pp. 1291 – 1294, October 2001.
- [3] T. Yang, W.A. Davis, and W.L. Stutzman, "Wearable ultra-wideband half-disk antennas", *Proc. IEEE AP-S Int. Symp.*, vol. 3A, pp. 500 – 503, July 2005.
- [4] C. E. Carr, S. J. Schwartz, and I. Rosenberg, "A wearable computer for support of astronaut extravehicular activity", *Proc. Int. Sym. Wearable Computers*, pp. 23 – 30, 2002.
- [5] M. Canina, D. J. Newman, and G. L. Trott, "Preliminary considerations for wearable sensors for astronauts in exploration scenarios", *Proc. IEEE/EMBS Int. Summer School on Medical Devices and Biosensors*, pp. 16 – 19, 2006.
- [6] L. J. Chu, "Physical limitations on omni-directional antennas" *J. Appl. Phys.*, vol. 19, pp. 1163 – 1175, December 1948.
- [7] W. A. Davis, T. Yang, E. D. Caswell, and W. L. Stutzman, "Fundamental Limits on Antenna Size – A New Limit" in preparation, 2010.
- [8] T. Yang and W. A. Davis, "Miniaturization of Planar Two-Arm Spiral Antennas Using Slow-Wave Enhancements", presented at URSI National Radio Science Meeting (Boulder, CO), January 2006.
- [9] FEKO Suite v.5.5, <http://www.feko.info>.
- [10] E. Chettiar, V. Natarajan, and D. Chatterjee, "Effect of slot width variation on performance of wideband, probe-fed U-slot patch antennas" *Proc. IEEE AP-S Int. Symp.*, vol. 2, pp. 1792 – 1795, June 2004.
- [11] P. Perlmutter, S. Shtrikman, and D. Treves, "Electric surface current model for the analysis of microstrip antennas with application to rectangular elements", *IEEE Trans. Ant. And Propagat.*, vol. AP-33, pp. 301 – 311, March 1985.
- [12] T. Yang, W. A. Davis, W. L. Stutzman, "Antenna Solution for Mitigation of Near-Field Interactions with Devices and Human Operators", presented at URSI National Radio Science Meeting (Boulder, CO), January 2008.
- [13] A. M. Nicolson and G. F. Ross, "Measurement of the intrinsic properties of materials by time domain techniques," *IEEE Trans. Instrum. Meas.*, vol. IM-17, pp. 395 - 402, Dec. 1968.
- [14] W. W. Weir, "Automatic measurement of complex dielectric constant and permeability at microwave frequencies," *Proc. IEEE*, vol. 62, pp. 33-36, Jan. 1974.
- [15] http://en.wikipedia.org/wiki/Primary_Life_Support_System.

Investigation of Miniaturized and Dual-Band Slot Antennas for RFID Systems

J. E. Ruyle and J. T. Bernhard

Department of Electrical and Computer Engineering

University of Illinois at Urbana-Champaign

Urbana, IL 61801

jruyle2@illinois.edu, jbernhar@illinois.edu

<http://antennas.ece.illinois.edu>

Abstract: RFID systems with “peel-and-stick” labels are currently limited to tracking items with nearly electromagnetically transparent material properties. This limitation stems from the antenna choice for these labels - a dipole variant. The slot antenna, the effective inverse of the dipole, is investigated as an alternative RFID antenna option. A miniaturization and dual-band design technique is shown.

1 Introduction

Most RFID antennas are “dipole-like” meander lines, loops, or folded dipoles. These antennas perform poorly near ground planes or any material that isn’t electromagnetically transparent [1, 2]. While there are RFID antennas designed to be attached to metallic objects [3, 4], these antennas are generally complicated, difficult to manufacture, and bulky compared to the traditional “peel-and-stick” antennas used in RFID. The present work details the investigation of the slot antenna, the inverse of the dipole, as a viable alternative for “peel-and-stick” RFID systems for non-electromagnetically transparent objects. Dual or multi-band operation is possible with the antenna structure pursued so that a final design will provide a flexible sensing option in a range of application areas. The present work focuses on the development of a design model that can be used to enable both single and dual-band behavior.

The next section provides a discussion of the miniaturization method chosen for the antenna design, loading the slot antenna. This miniaturization method also provides for multi-band operation. Section 3 details a transmission line model of a slotline inductor - a convenient loading method for a slot antenna. In section 4, to enable both single and dual-band behavior, the transmission line model is compared to simulated and measured results.

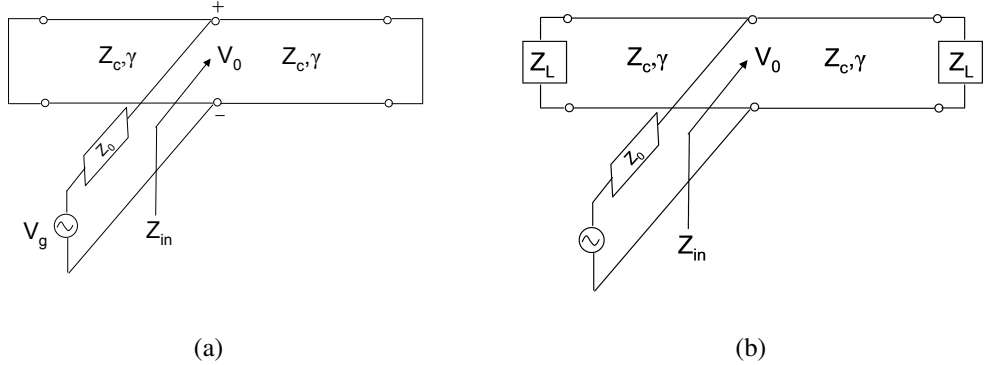


Figure 1: Transmission line model of slot antenna (a) traditional and (b) loaded slot.

Finally, an RFID antenna design is presented which is suitable for a “peel-and-stick” RFID system.

2 Loaded Slot Antennas

A traditional straight half-wavelength slot antenna would be too large for an RFID antenna at commonly used RFID frequencies. We investigated loading the slot antenna to reduce its size. We began our investigation with a transmission line model of the antenna.

The transmission line model for a slot antenna equates the power delivered to a lossy transmission line and the power radiated by a slot [5]. This model was originally derived by Himdi and Daniel in [5]. The model assumes that the slot antenna can be represented by two shorted lossy transmission lines in parallel, as shown in Fig. 1(a). Using the field requirements from transmission line theory, the far-field expressions for the radiated electric field are determined analytically. From these, the total power radiated is found in terms of the radiated loss per-unit-length (α). α is found by equating the power delivered to the slot and the power radiated by the slot.

This same method can be employed with loads at the end of the slot instead of shorts as seen in Figure 1(b). By loading the slot, the total size of the slot can be greatly reduced. If the slot antenna is correctly loaded for a particular frequency, the input impedance seen at the feedpoint is the same for the full-sized or loaded slot. The concept of loading the ends of an antenna is not new. The antenna used by Hertz to demonstrate electromagnetic radiation was a dipole antenna loaded with spheres on each end [6]. The authors in [7] displayed the effectiveness of end-loading for slot antennas in particular. If an effective length of less than a half-wavelength is desired for the slot, the loads should be inductive. A slotline inductor provides an easily integratable inductance for the slot antenna and was used for the present antenna design.

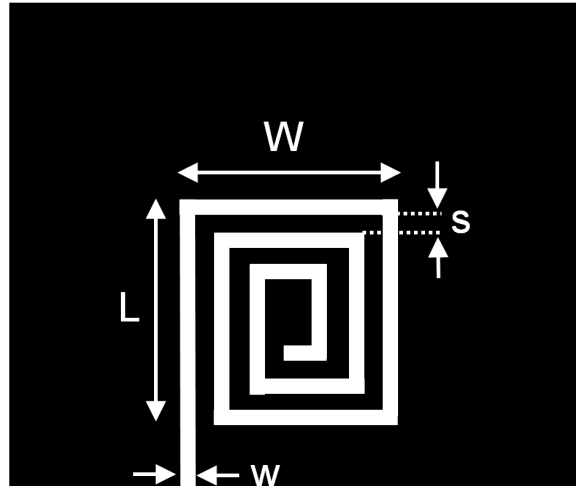


Figure 2: Image of slotline inductor with dimensions labeled.

3 Slotline Inductor Model

A transmission line model of the slotline inductor was pursued to aid in the design process of the inductor-loaded slot antenna.

A depiction of a three-turn slotline inductor is shown in Figure 2 with dimensions. As can be seen in the figure, the planar inductor is a set of four connected multi-conductor transmission lines. The transmission line model for the slotline inductor is based upon the work of Shepherd outlined in [8]. Since multi-line transmission line characteristics are time consuming and difficult to compute, the model by Shepherd seeks to use the characteristics of two-line coupled lines to approximate the multi-line transmission line.

Shepherd deconstructs the multiline transmission line into parallel singly coupled transmission lines. One side of the 3-turn inductor is depicted in Figure 3. The figure shows how the coupling lengths for a section of line are calculated. In the figure the coupling lengths for Line 1 coupling to Lines 2 and 3 are shown. In the figure the sections of the lines are denoted by L_{xy} . The x denotes the section to which the line belongs. The y denotes to which secondary line the primary line is coupling. In the square spiral inductor a length of line can be broken up into three sections. In the first section, the line is in isolation. In the second section, the line couples to the neighboring line. In the third section, the line is again in isolation. In the model the coupling length is an average of the two lengths of line. The difference between the coupling length and the actual physical lengths is halved and is used as the length of the line in sections one and three. If the section of line under consideration is an inner line and the coupling configuration under analysis is to a line further out in the inductor, the entire length of line is considered to be coupling to the outer line.

Current curving has long been noticed in corners of transmission lines. Shepherd assumed in his model that there was no current curving and merely used the midpoint of the diagonal line showing the intersection between sides of the inductor. We assumed, and

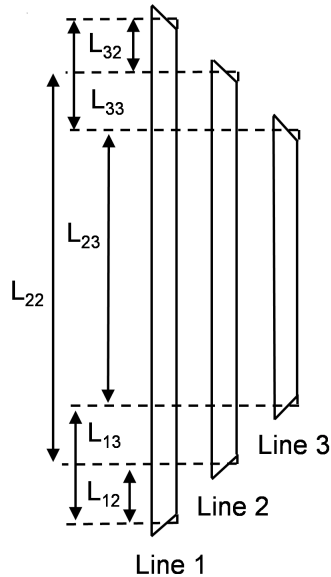


Figure 3: Image of one section of slotline inductor with line length dimensions labeled.

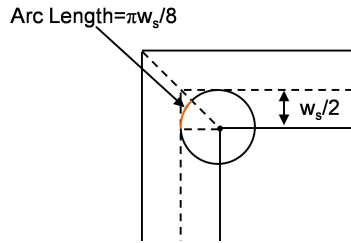


Figure 4: Image of a corner of the slotline inductor depicting the assumption of field curving at corners.

noticed this effect in images of fields in HFSS[®] [9], that the current curving phenomena occurred with electric fields in slot-line. The image in Figure 3 depicts how we calculate the effective length for the corner of a slot transmission line. This effective length is used in the calculation of lengths shown in Figure 3. The length we calculate is the same as is often used in microstrip. As can be seen in the figure, a circle (with a radius of half of the slot width) is placed with a center-point at the lower right of a corner. The arc (shown in grey), which is one-quarter of the total circumference of the circle, is the effective length of one-half of a corner in the slot-line inductor.

Using the lengths defined above, the method for assembling the transmission line model of the slotline inductor is as follows. An ABCD matrix is calculated for each pair of coupled lines in isolation. In the case of the three turn inductor, this would entail an ABCD matrix for the coupling configuration between Line 1 and Line 2 and another for the configuration between Line 1 and Line 3. These ABCD matrices are the result of multiplying three ABCD matrices together for each section of the line (as discussed earlier) where section

2 is the coupled line configuration and sections 1 and 3 are the line in isolation. Once the cascaded ABCD matrices are calculated each of these matrices are converted to Y-matrices. The Y-matrices are added together to create a parallel configuration. This Y-matrix describing the multi-line transmission line is then converted to an ABCD matrix. This process is repeated for every length of line in the inductor. Then, all of the ABCD matrices for every length of line are multiplied together in the proper order to obtain a total ABCD matrix describing the inductor.

4 Calculation of Coupled Slotline Characteristics

To perform the calculations described above, the even and odd mode characteristic impedance and effective wavelengths must be known. These quantities have been derived by Simons [10, 11]. The calculations are based upon Cohn's method [12] which finds characteristic impedance and effective wavelength for a single slot. Cohn's method must be understood first before Simon's method is explained. Therefore, Cohn's method is outlined below.

Two images depicting the setup for Cohn's method are shown in Figure 5. In essence, Cohn places electric (or magnetic) walls through and around the slot to create a waveguide structure with the slotline as a capacitive iris in the waveguide [12]. Cohn derives the susceptance for both electric and magnetic walls and shows that the solutions converge. The walls perpendicular to the slot are placed a half-wavelength apart which is the location of field nulls; therefore, they do not disturb the fields of the slot. The walls parallel to the slot are placed symmetrically far enough apart from the slot to not affect the slot fields. This distance was found by Cohn to be approximately one wavelength [12]. The susceptance formula derived by Cohn is in terms of a , which is defined in the figure as the separation between the wall perpendicular to the slot. The total susceptance at the slot is derived as a sum of the susceptance looking into the dielectric β_d and looking into the air β_a . When the susceptance that he derives for the capacitive iris is equal to zero, the slot is resonant according to the transverse resonance method. When the slot is resonant, a is equal to the half of the effective wavelength [12]. We found the value of a through an optimization routine in Matlab minimizing the value of the susceptance at the slot. An expression for the characteristic impedance is also derived based upon an iterative procedure using the susceptance formula for the slot [12].

The fields for odd (a) and even (b) modes on the coupled slot are shown in Figure 6. For the odd mode, a magnetic wall can be placed halfway between the two slots. This is the mode in which coplanar waveguide operates. For the even mode, an electric wall can be placed halfway between the two slots.

Simons [10, 11] slightly alters the configuration of Cohn to derive the characteristic impedance and effective wavelength of the even and odd modes of coupled slotline. His configuration is shown in Figure 7. Simons changed the setup of the walls parallel to the slotline to be asymmetric. Instead of being sufficiently far away to not disturb the fields

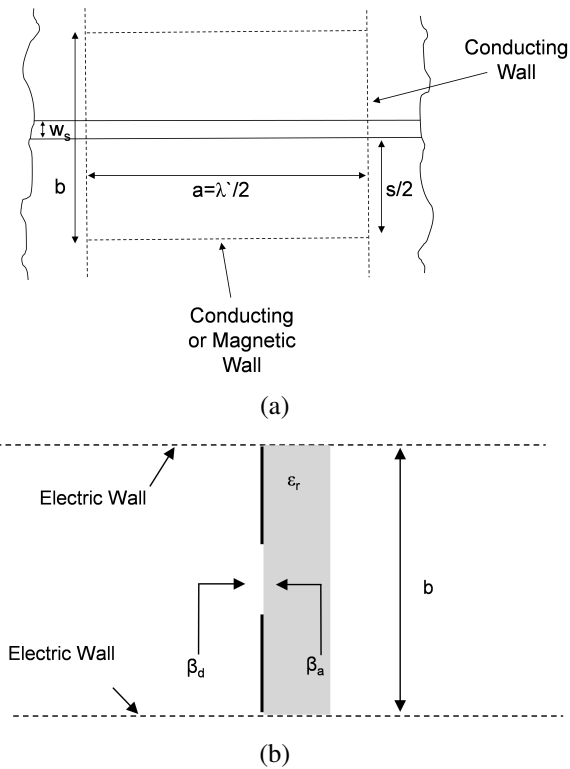


Figure 5: Image describing the setup Cohn used to analyze the slotline including (a) top view and (b) side view.

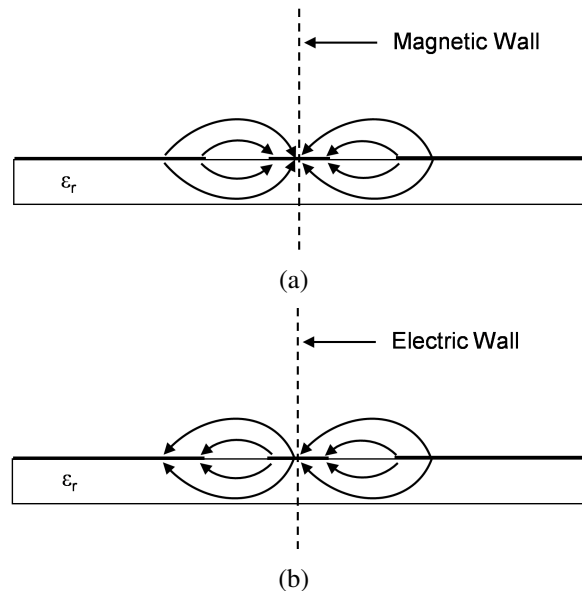


Figure 6: Image depicting the (a) odd mode and (b) even mode fields in a coupled slot configuration.

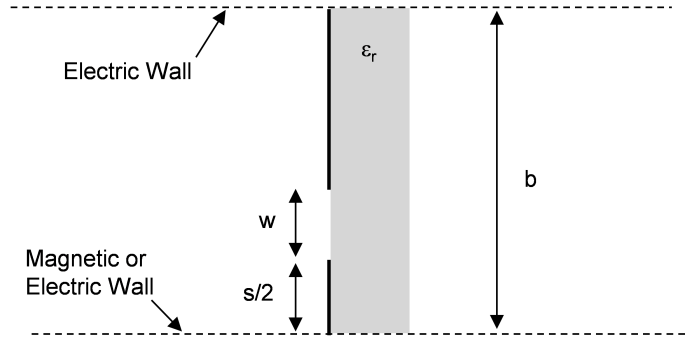


Figure 7: Image depicting the setup Simons [10, 11] used to analyze the coupled slotline.

Simons sets one wall to be half of the distance (s) of the separation between the coupled slots. For the odd mode, Simons derives the susceptance of the slot assuming the wall between the slots is magnetic. For the even mode, the wall is set to be electric. The expressions that Cohn derived for effective wavelength and characteristic impedance can be used with the susceptance derived by Simons to find the even and odd mode characteristic impedance and effective wavelength. Setting up the problem in this manner allows one to find the characteristic impedance and effective wavelength for a purely even or odd mode.

For the transmission line model of the slotline inductor, if the total length of the inductor (stretched out) is less than a quarter wavelength long, it is assumed that only the even mode exists. If the inductor length is between a quarter and a half wavelength, the odd mode is stepped in with frequency linearly such that by the time the inductor is a half-wavelength long, the assumed effective wavelength is the arithmetic average of the even and odd modes and the characteristic impedance is the geometric mean of the even and odd mode characteristic impedance.

A transmission line model for the slotline inductor was developed using the methods outlined above. The results of this model is compared with simulated (HFSS® [9]) and measured results in the next section.

5 HFSS Simulation Setup

The setup for the simulation of the slotline inductor in HFSS® [9] is shown in Figure 8. Two slotline inductors are excited in parallel with a lumped port. The impedance of a single slotline inductor is found by multiplying the impedance at the lumped port by two and then de-embedding using transmission line equations to the input port of the slotline inductor.

6 Results Comparison

The results of the transmission line model of the slotline inductor compared with the HFSS® simulation in the UHF band are shown in Figure 9. The dimensions of the in-

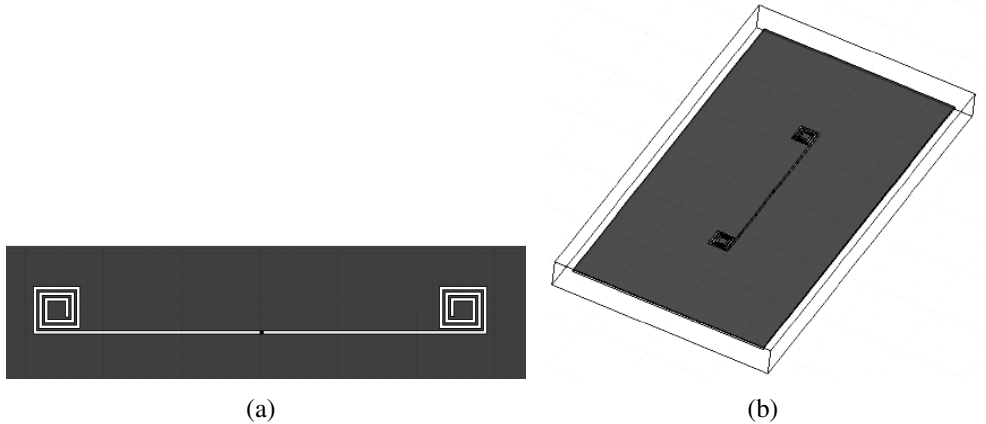


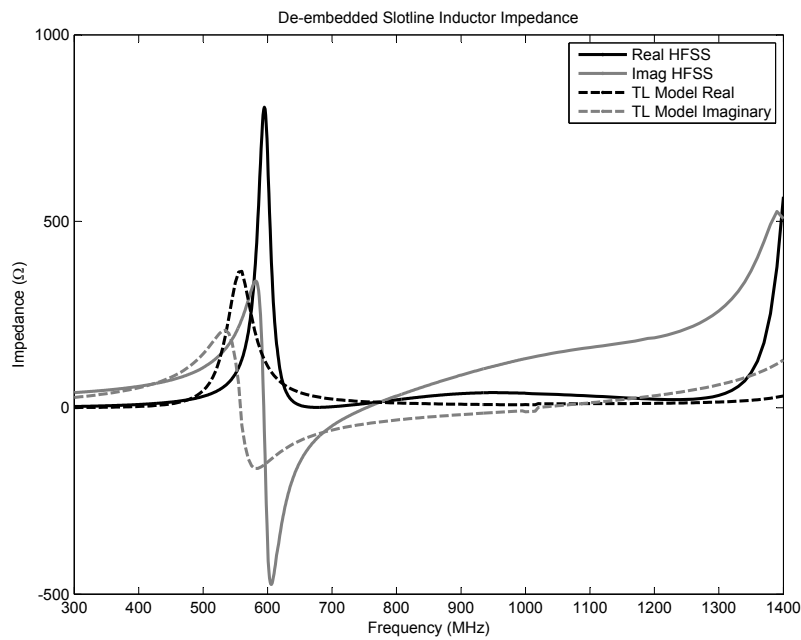
Figure 8: Images depicting the simulation setup for the slotline inductor in HFSS with views (a) zoomed in (b) zoomed out.

ductor under consideration are: $L = 15 \text{ mm}$, $W = 15 \text{ mm}$, $w_s = 1 \text{ mm}$, $h = 1.524 \text{ mm}$, $\epsilon_r = 2.94$, $L_{ext} = 107.5 \text{ mm}$. The dimensions not defined above are: h (height of substrate), ϵ_r (relative dielectric constant of substrate), and L_{ext} (length of transmission line to lumped port in simulation). A comparison with the HFSS® results de-embedded to the input port of the slotline inductor are shown in Figure 9(a). A comparison with the results from the HFSS simulation not de-embedded and the transmission line model extended by the necessary length of transmission line is shown in Figure 9(b). As can be seen in both figures, the model works well up to around 650 MHz. After this frequency, corner effects that are not taken into account in the model become important and the simulation results and transmission line model do not match well.

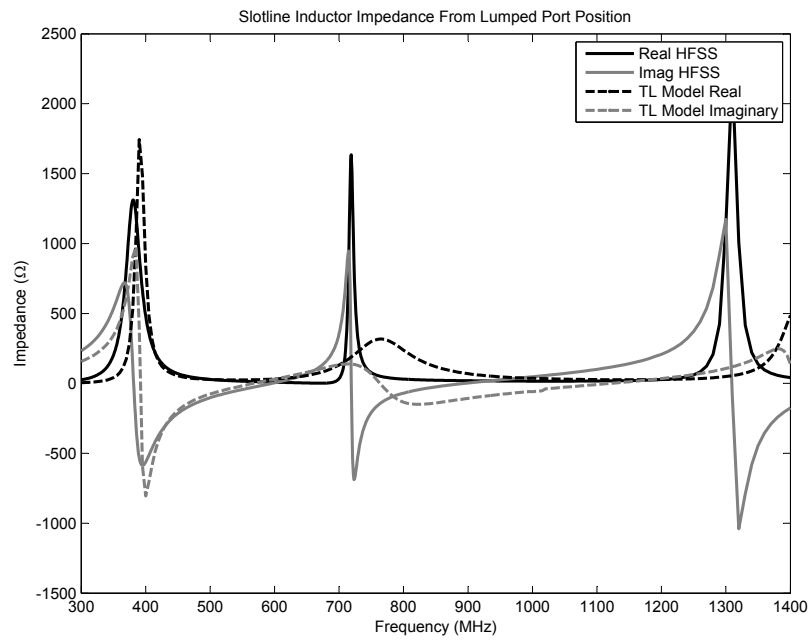
7 Antenna Measurement Results

A slot antenna was constructed with slotline inductors loading both ends. A picture of the constructed antenna is shown in Figure 10. The dimensions of the slotline inductor are identical to the dimensions discussed earlier except for the transmission line extension: $L = 15 \text{ mm}$, $W = 15 \text{ mm}$, $w_s = 1 \text{ mm}$, $h = 1.524 \text{ mm}$, $\epsilon_r = 2.94$, $L_{ext} = 2 \text{ mm}$. The slot that is fed connecting the two slotline inductors has dimensions, $w_a = 3 \text{ mm}$ (width of slot), $L_a = 15 \text{ mm}$ (length of slot). The slot is fed at the center.

The measured results were compared to the transmission line model and the HFSS® simulation. This comparison is shown in Figure 11. As can be seen in the figure, both the transmission line model and the HFSS simulation predict a lower frequency response than what is measured. This was thought to be due to the fact that the impedance of the coaxial probe is neglected. However, a model by Knorr [13] for the coaxial probe was included in the extraction and the frequency of the measured results was still approximately 100 MHz higher than the simulated results. Also, the response of the transmission line model is



(a)



(b)

Figure 9: Comparison of transmission line model versus HFSS[®] for slotline inductor impedance at UHF band (a) de-embedded to input port of slotline inductor (b) from lumped port position in HFSS[®] simulation.



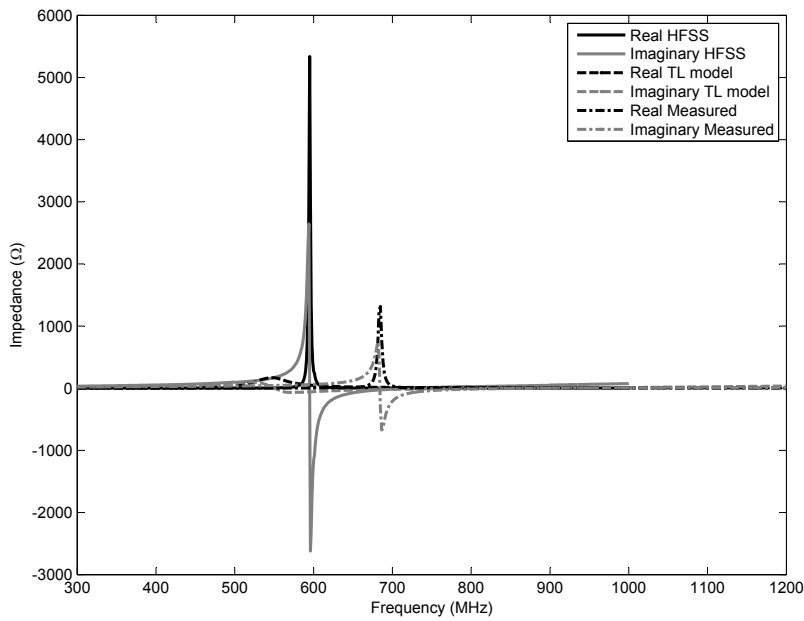
Figure 10: Picture of constructed and measured slot antenna. A penny is placed next to the antenna to show size. The ground plane is larger than what is shown; the picture is zoomed in to show detail. The ground plane is 30 mm by 20 mm.

much smaller in magnitude than either the simulation or measured results. This is due to the fact that the transmission line model calculates the attenuation constant for the slotline assuming the line is straight. Since the line is not straight but in fact coiled in the inductor, this assumption overestimates the attenuation constant.

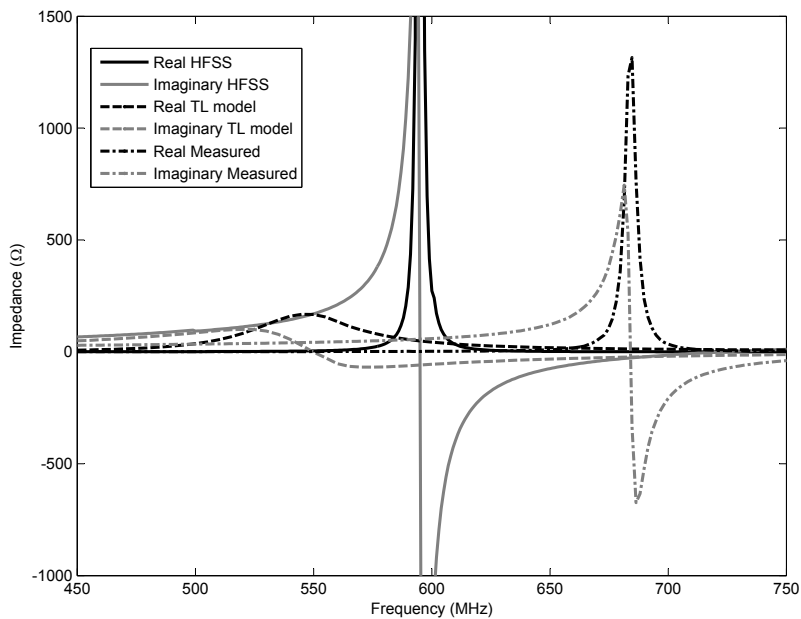
8 Miniaturized Slot Antenna with Reflecting Plane and Edge Serrations

A reflecting plane was added to the design of the miniaturized slot antenna. Slot antennas with reflectors (second ground plane) often couple energy into a parallel plate mode between the ground plane and the reflecting plane [14, 15, 16]. The parallel plate becomes a cavity with the walls appearing as reactive loads to the slot antenna. Instead of attempting to reduce this mode, as the authors did in [14, 15, 16], edge treatments could be used to help this mode escape the substrate. We showed in [17] that edge serrations can reduce the cavity effect in a parallel plate configuration.

A depiction of the miniaturized slot antenna with edge serrations and a reflecting plane is shown in Figure 12. The height of the substrate is 0.762 mm, which is suitable for a “peel-and-stick” form factor. A Smith Chart describing the simulated impedance characteristics of the antenna is shown in Figure 13. As can be seen in the figure, the antenna displays a near 50Ω impedance match. Although the radiation pattern is different for the slot with edge serrations than a traditional slot, these RFID antennas will likely be used in high scattering environments. Therefore, local scattering makes obtaining a pattern match to a traditional slot antenna of low importance.



(a)



(b)

Figure 11: Graph depicting comparison of input impedances found using transmission line model, HFSS[®], and measured results (a) zoomed out (b) zoomed in.

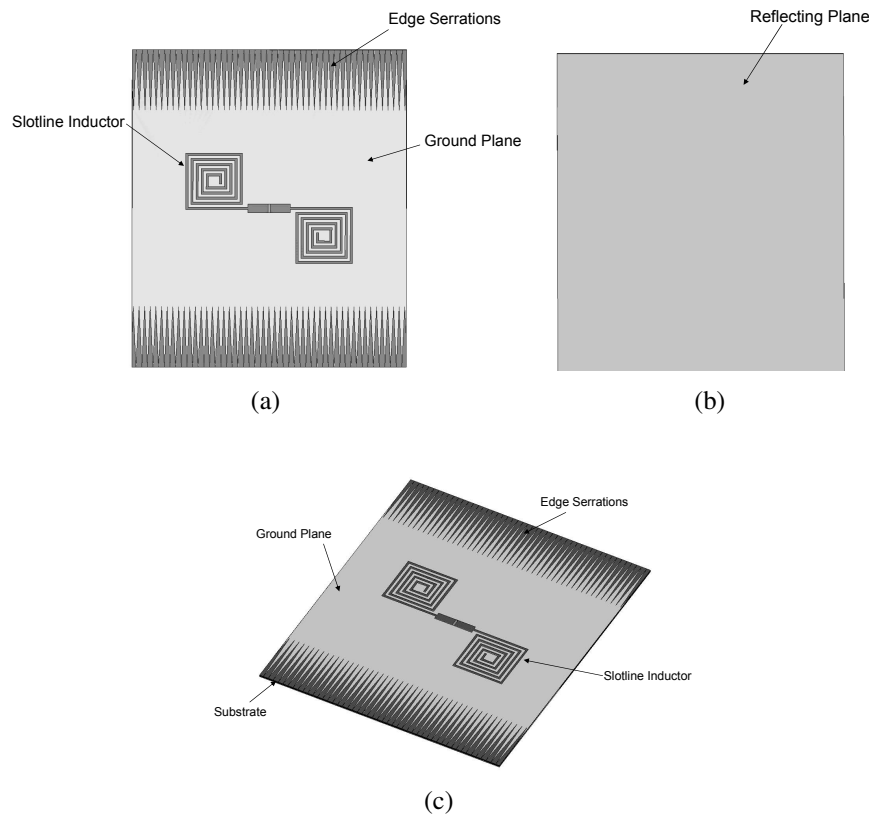


Figure 12: Depiction of miniaturized slot antenna with edge serrations and reflecting plane
 (a) top view (b) bottom view (c) isometric view.

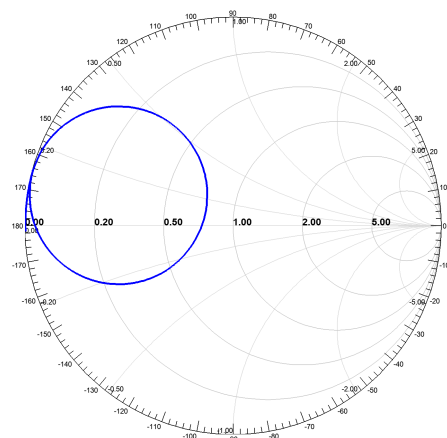


Figure 13: Smith Chart describing impedance properties of miniaturized slot antenna with edge serrations.

9 Conclusions and Future Work

An antenna suitable for a “peel-and-stick” RFID system for non-electromagnetically transparent objects was developed. A transmission line model for a rectangular slotline inductor was also developed to aid in the design of the antenna. This model is relatively accurate at low frequencies. However, at high frequencies, corner effects become important and the model no longer matches well. The slotline inductor model was incorporated into the transmission line model for the slot antenna. The transmission line model with the slotline inductor model predicted resonant frequency within 50 MHz, but the magnitude of the predicted response was incorrect. This was largely because the model assumes the slot is straight to predict the attenuation constant of the slotline. Since the effects of corners become more prominent as frequency increases, future work will pursue a circular inductor.

Future work will also develop a transmission line model for the circular inductor and use this model to optimize the design of the slotline-inductor-loaded slot antenna to operate at multiple frequency bands. A transmission line model for the slotline inductor at both low and high frequencies is needed for the reproducible, and optimizable, design of the slotline inductor loaded slot antenna. A transmission line model of the circular inductor should be more accurate than that of a rectangular inductor at higher frequencies due to the lack of corners. With a transmission line model for the slotline-inductor loaded antenna, a single antenna can be designed to work at multiple frequency bands.

10 Acknowledgments

This research was supported by the Laboratory Directed Research and Development program at Sandia National Laboratories. Sandia is a multiprogram laboratory operated by Sandia Corporation, a Lockheed Martin Company, for the United States Department of Energy’s National Nuclear Security Administration under contract DE-AC04-94AL85000.

References

- [1] J. Prothro, G. Durgin, and J. Griffin, “The effects of a metal ground plane on RFID tag antennas,” in *IEEE Antennas Propag. Soc. Int. Symp.*, pp. 3241–3244, 2006.
- [2] J. Griffin, G. Durgin, A. Haldi, and B. Kippelen, “RF tag antenna performance on various materials using radio link budgets,” *IEEE Antennas Wireless Propag. Lett.*, vol. 5, p. 247, 2006.
- [3] C. Cho, H. Choo, and I. Park, “Design of planar RFID tag antenna for metallic objects,” *Electron. Lett.*, vol. 44, no. 3, pp. 175–177, 2008.

- [4] H. Son, J. Yeo, G. Choi, and C. Pyo, “A low-cost, wideband antenna for passive RFID tags mountable on metallic surfaces,” in *IEEE Antennas Propag. Soc. Int. Symp.*, pp. 1019–1022, 2006.
- [5] M. Himdi and J. Daniel, “Analysis of printed linear slot antenna using lossy transmission line model,” *Electronics Letters*, vol. 28, no. 6, pp. 598–601, 1992.
- [6] J. Bryant, “The first century of microwaves-1886 to 1986,” *IEEE Transactions on Microwave Theory and Techniques*, vol. 36, no. 5, pp. 830–858, 1988.
- [7] R. Azadegan and K. Sarabandi, “A novel approach for miniaturization of slot antennas,” *IEEE Trans. Antennas Propag.*, vol. 51, no. 3, pp. 421–429, 2003.
- [8] P. Shepherd, “Analysis of square-spiral inductors for use in MMICs,” *IEEE Transactions on Microwave Theory and Techniques*, vol. 34, no. 4, pp. 467–471, 1986.
- [9] Ansys, “HFSS,” *Canonsburg, PA*, vs. 12.
- [10] R. Simons and R. Arora, “Double-slot fin-line structure for millimeter wave applications,” in *IEEE Proceedings*, vol. 67, p. 1159, 1979.
- [11] R. Simons, *Studies on microwave slot-line and integrated fin-line*. PhD thesis, Department of Electrical Engineering, Indian Institute of Technology, New Delhi, 1981.
- [12] S. Cohn, “Slot line on a dielectric substrate,” *IEEE Transactions on Microwave Theory and Techniques*, vol. 17, no. 10, pp. 768–778, 1969.
- [13] J. Knorr, “Slot-line transitions,” *IEEE Trans. Microwave Theory Tech*, vol. 22, no. 5, pp. 548–554, 1974.
- [14] M. Qiu and G. Eleftheriades, “Highly efficient unidirectional twin arc-slot antennas on electrically thin substrates,” *IEEE Trans. Antennas Propag.*, vol. 52, no. 1, pp. 53–58, 2004.
- [15] J. Kim and J. Yook, “A parallel-plate-mode suppressed meander slot antenna with plated-through-holes,” *IEEE Antennas Wireless Propag. Lett.*, vol. 4, 2005.
- [16] C. Locker, T. Vaupel, and T. Eibert, “Radiation efficient unidirectional low-profile slot antenna elements for X-band application,” *IEEE Trans. Antennas Propag.*, vol. 53, no. 8 Part 2, pp. 2765–2768, 2005.
- [17] J. E. Ruyle and J. T. Bernhard, “Investigation of edge serrations to eliminate cavity effect in parallel plate configurations,” in *Proc. USNC-URSI National Radio Science Meeting*, Boulder, CO, January, 2010.

Wideband Horizontally Polarized Omni-Directional Antenna

Raymond Pickles
Code 5317
U.S. Naval Research Laboratory
Washington, D.C. 20375

Abstract - A wideband horizontally polarized omni-directional antenna is presented. The antenna produces a radiation pattern with less than 0.5 dB variation over 360 degrees of azimuth and has better than a 20% bandwidth. The polarization purity is 15 to 20 dB, and can be improved at the expense of bandwidth.

The antenna consists of a square array of four vertical slots fed by a central coaxial transmission line. The shape of the slots and the conductors exciting the slots are designed to enhance the bandwidth of the antenna.

Details of the numerical simulations employed to design the antenna, and measured radiation patterns and impedance plots are presented.

The antenna was designed to be constructed using aluminum dip brazing technology. Some implications of aluminum dip brazing for microwave antenna design are discussed.

1.0 Introduction

The Naval Research Laboratory (NRL) is conducting tests with horizontally polarized omnidirectional antennas in the band from 2.9 Ghz to 3.7 Ghz. Since the antennas are operated at fairly high power levels[1], waveguides with slot doublets in the broad walls have been employed. One antenna had the inside dimensions of half height WR284, but oversized walls 1/10 inch thick. This was done because the waveguides were formed by stamping and bending aluminum sheet and welding the seams. Thick walls were required to attach a type N connector. The waveguide had to be kept at half height or larger to prevent breakdown between the coaxial stub and the waveguide. This antenna covered the lower 200 MHZ of the band. The omnidirectional pattern had a ripple of about 5 1/2 dB. A second scaled version was constructed to cover the upper 200 MHZ of the band, leaving no coverage for the middle 400 MHZ of the band. It was desired to have one antenna to cover the entire band for convenience and improved testing.

This paper describes the evolution from the slotted waveguide design to a new quad slot design with about four times the bandwidth and much lower ripple in the omnidirectional patterns.

Aluminum dip brazing was considered as a manufactured method from the start, and the design was tailored to optimize the dip brazing process.

Finally the paper ends with a brief discussion of dip brazing with the intent of helping the reader get started on a dip brazed antenna project of his own.

2.0 Waveguide with Slot Doublet

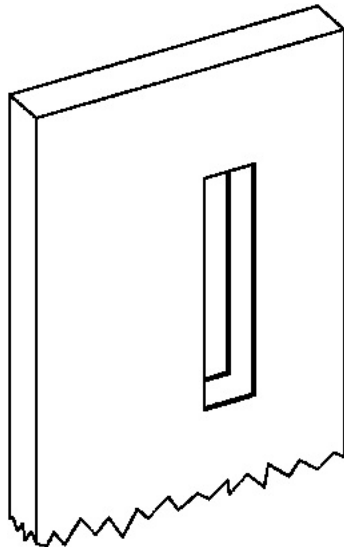


Figure 1 Waveguide with slot doublet.

With aluminum dip brazing as a construction option, it was possible to consider improvements to the existing NRL omnidirectional antennas. Simulations showed that reducing the wall thickness from 1/10 inch to 1/32 inch reduced the pattern ripple to 4 dB. Further simulations showed that reducing the height of the waveguide from half height to quarter height would reduce the omnidirectional pattern ripple to about 1 1/2 dB. Of course this would also require changing the coaxial transmission line to waveguide transition. Moving the short at the end of the waveguide close to the top of the slots increases the bandwidth a couple percent, but it causes the elevation pattern to squint upwards. Extending the outside of the waveguide beyond the short diminishes the squint. The end result of these improvements is shown in Figure 1

Typical radiation patterns in the omnidirectional plane of the slotted waveguide antenna in Figure 1 are presented in

Figure 2. It has a gain of about 2 dB and a cross polarization level about 30 dB below the co-polarization level. As the slots are moved apart their individual patterns tend to

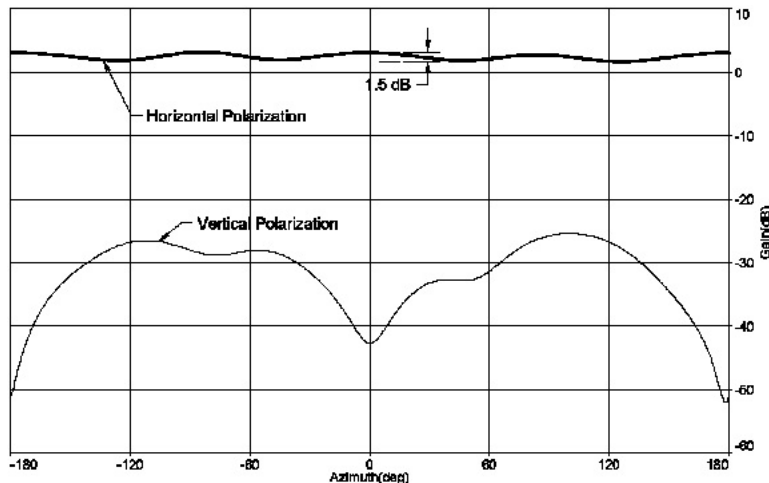


Figure 2 Quarter height slotted waveguide radiation patterns.

interfere with each other. If the waveguide is made thinner, the ripple in the pattern reduces, but exciting the waveguide is more challenging.

A slotted waveguide with a conducting rod inserted in the middle was simulated. The conducting rod converted the waveguide into a rectangular coaxial transmission line. Various means of exciting a pair of

slots on the broadwalls from the coaxial rod were tried. None produced results superior to those of the slotted waveguide shown in Figure 1. However, one configuration, similar to Ohmine's[2] led to the next model, which provided a more fruitful path.

3.0 Quad Slot Antenna

With the intent of investigating only the radiation patterns while ignoring impedance matching, the antenna shown in Figure 3 was simulated. It consists of a square tube roughly a quarter wavelength across with identical bowtie shaped slots cut in each face. A coaxial feed comes up the center of the square tube to the mid point of the slots. There probes connect the feed to one side of each slot. The radiation patterns in the omnidirectional plane, not shown here, were excellent, exhibiting a ripple of only a few tenths of a dB. The radiation patterns in the vertical plane were good too, with maxima on the horizon. The reflection coefficient was worse than -10 dB, but still good enough to merit further consideration.

Aluminum dip brazing of sheet aluminum parts was being considered as a fabrication method, so the round probes shown in Figure 3 were replaced with flat probes such as might be stamped from aluminum sheet. Surprisingly this

improved the impedance match. As the feed probes were made larger the match improved more. Eventually four bowtie slots, a design with an impedance match less than -10 dB from 2.9 Ghz to 3.7 Ghz was obtained. The dimensions were altered to simplify construction. The radius of the center conductor was changed slightly to produce a characteristic impedance of 50Ω in the square coaxial line. The thickness of the flat pieces was changed to $1/32$ or $1/16$ inch to match the thickness of stock sheet aluminum. The resulting design is shown in Figure 4.

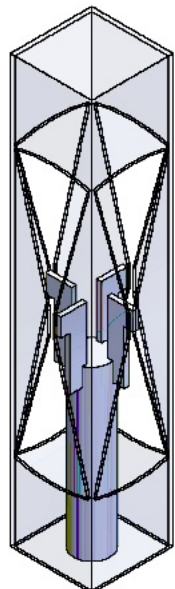


Figure 4 Quad centered bowtie slot antenna.

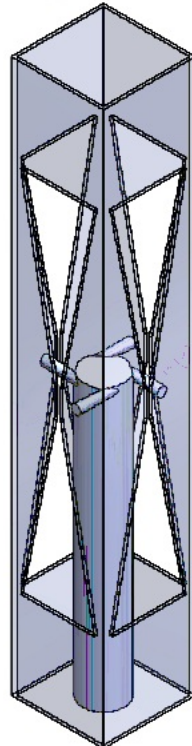


Figure 5a shows the simulated omnidirectional radiation patterns for the quad centered bowtie slot antenna in Figure 4. The ripple in the omnidirectional patterns is very low, about 0.2 dB, but the cross polarization level is quite high. The elevation pattern is shown in Figure 5b. The

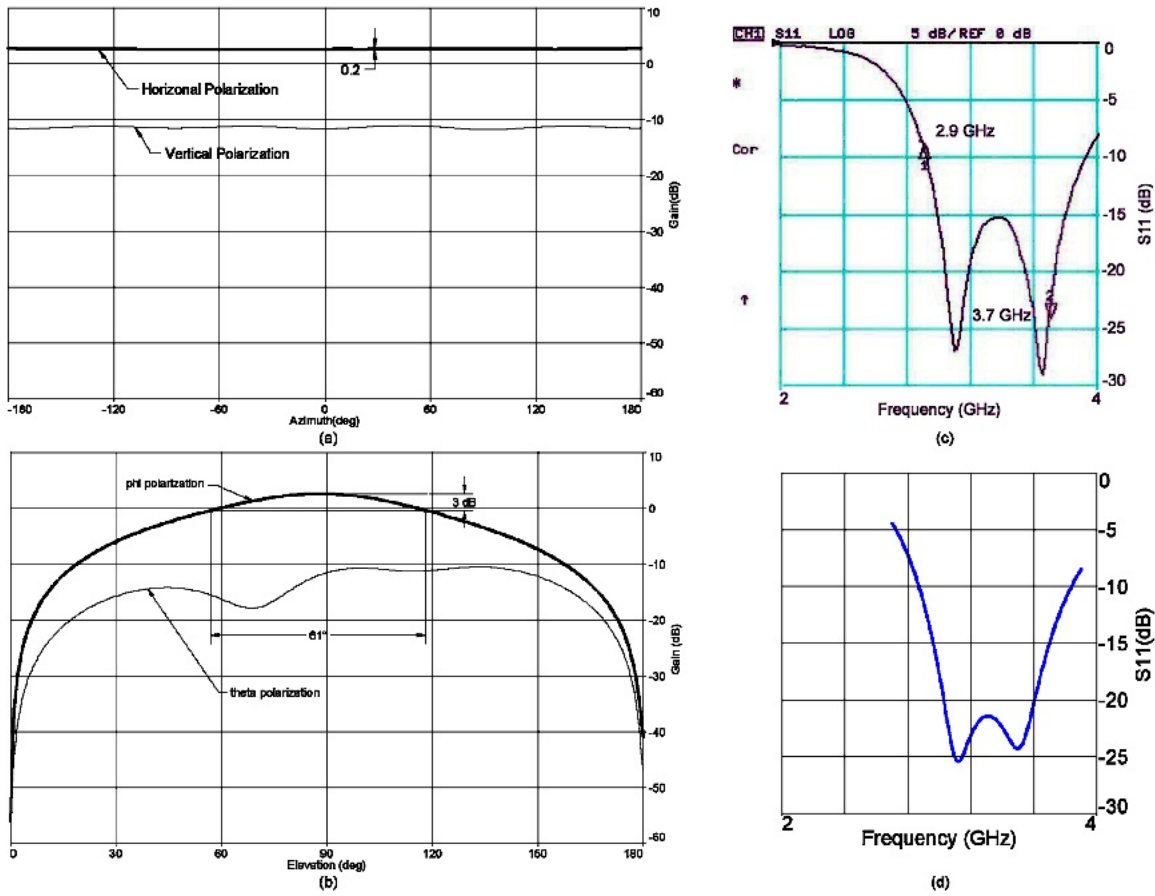


Figure 5 Quad centered bowtie slot antenna: (a) simulated omnidirectional radiation pattern, (b) simulated elevation radiation pattern, © measured reflection, (d) simulated reflection.

elevation beamwidth is 61° . Since the elevation beamwidth was broad enough for the intended application, and high cross polarization was not an issue a prototype was built and delivered. The measured impedance match is shown in Figure 5c and the simulated impedance match is shown in Figure 5d. Figure 5c is the only measured data in this report. Radiation patterns could not be measured in time for this report. The measured reflection curve in Figure 5c closely resembles the simulated reflection curve except that it is slightly shifted up in frequency. This caused the reflection at 2.9 Ghz to be slightly higher than the design goal of -10 dB. The bandwidth of the quad centered bowtie slot antenna can be calculated by estimating the frequencies where the curve in Figure 5c crosses the 10 dB level:

$$\text{Bandwidth} = 100\% \cdot 2 \cdot \frac{F_{\text{High}} - F_{\text{Low}}}{F_{\text{High}} + F_{\text{Low}}} \quad (1)$$

$$= 100\% \cdot 2 \cdot \frac{3.95\text{GHz} - 2.95\text{GHz}}{3.95\text{GHz} + 2.95\text{GHz}} = 29\%$$

4.0 Improvements

After the prototype was built and delivered for field use, a study was performed to understand the high cross polarized radiation exhibited by the quad centered bowtie slot antenna shown in Figure 4. The bowtie slots were replaced with straight slots as shown in Figure 6. As shown in Figure 7a, the cross polarization level dropped about 30 dB. Referring to Figure 7b, it can be seen that the elevation beamwidth increased by a quarter. Figure 7c shows the simulated impedance of the quad centered straight slot antenna transformed to the middle of the slots. The bandwidth can be calculated from the notations on the Smith chart which indicate the frequencies where the reflection equals -10 dB and using equation (1):

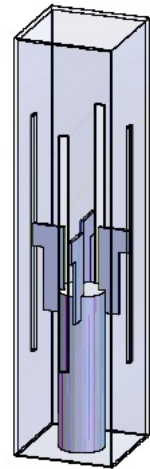


Figure 6 Quad centered straight slot antenna

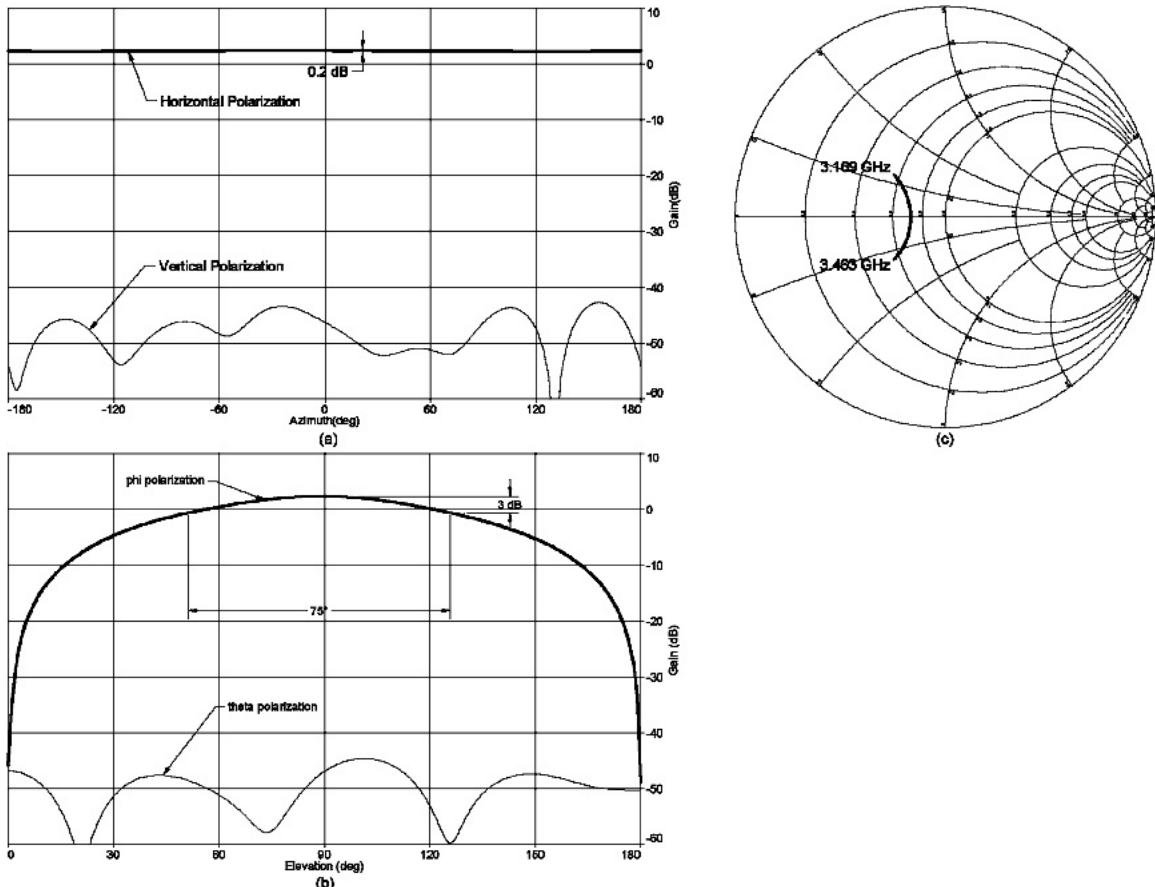


Figure 7 Quad centered slot antenna simulation data: (a) Omnidirectional radiation pattern, (b) Elevation radiation pattern, (c) Impedance transformed to slot centers.

$$\text{Bandwidth} = 100\% \cdot 2 \cdot \frac{3.463\text{GHz} - 3.169\text{GHz}}{3.463\text{GHz} + 3.169\text{GHz}} = 8.9\%$$

Changing bowtie slots to straight slots caused a large reduction in bandwidth.

It was found that if the slots and associated feed probes were moved off center, the bandwidth increased. The practical limit for offsetting the probes is reached when the

outside surface of the probes are flush with the radius of the center conductor. The diameter of the center conductor could have been increased to facilitate larger slot offsets. However, that would have required the addition of an impedance transformer. In the interest of simplicity and minimum size, that avenue was not pursued. A plot of bandwidth vs slot offset is shown in Figure 8. The maximum slot offset shown in Figure 8, namely 168.75 mils was obtained by subtracting half the slot width and the probe thickness from the center conductor radius.

Figure 8 Bandwidth vs slot offset for quad straight slot antenna.

The quad straight slot antenna with the maximum offset is shown in Figure 9. The corresponding omnidirectional radiation patterns are shown in Figure 10a. The ripple in the radiation pattern is minutely worse than with the centered straight slot antenna, but the cross polarization level is about 5 dB lower. The elevation pattern is shown in Figure 10b. The elevation beamwidth is slightly less than for the quad centered straight slot antenna. The impedance of the same antenna, transformed to the center of the slots is shown in Figure 10c. The bandwidth can be calculated from the notations on the Smith chart which indicate the frequencies where the reflection equals -10 dB and using equation (1):

$$\text{Bandwidth} = 100\% \cdot 2 \cdot \frac{3.546\text{GHz} - 3.062\text{GHz}}{3.546\text{GHz} + 3.062\text{GHz}} = 14.6\%$$

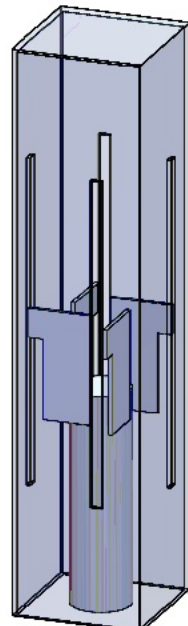


Figure 9 Quad offset straight slot antenna.

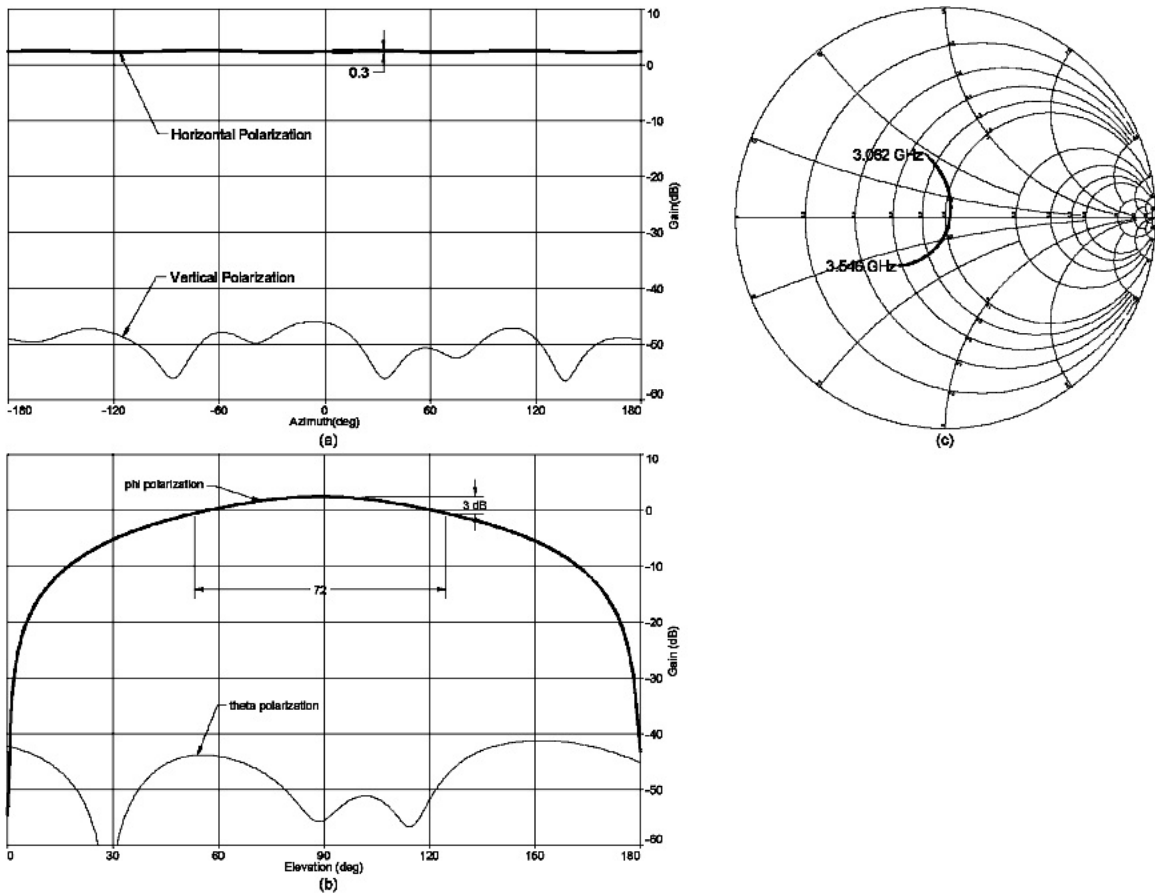


Figure 10 Quad offset straight slot antenna simulation data: (a) Omnidirectional radiation pattern, (b) Elevation radiation pattern, (c) Impedance transformed to slot centers.

If the offset straight slots in Figure 10 are replaced with offset bowtie slots, the antenna shown in Figure 11 is the result. The bowtie portion of the slots in Figure 11 are not as wide as those in Figures 3 and 4 because of the proximity of the edge of the antenna. Figure 12a shows the omnidirectional radiation patterns. The ripple in the patterns is marginally worse than that shown in Figure 5a, but the cross polarization level is 10 dB lower. The elevation pattern is shown in Figure 12b. The elevation beamwidth is closer to that of the quad centered bowtie slot than either of the quad straight slot antennas. The bandwidth can be calculated from the notations on the Smith chart, shown in Figure 12c which indicate the frequencies where the reflection equals -10 dB and using equation (1):

$$\text{Bandwidth} = 100\% \cdot 2 \cdot \frac{3.856\text{GHz} - 2.77\text{GHz}}{3.856\text{GHz} + 2.77\text{GHz}} = 33\%$$

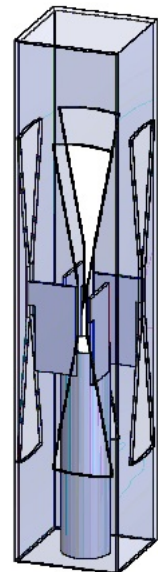


Figure 11 Quad offset bowtie slot antenna.

This is better than the antenna shown in Figure 4 which has a bandwidth of 29%.

Hence it is observed that offsetting the slots, whether straight or bowtie shaped improves the bandwidth and cross polarized radiation levels.

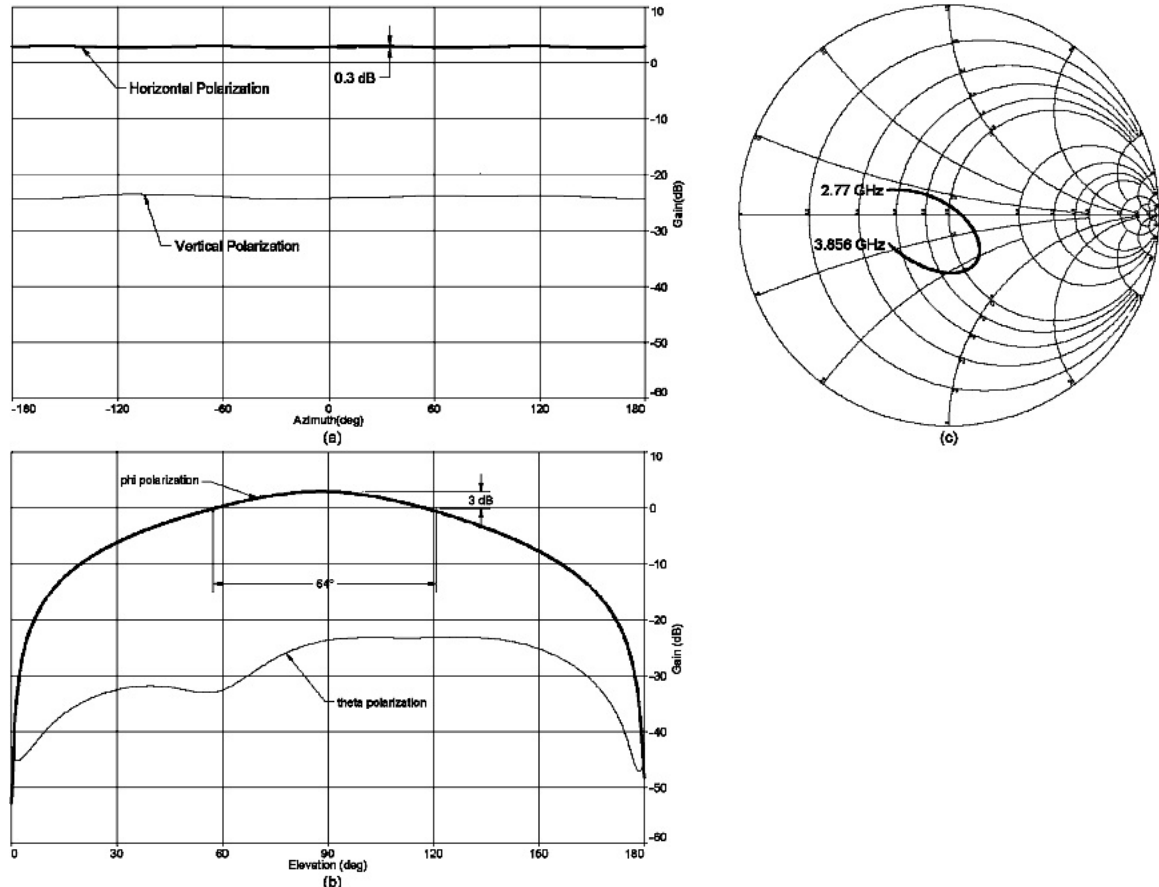


Figure 12 Quad offset bowtie slot antenna simulation data: (a) Omnidirectional radiation pattern, (b) Elevation radiation pattern, (c) Impedance transformed to slot centers.

5.0 Construction of Quad Centered Bowtie Slot Antenna.

The sides of the antenna and the probes which excite the slots are stamped from aluminum sheet. The sides are attached to a base which serves as an attachment point for a connector and a radome. Simulations showed that the diameter of the base should be kept as small as possible to limit upward squinting of the radiation pattern. The base and center conductor are machined from solid aluminum. All the parts of the antenna are designed to be held together with one aluminum screw and several pins and a fixture made of stainless steel. This assembly is dip brazed into a solid piece.

After dip brazing the fixture and pins are removed, the various tabs and protrusions that

were used as hooks or anchors for the pins are cut off, and a finishing machining operation is performed. Finally the connector is screwed into the bottom of the center conductor and attached to the base.

6.0 Aluminum Dip brazing guidelines

Aluminum dip brazing is a process by which aluminum alloy parts are bonded together with an aluminum filler. The aluminum filler is a mixture of aluminum, silicon, and some other metals, and has a lower melting point than the aluminum alloy parts. The assembly of parts and filler are submerged in a molten salt which is maintained at a temperature between the melting points of the parts and the filler. The filler melts and flows into the spaces between the parts. The assembly is removed from the molten salt and allowed to cool. Any salt residue remaining on the assembly is washed away. At this point the assembly is soft, and warpages are removed to the extent possible. After aging final machining operations are performed on the assembly.

Aluminum dip brazing permits the construction of complex shapes from simple shapes. In some cases the complex shapes are more economically constructed from simple shapes. In other cases the complex shapes simply can not be constructed without recourse to dip brazing. Only certain aluminum alloys are acceptable for dip brazing. Use of the wrong alloy results in an adverse chemical reaction with the molten salt. Table 1 separates the permissible dip brazing alloys into categories of "Heat Treatable", "Not Heat Treatable", "Wrought", "Clad Brazing Sheet" and "Cast."

The ideal assembly for dip brazing is self-fixture and self-aligning. When the assembly is put together, it should require only a few external clamps to stay together. Features which can be employed to make an assembly self-fixture and self-aligning include:

- Slots and Tabs
- Self-locking Joints
- Aluminum Threaded Rods
- Aluminum Screws
- Aluminum Rivets
- Stakes, and
- Pins.

Alloy Type	Heat Treatable	Not Heat Treatable
Wrought	6061, 6062, 6063, 6053, 6951, 7072	1100, 3003, 3004, 3005
Clad Brazing Sheet	#21, #22	#11, #12
Cast		A712.0, C712.0, D712.0 A356.0, A357.0, A359.0, A443.0

Table 1 Dip brazable aluminum alloys.

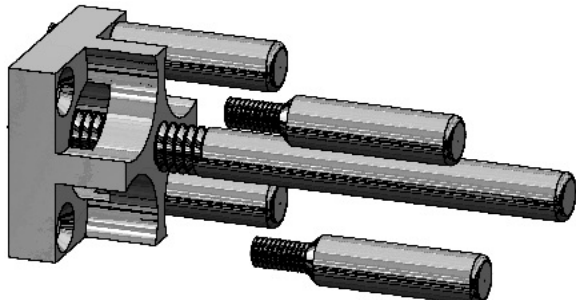


Figure 13

lead to an incomplete braze. As the assembly is withdrawn from the molten salt, there needs to be a path for the molten salt to flow out.

If the assembly has poor ventilation, the dip brazer may drill holes in the assembly to increase ventilation. After brazing the brazer will weld plugs into those holes. If warping is an issue, the brazer may fill the holes with conducting epoxy which is not as conductive as a weld.

Occasionally an external fixture is required to hold an assembly together for dip brazing. The preferred material for fixtures is stainless steel alloy 316. Fixtures should be kept simple. Aluminum has a coefficient of thermal expansion about 1/3 greater than 316 stainless, so poorly placed fixtures may cause warpage. The fixture used to keep the center conductor of the bowtie slot antenna in place is shown in Figure 13. The fixture attaches to the threaded holes which will eventually be used to attach a type N connector. The fixture was also used on a horn antenna where ventilation was a consideration so it is designed to provide ventilation past the center conductor as well as holding the center conductor in place.

At times it may be necessary to join two aluminum sheet parts along their edges. This is a structurally weak joint and thus should not be relied upon for mechanical strength.

In addition it may be possible to tackweld or spotweld the assembly together before it is brazed.

When designing an assembly for dip brazing it is important to consider ventilation. As the assembly is submerged in the molten salt, air needs to escape from the assembly. Air bubbles trapped in the assembly can prevent the assembly from being heated uniformly which in turn can

However it may still be necessary to obtain electrical conduction across such joints. This is facilitated by putting a 10 mil chamfer on the edges to be joined. The dip brazer will fill the void with a paste containing powdered filler metal and flux. When the filler metal melts it will fill the chamfers and seep into the edge joint below.

The Antenna Section at NRL has had good success stamping parts for dip brazed assemblies from aluminum sheet.

Stamping is a low cost manufacturing method and the tolerances associated with stamping (± 0.005 inches) are comparable to the spaces that can closed up by aluminum fillers. The Antenna Section has constructed an S-band horn array which was feed by a four column x eight row waveguide power divider. All the parts were stamped from 1/16 inch aluminum. The measured patterns of the array were very symmetrical, indicating excellent uniformity in both the stamping and dip brazing process. Occasionally however, it is necessary to hold tighter tolerances. Figure 18 shows a wideband coaxial transmission line to waveguide transition designed at the Antenna Section. It was designed to have a reflection coefficient below -20 dB. To obtain this level of performance it was necessary to hold tolerances of about ± 0.001 inch on the stepped ridges. This required that the top and bottom halves of the transition be machined rather than stamped. If the ridges had been machined separately and then brazed to the outer waveguide parts, the tolerance build up would have been excessive.

7.0 Conclusion

An unusual concept for wideband horizontally polarized omnidirectional antennas has been presented. The design exhibits a ripple of only a few tenths of a dB in the omnidirectional pattern. Two configurations were presented. In one configuration, using bowtie shaped slots, this antenna design has a bandwidth of about 33 percent and a cross polarization level about 25 dB below the co-polarization level. In the other configuration, using straight slots, this antenna design has a bandwidth of about 15 percent and cross polarization level about 50 dB below the co-polarization level.

The prototype of this antenna design was constructed using aluminum dip brazing. This led into a brief discussion of the issues encountered when designing assemblies for dip brazing.

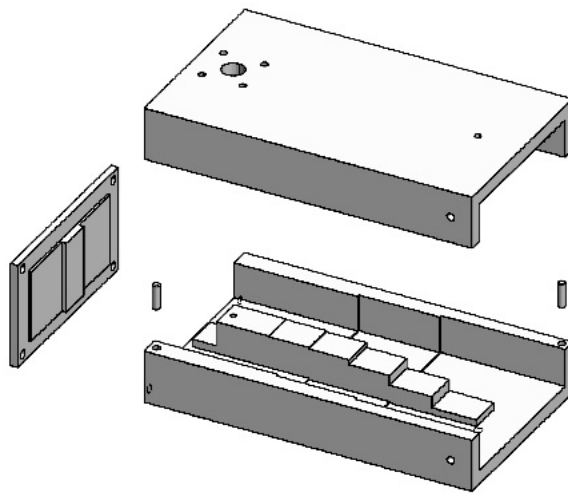


Figure 14

8.0 Acknowlegements

Much of the information about aluminum dip brazing came from Coleman Microwave Company, either through private communications with Coleman Microwave employees, or from the Coleman Microwave website.

9.0 References

- [1.] Mark Dorsey and John Valenzi, "Design of Horizontally Polarized S-Band Beacon Antennas," Technical Report, U.S. Nav. Res. Lab., March 28, 2008.
- [2.] Hiroyuki Ohmine, Yonehiko Sunahara, Shin-ichi Sato, Takashi Katagi, Shusou Wadaka, "Omnidirectional Slot Antenna," U.S Patent 5717410, Feb. 10, 1998

INVESTIGATION INTO A FREQUENCY RECONFIGURABLE MIMO DIELECTRIC RESONATOR ANTENNA

Jie-Bang Yan* and Jennifer T. Bernhard

Electromagnetic Laboratory

Department of Electrical and Computer Engineering

University of Illinois at Urbana-Champaign

Urbana, IL 61801, USA

<http://antennas.ece.illinois.edu>

Email: yan12, jbernhar@illinois.edu

Abstract: Two different techniques for implementing frequency reconfiguration in a Multiple-Input Multiple-Output (MIMO) Dielectric Resonator Antenna (DRA) are investigated. The first method is derived from perturbation theory which involves manipulating the intrinsic relative permittivity of a DRA. Instead of varying the relative permittivity constant of the entire dielectric block, the proposed method determines the optimum location for material perturbation for frequency reconfiguration. A distinctive feature of this method is that it allows the operating frequency of a particular antenna port to be individually tuned while maintaining very low mutual coupling between the antenna ports. A detailed set of full-wave simulations demonstrates the technique. The second modality for frequency reconfiguration is achieved by the addition of tunable parasitic slots in proximity to the feed of the antenna. This technique not only allows individual and continuous frequency tuning to the antenna ports, but also covers a wider frequency range. Detailed simulation results support the proposed method.

1. Introduction

Multiple-Input Multiple-Output (MIMO) antennas are becoming a standard feature in next generation wireless devices due to the outstanding performance of MIMO link in rich-scattering environments over the traditional Single-Input Single-Output configuration. The technology enables a leap in channel capacity without additional spectrum or transmission power, and the capacity gain is proportional to the minimum of the number of transmit and receive antennas [1]. MIMO antennas are different from a classical antenna array, since each antenna port has no prescribed amplitude and phase relation to the signals on the other ports. Hence, each of the antenna ports can be characterized as a single antenna and the signals that appear at each port are processed

incoherently and independently to optimize system performance. The intrinsic properties of MIMO antennas such as mutual coupling, gain and radiation patterns can greatly affect the resultant channel capacity. The major design requirement of MIMO antennas is to have low signal correlation and mutual coupling such that the antennas can resolve the multiple signals effectively.

One recent application of MIMO technology is Cognitive Radio (CR) [2] – [3]. While MIMO technology improves the channel capacity, CR is proposed for a more efficient utilization of the scarce radio spectrum [4]. It is estimated that the licensed spectrum remains idle or underutilized for an average of 90% of time [5]. CR promises to take advantage of this and establish a communication link whenever spectrum holes (also known as white spaces) in proximity are sensed. With the newly released “700 MHz spectrum” due to the analog to digital television broadcast transition [6], MIMO CR could be a winning technology. The 700 MHz spectrum, also known as the white space spectrum, covers from 512 MHz to 806 MHz. Therefore, to implement a CR system with MIMO capability, a MIMO antenna that covers the white space spectrum is required (which corresponds to more than 40% bandwidth).

This paper investigates two antenna solutions by considering a frequency reconfigurable MIMO antenna. Frequency Reconfigurable Antenna (FRA), rather than a wideband one, is chosen because FRAs are generally more compact in size and have better impedance matching if properly designed. FRAs may also eliminate the need of a band selection filter at the radio frequency front end, which can help to reduce cost. Our approach is to investigate the feasibility of adding frequency reconfigurability into the MIMO Dielectric Resonator Antenna (DRA) previously developed in [7]. As compared to conventional MIMO antennas based upon multiple dipoles, patches, slots, planar inverted F antennas (PIFAs), or combinations of the above antenna types, MIMO DRAs are more compact in size. Given that the antenna ports in the MIMO DRA are mutually orthogonal [7], physical separation or decoupling elements between antenna ports are no longer necessary. This contributes to further reduction in size and design complexity of the antenna unit. Moreover, the orthogonality between the ports allows the antenna ports to be tuned individually without severely deteriorating the mutual coupling or the radiation characteristics. The following section will first give a brief review of the existing design. Then two different modalities for adding frequency reconfigurability to the base design are described in detail in Section 3. Finally in Section 4, a conclusion with an emphasis on future work will be given.

2. Base Antenna Configuration

The antenna configuration is based on a perturbed half-cylindrical DRA described in [7]. The antenna has a relative permittivity ϵ_r of 18 and is shown in Figure 1. To achieve a MIMO configuration, we would like to simultaneously excite the $TE_{011+\delta}$ and $HE_{11\delta}$ modes of the resonator (see Figure 1). The two modes are made degenerate by

introducing an inward boundary perturbation from the base of the dielectric block as illustrated in Figure 2. The required amount of perturbation is found to be 13 mm and can be estimated using,

$$\frac{\omega - \omega_0}{\omega_0} \approx \frac{\iiint_{\Delta v} (\mu|H_0|^2 - \varepsilon|E_0|^2) dv}{\iiint_V (\mu|H_0|^2 + \varepsilon|E_0|^2) dv}, \quad (1)$$

where ε and μ are the permittivity and the permeability of the dielectric resonator respectively; ω and ω_0 are the resonant frequencies of the perturbed (desired) and unperturbed resonator, respectively; Δv and V are the perturbed volume and the original volume of the resonator; and E_0 and H_0 represents the unperturbed fields. The final dimensions of the DRA are 80 mm \times 84 mm \times 31 mm. Figures 3 and 4, respectively, give the simulated and measured S-parameters of the antenna. It can be observed that the original operating frequencies of the TE and HE modes of the DRA were 654 MHz and 550 MHz respectively, and the applied boundary perturbation changed both operating frequencies to 700 MHz. The measured mutual coupling between the modes is lower than -30 dB due to the mode orthogonality.

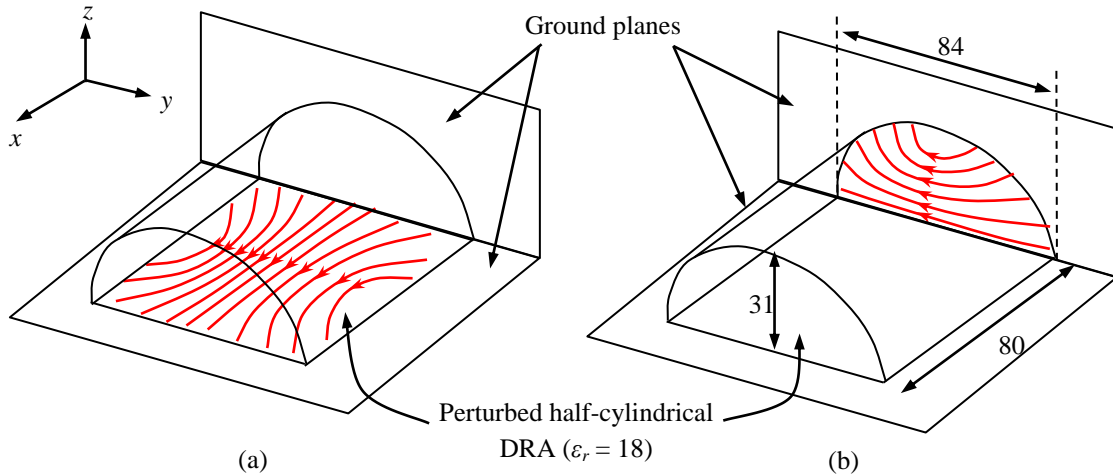


Figure 1. Base antenna configuration with magnetic field distribution (represented by bold arrows) of the (a) $TE_{011+\delta}$ mode, (b) $HE_{11\delta}$ mode (dimensions in mm).

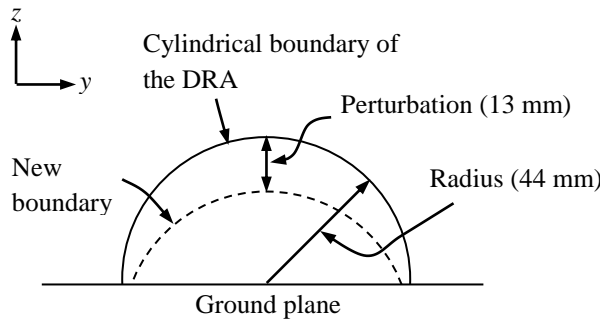


Figure 2. Boundary perturbation from the base of the DRA.

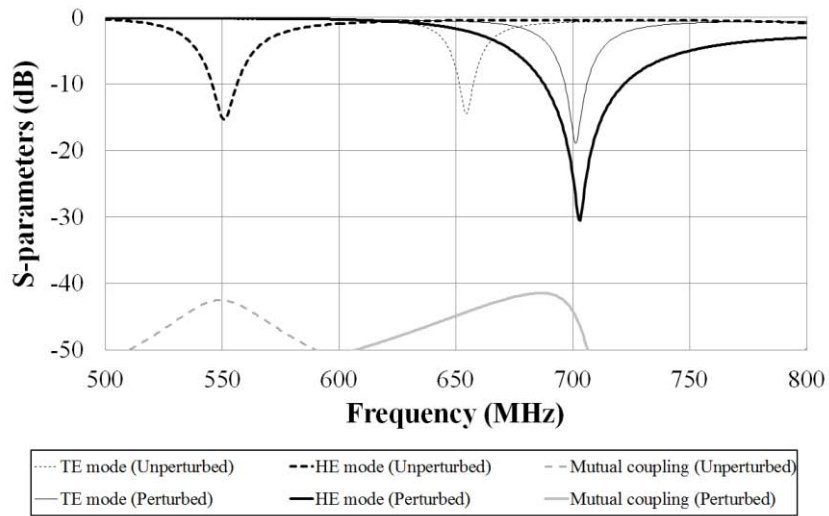


Figure 3. Simulated S-parameters of the DRA before and after boundary perturbation. Simulation results are computed using Ansoft HFSS®.

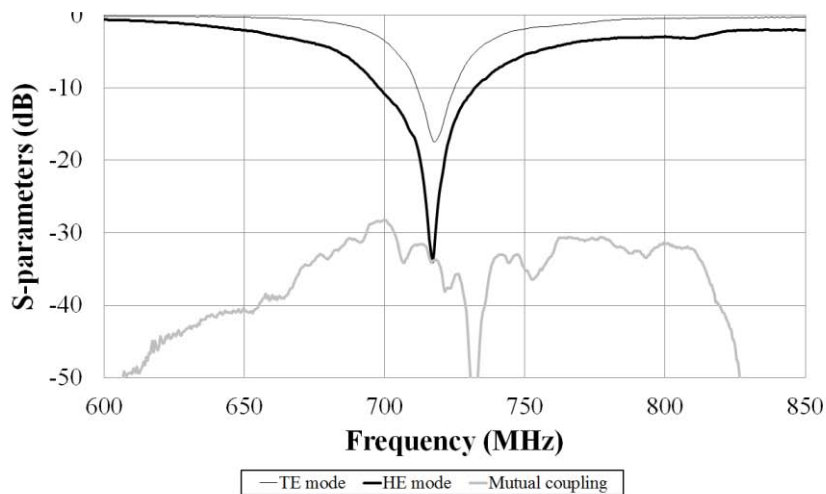


Figure 4. Measured S-parameters of the perturbed MIMO DRA.

3. Frequency Reconfigurable MIMO DRA

The antenna configuration described in the previous section is a two-port MIMO antenna operating at 700 MHz. It is desired to introduce frequency reconfigurability to the antenna such that it could be used in CR systems. A literature search reveals that there are only a handful of works on the design of frequency reconfigurable DRAs [8] – [10]. O’Keefe et al. in [8] and Huff et al. in [9] proposed frequency reconfigurable DRAs based on varying the dielectric boundary electrically, while Petosa et al. in [10] suggested a frequency tunable DRA with switchable metal-loading. In this paper, we take two fundamentally different approaches for adding frequency agility to our antenna.

3.1 Material Perturbation Technique

Instead of varying the dielectric boundary for frequency tuning [8] – [9], we would like to investigate how the resonance frequency of a mode changes in response to a material perturbation inside the dielectric block. Such an idea has already been demonstrated experimentally in microstrip antenna by Huff et al. in [11]. Our interest is to extend the idea to our MIMO DRA and determine an optimum solution for placing the material perturbation inside the antenna.

Consider an arbitrarily shaped DRA which can be modeled by a cavity bounded by perfect magnetic walls. The change of its resonance frequency due to a material perturbation inside the cavity V can be estimated using the perturbation technique [12],

$$\frac{\omega - \omega_0}{\omega_0} \approx - \frac{\iiint_V (\Delta\epsilon |E_0|^2 + \Delta\mu |H_0|^2) dv}{\iiint_V (\epsilon |E_0|^2 + \mu |H_0|^2) dv} \quad (2)$$

where $\Delta\epsilon$ and $\Delta\mu$ denote the amount of changes in relative permittivity and permeability, respectively, in ΔV inside the cavity V . The above equation implies that the change of resonance frequency would be maximized if the perturbation is placed at maximum E or H , and this in turn leads to a design with maximized frequency agility.

3.1.1 Solution via Eigenvalue Perturbation

Equation (2) would suffice for practical applications if the locations of field maxima are known. However in some situations, the locations of field maxima may not be known explicitly. Eigenvalue perturbation offers an alternative approach to determine the location of the perturbation in order to maximize the amount of change of frequency [13] – [14]. Assuming that the DRA of interest is modeled by a perfect magnetic conductor

(PMC) cavity V , the Helmholtz vector equation governing the wave phenomenon inside the cavity is,

$$\nabla \times \left(\frac{1}{\epsilon_r} \nabla \times \mathbf{H} \right) - k_0^2 \mu_r \mathbf{H} = 0 \quad \text{in } V \quad (3)$$

with the boundary conditions $\mathbf{n} \times \mathbf{H} = 0$ on the magnetic walls and $\mathbf{n} \cdot \mathbf{H} = 0$ on electric walls. By applying the Galerkin procedure in finite element analysis, one obtains the generalized eigenvalue problem [15],

$$[A_0] \{H_0\} = k_0^2 [B_0] \{H_0\} \quad (4)$$

where,

$$[A_0] = \sum_{e=1}^M [A_0^e] = \sum_{e=1}^M \iiint_{V^e} \left[\frac{1}{\epsilon_r^e} \{ \nabla \times \mathbf{N}^e \} \cdot \{ \nabla \times \mathbf{N}^e \}^T \right] dV \quad (5)$$

$$[B_0] = \sum_{e=1}^M [B_0^e] = \sum_{e=1}^M \iiint_{V^e} \mu_r^e \{ \mathbf{N}^e \} \cdot \{ \mathbf{N}^e \}^T dV \quad (6)$$

and M is the total number of elements; V^e denotes the volume of an element; ϵ_r^e and μ_r^e are the relative permittivity and permeability in the e -th element, respectively; \mathbf{N}^e is the vector basis function used for the magnetic field expansion. Hence, with the given boundary conditions, Equation (4) can be solved for eigenvalues k_0^2 and the corresponding eigenvectors $\{H_0\}$.

Now suppose a material perturbation is introduced to the DRA, such that,

$$\epsilon_r^e = \begin{cases} \epsilon_p^e = \epsilon_r^e + \Delta\epsilon & \text{for } e \in \mathbb{S} \\ \epsilon_r^e & \text{otherwise} \end{cases} \quad (7)$$

where \mathbb{S} is a subset of the elements $\mathbb{M} = \{1, 2, 3, \dots, M\}$. We expect the matrix $[A]$ would be changed by a small amount as it has a dependence on ϵ_r^e , i.e.,

$$[A] = [A_0] + [\delta A] \quad (8)$$

Therefore, it is expected that the corresponding eigenvalues and would be varied by a small amount, i.e.,

$$k^2 = k_0^2 + \delta k_0^2 \quad (9)$$

and,

$$k^2 = k_0^2 + \{H_0\}^T [\delta A] \{H_0\} \quad (10)$$

Hence, it is possible to efficiently do a sensitivity analysis on k^2 as a function of changes in the entries of $[A]$. Following the derivations in [14], one obtains,

$$\frac{\partial k^2}{\partial A_{(ij)}} = \{H_0\}_{(i)} \{H_0\}_{(j)} (2 - \delta_i^j) \quad (11)$$

where i and j are the indexes of matrix $[A]$; δ_i^j denotes the Kronecker delta. Thus, using Equation (11), we could accurately resolve the entries in $[A]$ that maximize the change of k^2 . This in turn allows us to determine the set of elements \mathbb{S} that needs to be perturbed for maximizing the amount of change of resonant frequency.

3.1.2 Simulation Results

It is known that the electric field of the HE mode is the strongest near the feeding coaxial probe while that of the TE mode is the strongest around the feeding slot on the bottom ground plane [7]. From Equation (2), it is evident that the perturbation should be done at those field maxima for maximum frequency agility. Now consider the material perturbation at two different locations as illustrated in Figure 5. The first perturbation is located above the slot feed (*Perturb. A*) while the second one is next to the vertical ground plane (*Perturb. B*). A fullwave simulation using Ansoft HFSS® [16] has been carried out to compute the change of operating frequency of the modes due to the perturbations. Figures 6 – 9 show the simulated S -parameters of the perturbed MIMO DRA as the relative permittivity of the perturbation volume ϵ_p changes from 1 to 60. It is observed that for *Perturb. A*, as ϵ_p increases, the operating frequency of the TE mode (S_{11}) shifts downwards from 700 MHz to 538 MHz, while that of the HE mode (S_{22}) remains fairly constant (except when ϵ_p is lower than 18 which is the original relative permittivity of the DRA). A similar behavior can also be observed for *Perturb. B* with only the operating frequency of the HE mode sensitive to the changes in ϵ_p , tunable from 800 MHz to 665 MHz. It is also noticed that, for both perturbations, the mutual coupling (S_{21}) between the modes is always kept below -40 dB. This indicates the modes are fairly decoupled and their operating frequencies can be adjusted individually.

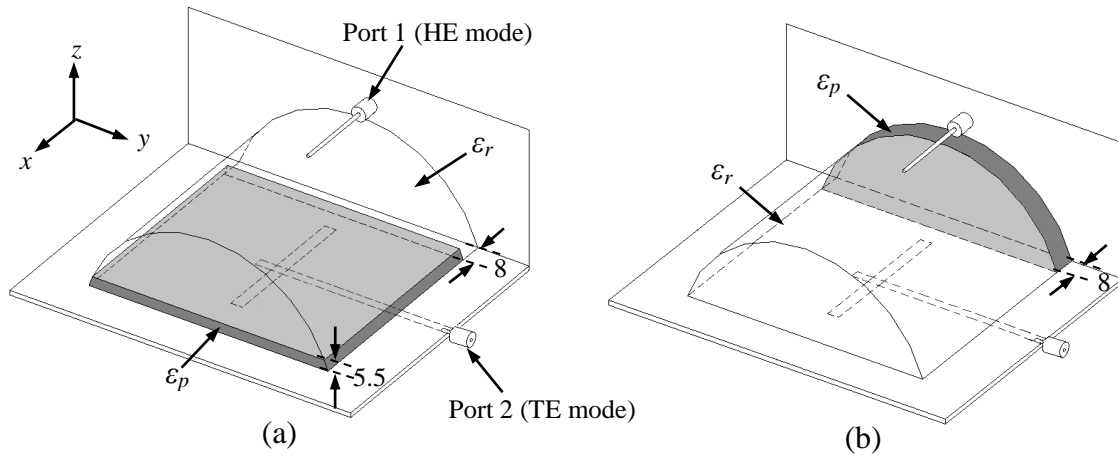


Figure 5. A MIMO DRA with material perturbation. The grey volumes indicate the portion of the dielectric cavity perturbed (a) *Perturb. A* and (b) *Perturb. B* (dimensions in mm).

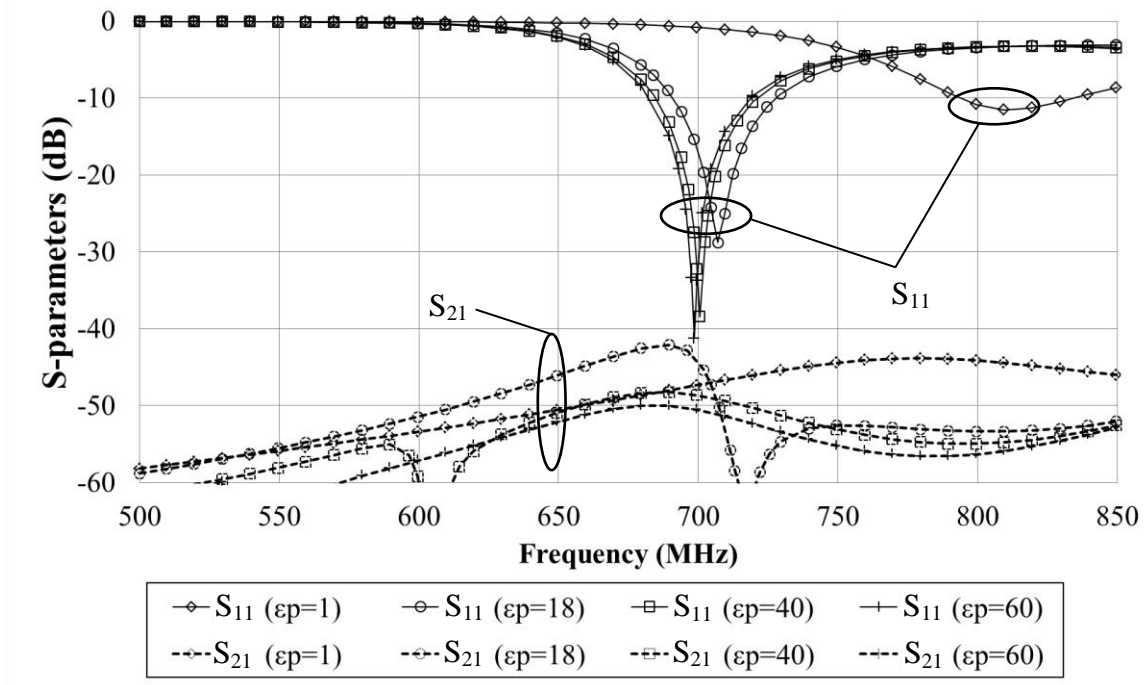


Figure 6. Simulated S_{11} (HE mode) and S_{21} (mutual coupling) of the MIMO DRA with *Perturb. A*.

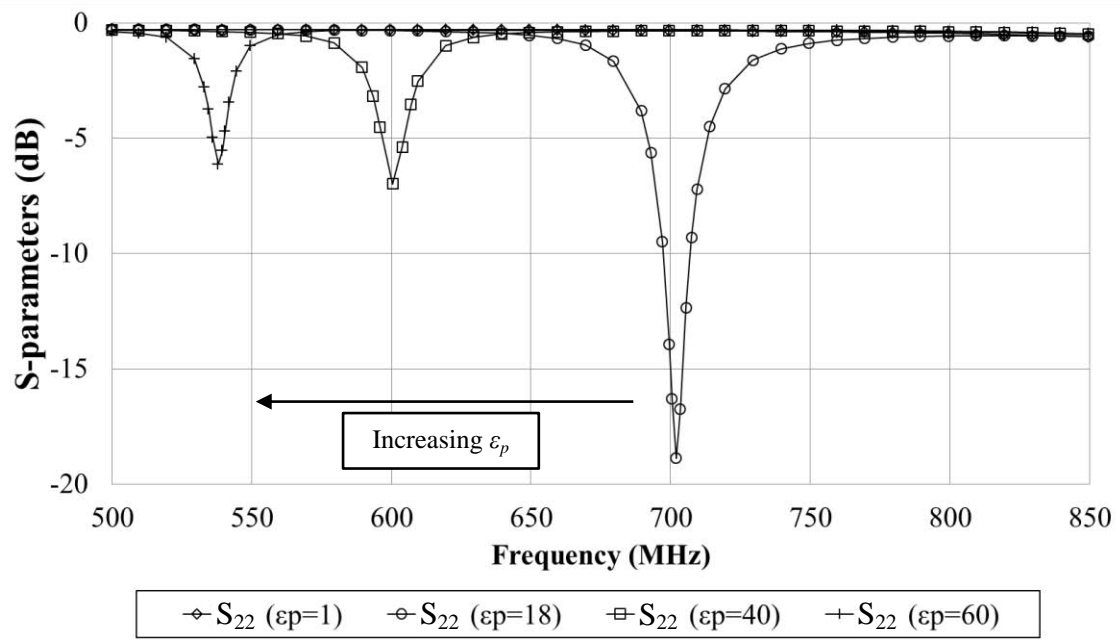


Figure 7. Simulated S_{22} (TE mode) of the MIMO DRA with *Perturb. A*.

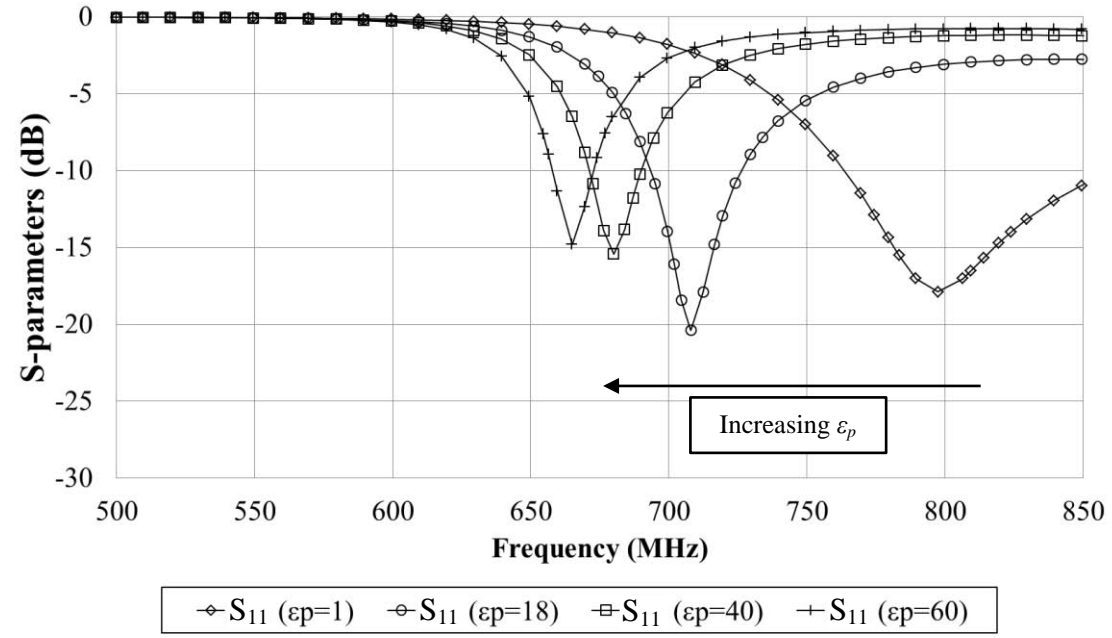


Figure 8. Simulated S_{11} (HE mode) of the MIMO DRA with *Perturb. B*.

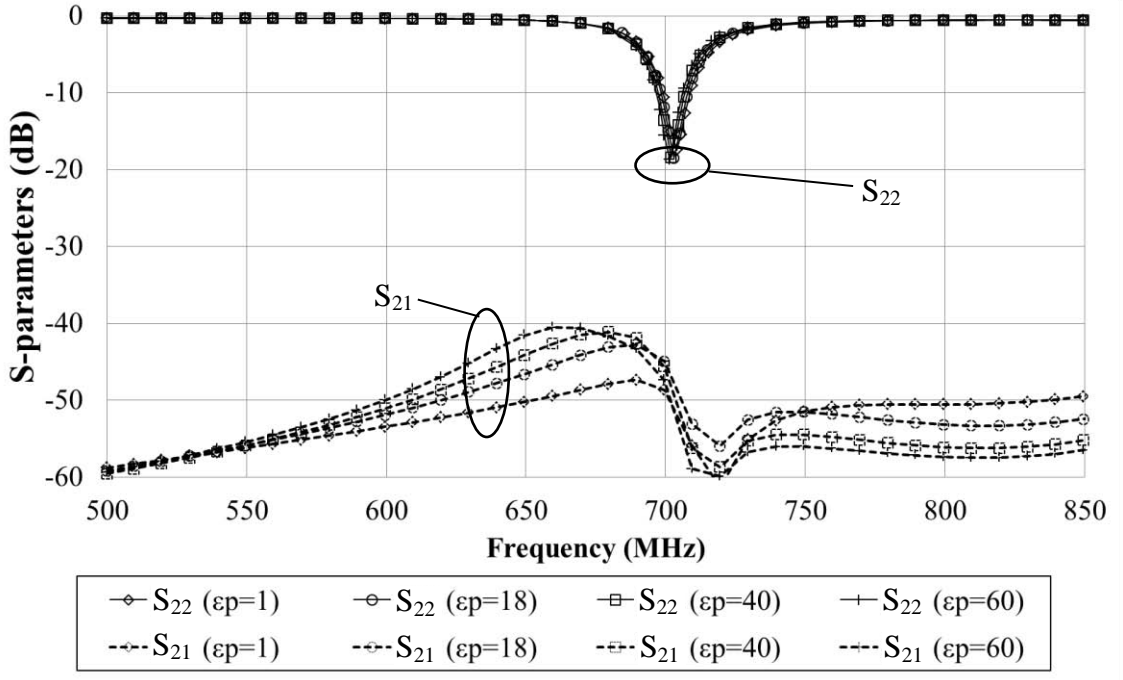


Figure 9. Simulated S_{22} (TE mode) and S_{21} (mutual coupling) of the MIMO DRA with *Perturb. B*.

3.2 Parasitic Slot Loading

In the previous section, material perturbation is studied as a means to add frequency agility to the MIMO DRA. Although the TE port is able to reconfigure from 538 MHz to 700 MHz and HE port from 665 MHz to 800 MHz, the overlapping tunable range for MIMO operation is only from 665 MHz to 700 MHz which is very narrow. Moreover, it is practically difficult and cumbersome to vary the relative permittivity in a selected volume, even though it has been experimentally demonstrated in [9]. A second modality for frequency reconfiguration is therefore presented in this section.

It is known that the presence of a parasitic slot on the ground plane of a DRA can detune the resonant frequency of the antenna [17]. Both theoretical and measurement results in [17] show that the amount of detune is directly related to the length of the parasitic slot. In this section, we investigate how the parasitic slot can be incorporated into the MIMO DRA to provide frequency agility.

3.2.1 Antenna Configuration

Consider the MIMO DRA shown in Figure 10. The dielectric block is the same as the one used in [7] but the two modes are now excited by two slots which are fed directly by coaxial probes. The coaxial feed of the slot for HE mode excitation is located at the center of the slot while that for the TE mode excitation is placed at 2.5 mm from the end of the slot. The corresponding simulated S-parameters of the antenna are given in Figure 11, which is almost the same as that shown in Figure 3, except for a slight frequency shift. Now, in order to enable frequency reconfigurability, the ground planes are modified to include parasitic slots as depicted in Figure 12. The parasitic slot on *Ground Plane A* has four switches (hard-wired for proof of concept) SW_{A1} , SW_{A2} , SW_{A3} and SW_{A4} (SW Set A), and a varactor C_{HE} . When SW_{A4} is OFF, the length of the parasitic slot can be varied electronically, depending of the states of SW_{A1} , SW_{A2} and SW_{A3} . On the other hand, when SW_{A4} is ON while all other switches in SW Set A are OFF, the parasitic slot is then loaded with the varactor C_{HE} . For the excitation slot on *Ground Plane B*, two varactors (C_{TE1} and C_{TE2}) can be switched to load the slot. Selection between the two loading slots can be made by controlling the switches SW_{B1} and SW_{B2} (SW Set B).

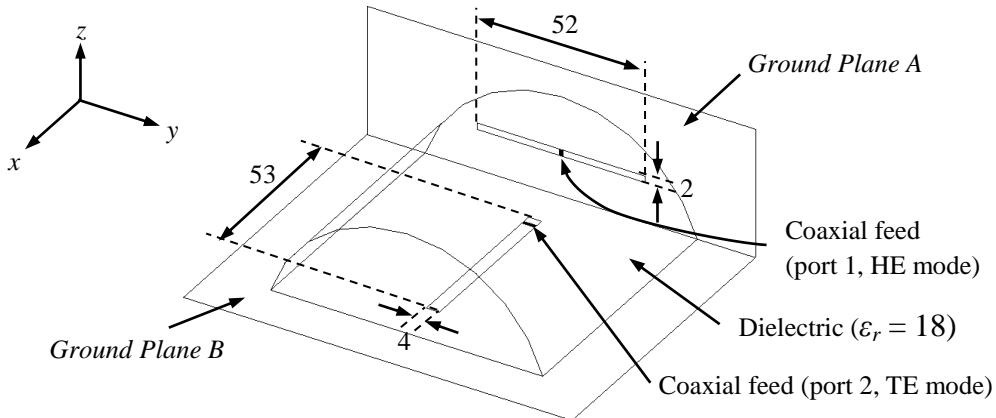


Figure 10. A MIMO DRA excited by two slots fed by coaxial cables (dimensions in mm).

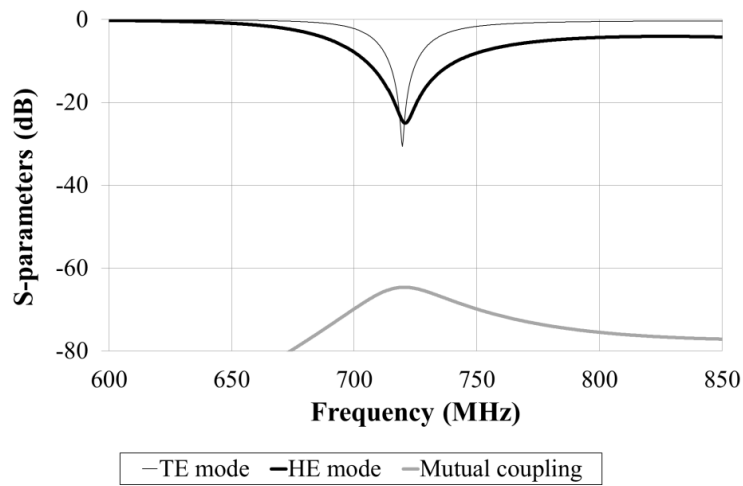


Figure 11. Simulated S-parameters of the MIMO DRA shown in Figure 10.

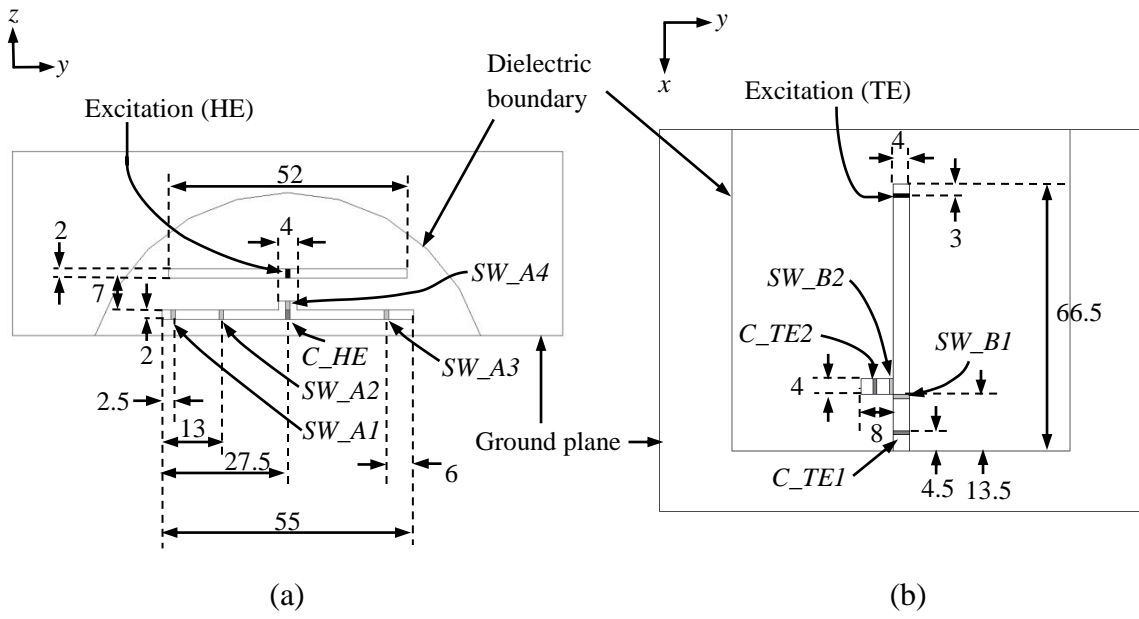


Figure 12. Ground planes with parasitic slots (a) *Ground Plane A* with a slot for HE mode excitation (b) *Ground Plane B* with a slot for TE mode excitation (dimensions in mm).

3.2.2 Simulation Results

The performance of the MIMO DRA with the above described modified feeds was characterized using Ansoft HFSS®. The first set of simulations was done to investigate the reconfigurability of the HE mode (port 1). During the simulations, SW_B1 was kept OFF while SW_B2 was switched ON and C_TE1 was tuned to 11 pF. Figure 13 shows the corresponding simulated S-parameters of the antenna. It can be seen that in Figure 12 (a), SW_A1 , SW_A2 and SW_A3 are distributed along the parasitic slot. Different combinations of the switch states lead to six different slot lengths and therefore different operating frequencies. To achieve further frequency agility, varactor C_HE can be loaded to the parasitic slot by switching SW_A4 ON. As the value of C_HE reduces from 15 pF to 4 pF, f_{HE} can be continuously tuned from 701 MHz to 810 MHz. In summary, the operating range of the HE mode effectively covers from 630 MHz to 810 MHz. From Figure 13 (b), it can also be seen that the operating frequency of the TE mode (f_{TE}) remains unchanged at 719 MHz during the reconfiguration, and the mutual coupling between the modes (S_{21}) is also maintained under -17 dB. This implies that individual tuning of the HE mode is feasible without deteriorating the coupling between the antenna ports.

The second set of simulations focused on the frequency agility of the TE mode (port 2). $SW\ Set\ A$ was kept OFF throughout the simulations, except that SW_A4 is switch ON and C_HE was tuned to 15 pF. The simulated S-parameters of the antenna were shown in Figure 14. When SW_B2 is switched ON while SW_B1 is OFF, the excitation slot of the TE mode is loaded with C_TE1 . f_{HE} can be reconfigured from 650 MHz to 818 MHz as the value of C_TE1 changes from 70 pF to 7 pF. When SW_B1 is ON while SW_B2 is OFF, the excitation slot of the TE mode is loaded with C_TE2 . f_{TE} can then be tuned continuously from 609 MHz to 642 MHz, as the value of C_TE2 changes from 9 pF to 4 pF. Hence the TE mode is able to cover from 609 MHz to 818 MHz. Similar to the first set of simulations, f_{HE} is invariant at 718 MHz during the reconfiguration and the mutual coupling at the operating frequency can be kept below -20 dB, as seen in Figure 14 (b). Again, this signifies the individual tunability of the TE mode.

From Figures 13 and 14, it can be seen the mutual coupling is relatively high when the tuning of the HE mode and TE mode is achieved by changing L_{slot} and the activation of the slot loading connected through SW_B2 , respectively. This is because the slot loadings are asymmetric about x -axis and this disturbs the symmetry of the mode distributions.

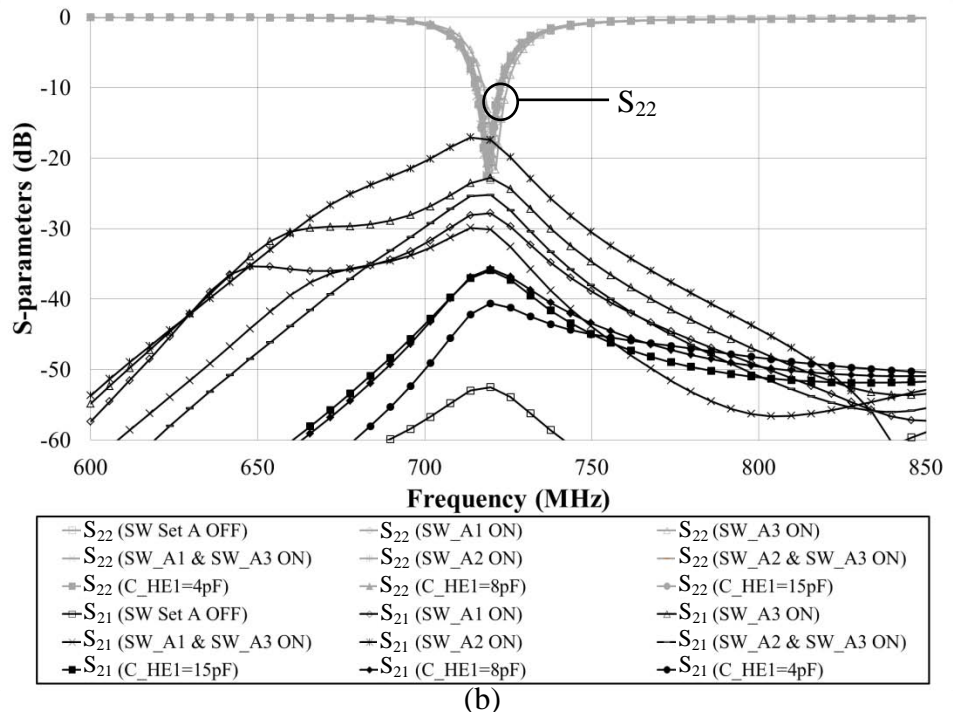
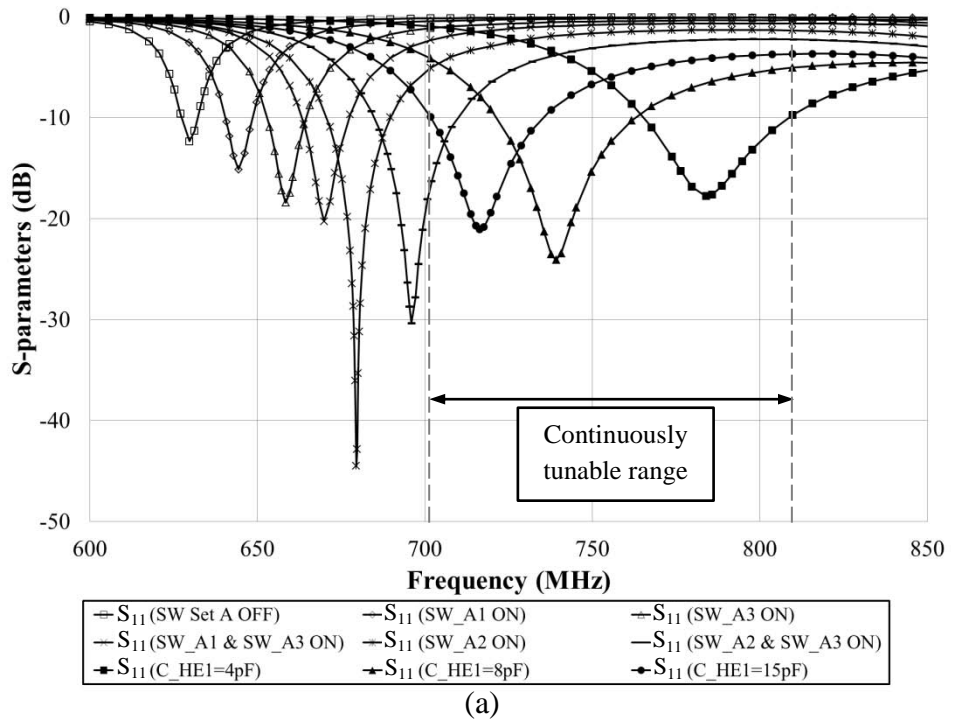
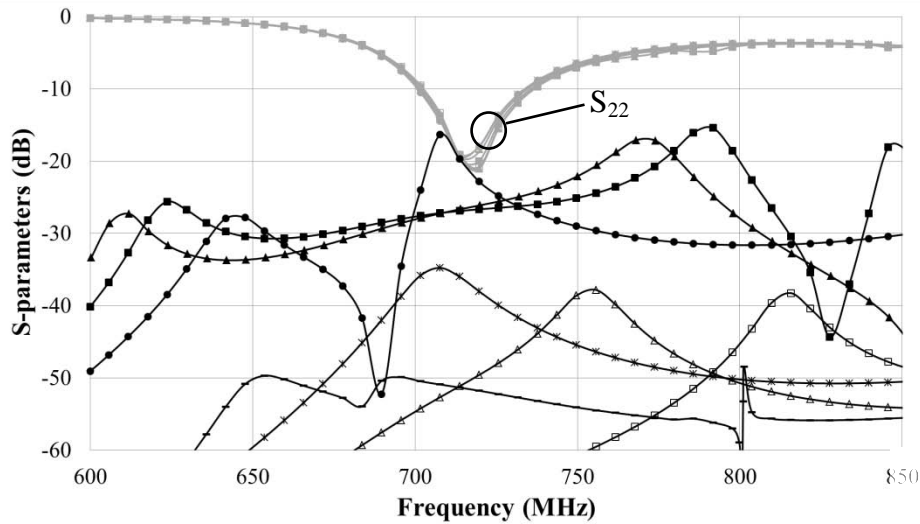
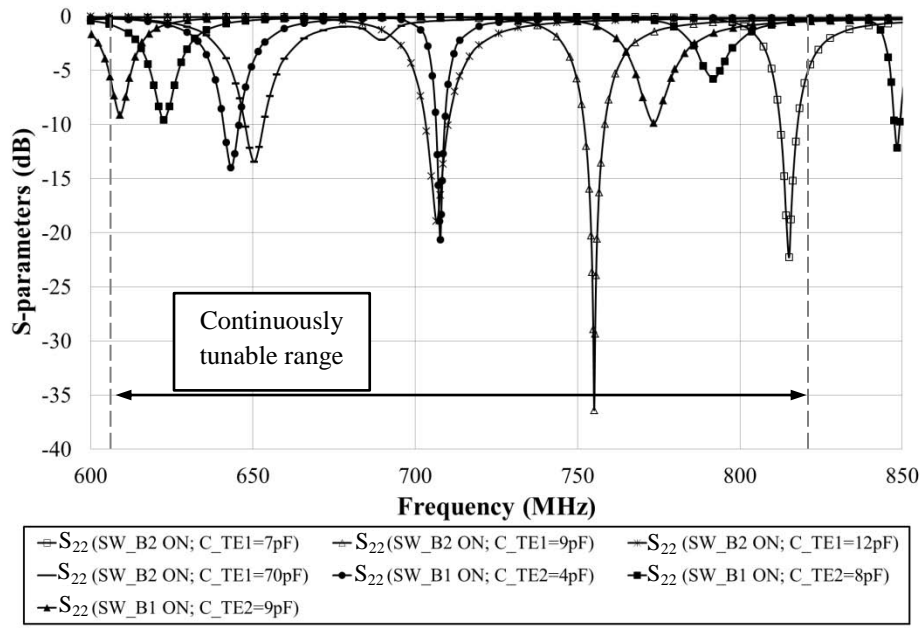


Figure 13. Simulated S -parameters of the frequency reconfigurable MIMO DRA. The frequency agility is achieved by reconfiguring the parasitic slot on *Ground Plane A* (a) S_{11} -HE mode, and (b) S_{22} -TE mode and S_{21} -mutual coupling.



(a)



(b)

Figure 14. Simulated S-parameters of the frequency reconfigurable MIMO DRA. The frequency agility is achieved by switching the slot loading on *Ground Plane B* (a) S₁₁-HE mode and S₂₁-mutual coupling, and (b) S₂₂-TE mode

Table I summarizes the antenna parameters for various configurations of the antenna. Frequency reconfigurable MIMO operation can be achieved from 630 MHz to 810 MHz (with a continuously tunable range from 701 MHz to 810 MHz, given the capacitance range specified in Table I). The operating frequency of an individual mode can also be tuned separately. This is a new functionality for frequency reconfigurable MIMO antenna that yet to be found in the literature. Furthermore, it should be emphasized that the gain of the stationary mode (modes with invariant operating frequency during reconfiguration) is fairly steady. Therefore this allows a minimal gain calibration throughout the band of reconfiguration, easing the burden on the gain control unit. Figure 15 further shows the simulated *S*-parameters of the antenna for three different configurations (See Table II) which span the entire bandwidth of reconfiguration. The corresponding radiation patterns are given in Figures 16 and 17. It can be observed that the radiation patterns do not have abrupt changes during reconfigurations, except that the cross polarization levels in some cases increase.

Table I. A summary of the antenna parameters for various configuration settings.

SW Set A				SW Set B		<i>C_{HE}</i>	<i>C_{TE1}</i>	<i>C_{TE2}</i>	<i>f_{HE}</i>	<i>f_{TE}</i>	max(S21)	<i>Gain_{HE}</i>	<i>Gain_{TE}</i>
<i>A1</i>	<i>A2</i>	<i>A3</i>	<i>A4</i>	<i>B1</i>	<i>B2</i>	(pF)	(pF)	(pF)	(MHz)	(MHz)	(dB)	(dBi)	(dBi)
ON				ON			11		630	719	-52.6	3.43	3.95
				ON			11		644	719	-27.8	3.46	3.97
				ON	ON		11		659	721	-23.1	3.62	3.97
ON				ON			11		670	719	-30.3	3.64	3.93
				ON			11		680	719	-17.2	3.7	3.94
	ON	ON		ON			11		696	719	-25.4	3.78	3.93
				ON	ON	4	11		784	719	-35.7	4.21	4.38
				ON	ON	8	11		739	719	-37.3	3.97	4.18
				ON	ON	15	11		717	719	-40.6	3.86	3.88
				ON	ON	15	7		718	818	-37.7	3.9	4.27
				ON	ON	15	9		718	755	-38.1	3.89	4.03
				ON	ON	15	12		718	708	-35.6	3.86	3.88
				ON	ON	15	70		718	650	-49	3.91	3.48
	ON	ON				15		9	717	609	-27.2	3.88	2.24
	ON	ON				15		8	717	622	-26	3.9	2.74
	ON	ON				15		4	717	642	-27.6	3.84	3.03

Table II. Antenna configurations for frequency reconfigurable MIMO functionality.

Config.	SW Set A				SW Set B		C_HE	C_TE1	C_TE2
	A1	A2	A3	A4	B1	B2	(pF)	(pF)	(pF)
1						ON			6.6
2					ON	ON	15	11	
3					ON	ON	4	8	

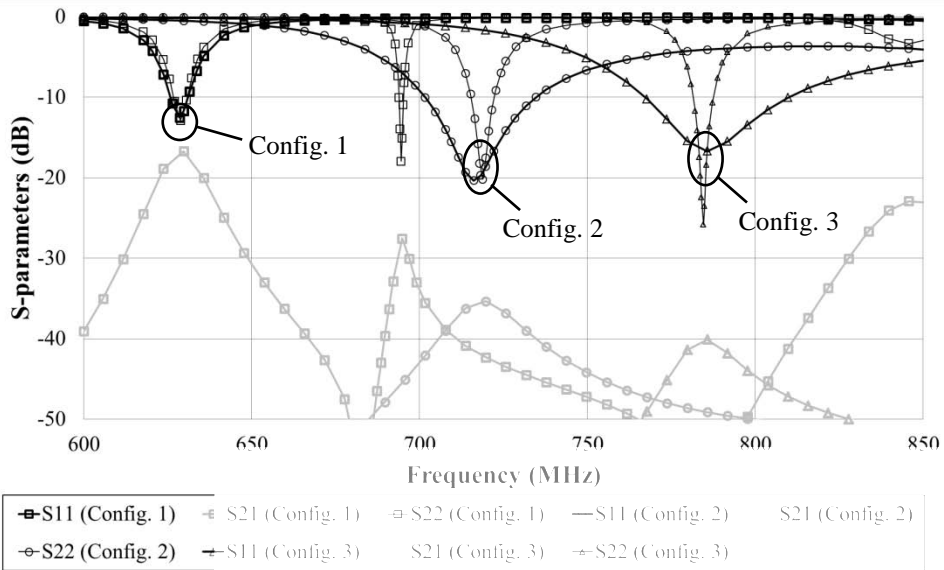


Figure 15. Simulated S-parameters of the frequency reconfigurable MIMO DRA.

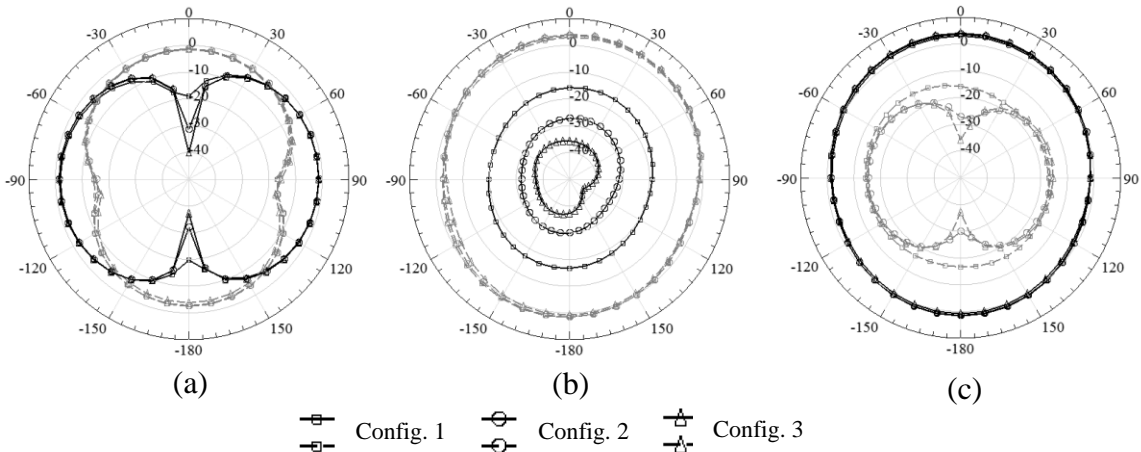


Figure 16. Simulated HE mode (port 1) radiation patterns of the frequency reconfigurable MIMO DRA (a) xy-plane, (b) xz-plane, and (c) yz-plane
(Solid line: Gain_φ; Dotted line: Gain_θ)

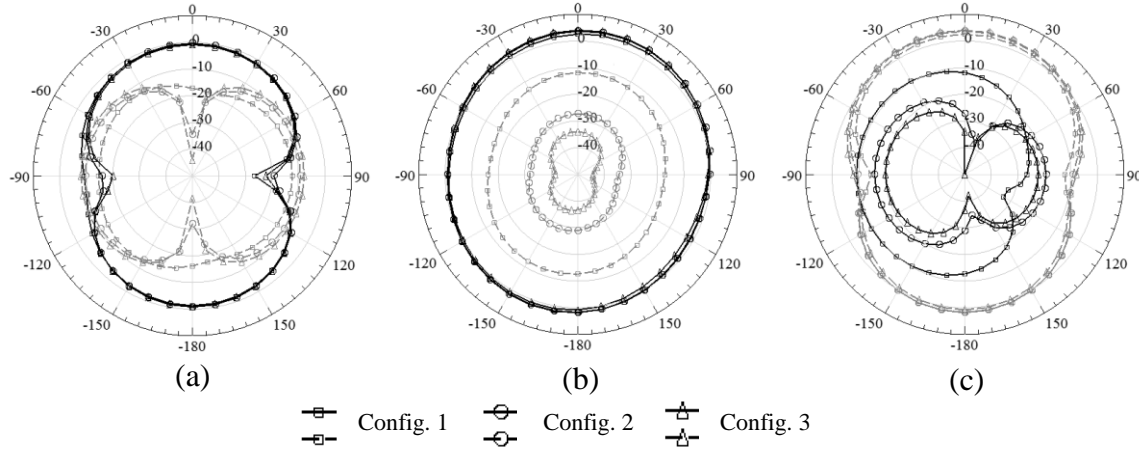


Figure 17. Simulated TE mode (port 2) radiation patterns of the frequency reconfigurable MIMO DRA (a) xy -plane, (b) xz -plane, and (c) yz -plane (Solid line: Gain_ϕ ; Dotted line: Gain_θ).

4. Conclusion and Future Work

This paper investigates two different modalities for adding frequency agility into the previously developed MIMO DRA. The first modality is achieved by introducing a material perturbation in the dielectric block. The technique for placing the perturbation in an adequate location inside the dielectric cavity for maximum frequency agility has been outlined. The addition of parasitic slot loading was studied as a second method to introduce frequency reconfigurability into the MIMO DRA. It has been shown that the proposed MIMO DRA is able to reconfigure from 630 MHz to 810 MHz, which covers more than half of the CR band. The major features of the proposed frequency reconfigurable MIMO DRA include the ability to allow individual tuning to the antenna ports and very small antenna performance variation across the band of reconfiguration. Fabrication and measurement of the proposed frequency reconfigurable DRA using the parasitic slot loading will be the major future work of this research.

5. Acknowledgment

The authors would like to acknowledge Motorola Center for Communications at the University of Illinois at Urbana-Champaign and the Croucher Foundation Scholarship for supporting this research.

6. References

- [1] G. J. Foschini, and M. J. Gans, "On limits of wireless communications in a fading environment when using multiple antennas," *Wireless Personal Commun.*, no. 6, pp. 311-335, 1998.
- [2] G. Scutari, D. Palomar, and S. Barbarossa, "Cognitive MIMO radio," *IEEE Signal Processing Magazine*, vol. 25, no. 6, pp. 46-59, Nov. 2008.
- [3] S. Sridharan and S. Vishwanath, "On the capacity of a class of MIMO cognitive radios," *IEEE Journal of Selected Topics in Signal Processing*, vol. 2, no. 1, pp. 103-117, Feb. 2008.
- [4] Federal Communications Commission, Cognitive Radio Technologies Proceeding (CRTP), ET Docket 03-108 [Online]. Available: <http://www.fcc.gov/oet/cognitiveradio/>
- [5] FCC Spectrum Policy Task Force, "FCC Report of the Spectrum Efficiency Working Group," Nov. 2002 [Online]. Available: <http://www.fcc.gov/sptf/files/SEWGFinalReport1.pdf>
- [6] Federal Communications Commission. "700 MHz band," Auction 73, Feb. 2009.
- [7] J.-B. Yan, and J.T. Bernhard, "Design of a MIMO dielectric resonator antenna for 700 MHz wireless applications," in *Proc. URSI 2010 National Radio Science Meeting*, Boulder, CO, USA, Jan. 6-9, 2010.
- [8] S. G. O'Keefe, and S. P. Kingsley, "Tunability of liquid dielectric resonator antennas," *IEEE Antennas Wireless Propag. Lett.*, vol. 6, pp. 533-536, 2007.
- [9] G. H. Huff, D. L. Rolando, P. Walters, and J. McDonald, "A frequency reconfigurable dielectric resonator antenna using colloidal dispersions," *IEEE Antennas Wireless Propag. Lett.*, vol. 9, pp. 288-290, 2010.
- [10] A. Petosa, and S. Thirakoune, "Frequency tunable rectangular dielectric resonator antenna," in *Proc. IEEE Antennas and Propagation Society Int'l Symp.*, Charleston, SC, USA, Jun. 2009.
- [11] G. H. Huff, S. Goldberger, and S. A. Long, "Operational perspectives of biologically inspired capillary-based reconfiguration mechanisms in microstrip patch antennas," in *Proc. Antenna Application Symp.*, Allerton, IL, USA, pp. 142-157, Sep. 2009.
- [12] R. F. Harrington, *Time-harmonic electromagnetic fields*. New York: IEEE Press, 2001.
- [13] S. Gunel, and E. Y. Zoral, "Parametric history analysis of resonance problems via step by step eigenvalue perturbation technique," *IET Microwaves, Antennas and Propagation*, vol. 4, no. 4, pp. 466-476, 2010.
- [14] L. N. Trefethen, *Numerical Linear Algebra*. Philadelphia: SIAM, 1997.
- [15] J. M. Jin, *The Finite Element Method in Electromagnetics*. New York: Wiley, 2002.
- [16] Ansoft HFSS®, Ansys, Inc, 2010 Version 12.1.
- [17] K. K. So, and K. W. Leung, "Bandwidth enhancement and frequency tuning of the dielectric resonator antenna using a parasitic slot in the ground plane," *IEEE Trans. Antennas Propagat.*, vol. 53, no. 12, pp. 4169-4172, Dec. 2005.

Millimeter-wave dielectric loss characterization with one-dimensional grating

V.I. Litvinov, V.A. Manasson, M. Felman, and L.S. Sadovnik

Sierra Nevada Corporation

17245 Alton Pkwy, Suite 100, Irvine CA, 92618

Abstract. W-band dielectric loss characterization is proposed in the frequency region where material data are not normally available. The method uses the near-field measurements of the leaky wave dielectric grating in combination with finite element simulations. As an example, the actual loss tangent of Rexolite at 94.3 GHz is shown to be 75% larger than its 10 GHz value given in a formal material specification.

I. INTRODUCTION

Dielectric characterization (dielectric constant and loss tangent) is a basic element of microwave applications of dielectrics. Dielectrics are often used in W-band antennas, waveguides, and various high-frequency passive elements [1,2]. However, dielectric materials are normally characterized at a relatively low frequency of about (1-10) GHz. As far as an application of the materials in the 100 GHz range is concerned, the low-frequency data may fail especially in large dielectric antenna apertures where the dielectric losses determine the antenna efficiency to a great extent.

In this paper we determine the W-band dielectric loss tangent at an antenna operating frequency using the standard antenna near-field measurements combined with finite element simulations. For this purpose, we use the dielectric grating as a serial-fed antenna array where the grating period and the propagation constant determine the far-

field direction angle whereas the near-field distribution along the antenna aperture determines the radiative and dielectric losses. Then, experimental data being compared to that obtained from simulations, gives us the actual value of the material loss tangent. It is shown that the actual loss tangent of Rexolite at 94 GHz differs from that supplied in the low-frequency datasheet.

II. RADIATIVE COUPLING IN LEAKY WAVE ANTENNA

The serial-fed linear array comprises the dielectric grating, namely, the set of grooves in a dielectric substrate as shown in Fig.1. The grating period $p=2.2$ mm is chosen to preserve the only diffraction order $n=-1$ in the far-field at $f = 94.3$ GHz.

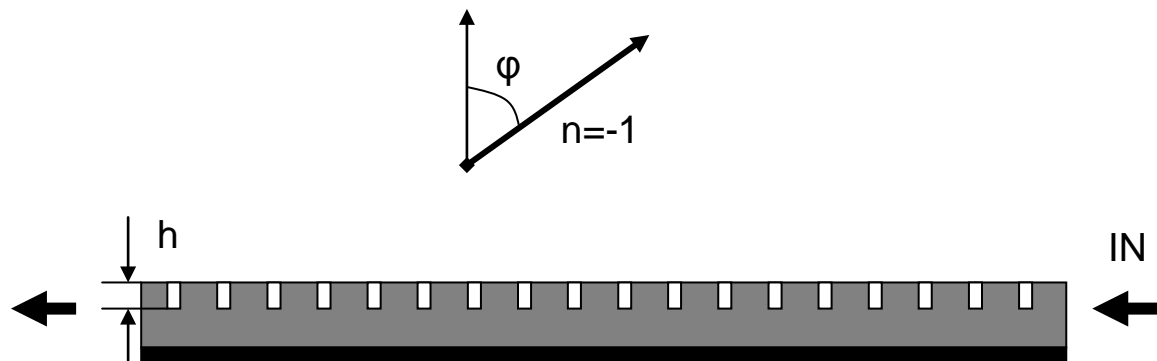


Fig.1. *Ground plane backed dielectric grating. Angle φ represents the direction of the maximum far-field, grating order $n=-1$. Linear polarization is perpendicular to the plane of the picture.*

Signal traveling along the substrate couples to grooves thus making them radiating array elements. We define the radiative coupling coefficient κ (loss coefficient

α) per period as a part of the power, incoming into a certain period, that is radiated (absorbed) by this period. The part of input power that radiates from a certain period i , ($i = 1 \dots N$, N is the total number of grooves) can be written as follows:

$$p_r(i) = (1 - |S_{11}|^2)\kappa(1 - \kappa - \alpha)^{i-1}, \quad (1)$$

where $|S_{11}|^2$ is the reflection coefficient. The Eq.(1) represents the near-field power distribution $p_r(i)$ along an array aperture. Total radiative part of an input power can be calculated as follows:

$$\begin{aligned} P_{rad} &= (1 - |S_{11}|^2) \sum_{i=1}^N \kappa(1 - \kappa - \alpha)^{i-1} = \\ &= \frac{\kappa}{\kappa + \alpha} (1 - |S_{11}|^2) [1 - (1 - \kappa - \alpha)^N] \end{aligned} \quad (2)$$

The part of input power that is lost in a certain period i can be written as follows,

$$p_{loss}(i) = (1 - |S_{11}|^2)\alpha(1 - \kappa - \alpha)^{i-1}, \quad (3)$$

so the total lost part of input power along the array aperture has the form:

$$\begin{aligned} P_{loss} &= (1 - |S_{11}|^2) \sum_{i=1}^N \alpha(1 - \kappa - \alpha)^{i-1} = \\ &= \frac{\alpha}{\kappa + \alpha} (1 - |S_{11}|^2) [1 - (1 - \kappa - \alpha)^N] \end{aligned} \quad (4)$$

Eq's (2) and (4) relate the coupling and loss coefficients to S-parameters of a two-terminal array:

$$|S_{11}|^2 + |S_{12}|^2 + P_{loss} + P_{rad} = 1,$$

or

$$\kappa + \alpha = 1 - \left[\frac{|S_{12}|^2}{1 - |S_{11}|^2} \right]^{1/N} \quad (5)$$

Antenna radiation efficiency R , defined as a ratio of a radiation power to an accepted one, can be written as

$$R = \frac{P_{rad}}{(1 - |S_{11}|^2 - |S_{12}|^2)} = \frac{\kappa}{\kappa + \alpha} \quad (6)$$

The loss coefficient can be found from Eq's (5) and (6):

$$\alpha = \kappa \left(\frac{1}{R} - 1 \right) \quad (7)$$

If one starts from HFSS simulation of the leaky wave antenna made of real materials with the account for dielectric and metal losses, Eq's (5) and (7) present the system that allows finding the coupling coefficient κ and the loss coefficient α , using simulation data for S-parameters and radiation efficiency.

Parameter κ plays important role in design of low sidelobes leaky wave antenna, as the coupling coefficient determines the taper profile that could be implemented by varying groove depth or width along the antenna aperture.

In order to illustrate the near-field distribution depending on a loss coefficient α , we choose the Rexolite ($\epsilon = 2.54$) grating with 0.5mm wide and 0.5mm deep grooves. Near-field power distribution from Eq.(1) is shown in Fig.2, where $\kappa = 0.02$ has been found from Eq.(5) using S-parameters from simulation data for the lossless material.

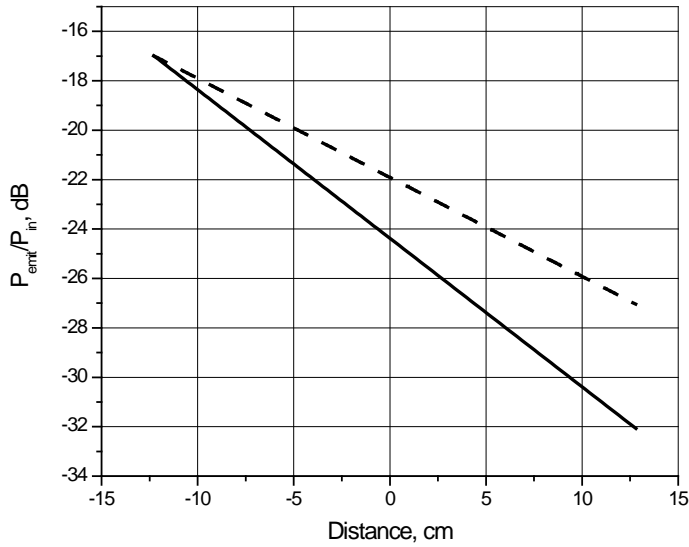


Fig.2. Near-field power distribution along the antenna aperture, solid line- $\alpha = 0.01$; broken line- $\alpha = 0.0001$; $\kappa = 0.02$.

The emitted power shown in Fig.2 has been obtained from Eq.(1) and can be characterized with the slope of the log-scale graph.

Loss coefficient α is related to a material loss, but it also depends on a grating geometry. In order to single out the material loss ($\tan\delta$), we combined HFSS simulations with experimental measurements of near-field distribution along the antenna aperture.

III. ANTENNA MEASUREMENTS AND SIMULATIONS

In this section we use the experimental way to find the material loss coefficient. The simulation results will be compared to the experimental near-field data that allows us calculating the material loss coefficient at the actual frequency of the experiment.

Measurements have been performed with the NSI-near-field scanner with the accuracy not less than of 0.1 dB. Polarization was parallel to the grooves. Experimental

near-field distribution along the aperture is shown in Fig. 3. The slope of the linear approximation in Fig.3 gives us a decay of the near field which is determined by both the radiative and dielectric losses.

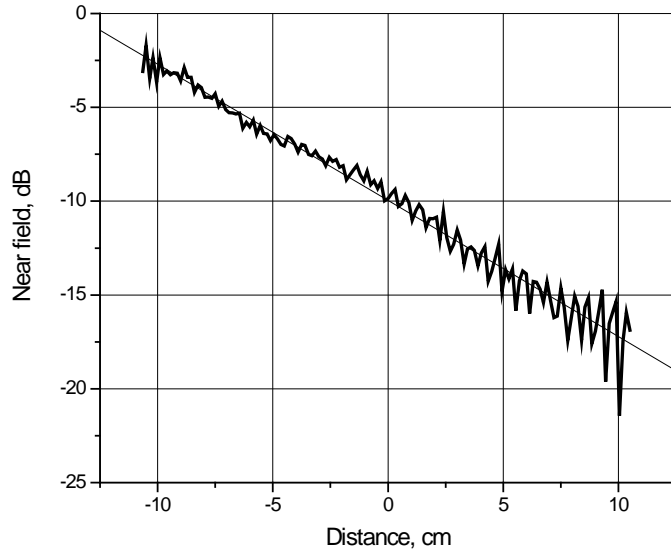


Fig.3. Experimental near-field distribution along the antenna aperture.

Fig.3 illustrates the slope (0.72 ± 0.01) dB/cm as total (dielectric and radiative) loss characteristics.

The slope in Fig.3 is to be compared to those we obtain from HFSS simulations. Simulations were performed with the material dielectric loss $\tan \delta$ as a parameter. Fig.4 illustrates the near-field distribution for an lossless dielectric (dielectric constant $\epsilon = 2.54$) and that with the loss tangent of 0.003.

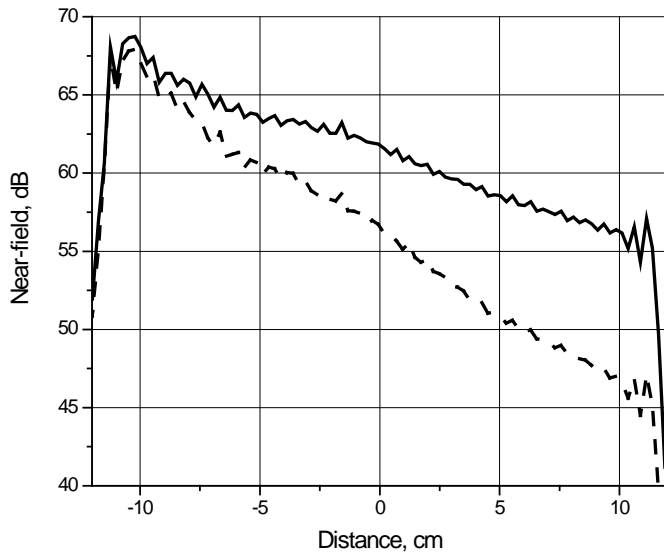


Fig.4. *Simulation results on near-field distribution along the antenna aperture.*
Solid line- $\tan \delta = 0$, broken line- $\tan \delta = 0.003$.

Simulations illustrated in Fig.4 have been performed for various loss tangents and near-field slope coefficient has been calculated from the simulation data. The results are shown in Fig.5 where the near-field slope coefficient is depicted as a function of the loss tangent.

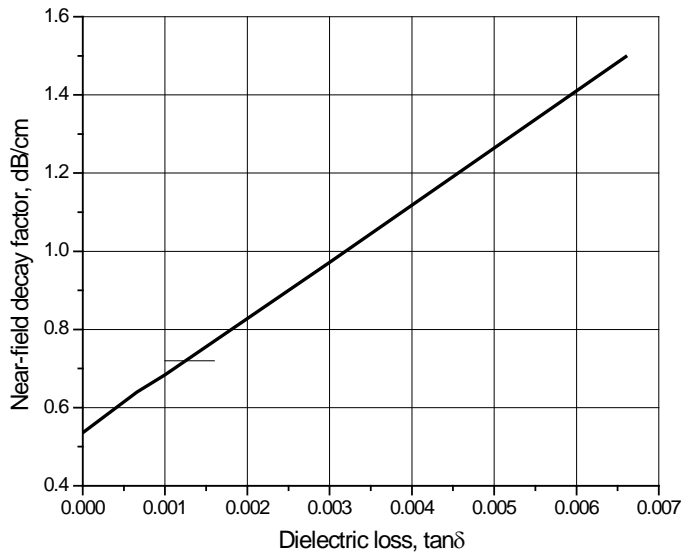


Fig.5. Simulated near-field slope coefficient.

Data illustrated in Fig.5 allows us to find out that the experimental slope of 0.72 dB/cm at 94.3 GHz corresponds to a loss tangent of 0.001153 ± 0.0007 .

IV. CONCLUSIONS

We propose the method which enables dielectric loss characterization of the materials widely used in various high frequency antenna applications, where the material data are hardly available. This method relies on simultaneous measurements and simulations of the near-field distribution along the antenna aperture. In the example considered in this paper, the actual loss tangent of Rexolite at 94.3 GHz is equal to 0.001153 that is 75% larger than the low-frequency value of 0.00066 given in the datasheet specification obtained in 10 GHz frequency region.

References

¹ D.M. Pozar, and D. Schaubert, “Microstrip Antennas”, IEEE Press, Piscataway, NJ , 1995.

² R.N. Simons, “Coplanar Waveguide Circuits, Components and Systems”, John Wiley & Sons, Inc, New York, NY, 2001.

A Low Cost, Multi-Channel, S-Band Transmit/Receive Module for Phased Array Communication Systems

Sarjit S. Bharj⁽¹⁾, Boris Tomasic⁽²⁾, John Turtle⁽³⁾, Roger Turner⁽⁴⁾, Gary Scalzi⁽⁵⁾, and Shiang Liu⁽⁶⁾

⁽¹⁾Princeton Microwave Technology, Inc., 3 Nami Lane, Merverville NJ 08619,
sarjit@princetonicrowave.com

⁽²⁾Air Force Research Laboratory, Hanscom AFB, MA 01731-2909, boris.tomasic@hanscom.af.mil

⁽³⁾Air Force Research Laboratory, Hanscom AFB, MA 01731-2909, john.turtle@hanscom.af.mil

⁽⁴⁾Air Force Research Laboratory, Wright-Patterson AFB, OH 45433 roger.turner@wpafb.af.mil

⁽⁵⁾Air Force Research Laboratory, Wright-Patterson AFB, OH 45433 gary.scalzi@wpafb.af.mil

⁽⁶⁾The Aerospace Corporation, P.O. Box 92957, Los Angeles, CA 90009-2957, shiang.liu@aero.org

Abstract – A multi-channel S-Band Transmit/Receive [T/R] Module has been designed and produced for future satellite communication applications. The module consists of two independent receive channels and a single transmit channel with dual polarization for LHCP and RHCP applications. The design of the module consists of a large number of MMICs in various technologies which are useful for low noise, power, and high efficiency operation. The digital logic for the T/R module is implemented locally using a powerful, low cost microcontroller. It has full capability of on-demand telemetry for health status and operational parameters such as low noise and power amplifier currents, temperature, and other built in tests. This paper will discuss the T/R module block diagram and focus on the statistical measurements associated with the production of the T/R modules.

1. INTRODUCTION

Low-cost transmit/receive (T/R) module design and implementation issues are critical in developing a practical phased array antenna. Combining RF, digital, and monolithic circuits is not only important but essential to achieve an affordable system. Modern phased array antennas operating at microwave frequencies consist of active modules at each element which utilize a large number of MMICs (Monolithic Microwave Integrated Circuits) for transmit and receive beamforming/steering and array control. Princeton Microwave Technology [PmT] has developed a multi-channel T/R module that has achieved a power output and noise figure in accordance with the specifications in Tables 1 and 2. The main objective for the development was low cost associated with the active

and passive components, assembly costs, and testing issues. An automated measurement system was implemented both for the small signal and large signal measurements. 100% testing was conducted on all the RF parameters and stored for further statistical and manufacturability analysis.

Table 1. Transmit channel specifications

Parameter	Specifications
Frequency	1.75-2.1 GHz
Gain	20 dB
Power output per channel	33dBm
Phase shift	4 bit
Control	Microcontroller
Retrofit	Hot swap
Efficiency	>40 %
Spurious	<-85
Built in Test	Current monitoring
Isolation at 2.15 GHz	>45 dB
Tx Rejection at RX band	>55 dB

Table 2. Receive channel specifications

Parameter	Specifications
Frequency	2.2-2.3 GHz
Gain	26dB
Noise Figure	1.2 dB
Phase shift	4 bit
Built in Test	Current monitoring
Isolation at 2.15 GHz	>45 dB
RX rejection at TX Band	>55 dB

The T/R module design is based on full-duplex operation and therefore required very high Q factor diplexers. The diplexer's requirements demanded the use of surface-mount methodology with very high rejection criteria. In order to achieve low loss, high rejection, and small size, diplexers based on high dielectric constant ceramic coaxial resonators were procured to meet the specifications.

Since a large quantity of modules is required for a viable system, module weight, mechanical integrity, and costs are important. In order to reduce the mechanical costs, aluminum extrusions were designed for the main body of the module.

2. T/R MODULE BLOCK DIAGRAM

The block diagram of the T/R module is shown in Figure 1. Each T/R module

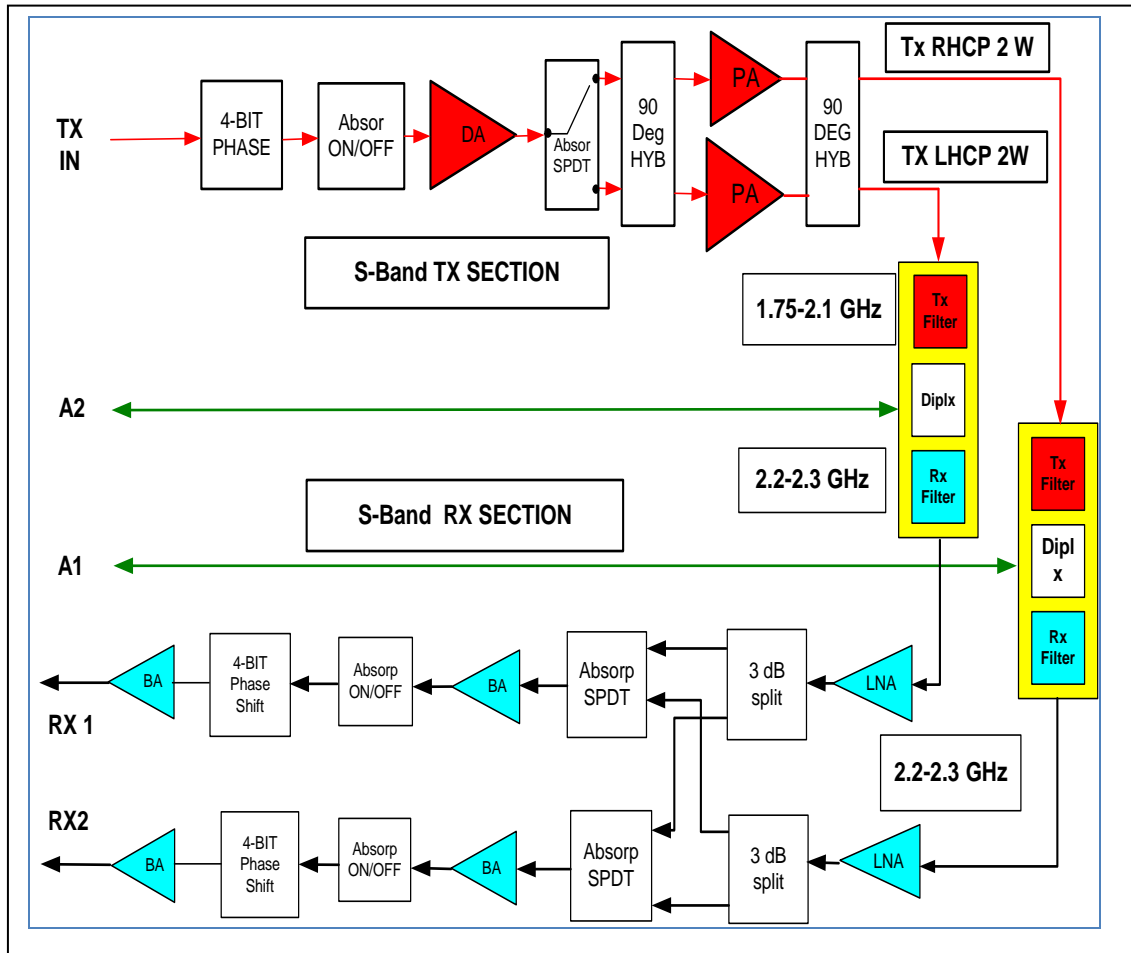


Figure 1. Transmit/Receive module block diagram

consists of two RF/DC boards. The microcontroller and transmit (Tx) section are on one board and the receive (Rx) section is on the other board. The module has one Tx and two Rx channels. In the figure, the transmit path is shown by a red line to distinguish it from the receive path. The transmit band is 1.75-2.1 GHz and the receive band is 2.2-2.3 GHz.

The transmit path consists of an input at the TX IN port and two output (A1/A2) ports connected to the radiating element. The Tx signal passes through a four-bit phase shifter (22.5° , 45° , 90° , 180°), a SPDT switch to open/close the RF paths, a pre-amplifier, and then through a SPDT polarization selection switch before reaching the 90 deg hybrid. Each output of the hybrid is amplified to 1W (30 dBm) and subsequently combined in a second 90 deg hybrid, yielding 2W (33 dBm) total power. The Tx signal then passes through a high rejection ceramic filter. The overall gain of the Tx channel is 20 dB.

The two Rx channels are shown in the bottom half of Figure 1. The Rx signals coming from ports A1 (RHCP) and/or A2 (LHCP) pass through the Rx part of the diplexers and are amplified by the low-noise amplifiers (LNAs). The LNA output signals are then split and subsequently redirected by two SPDP switches toward the Rx1 or Rx2 output ports. Each signal then passes through another set of amplifiers and four-bit phase shifters forming two independent receive beams.

3. DIPLEXERS

Two high-rejection ceramic diplexers were required to maintain optimum performance. The Tx side of the diplexer prevents out-of-band spurious signals from entering the Rx which could saturate the LNAs and increase the noise level, thus degrading the performance. The Rx section of the diplexer prevents the coupled Tx signals from saturating and degrading the linearity of the LNAs.

4. LOW-NOISE AMPLIFIERS, HIGH POWER AMPLIFIERS

A two stage low-noise amplifier was implemented in both channels of the Rx sections. The first stage was a low-noise, N-channel, heterojunction field effect transistor with a noise figure (NF) of 0.4 dB at 2 GHz and a gain of 17 dB. The second stage is a pHEMT low-noise MMIC amplifier with a NF of 0.6 dB and a gain of 18 dB. These devices were matched for low noise performance using a few lumped element reactive components. The important parameters for the LNA are a low noise figure, high gain, high compression point, and low inter-modulation products.

The driver amplifiers and the power amplifiers are general purpose heterojunction bipolar transistors (InGaP HBT) that are pre-matched and designed for broadband Class A, small signal, high linearity applications. They have a gain of 15 dB, a 1 dB compression point at 30 dBm, and the third-order intercept is 47 dBm. The amplifiers operate from a single

supply of 5 Volts. Both the driver and power stages use the same amplifier to simplify the design and reduce the production cost.

5. PHASE SHIFTERS, DIGITAL CONTROL ELECTRONICS AND BUILT-IN-TEST

The phase shifter design is based on MMIC dual single-pole double-throw switches (SPDT) for each phase bit. Grounded coplanar transmission lines were inserted between the switches to produce the required delay. For the Rx channels the required bandwidth is low and therefore the implementation was very simple. However, because the required bandwidth of the Tx channel is 35%, a pseudo-lumped approach was used. This resulted in a wide bandwidth phase shifter with a smaller footprint in comparison to a delay line design.

The PIC microcontroller is implemented on the same side as the Tx RF electronics. The T/R module receives inputs from the main controller through the RS-485 bus. The PIC controls the phase shifter bits for each channel, polarization switching, RF power amplifier on/off, and LNA on/off. Inputs to the microcontroller from the T/R module include temperature, power amplifier currents, and LNA currents. Figure 2 illustrates the main aspects of the digital control. The controller consumes approximately 10 mA.

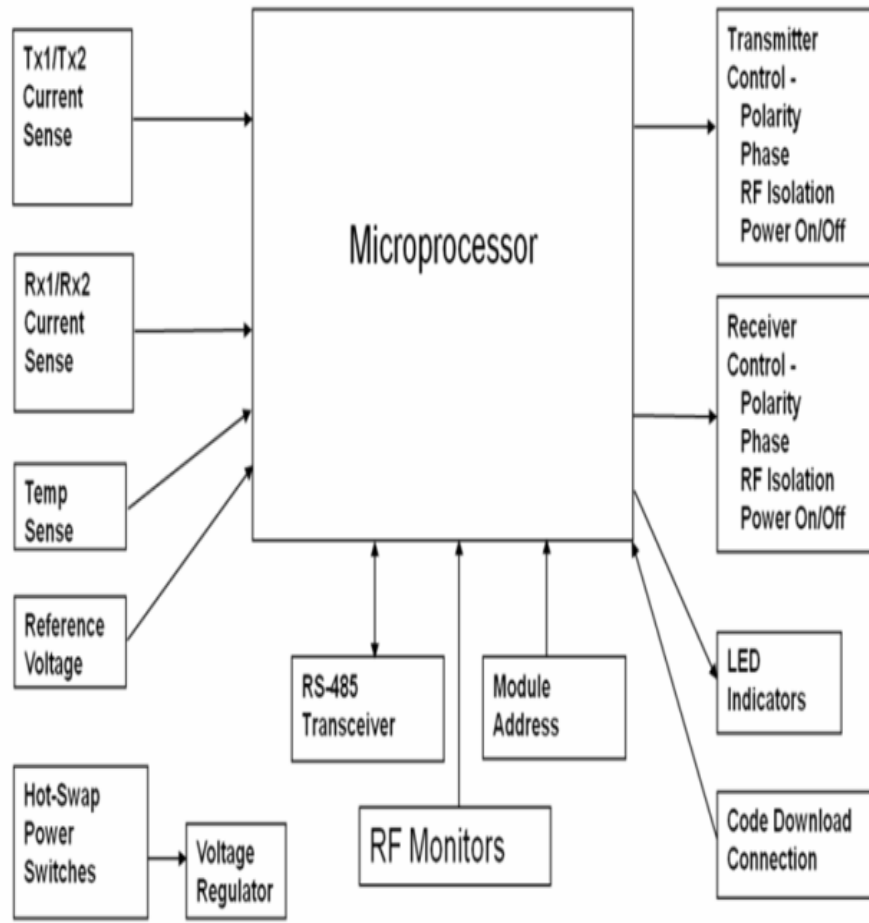


Figure 2. Block diagram of the microcontroller

6. MECHANICAL STRUCTURE AND INTERFACE TO THE BEAMFORMER

The design of the T/R module took into account its size, weight, ease of fabrication, and cost. To reduce the machining cost of the housing, precision aluminum extrusions were used. The front plate, encompassing the MMBX connectors and DC control headers, the back plate, and the main housing were all extruded and post machined. Dowel pins were used for the insertion and removal of the T/R modules and assured accurate alignment with the connectors on the RF manifold/beamformer. Internal shields in the T/R modules

provided RF isolation. Their design was suitable for automatic pick-and-place fabrication processes. The main features of the module can be seen in Figure 3.



Figure 3. Tx side of T/R module

7. AUTOMATED LARGE AND SMALL SIGNAL MEASUREMENTS

In order to meet the cost objectives of the T/R modules, fully automated small and large signal systems were used to measure the phase shifters, the gain, and the gain control and isolation of various devices.

A large signal system consisting of a network analyzer was used to measure the power compression, gain, noise figure, and inter-modulation products. The network analyzer had two frequency sources used for the inter-modulation tests. The large signal measurement system is based on a system that was produced for handset testing with power output capability of 5W. The system, detailed in Figure. 4 below, can measure two tone performance of each power amplifier channel up to the seventh order, the one db compression power, the power gain, the receiver gain, and the receiver noise figure in

a single setup. The total time of measurement per T/R module is in the order of five minutes.



Figure 4: Automated Large Signal Test System

A small signal system was used to measure other parameters, such as return loss. The system consists of a fully automated vector analyzer which is used to measure the gain of each receive channel, the gain of the transmit channels in the LHCP and RHCP, each phase shift bit for each channel, as well as amplitude tracking and phase error. This system was replicated at the location where the T/R modules were assembled and a two day training was conducted. This ensured that the modules we received were 99% good in terms of functionality. The return rate was eliminated altogether. The automated test system is the first pass/fail system in the production process. The total test time per module, including insertion and removal from test fixture, is in the order of two minutes. Figure 5 shows the measurement system with the test fixture. Table 3 shows the measured output of the small signal tests.



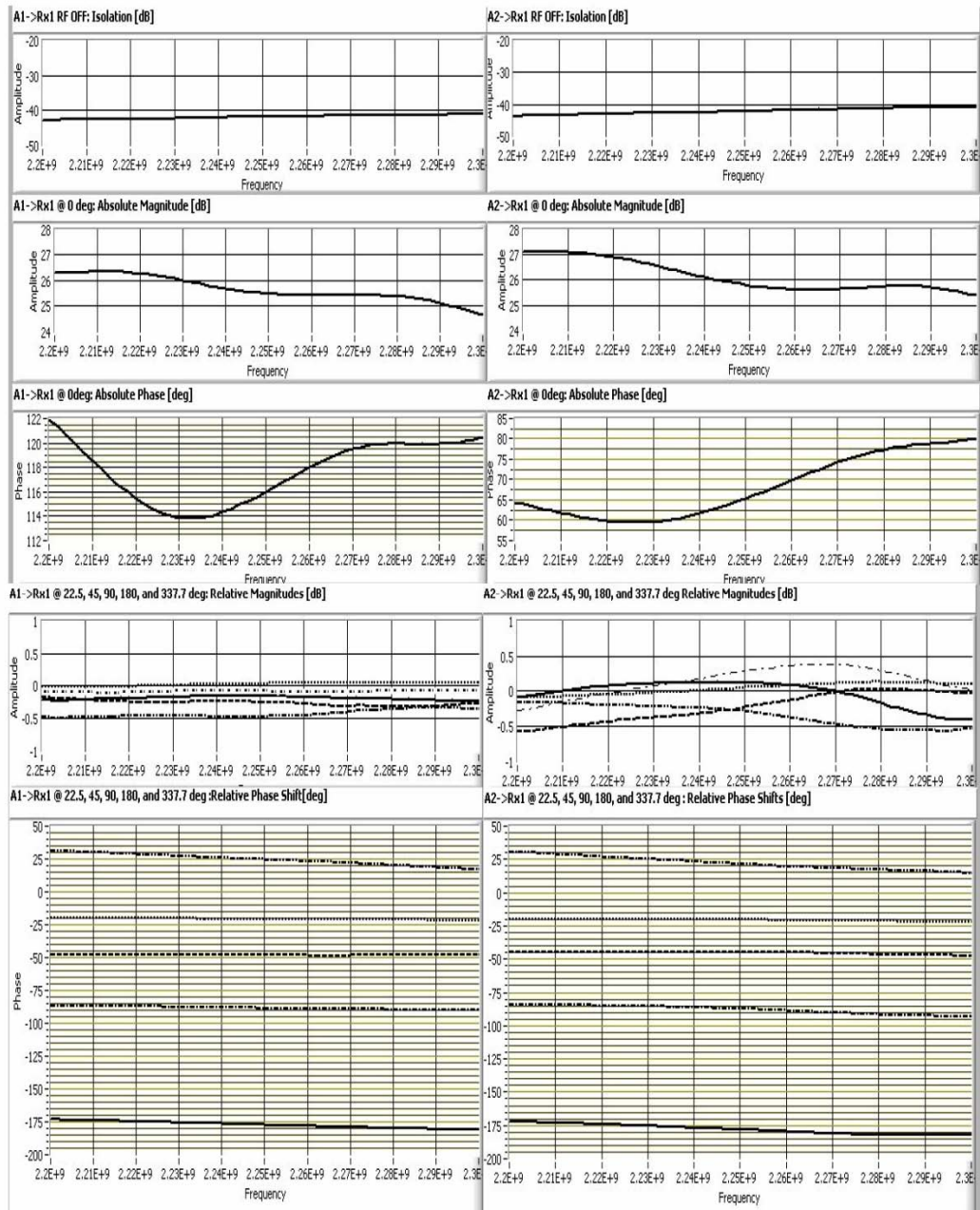
Figure 5: Fully Automated Small Signal Measurement System

TABLE 3: Measured Small Signal Parameters using Automated Measurement System

6/25/2008 2:35 PM

TEST DATA OF MODULE: SN 2363
Receiver Rx1

Princeton Microwave

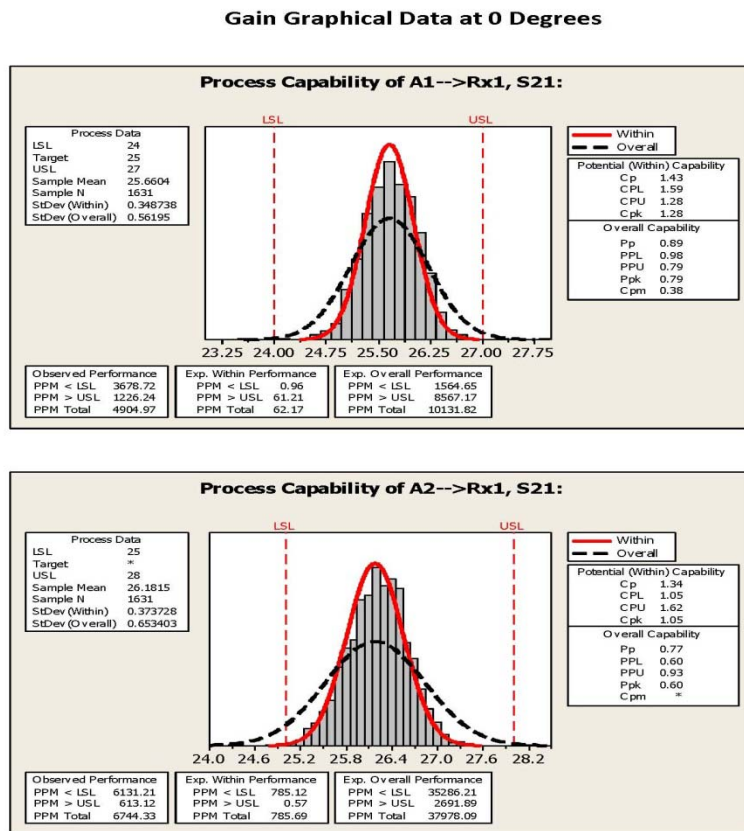


Display_Rx1.vi

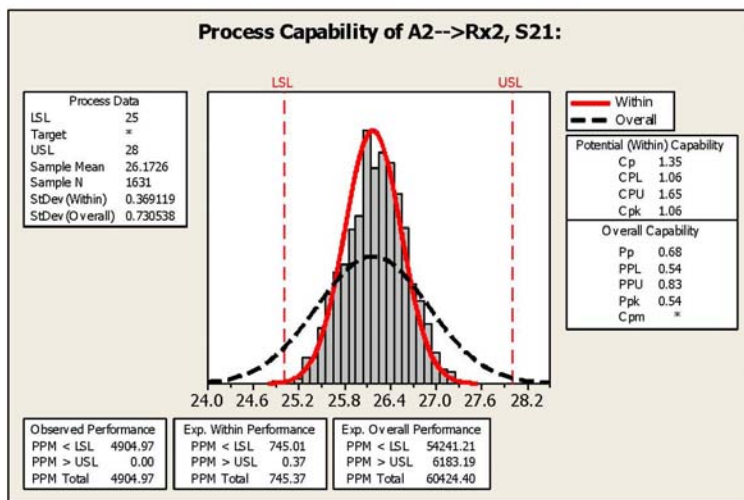
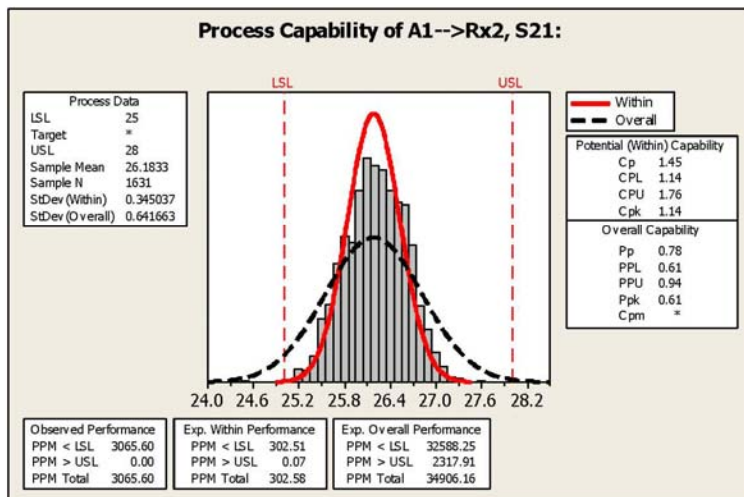
8. T/R MODULE PRODUCTION

A total of 4300 T/R modules were fabricated, assembled, fully tested, and installed in a system. Figures 14 to 17 show a small glimpse of the measurements that were conducted and statistically plotted. Based on these graphs all design and performance goals were met. A manufacturing process capability Cpk of 1.33 was achieved.

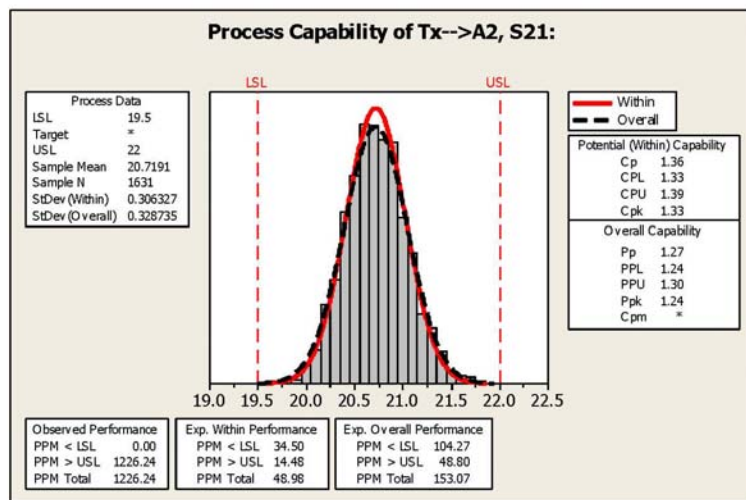
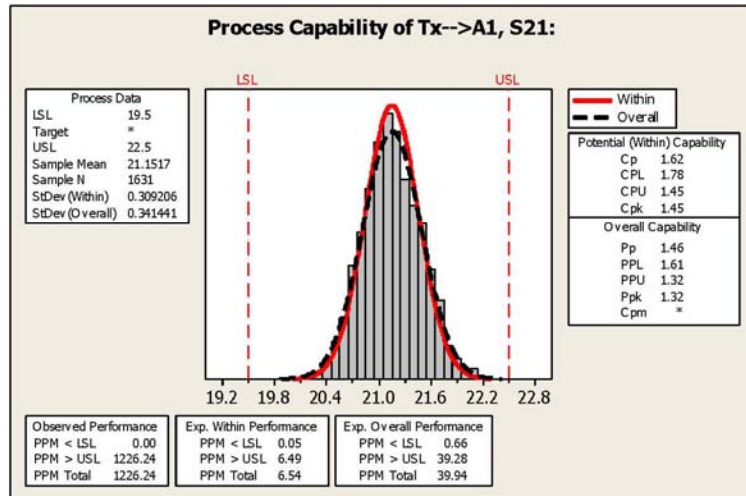
The tables below detail the process capability of various parameters for receiver channels RX1 and RX2, and transmit channels TX1 and TX2 to and from the antenna ports A1 and A2.



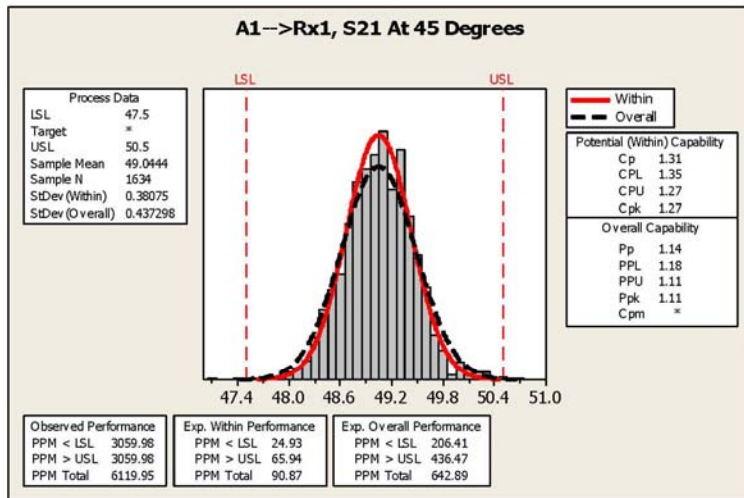
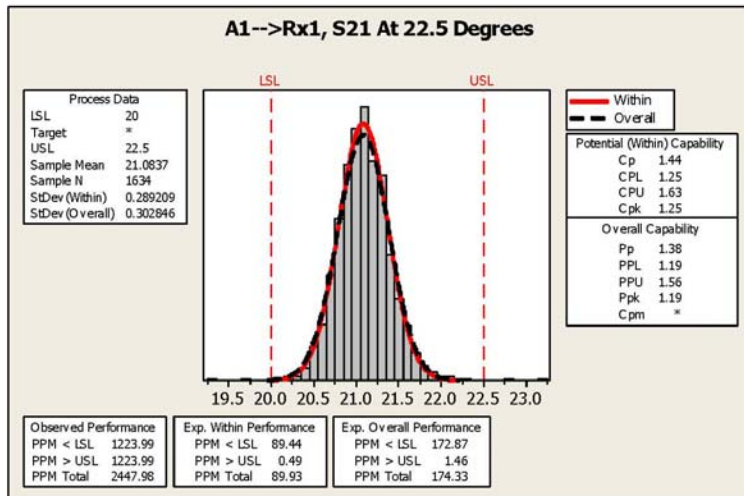
Gain Graphical Data at 0 Degrees



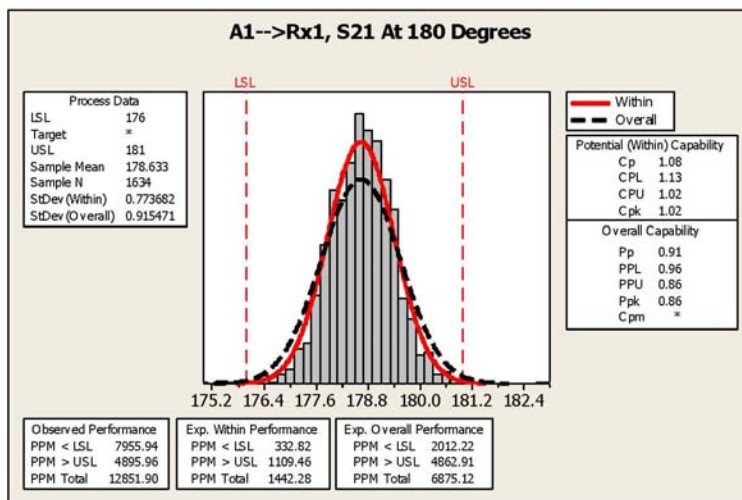
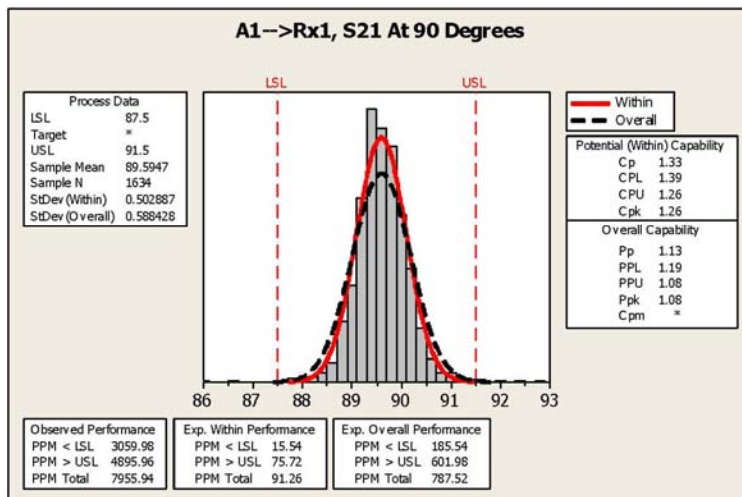
Gain Graphical Data at 0 Degrees



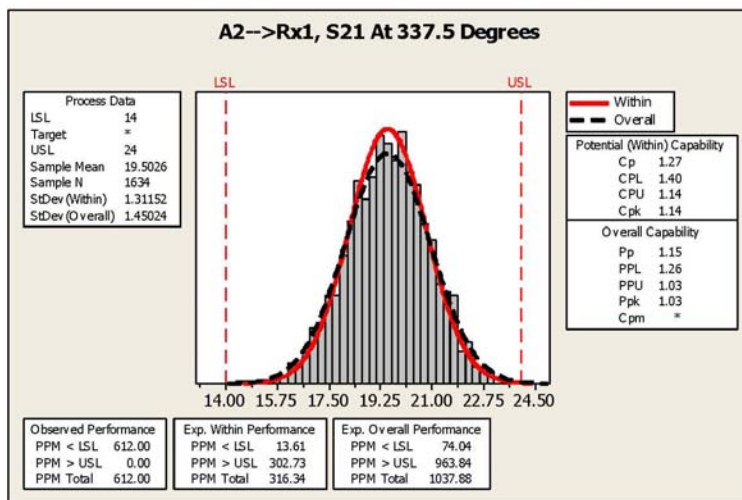
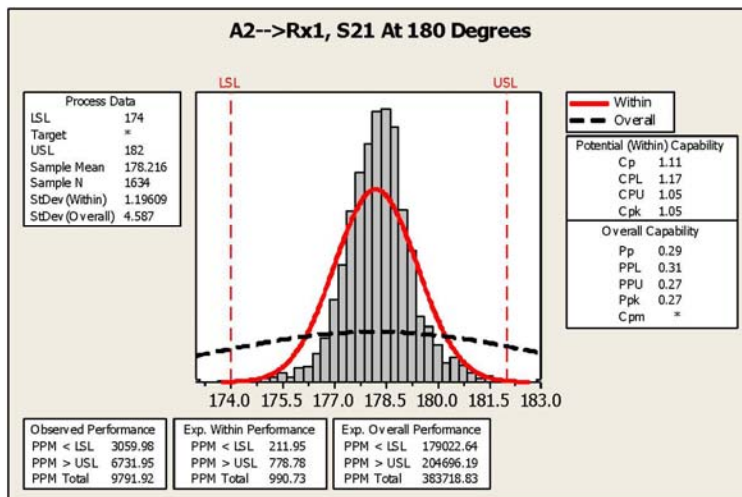
Phase Angle Graphical Data



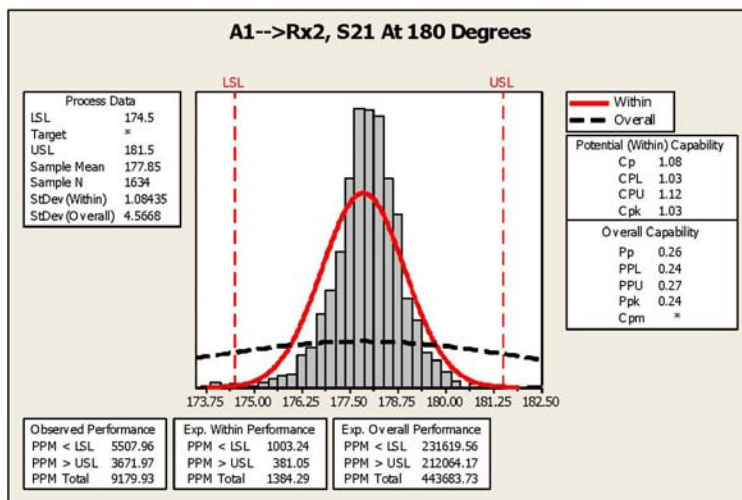
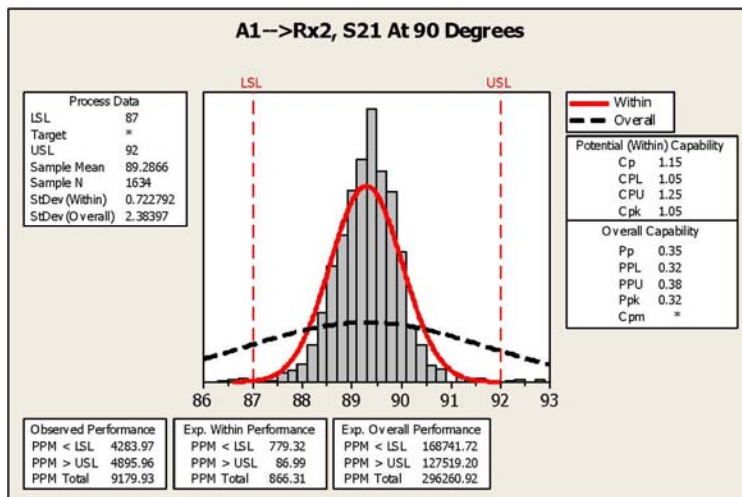
Phase Angle Graphical Data



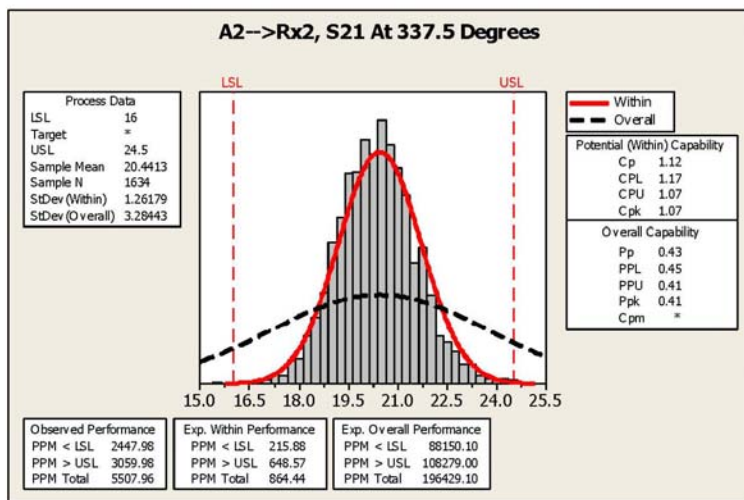
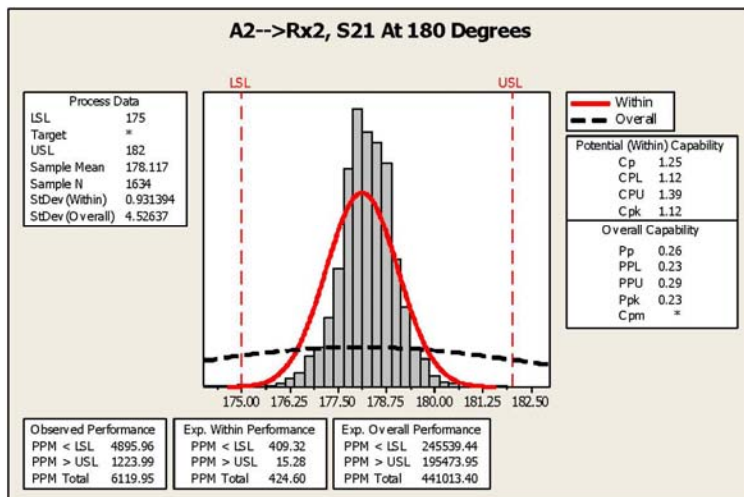
Phase Angle Graphical Data



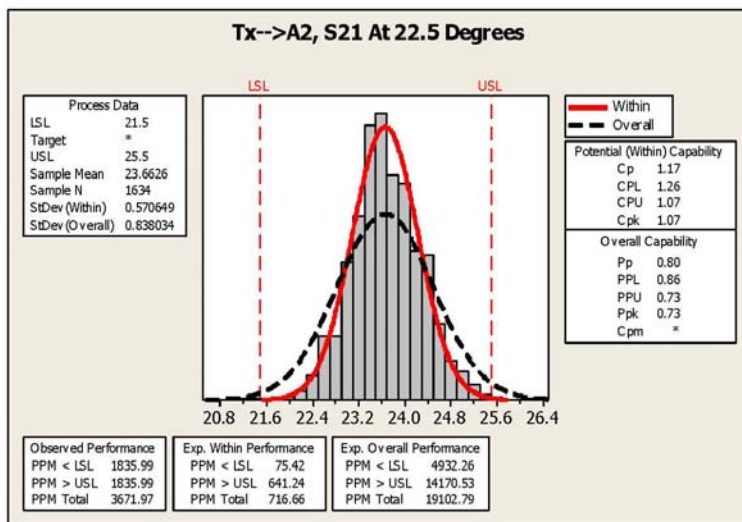
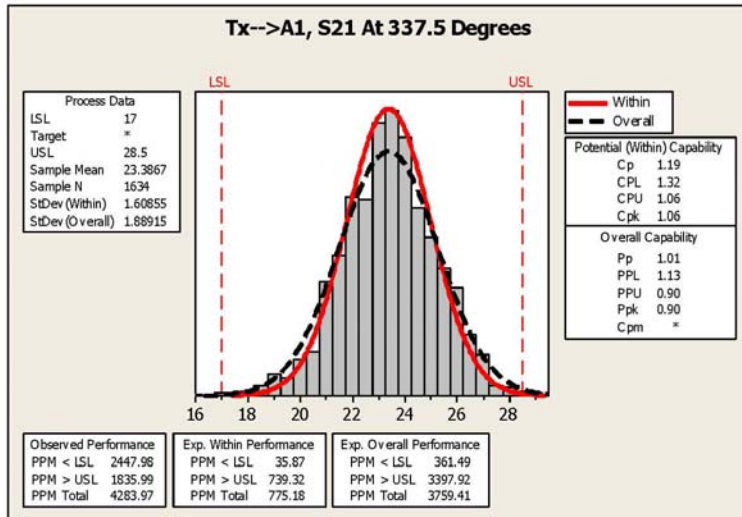
Phase Angle Graphical Data

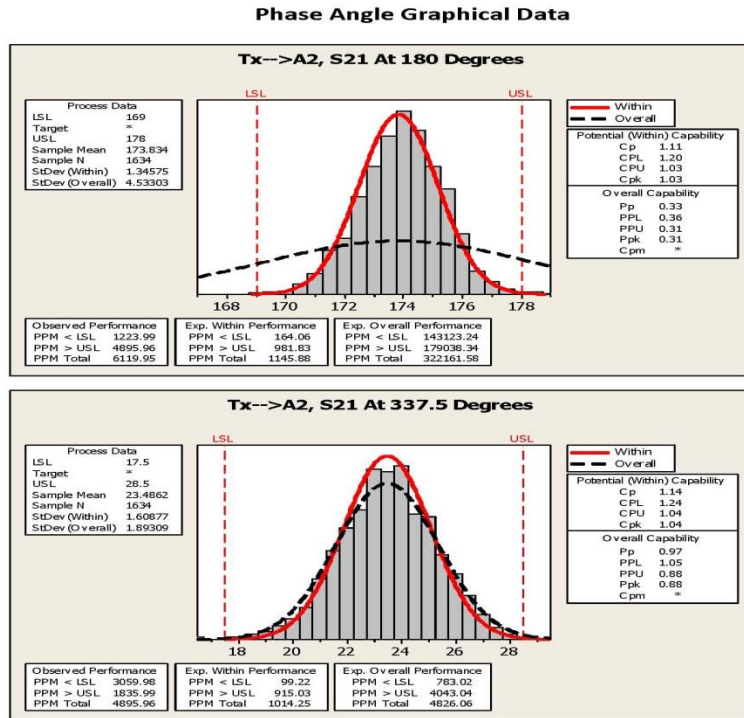


Phase Angle Graphical Data



Phase Angle Graphical Data





12. CONCLUSION

A full duplex, multi-channel, S-Band Transmit/Receive module has been achieved from its initial design through full production. The T/R module utilizes in excess of 90 MMICs. The manufacturing process was measured by statistical methods and a Cpk of greater than 1.33 was achieved. The module has a very high MTBF and the per unit production cost is well under \$200 for quantities of 50,000.

REFERENCES

[1] Sarjit Bharj, Paul Oleski, Boris Tomasic, and John Turtle, T/R module for satellite TT and C ground Link, US Patent# 7,071,873